Development, Implementation and Performance Report of Dimuon High Level Trigger of ALICE

by

Indranil Das
Saha Institute of Nuclear Physics
Kolkata

A thesis submitted to the
Board of Studies in Physical Science Discipline
In partial fulfillment of requirements
For the Degree of

DOCTOR OF PHILOSOPHY

of

HOMI BHABHA NATIONAL INSTITUTE

2011

Homi Bhabha National Institute

Recommendations of the Viva Voce Board

As members of the Viva Voce Board, we certify that we have read the dissertation prepared by Indranil Das entitled "Development, Implementation and Performance Report of Dimuon High Level Trigger of ALICE" and recommended that it may be accepted as fulfilling the dissertation requirement for the Degree of Doctor of Philosophy.

Date :

Chairman : **Prof. J. B. Singh**, Punjub University

Date :

Convener : **Prof. P. Mitra**, SINP

Date :

Guide : **Prof S. Chattopadhyay**, SINP

Date :

Member : **Prof. K. Kar**, SINP

Date :

Member : **Prof. A. K. Dutt-Mazumdar**, SINP

Date :

Member : **Prof. S. Saha**, SINP

Final approval and acceptance of this dissertation is contingent upon the candidates submission of the final copies of the dissertation to HBNI.

I hereby certify that I have read this dissertation prepared under my direction and recommended that it may be accepted as fulfilling the dissertation requirement.

Date :
Place :

STATEMENT BY AUTHOR

This dissertation has been submitted in partial fulfillment of requirements for an advanced degree at Homi Bhabha National Institute (HBNI) and is deposited in the Library to be made available to borrowers under rules of the HBNI.

Brief quotations from this dissertation are allowable without special permission, provided that accurate acknowledgment of source is made. Requests for permission for extended quotation from or reproduction of this manuscript in whole or in part may be granted by the Competent Authority of HBNI when in his or her judgment the proposed use of the material is in the interests of scholarship. In all other instances, however, permission must be obtained from the author.

INDRANIL DAS

DECLARATION

I, hereby declare that the investigation presented in the thesis has been carried out by myself. The work is original and has not been submitted earlier as a whole or in part for a degree / diploma at this or any other Institution / University.

INDRANIL DAS

অন্ধকারের উৎস হতে উৎসারিত আলো
সেই তো তোমার আলো ।
সকল দ্বন্দ্ব - বিরোধ - মাঝে জাগ্রত যে ভালো
সেই তো তোমার ভালো ।

— রবীন্দ্রনাথ ঠাকুর

Yours is the light
that breaks forth from the dark,
and the good that sprouts.
from the cleft heart of strife.

– *Rabindranth Tagore*

ACKNOWLEDGMENTS

It is the time of sunset at the seashore and when I look back, I discover a long busy day with colourful activities and golden moments. This small part of beach has been transformed into a lonely island which has the roaring sound of the waves and the long shadows of the trees. Undoubtedly, the longest shadow of the person through out this thesis work belongs to my supervisor Sukalyan Chattopadhyay. After six years of uninterrupted sharing of all serious and informal ideas, I find it hard to describe his role in single paragraph. In Hindu philosophy there is a concept of five fathers, জন্মদাতা, শিক্ষাদাতা, দীক্ষাদাতা, কন্যাদাতা, অন্নদাতা which are, father by birth, man who teaches us (guru), man who shows us path of spiritual life like the father of church, father in law, and the man who provides us food (boss), respectively. I have respected Sukalyan-da as guru-ji and without his constant courage, support and approval nothing was possible to accomplish.

The lonely moments force us nothing but to think. The soothing breeze with tiny water droplets is taking away my tiredness. It pulls me back to the night, when Volker Lindenstruth drove us (me and Jochen) to the ALI-CR2 where I found the first glimpse dismantled HLT machines. I am in debt to Volker Lindenstruth and Dieter Rohrich for their important suggestions at every stage and for the support during my stay at CERN. Probably the most interesting part of the HLT project is that it is fully operated by young students. I feel lucky to be the part of it and to have Jochen, Artur, Oystein, Timm, Matthias, Timo, Pierre, Arshad, Torsten, Stefan, Sergey, Kennith, Kalliopi, Svein, Federico, Olav as friends and collaborators. At one stage of the thesis work I was very confused with different tracking methods, when Ivan Kisel helped me to get rid of this confusions. I am thankful to him and Volker for the support. In addition, I am very much thankful to the dHLT team specially Corrado Cicalo, Zebulon Vilakazi and Bruce.

It is now the winter season in India, the most pleasant time for picnic and outing. In my childhood (and college life), I used to visit the big lakes of the forest close to our university, in order to watch the migratory birds from Siberia. They were the first foreign delegates. Since I started my research carrier, the winter season became the season for symposiums, conferences and workshops, the time when a large number of our foreign collaborators love to visit India. In the winter of 2005, I met with our foreign collaborators of "Forward" Muon Spectrometer, Gines Martinez, Christian Finck, Herve Borel, Florent Staley, Zebulon Vilakazi. This was a turning point, since then I became interested with AliRoot, offline activities of Muon Spectrometer and dimuon High Level Trigger (dHLT) and the wheel started to roll. After that meeting, I slowly acquainted with other collaborators like Philippe Crochet, Ivana Hrivnacova, Laurent Aphecetche, Ermanno Vercellin, Christophe Suire, Alberto Baldisseri, Philippe Pillot, Pascal Dupieux. They helped to understand the different components of the Spectrometer. The first version of dHLT code for hit-

reconstruction was implemented in AliRoot with the help from core offline people, Federico Carminati, Peter Hristov and Cvetan Cheshkov. At different stages of this thesis I have learned several important facts from Andreas Morsch, Matevz Tadel and Latchezar Betev and I owe to them for their patience and help.

However, the winter in CERN is not a very enjoyable time, which I have realized in the first visit. But, it is the warmth of the friends and colleagues like Badri, Jacob, Miranda, Sabyasachi (Gudda), Dilip, that helps to survive at this odd environment. In fact, in bigger sense I have to thank the point II crew and all ALICE members for the friendly atmosphere.

The memory pages of our brain does not follow the chronological order, therefore, the colleagues and friends who were associated with me even before the starting of this course appear at the bottom of the page. It is my greatest pleasure to have Sanjoy-da, Purnendu-da, Pradip-da, Dabasish-da, Santosh, Bhola, Satya, Safi, Bhabesh, Lipy-di, Dipankar-da, Sampa, Pappu-da and Sanjib-da around all the time, whenever I needed them. I would like to convey my sincere thanks to Suvendu Bose and Tinku Sinha for their suggestions and effort to maintain the homely atmosphere during the stay at CERN. I would also like to thank Abhee K. Dutt-Mazumdar and specially to Pradip Roy for the theoretical lessons of heavy ion collisions before the start of this thesis work. In similar way, I am also thankful to Dinesh Srivastava for the important discussions and suggestions regarding the HIJING Monte Carlo. People who know Bikash Sinha, would agree that the Indian effort to the QGP study at large scale has been started by him. But even within his busy schedule he always had time for the students and always tried to motivate us towards the fundamental laws of nature. I would like to thank him for his constant support at every stage whenever it was needed.

Now only the half of the sun is visible in the horizon and the birds are coming back to their nests. I remember the appreciation and courage of both of my families (by birth and in-law's) that always recharges me at the moment, when I am tired and shattered. I owe my life to my, father, mother, father-in-law, mother-in-law and two grown up children my sister and brother-in-law. In this occasion, I also like to thank our well wisher Kaushik Mazumder for sharing the wonderful moments with us.

This sunset at the seashore is the moment when the night slowly embraces the day light at a place where the earth kisses the sea. The ambiance reminds me the better half of mine, and I like to thank her for everything. A large part of this work is based on the sacrifice of the sweetest moments of our life. I am fortunate to have Gargi as wife and without her appreciation, adjustment, sacrifice nothing was possible to complete.

I am thankful to all of the above persons from the bottom of my heart to help me to complete this thesis work. When we remember people at our leisure time we do not mark them with their titles (Prof. or Dr.), but rather by their role in our life. Therefore, I apologize for my daring thanksgiving which I have cherished in the serene beach at Goa.

Lastly, I beg apology to all the people whom I have missed to mention in this page.

.

Contents

List of Figures

List of Tables

Listings

Chapter 1

Physics Motivation

A new journey of High Energy Physics has begun with the start of Large Hadron Collider (LHC). In the ultra-relativistic proton-proton collisions, the experiments of LHC namely, ALICE, ATLAS, CMS and LHCb are retesting and re-validating the few decades old Standard Model, which governs the basic laws of interaction of elementary particles. The search for the Higgs Boson is the central attention of the LHC program. But this is not the only interest of LHC operation. It extends to the search of CP violation for matter anti-matter asymmetry or the experimental verification of a entirely new theory named SUSY (Supersymmetry). There is possibility of a lot of exciting phenomena at LHC, such as the creation of miniature black holes which will decay immediately into the elementary particles by Hawking radiation.

But the understanding of such high energy phenomena is never complete unless the proper estimation of collective behaviour of collision is realized. Thus, ALICE (A Large Ion Collider Experiment) plans to study the heavy ion collision, in order to understand the bulk properties of matter. It is a dedicated experiment for the heavy ion physics of LHC. The main motivation of ALICE is to investigate the astounding

feature of phase transition of quantum fields under characteristic energy densities. This striking phenomena of phase transition is predicted by the collective feature of Standard Model. It is supposed that in this new phase, the quarks and gluons will exist as free particles unlike the bound states inside hadrons. Therefore, the new phase is known as Quark Gluon Plasma (QGP). The following sections describe the key concepts of Standard Model and a short review of the possible signatures of QGP.

1.1 Standard Model and Quark Gluon Plasma Phase transition

The Standard Model of particle physics provides the theoretical backbone concerning the electromagnetic, weak and strong nuclear interactions which mediate the dynamics of the known subatomic particles. The matter is built from quarks and leptons, also known as the "elementary particles" [see Fig. 1.1]. In the present Standard Model, there are six "flavors" of quarks. They can successfully account for all known mesons and baryons. The quarks are always observed to occur only in combinations of two quarks (mesons) and three quarks (baryons). The reason for the lack of direct observation is that, the color force does not drop off with distance like the other observed forces. It is postulated that it may actually increase with distance at the rate of about 1 GeV per fermi. A free quark is not observed because by the time the separation is on an observable scale, the energy is far above the pair production energy for quark-antiquark pairs. This idea of binding of quark bonds is known as quark confinement.

Another interesting feature of Standard Model is the asymptotic nature of strong forces. It is a property of gauge theories which predict that the interactions between

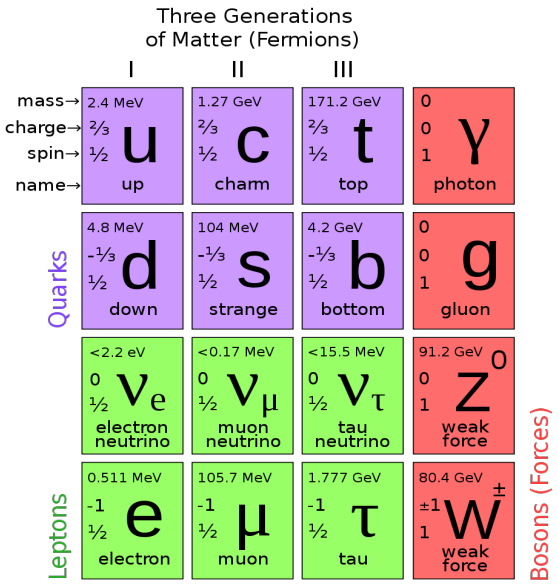

Figure 1.1: The three generation of quarks, leptons and the force carrying mediators.

the quarks (and gluons) become arbitrarily weak at shorter distances, i.e. length scales that asymptotically converge to zero (or, equivalently, energy scales that become arbitrarily large). This implies that in high-energy scattering, for large momentum transfer, when the quarks come very close together, they behave as free particles.

The concept of asymptotic freedom can be further extended to coalesce the neutrons and protons, by compression, so that the quarks and gluons can freely move within the domain of nucleus. The nucleus then is no more a nucleonic matter but a "quark matter". It was first suggested in 1970 by Naoki Itoh [1] during the description of stars with density more than hyperon stars, when the asymptotic freedom has not been proposed. He pointed out the possibility of unbound states of fundamental particles in the interior of the superdense stars. At a later stage, the formal derivation of the existence of quark matter from asymptotic freedom has been carried out by Collins and Perry 1975 [2].

It has been also realised that quark matter can be formed not just when the

density of baryons is large but also when the temperature becomes large. In 1978, Edward Shuryak [3] did the first high temperature computation, followed closely by Joseph Kapusta [4]. The rename of quark matter at finite temperature as Quark Gluon Plasma (QGP) was coined by Shuryak. The QCD predicts a phase transition, above a critical temperature T_c, from ordinary hadronic matter to a phase of deconfined quarks and gluons called the quark gluon plasma. The system of free quarks and gluons at high temperatures is also expected to have the QCD symmetry of color, i.e. chiral symmetry is restored. With the restoration of chiral symmetry, the (light) quarks are expected to regain their small current quark masses and appear as nearly massless particles compared to their larger constituent quark masses when confined inside hadrons.

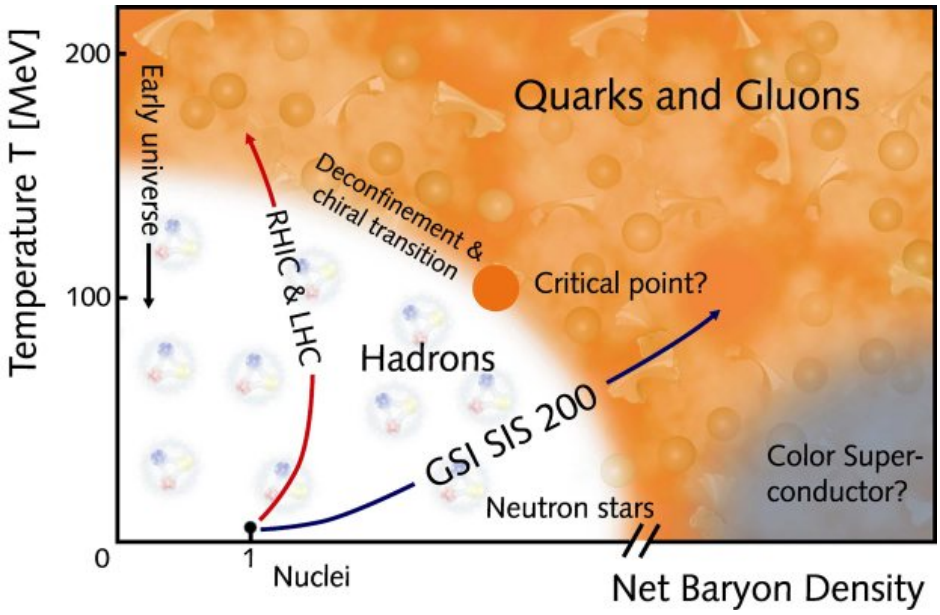

Figure 1.2: The phase diagram of strongly interacting matter, where the normal nuclear matter is shown as the black dot close to horizontal axis.

The phase diagram of the transition of strongly interacting matter from confined state to deconfined state is shown in Fig. 1.2. In the 1990s, the first signs of a new phase have been found in the form of anomalous suppression of J/Ψ at the CERN Super Proton Synchrotron (SPS). But the extent of suppression as predicted by SPS

was not cross confirmed by the similar experiment at Brookhaven National Laboratory (BNL). Therefore, the existence of a Quark Gluon Plasma was still in question in the beginning of this decade. However, the recent experimental data of Flow [5] and Fluctuation studies [6], back to back jet suppression in heavy ion collision [7] and several other indications of RHIC (Relativistic Heavy Ion Collider at BNL) show strong evidence for the existence of the QGP. Thus, the investigation of its properties and in-medium effects have moved into focus. Formerly considered to be a state like a gas where particles are loosely bound, QGP turned out to have more the character of a fluid.

The energy density and the strong coupling makes perturbative approaches of QCD inappropriate for theoretical calculations. The most used method for theoretical calculations and predictions is "Lattice Gauge Theory" where space-time has been discretized onto a lattice [8]. It predicts that at a critical temperature of $\simeq 170$ MeV, corresponding to an energy density of $\epsilon_{\mathrm{c}} \simeq 1$ GeV/fm^3, nuclear matter undergoes a phase transition to a deconfined state of quarks and gluons.

However, it is to be noted that the exact order of the phase transition is not known. The most recent calculations indicate that at zero chemical potential ($\mu_B = 0$), it is likely to be a smooth cross-over between the confined and deconfined state.

The concept of deconfinement is described as an effect of color screening. The confining potential between the quark and anti-quark separated by a distance r can be written in the form:

$$V(r) \sim kr - \frac{\alpha_{eff}}{r}, \tag{1.1}$$

where α_{eff} is the effective coupling constant and $k \simeq 0.8$ GeV/fm is the string tension. This expression shows that to break a hadron into its colored constituents an infinite

amount of energy is required.

On the other hand, atomic physics suggest that in a dense medium, the presence of many charges induce a charge screening, which reduce the range of the forces between the charges and can be responsible for the dissociation of bound states. The Debye-Huckle theory for plasma of electric charges predict a change in the $1/r$ term in the coulomb potential in the following way:

$$V(r) \sim \frac{1}{r} \rightarrow \frac{1}{r} e^{-\mu r} \rightarrow \frac{1}{r} e^{-\frac{r}{\lambda_D}} \tag{1.2}$$

where $\lambda_D (\mu \equiv \frac{1}{\lambda_D})$ is the Debye radius that represents the range of the effective forces. It depends on the medium density and it decreases with increase of density. According to Mott's theory, if the Debye radius is smaller than the Bohr radius we have a metal, otherwise we have an insulator. The same argument can be extended to Eqn. 1.1 as the quarks carry the colour charge and then the expression for screened inter-quark potential is,

$$V(r) \sim kr \rightarrow kr \left[\frac{1 - e^{\mu r}}{\mu r} \right] - \frac{\alpha_{eff}}{r} e^{-\mu r}. \tag{1.3}$$

As for the electric charge case, we can expect that if μ^{-1} is bigger than the typical hadron size, we have a color insulator hadronic matter made of colorless bound state, while in the other case, we have a color conductor plasma state made of deconfined colored quarks and gluons.

The possible existence of this deconfined state of matter is explored in the heavy ion collisions.

1.2 Heavy Ion Collision and Experimental observables

The ultra-relativistic nucleus-nucleus collisions are described by Bjorken's hydrodynamical model [9]. In the centre of mass frame of the colliding nuclei at relativistic energies, the shape of the nuclei are viewed as two thin disks due to Lorentz contraction along the longitudinal direction [see Fig. 1.3]. The particles with wide range of momentum distribution are produced after the collision as shown in right side of the figure. It has been pointed out [Ref. [10]], that the hadrons with low energy are produced after the high energy hadrons. This feature of nucleus-nucleus collision is the known as the inside-outside cascade.

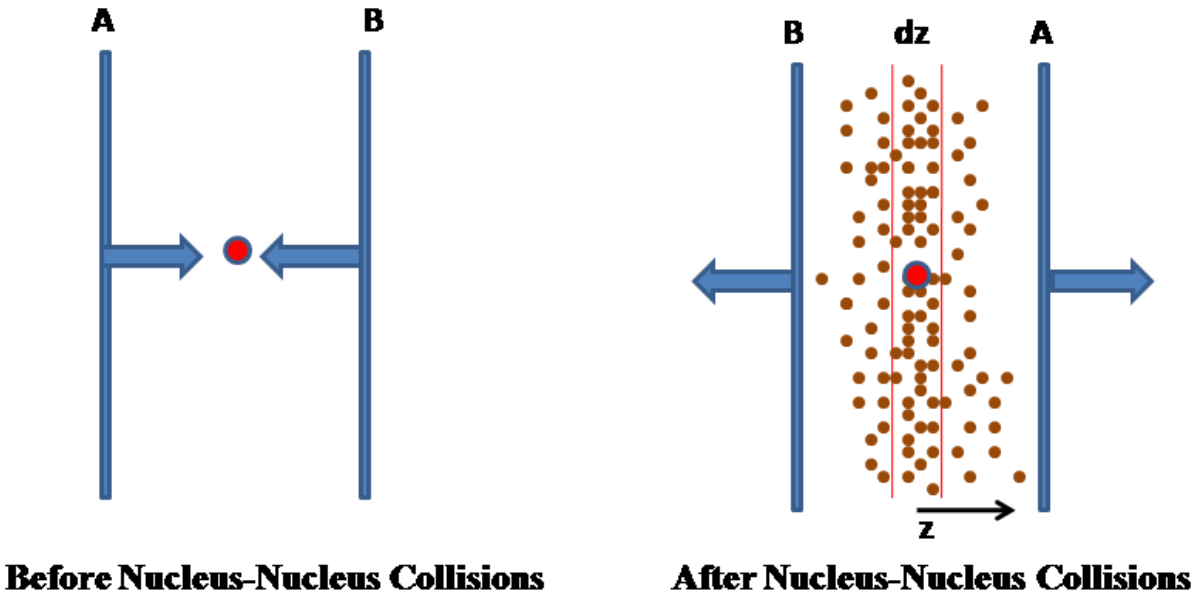

Figure 1.3: The geometry of high energy nucleus nucleus collision, where the nuclei are squeezed to straight line due to Lorentz contraction along the direction of motion (i.e. longitudinal direction). The figures on the left and right side show nuclei before and after the collision, respectively.

The space time evolution of nucleus-nucleus collisions are shown in Fig. 1.4. In the left side of the figure, the evolution has been shown for no QGP. Whereas, the

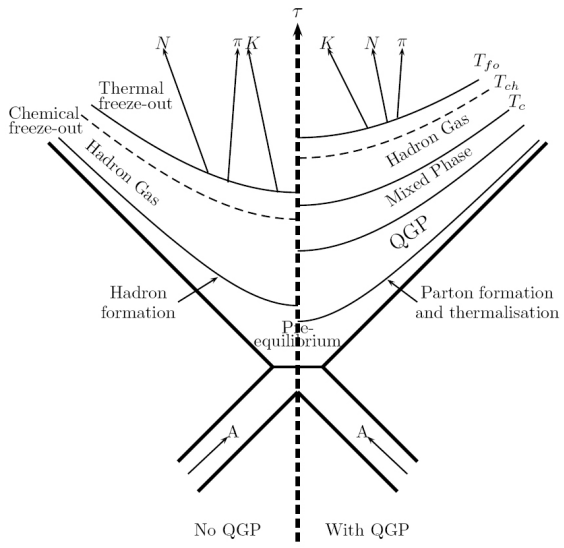

Figure 1.4: The space time evolution of heavy ion collisions are shown for two scenarios with (right side) or without (left side) the formation QGP, where the vertical axis shows the proper time in the centre of mass fame of the colliding nuclei. The lines of constant temperature indicate the hadronization (T_c), chemical freeze-out (T_{ch}) and kinetic freeze-out temperature(T_{fo}).

scenario of expected formation of thermalised quark-gluon plasma is shown in the right side of the figure.

The variables and notation for the understanding of nucleus-nucleus collision are described below,

Kinematic variables

The properties of the high energy collisions are studied using the following kinematic variables,

- **Transverse momentum :** The transverse momentum of a particle with momentum (p_x, p_y, p_z) is defined as

$$p_t = \sqrt{p_x^2 + p_y^2}$$

- **Transverse mass :** In the similar way, the transverse mass of a particle with rest mass m is defined as,

$$m_t = \sqrt{p_t^2 + m^2}$$

- **Rapidity :** Often in high energy physics theory, the evolution of the collision is characterized by a dimensionless quantity, which is known as rapidity. It is related with the energy E and longitudinal momentum component p_z as,

$$y = \frac{1}{2} \ln \left(\frac{E + p_z}{E - p_z} \right). \tag{1.4}$$

The rapidity is not an Lorentz invariant quantity, but changes by an additive constant. If y_A and y_B represents the rapidity of a particle in two reference frames A and B, respectively, under Lorentz boost along the z-direction, they are related as,

$$y_A = y_B + y_\beta$$

Where,

$$y_\beta = \frac{1}{2} \ln \left(\frac{1 + \beta}{1 - \beta} \right)$$

with $\beta = v/c$.

- **Pseudorapidity :** In experiments, sometimes the kinematic properties of the

particles are expressed in terms of pseudorapidity variables instead of rapidity, which is defined as,

$$\eta = -\ln\left[\tan\left(\frac{\theta}{2}\right)\right] = \frac{1}{2}\ln\left(\frac{|\vec{p}| + p_z}{|\vec{p}| - p_z}\right). \tag{1.5}$$

where, θ and $|\vec{p}|$ are the angle of particle trajectory with respect to beam axis and magnitude of momentum, respectively. It is more useful in case of detectors where the energy of the particles are not directly estimated using calorimeters. Using Eqn. 1.4 and 1.5 the rapidity y can be expressed in terms of pseudorapidity η as,

$$y = \frac{1}{2}\ln\left[\frac{\sqrt{p_T^2\cosh^2\eta + m^2} + p_T\sinh\eta}{\sqrt{p_T^2\cosh^2\eta + m^2} - p_T\sinh\eta}\right].$$

and vice-verse as,

$$\eta = \frac{1}{2}\ln\left[\frac{\sqrt{p_T^2\cosh^2 y + m^2} + p_T\sinh y}{\sqrt{p_T^2\cosh^2 y + m^2} - p_T\sinh y}\right].$$

If the particle have a distribution $dN/dydp_T$ in terms of the rapidity variable y, then the distribution in terms of the pseudorapidity variable η is

$$\frac{dN}{d\eta dp_T} = \sqrt{1 - \frac{m^2}{m_T^2\cosh^2 y}}\frac{dN}{dydp_T}. \tag{1.6}$$

Experimental observables

A experiment can not directly probe the evolution of the nucleus-nucleus collisions, but several indirect model dependent methods are applied on the experimental data to back-trace the nature of collisions. Therefore, it is essential

to study the properties of the collisions using all possible observables in order to test the expected formation of the QGP. The ALICE is studying the following observables to understand the collision dynamics.

1. **Particle Multiplicity**
2. **Particle Spectra**
3. **Particle Correlation**
4. **Fluctuations**
5. **Jets**
6. **Direct Photons**
7. **Dileptons**
8. **Heavy quarkonia study**

1.2.1 Particle multiplicities

Since the energy density of the initial fireball after collision is the key parameter in the analysis of heavy ion physics, one of the important observable of the heavy ion experiments is the charged particle multiplicity distribution (or in short multiplicity distribution). The charged particle multiplicity per rapidity (rapidity density) is related with the energy density ϵ_0 averaged over the transverse overlapping area A of colliding nuclei as,

$$\epsilon_0 \propto \frac{1}{A\tau_0}\frac{dN}{dy}\bigg|_{y=0} \tag{1.7}$$

where τ_0 is the proper time in the centre of mass frame of the nuclei. In the experimental measurements the pseudorapidity density is more favourable observable

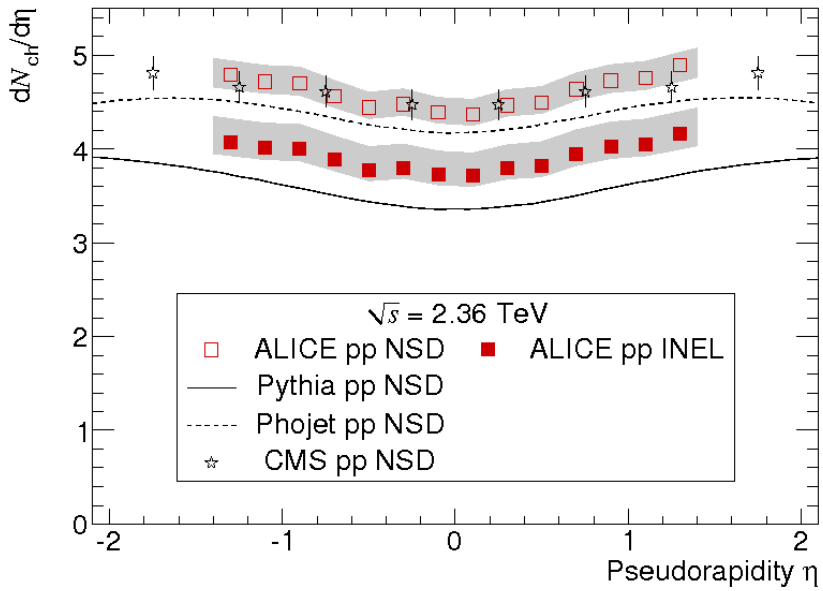

Figure 1.5: The pseudorapidity distribution of ALICE for inelastic (INEL) and non-single diffractive (NSD) collisions for p-p collision at $\sqrt{s} = 2.36$TeV [11].

compared to rapidity density due to its simple dependence on single track parameter (i.e. track angle with beam axis). The pseudorapidity distribution of ALICE in the p-p run at $\sqrt{s} = 2.36$ TeV is shown in Fig. 1.5, for inelastic and non-single diffractive collisions. It is observed from the figure that in both cases the PYTHIA fail to explain the enhanced multiplicity spectra. The dependency of rapidity distribution with $\sqrt{s}$ is shown in Fig. 1.6. An increase of $57.6\%\pm0.4\%(\text{stat.})^{+3.6}_{-1.8}(\text{syst.})$ has been found for $\mathrm{dN_{ch}/d}\eta$ measurement at $\sqrt{s} = 7$ TeV when compared with 900 GeV pp collisions. In case of heavy ion collision, the energy density can be calculated from the pseudorapidity density using Eqn. 1.7 and p_{t} integrated relation of Eqn. 1.6.

1.2.2 Particle spectra

In nucleus-nucleus collision a large number of particles are produced in the low transverse kinetic energy (<2 GeV) from the late hadronic freeze-out [(T_c) of

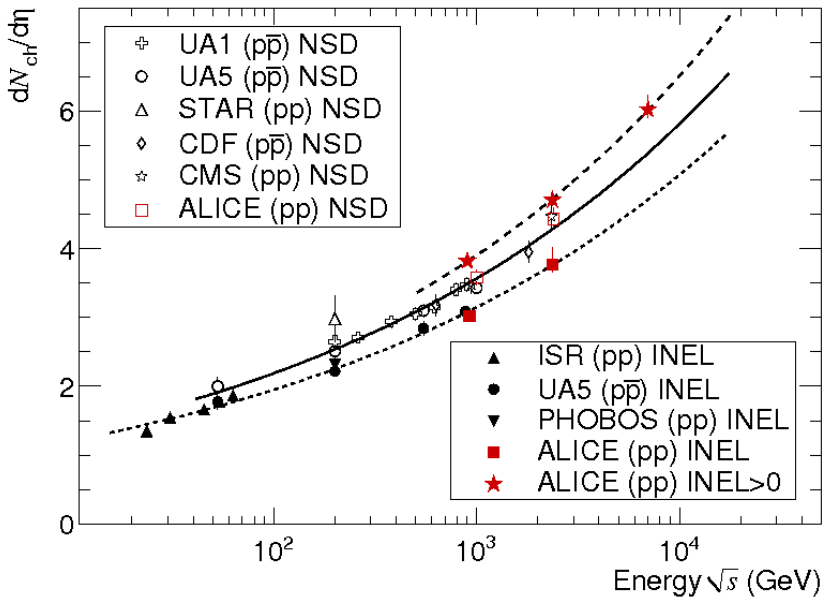

Figure 1.6: The Charged-particle pseudorapidity density in the central pseudorapidity region $|\eta| < 0.5$ for inelastic and non-single-diffractive collisions, and in $|\eta| < 1$ for inelastic collisions with at least one charged particle in that region (INEL>0 $|\eta|$ <1), as a function of the centre of mass energy [12].

Fig. 1.4] stage of the evolution. Since these particles are emitted from the later stage of evolution, these are useful for the study of the Chemical and Kinetic freeze-out and particle Flow [8, 13, 14, 15, 16, 17, 18].

Chemical and Kinetic freeze-out

After the first impact, the matter produced expands and cools down to attain a state called *pre-equilibrium state*. This state then evolves to a state of interactive hadron gas, either from the QGP phase or not [see Fig. 1.4]. The temperature of conversion of QGP state to interactive hadronic state is called *Chemical freeze-out* temperature. But since the fireball has not yet expanded, the hadrons interact among themselves, to create other species of hadrons by method of rescattering. These hadronic reactions stop when the system expands and hadrons move far apart so that they no longer interact and the corresponding temperature is called *Kinetic freeze-*

out temperature. This freeze-out temperature of a specific hadron group is estimated from the $p_{\rm t}$ spectrum of that group.

Flow

The collective spacial expansion of the fireball created in nucleus-nucleus collision is termed as *Flow*. In a perfect head-on collision of heavy ion nuclei, the expansion is isotropic, whereas for non-central collision it follows anisotropic expansion pattern. The shape of the expansion in the transverse plane of the collision is found out by the Fourier expansion of the density distribution into the azimuthal angles (φ) as

$$\frac{{\rm d}N(b)}{{\rm d}y\, m_{\rm t}{\rm d}m_{\rm t}{\rm d}\varphi} = \frac{1}{2\pi}\frac{{\rm d}N(b)}{{\rm d}y\, m_{\rm t}{\rm d}m_{\rm t}}\Big(1 + 2v_1(p_{\rm t}, y; b)\cos(\varphi) + 2v_2(p_{\rm t}, y; b)\cos(2\varphi) + \dots\Big).$$

where $m_{\rm t}$ and b are the transverse mass and impact parameter, respectively. The coefficient of direct flow (v_1) at mid-rapidity ($y = 0$), vanishes due to symmetry and the first nonzero coefficient (also called *elliptic flow coefficient*) $v_2(p_{\rm t}; b)$ is the largest among all other non-zero coefficients [5]. It is expected that due to high initial energy density in heavy ion collision at LHC, the elliptic flow is generated before the hadronization. Thus, a systematic comparison of v_2 from the azimuthally averaged spectra, for different types of hadrons at given freeze-out will correspond to the ratio of pressure to energy density of the initial QGP state [19]. The recent results of elliptic flow signal, v_2, in Pb-Pb collisions at $\sqrt{s_{\rm NN}}$=2.76 TeV has been measured as $0.087 \pm 0.002(stat) \pm 0.004(sys.)$ using 4-particle correlation method averaged over $p_{\rm t}$ and η for 40-50% centrality [Ref. [20]]. This is about 30% increase in the elliptic flow as compared to RHIC Au-Au collision at $\sqrt{s_{\rm NN}}$=200 GeV.

1.2.3 Particle correlations

The particle correlation technique provide a useful method to study the size of the fireball, its expansion, and its phase-space density. It is also possible to calculate the timing of hadronization or the sequence of emission of individual species (Refs. [21, 22, 23]). At high particle multiplicity, the two types of methods are followed to study the properties of evolution of collision are,

- Hanbury-Brown-Twiss Effect
- Final State Interaction

Hanbury-Brown-Twiss (HBT) Effect

A correlation method of two photons have been used to measure the angular diameter of distant star by Hanbury-Brown and Twiss [24]. Similar method has been applied to study the size and evolution of the fireball by photon [25] and pion interferometry [26]. The order of phase transition during the first impact of collision using this method. If $P(k)$ and $P(k_1, k_2)$ represents the single particle and two particles momentum distributions, respectively, the correlation function is defined as,

$$C(k_1, k_2) = \frac{P(k_1, k_2)}{P(k_1)P(k_2)}$$

The ratio of the inverse width of this two particle correlation function along the outward and sideward direction is used to calculate the lifetime of the emitted source [27]. These HBT radius of ALICE experiment shows an increasing behaviour with the increase of event multiplicity [Ref. [28]].

Final State Interaction (FSI)

The HBT effect arises due to the momentum correlation of the identical particles, whereas the final state interaction method uses the correlation of the non-identical particles to study the emission time of the different species of hadrons. This is achieved by taking the ratio of two correlation functions with opposite orientation of their relative momentum vector $k_1 - k_2$. The correlation asymmetry in the outward direction is determined by the difference of emission times of the hadronic species used [29] and by the intensity of the transverse collective flow [30]. Thus, FSI is an useful method to probe the hot matter produced in nucleus-nucleus collisions.

1.2.4 Fluctuations

The physical quantities which measure the properties of the collisions exhibit fluctuations. The fluctuations arise from different sources, for instance, the fluctuations of an observable of system reflect the bulk properties of the system or the fluctuation in the charge particle multiplicity in the central rapidity reflects the susceptibility of the system under external electrostatic field. But most interestingly, the study of the fluctuations of multiplicity is helpful to identify the order of phase transition. In case of first order phase transition or smooth cross over a large fluctuation in multiplicity in a given rapidity interval is expected as compared to a second order phase transition [6]. Therefore, the fluctuation study is useful to understand the evolution of the system. It is interesting to note that heavy ion collisions at LHC energies will produce substantially larger particle multiplicities [31], which will allow event-by-event fluctuation studies for the first time.

1.2.5 Jets

In hard nucleus-nucleus collisions, the scattered partons are sometimes emitted with a large cascade of secondary partons. This bunch of partons when transformed into the hadrons at the final stage produce a large hadronic flux along the direction of first pair of scattered partons, which is known as Jets. If a hot equilibrated medium is formed after the collision and a scattered parton propagates through this medium, the momentum of the parton will be modified due to collisional and radiative energy losses. These effects are studied for back to back jets to experimentally measure the

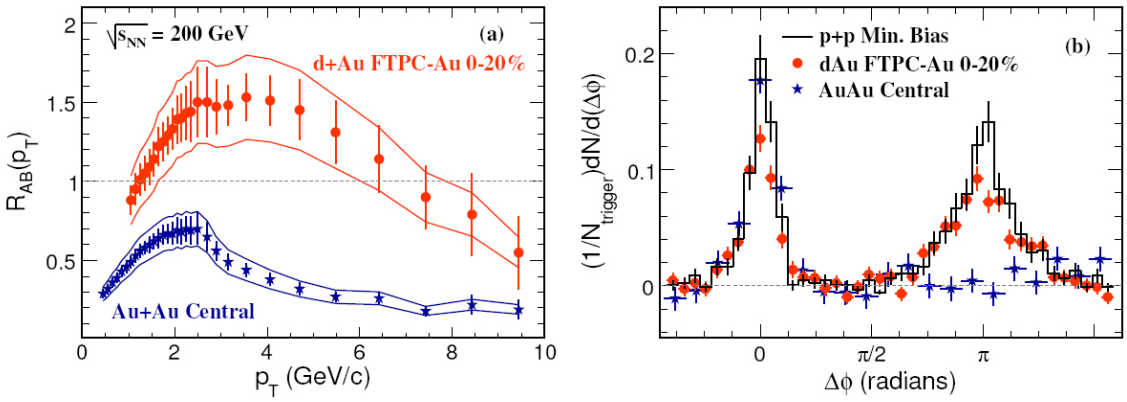

Figure 1.7: The left figure shows the nuclear modification factor R_{AA} and the right figure shows the azimuthal distribution of back to back jets for pp and nucleus-nucleus collisions at RHIC energies [7].

formation of hot hadronic or quark matter. The figure 1.7 shows effect of momentum broadening due to partonic energy loss inside hot fireball by STAR collaboration [7]. The left figure shows the large suppression in hadron production at large p_t for d-Au and central Au-Au collisions. It is also observed from this figure that central Au-Au is more suppressed than the d-Au collisions. The right figure shows that back to back jets are more suppressed in the central Au-Au collisions than that in the d-Au collisions. This is indicative of more dense matter which is formed in central Au-Au collisions compared to d-Au and the jets passing through this dense medium are

suppressed. This observation opens up the possibility of the creation of a superdense matter in nucleus-nucleus collisions at LHC.

1.2.6 Direct photons

The photon as probe to study the properties of matter, is the oldest of all known observables. The main reason is that it carries unscattered information about the state of their formation. In nucleus-nucleus collision, the photon being an electro-magnetically interacting particle, carries the signature of initial state of the collision. Since the hard photons are produced from partonic scattering, the momentum distribution of these photons corresponds to the partonic momentum distribution. But the photons are emitted from all stages nucleus-nucleus collisions, such as,

- photons from the pre-equilibrium state of the collision
- photons produced in QGP (if any)
- photon emission from during the phase transition
- photons from the hadronic phase after chemical freeze-out
- photons from the hadronic decays after kinetic freeze-out (also known as decay photons)

The photon of the first four stages are called *direct photons*, which are grouped in two categories according to nature of their origin,

- *Prompt* photons are produced from the hard process at the very first moment after collision.

- *Thermal* photons are the rest of photons that are emitted after the equilibrium has been achieved for QGP or the hadronic phase

Therefore, the study of the photon spectrum is an important marker of evolution of the fireball in p-p and A-A collisions [32].

1.2.7 Dileptons

In a similar way of photon radiation from all stages, the lepton pairs are also emitted throughout the evolution of the system. The dilepton sources in nucleus-nucleus collisions are, prompt production from hard collisions, thermal generation from the QGP and hot hadronic phases, and as final-state meson decays after freeze-out. The momentum distribution of the prompt and thermal dileptons closely follow momentum distribution of quark-antiquark pair. The prompt contribution in the dilepton mass range above pair mass $M \sim 2$ GeV is dominated by semileptonic decays of heavy-flavour mesons and by the Drell-Yan process [33]. It is found from theoretical calculations that the dilepton mass above ∼1.5 GeV thermal radiation is sensitive to temperature variations and thus believed to be originated from the early hot phases. Therefore, the physics objective [34, 35] is to discriminate of thermal QGP radiation from the large prompt background [33]. However, at low masses, less than 1.5 GeV, thermal dilepton spectra are dominated by radiation from the hot hadronic phase [36].

1.2.8 Heavy-quark and quarkonium production

The study of heavy quarks (charm and bottom) and quarkonium spectra provide an important tool to probe the expected formation of QGP. Since the heavy quarks

are produced at a very earlier stage ($1/m_Q$) of collision and have long lifetime, they are expected to live through the thermalisation phase of the plasma (if present). If the heavy quark pair create a quarkonium bound state (J/Ψ for $c\bar{c}$ and Υ for $b\bar{b}$) before the expected formation of QGP, it will pass through the deconfined state of QGP. It has been proposed that the heavy quarkonium will then melt due to color screening in the deconfined medium [37].

As the binding energies are different for different resonances, the resonance with lowest binding energy is expected to melt first inside QGP. Therefore, a study of sequential suppression of different resonance species produce more convincing results of the formation hot deconfined matter (see Fig. 1.8). The suppression of J/Ψ and

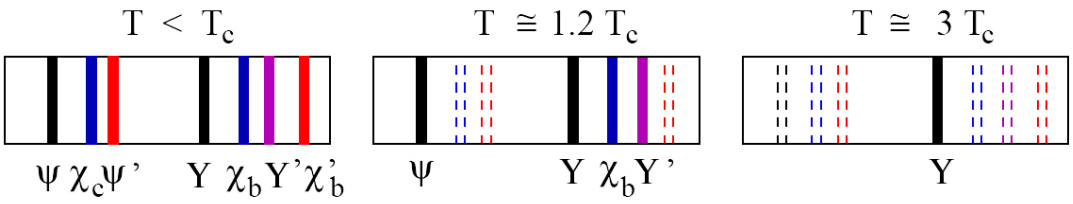

Figure 1.8: The sequential suppression of different heavy quark resonances

Ψ' production relative to Drell-Yan continuum has been reported at SPS energies ($\sqrt{s_{NN}}$ = 17.3 AGeV) for central nucleus-nucleus collisions [38]. It has been found that the Ψ' is more suppressed than J/Ψ. But interestingly the ratio of J/Ψ to Ψ' has been found to be constant for proton-proton and proton-nucleus collisions.

The ratio of measured J/Ψ to the conventionally expected production has been plotted as a function of the energy density in Fig. 1.9. It indicates a clear suppression of J/Ψ production for the central Pb-Pb collisions at SPS.

However, the PHENIX experiment [39] of the Relativistic Heavy Ion Collider (RHIC) at energy $\sqrt{s_{NN}}$ = 200 GeV, has reported that the suppression observed in

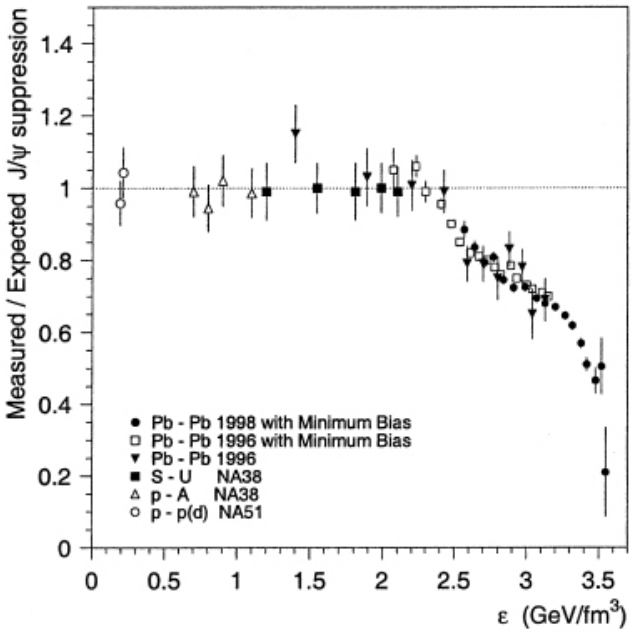

Figure 1.9: The ratio of measured J/Ψ production to the conventional expectation as a function of the energy density produced in the collision is measured by the NA50 experiment at SPS

this experiment does not scale with SPS as a function of energy density. The models which explain the lower energy J/Ψ data at the Super Proton Synchrotron (SPS) invoking only J/Ψ melting based on the local medium density, predict a significantly larger suppression at RHIC. In addition, it has been suggested from SPS extrapolation that more suppression at mid rapidity is expected than at forward rapidity for RHIC energies. But a opposite scenario has been observed in PHENIX.

In RHIC the modification have been measured in terms of nuclear modification factor R_{AA} as,

$$R_{AA} = \frac{d^2N^{AA}_{J/\Psi}/dp_T dy}{N_{coll} d^2N^{pp}_{J/\Psi}/dp_T dy} \tag{1.8}$$

where $d^2N^{AA}_{J/\Psi}/dp_T dy$ being the J/Ψ yield in Au-Au collisions, N_{coll} the corresponding mean number of binary collisions and $d^2N^{pp}_{J/\Psi}/dp_T dy$ the J/Ψ yield in p-p inelastic collisions. The Fig. 1.10(I) shows the R_{AA} of J/Ψ vs. p_T for different centrality

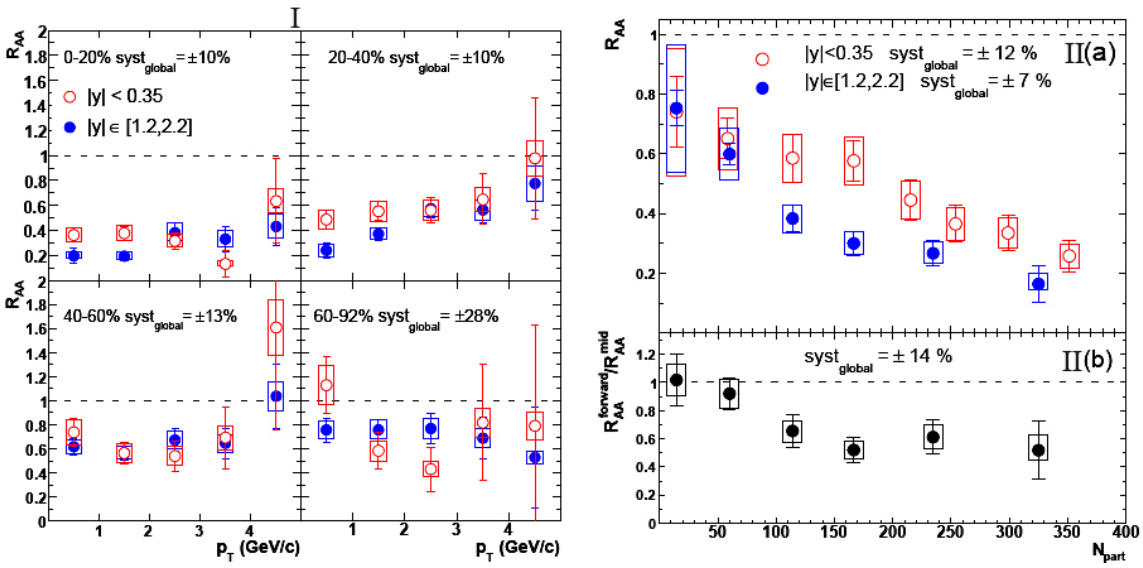

Figure 1.10: (I) The R_{AA} of J/Ψ vs. p_T for different centrality bins, (II a) R_{AA} of J/Ψ vs. N_{part} and (II b) ratio of forward/mid rapidity R_{AA} vs. N_{part}, in $Au + Au$ collisions at $\sqrt{s}$ = 200 GeV/nucleon at RHIC.

bins and Fig. 1.10(II a) shows the p_T integrated R_{AA} vs. N_{part} at mid and forward rapidity. It is observed that for each rapidity, R_{AA} decreases with increasing N_{part}. The Fig. 1.10(II b) shows ratio of forward/mid rapidity R_{AA} vs. N_{part}. The ratio first decreases then reaches a plateau of about 0.6 for $N_{part} > 100$. This appearance of plateau region has not been expected from SPS data, which suggests that probably there is effect of recombination in RHIC energy.

Thus, ALICE will play a crucial role to study properties of the fireball formed in nucleus-nucleus collision through the suppression/enhancement pattern of heavy quark resonances. ALICE Muon Spectrometer will measure both J/Ψ and Υ yields at LHC energies. This feature will help to investigate the recombinatorial effects, since ∼115 $c\bar{c}$ pairs are expected to be produced in central Pb-Pb collision, while only ∼5 $b\bar{b}$ pairs [see Table 6.53 of Ref. [40]] are expected and this will indicate that Υ yield is not expected to have any contribution due to recombination.

In the next section the results of a simulation study has been discussed using the HIJING (Heavy Ion Jet Interaction Generator, version 1.3) Monte Carlo program. The motivation for this study is to understand the underlying physics processes in heavy-ion collision.

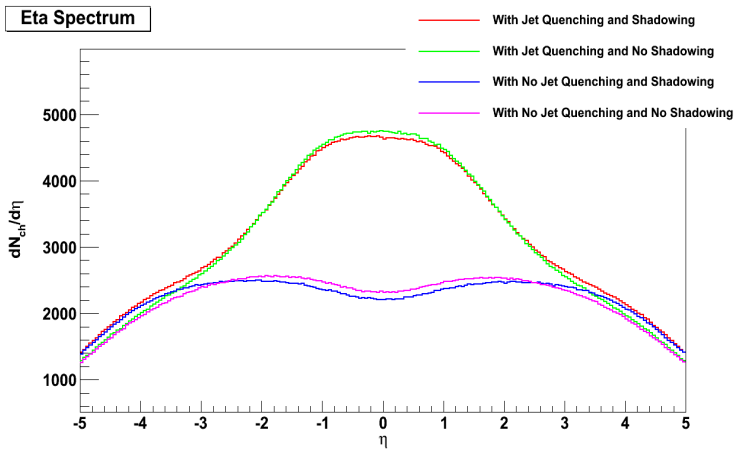

(a) The charged particle η-distribution for a combination of with or without jet quenching and nuclear shadowing effects in case of most central (10%) Pb-Pb collision at 5.5 TeV/nucleon

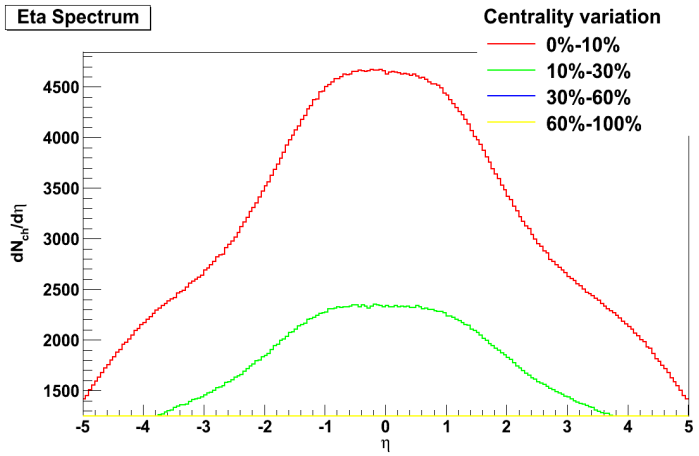

(b) The charged particle η-distribution at different centrality bins for Pb-Pb collision at at $\sqrt{s} = 5.5$ TeV/A with jet quenching and shadowing effect

Figure 1.11: The event averaged charged particle η-distribution for Pb-Pb at $\sqrt{s} = 5.5$ TeV/A.

1.3 Simulation of heavy ion collisions at LHC energies

1.3.1 HIJING Generation Method

HIJING is a Monte Carlo program, for particle production in hadron-hadron (h-h) collisions. It is based on the generation of the multiple minijets in the h-h collisions, which then transformed to the final products of hadrons and leptons. The QCD interactions of the partons are calculated by the perturbative methods using PYTHIA (Monte Carlo program for proton-proton collision), which are incorporated into the multiple minijets production via the pQCD models. In order to scale for the nucleus-nucleus (A-A) collision, the Glauber model is used to calculate the multiple proton-proton interactions. In addition, it uses a parametrised parton distribution function to incorporate the parton shadowing. It also includes the Jet Quenching mechanism of the partons through the dense medium produced in the collision and Lund jet-fragmentation model for hadronization of the jets. The detail explanation of HIJING can be found in Ref. [41].

1.3.2 HIJING Simulation

It has been pointed out in Eqn. 1.7 that the first observable to measure in the relativistic collision is the pseudorapidity (η) distribution of produced charge particles, since it can be used to estimate the energy density of the fireball produced. In Fig. 1.11, the event averaged pseudorapidity distribution has been plotted for Pb-Pb collision at $\sqrt{s}$ = 5.5 TeV/A. Since jet quenching and nuclear shadowing play important roles to determine the temperature of the fireball and hence the phase

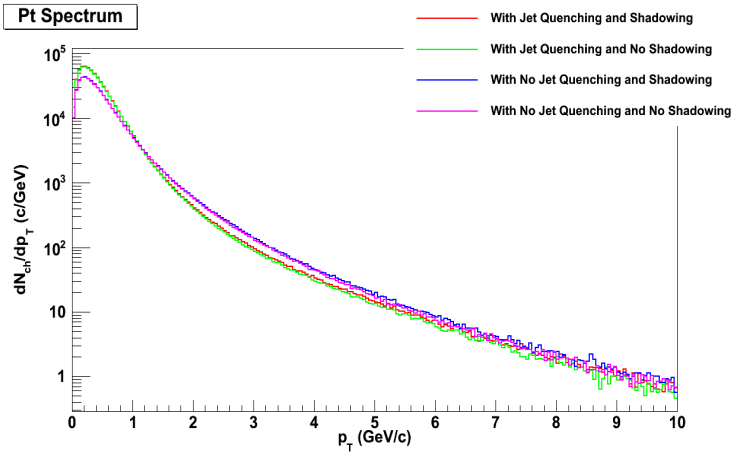

(a) The charged particle p_{t}-distribution for a combination of with or without jet quenching and nuclear shadowing effects in case of most central (10%) Pb-Pb collision at 5.5 TeV/nucleon

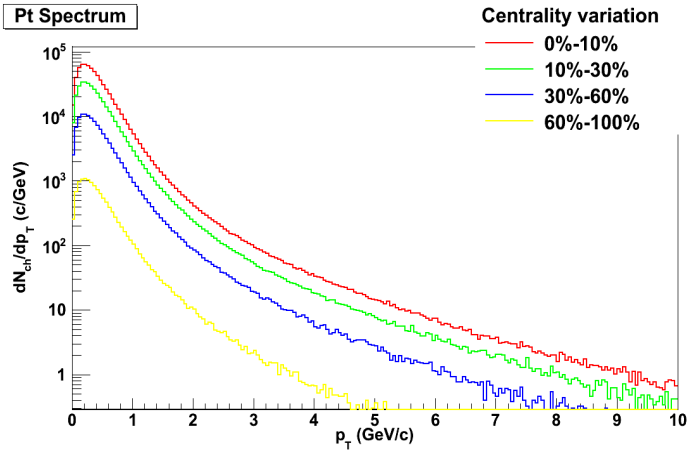

(b) The charged particle p_{t}-distribution at different centrality bins for Pb-Pb collision at at $\sqrt{s} = 5.5$ TeV/A with jet quenching and shadowing effect

Figure 1.12: The event averaged charged particle p_{t}-distribution for Pb-Pb at $\sqrt{s} = 5.5$ TeV/A.

transitions, a combination of the jet quenching and shadowing effect has been studied in Fig. 1.11(a) for most central (10%) collisions. It is found from the figure that a larger number of particles with low p_{t} are produced in the presence of jet quenching phenomena. This can be understood as when a partonic jet is quenched in the dense medium it fragments into a large numbers partons which results into the increase

of number of particles produced with low $p_{\rm t}$. The effect can also be seen in the figure 1.12(a), where a large number of low $p_{\rm t}$ particles are produced in case of jet quenching compared to the scenario of no jet quenching. The effect of shadowing of the parton distribution function inside the nucleus is also manifested in Fig. 1.11(a). Since in the presence of shadowing the cross section of the minijets are reduced, therefore, less number of particles are produced in the transverse direction due to the influence of shadowing. This effect is less visible in the $p_{\rm t}$ spectrum of figure 1.12(a) due to the stronger effect of jet quenching. However, the influence of quenching or nuclear shadowing effect is not visible in the net baryon pseudorapidity spectrum in Fig. 1.13(a).

The figure 1.13(a) clearly shows that a net baryon free region is produced in the mid-rapidity region in the Pb-Pb collision at $\sqrt{s}$ = 5.5 TeV/A. However, it is interesting to note that the net baryon density does not vanish for Au-Au collisions at $\sqrt{s}$ = 200 GeV/A in RHIC [see Fig. 1.13(b)]. Therefore, for the first time at LHC an net baryon free region is produced, which will be ideal place to test the Lattice QCD calculations [Ref. [42]]. The recent measurements of $p\bar{p}$ ratio in the mid rapidity region of ALICE experiment has been found to be unity [Ref. [43]], which is a clear indication to the possibility of net baryon free region in Pb-Pb collisions at $\sqrt{s}$ = 5.5 TeV/A.

The expected variation of the particle production with centrality is shown in figures 1.11(b), 1.12(b) and 1.13(c). It is found form the figures that the particle abundance is governed by the centrality of the collision. The $p_{\rm t}$-spectrum shows the information about soft and hard scattering processes [44]. The calculations predict almost a factor of two increase in particle production for most central (0-10%) compared to the peripheral (60%-100%) collisions for Pb-Pb collisions at $\sqrt{s}$ = 5.5 TeV/A.

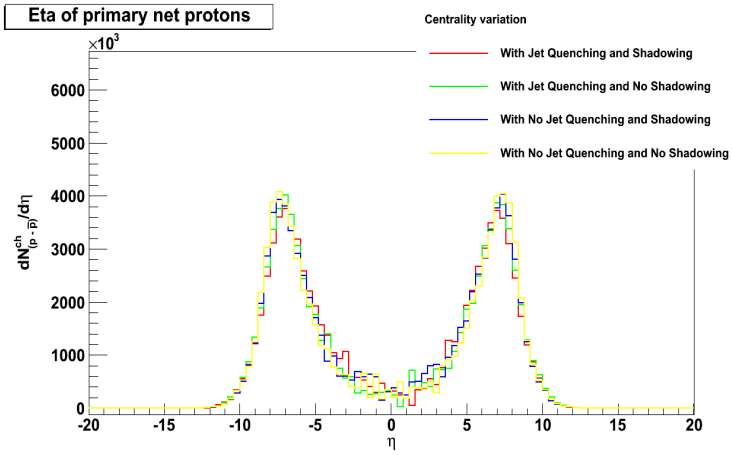

(a) The net baryon η-distribution for a combination of with or without jet quenching and nuclear shadowing effects in case of most central (10%) Pb-Pb collision at 5.5 TeV/nucleon

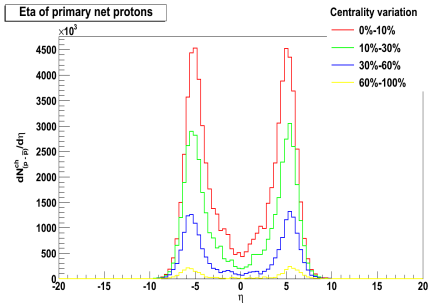

(b) The net baryon η-distribution at different centrality bins for Au-Au collision at at $\sqrt{s} = 200$ GeV/A with jet quenching and shadowing effect

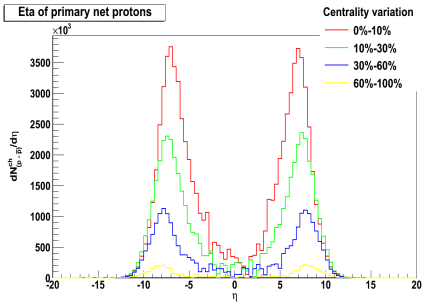

(c) The net baryon η-distribution at different centrality bins for Pb-Pb collision at at $\sqrt{s} = 5.5$ TeV/A with jet quenching and shadowing effect

Figure 1.13: The event averaged net baryon η-distribution for Pb-Pb at $\sqrt{s} = 5.5$ TeV/A.

Strangeness enhancement has been identified as a possible signature for the formation of QGP. This has been reported in terms of K/π ratio in the Au-Au collisions at RHIC in Ref. [45]. This data shows a large production of strange quarks ($K^+ = u\bar{s}$) in the heavy ion collisions, which gets slowly saturated when the energy is increased beyond 20 GeV/A. The figure 1.14 shows that the enhancement of K^+/π^+ and K^-/π^- ratios at low energies is not accounted by the present simulation with HIJING-1.3. The increase of K^+/π^+ compared to K^-/π^- close to 5 GeV center of

mass energy is attributed due to increased K^+ production compared to K^-, whereas, the $\pi^+/\pi-$ ratio is close to unity at this energy [46, 47].

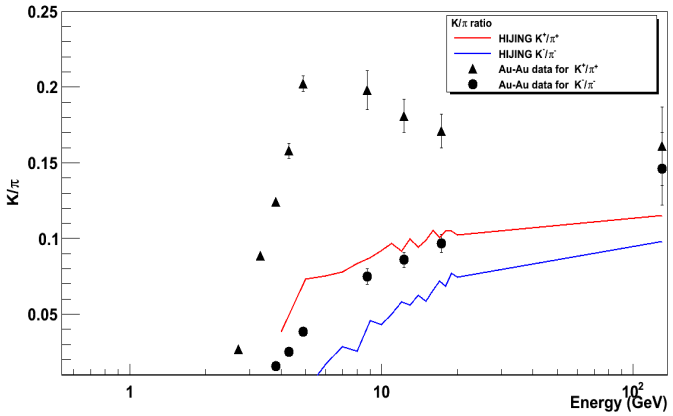

Figure 1.14: The strangeness enhancement signature in K/π ratio and comparison with HIJING-1.3 prediction

These predictions of Pb-Pb collisions at $\sqrt{s} = 5.5$ TeV/A are being tested by the ALICE detector at CERN, which is the only dedicated detector for heavy ion collisions. This detector system has been described in the following chapter.

Bibliography

[1] Naoki Itoh. Prog. Theor. Phys. **44** (1970) 291-292.

[2] J. C. Collins and M. J. Perry. Phys. Rev. Lett. **34** (1975) 1353.

[3] Edward V. Shuryak. Phys. Lett. B **78** (1978) 150.

[4] Joseph I. Kapusta Nucl. Phys. B **148** (1979) 461-498.

[5] STAR Collaboration. Phys. Rev. Lett. **86** (2001) 402.

[6] STAR Collaboration. Nucl. Phys. A **757** (2005) 102-183

[7] STAR Collaboration. Phys. Rev. Lett. **91** (2003) 072304.

[8] H. Satz, Rep. Prog. Phys. **63** (2000) 1511.

[9] J.D. Bjorken, Phys. Rev. D **27** (1983) 140

[10] A. Bialas and M. Gyulassy, Nucl. Phys. B **291** (1987) 793

[11] ALICE Collaboration. Eur. Phys. J. C **68** (2010) 89-108.

[12] ALICE Collaboration. Eur. Phys. J. C **68** (2010) 345-354.

[13] J.W. Harris and B. Müller, Annu. Rev. Nucl. Part. Sci. **46** (1996) 71;
S.A. Bass, M. Gyulassy, H. Stöcker and W. Greiner, J. Phys. **G25** (1999) R1.

[14] U. Heinz, Nucl. Phys. **A638** (1998) 357c; J. Phys. **G25** (1999) 263; Nucl. Phys. **A661** (1999) 140c.

[15] R. Stock, Phys. Lett. **B456** (1999) 277; Prog. Part. Nucl. Phys. **42** (1999) 295.

[16] J. Stachel, Nucl. Phys. **A654** (1999) 119c.

[17] U. Heinz, Nucl. Phys. **A685** (2001) 414c.

[18] P. Braun-Munzinger and J. Stachel, Nucl. Phys. **A606** (1996) 320.

[19] ALICE Collaboration. J. Phys. G: Nucl. Part. Phys. **30** (2004) 1517-1763.

[20] ALICE Collaboration, arXiv:1011.3914v1 [nucl-ex].

[21] U.A. Wiedemann and U. Heinz, Phys. Rep. **319** (1999) 145.

[22] R.M. Weiner, Phys. Rep. **327** (2000) 249.

[23] T. Csörgő, Heavy Ion Phys. **15** (2002) 1.

[24] R. Hanbury Brown and R. Q. Twiss. Nature **178** (1956) 1046.

[25] D. Das et al., arXiv:0511055v1 [nucl-ex].

[26] ALICE Collaboration. arXiv:1012.4035 [nucl-ex].

[27] M Herrmann and G.F.Bertsch Phys. Rev C **51** (1995) 328.

[28] ALICE Collaboration. Phys. Rev. D **82** (2010) 052001.

[29] R. Lednický, V.L. Lyuboshits, B. Erazmus and D. Nouais, Phys. Lett. **B373** (1996) 30.

[30] R. Lednický, arXiv:nucl-th/0112011.

[31] ALICE Collaboration. arXiv:1011.3916 [nucl-ex].

[32] K. Reygers. Eur. Phys. J. C **43** (2005) 393-398

[33] S. Gavin, P. L. McGaughey, P. V. Ruuskanen and R. Vogt, Phys. Rev. C **54** (1996) 2606.

[34] E. V. Shuryak, Phys. Rept. **61**, 71 (1980).

[35] R. Rapp and E. V. Shuryak, Phys. Lett. B **473**, 13 (2000).

[36] R. Rapp, Phys. Rev. C **63**, 054907 (2001).

[37] T. Matsui, H. Satz. Phys. Lett. B **178** (1986) 416-422.

[38] NA50 Collaboration. Phys. Lett. B **521** (2001) 195-203.

[39] PHENIX Collaboration. Phys. Rev. Lett. **98** (2007) 232301.

[40] ALICE Collaboration. J. Phys. G: Nucl. Part. Phys. **32** (2006) 1295-2040.

[41] X.N. Wang and M. Gyulassy, Phys. Rev D. **44** (1991) 3501.

[42] R. V. Gavai, arXiv:hep-ph/0010048v1.

[43] ALICE Collaboration. Phys Rev Lett **Vol.105, No.7,** (2010)

[44] ALICE Collaboration. Physics Letters B **693** (2010) 5368

[45] STAR Collaboration, Phys. Lett. B **595** (2004) 143150.

[46] STAR Collaboration, Phys. Rev. C **81** (2010) 024911.

[47] D. Das, arXiv:0906.0630v1 [nucl-ex].

Chapter 2

ALICE Detector and Dimuon Spectrometer

2.1 Overview

ALICE [Fig. 2.1] is designed to study the properties of matter at extreme high temperatures and densities in ultra relativistic proton-proton and heavy ion collisions [1]-[2]. It has seventeen different type of detectors which can be broadly divided into two groups, central and forward detectors, in terms of centrality coverage of the detectors. These detectors record the path marks of bended charged particle tracks under the influence of magnetic field. ALICE uses two magnets for this purpose.

The central detectors of the ALICE is housed inside the L3 magnet, which is a solenoidal magnet with an internal length of 12 m and radius of 5 m and has the nominal field of 0.5 T. On the other hand the Dimuon Spectrometer, a forward detector, uses a warm dipole magnet with resistive coil which has conical field integral of 3 Tm.

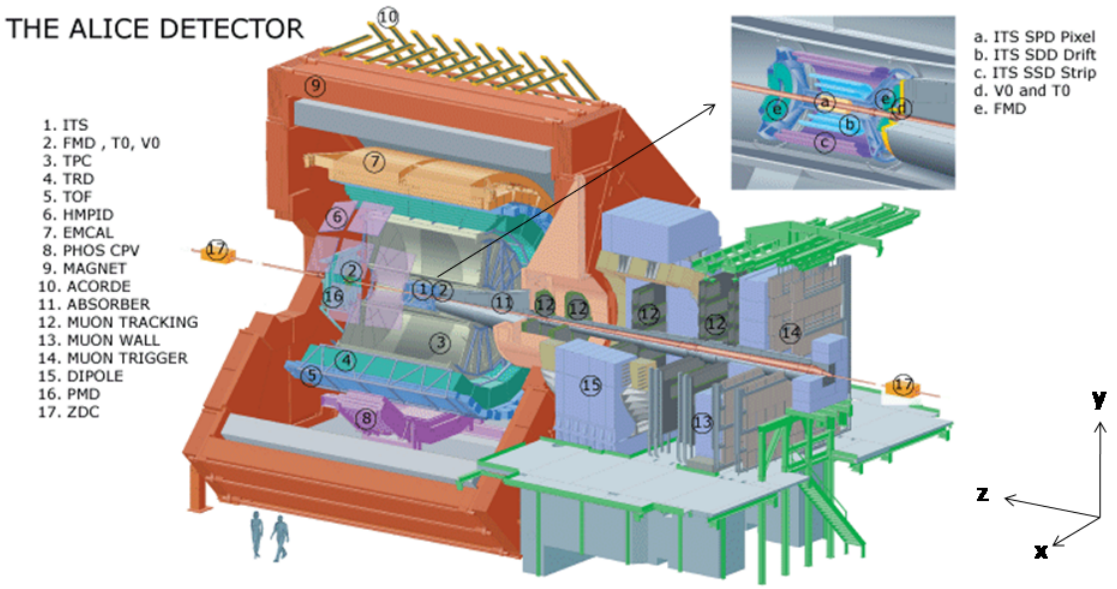

Figure 2.1: ALICE detector arrangement and co-ordinate system. The positive and negative z-directions are also known as A-side C-side,respectively, following the LHC convention of beam rotation along anti clockwise and clockwise direction.

The ALICE detector has been discussed in short in the following sections.

2.2 Central Barrel Detectors

The set of central barrel detectors are placed inside the L3 magnet and are dedicated detectors to study the matters produced in the central region after collision. As seen from the Fig. 2.1 and Fig. 2.2, it is composed of the following group of detectors which detects the particles over full azimuth angle and pseudo-rapidity range $-0.9 \leq \eta \leq 0.9$,

- ITS : Inner Tracking System
- TPC : Time Projection Chamber
- TRD : Transition Radiation Detector
- TOF : Time of Flight

and the rest of the central barrel detectors cover partial azimuth angle, such as,

- EMCAL : Electromagnetic Calorimeter ($|\eta| \leq 0.7$, $60^\circ \leq \varphi \leq 180^\circ$)
- PHOS : Photon Spectrometer ($|\eta| \leq 0.12$, $\Delta\varphi = 100^\circ$)
- HMPID : High-Momentum Particle Identification Detector ($|\eta| \leq 0.6$, $\Delta\varphi = 57.61^\circ$)

2.2.1 Inner Tracking System (ITS)

The Inner Tracking System (ITS) [Fig. 2.3 [3]] is the closest detector to the interaction point and it has inner diameter of 8 cm and outer diameter of 86 cm. It consists of six cylindrical layers of silicon detectors, located at radii, $r = 3.9$, 7.6,

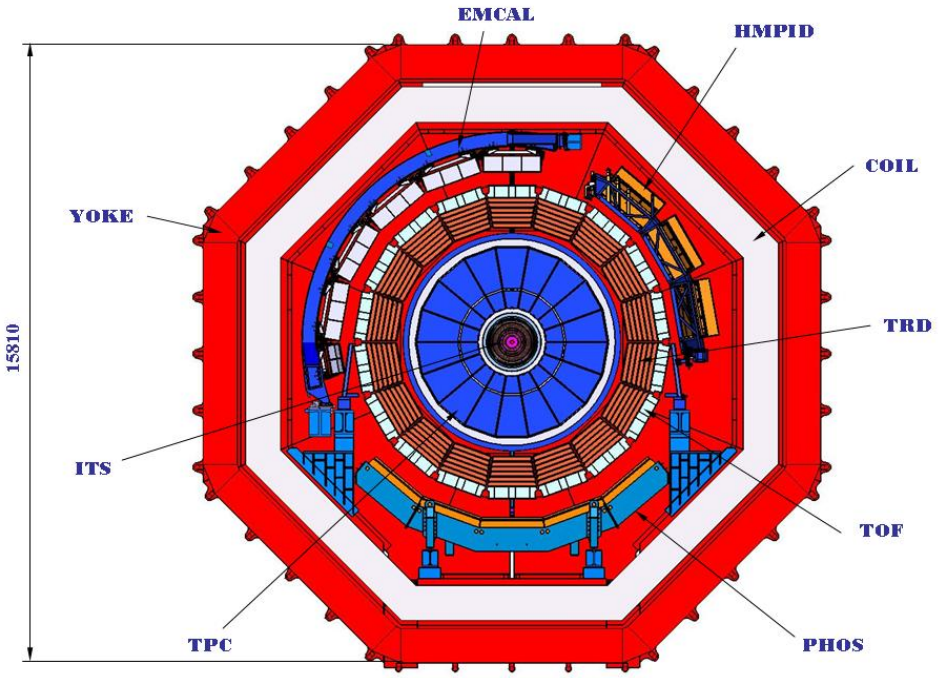

Figure 2.2: The front view of central barrel showing the layout of different detectors.

15.0, 23.9, 38.0 and 43.0 cm. The six layers of ITS are grouped in three pairs, which form three different detectors systems. The innermost two layers are silicon pixel detectors and therefore it is called Silicon Pixel Detector (SPD). It can handle up to 80 particles per cm^2. The following two layers are known as Silicon Drift Detector (SDD), which deals with particle density of about 7 cm^{-2}. On the outer side of SDD, there is Silicon Strip Detector (SSD), where the track densities are below one particle per sq. cm. The salient features of these detectors are listed in the table 2.1.

The main physics motivation of ITS is to reconstruct the vertex with an accuracy better than 100 μm, so that the momentum estimation of the track gets improved. It also plays an important role to find out the secondary vertices from the decays of hyperons (Σ, Λ, Ξ, Ω), open-charm (D) and open-beauty (B) decays. The other main capabilities of ITS are listed below :

- Improvement of the momentum resolution, in order to observe the predicted chiral symmetry. This is due to the fact that the precision in the mass resolution of the resonance mesons (ρ, ω and ϕ) has to be comparable to, or better than, the natural width of the resonances to establish the expected chiral symmetry restoration and the mass resolution of any track depends on momentum resolution.

- Identification of particles with momentum below 100 MeV/c.

- Improvement of the momentum and angular resolution for the high-p_{t} tracks which also traverse the TPC.

- Reconstruction of the particles which passes through the dead regions of the TPC.

- Improvement of mass measurements for heavy-flavour states with better momentum resolution, so that the signal-to-background ratio of heavy-quarkonia suppression, such as J/ψ and Υ, can be better estimated.

- Enhancement of momentum resolution increases the performance in the observation of jet production and jet quenching, i.e. the energy loss of partons in strongly interacting dense matter.

Table 2.1: Parameters of the various ITS detectors detector [1]

Parameter	Silicon Pixel	Silicon Drift	Silicon Strip
Spatial precision rφ (μm)	12	38	20
Spatial precision z (μm)	100	28	830
Two track resolution rφ (μm)	100	200	300
Two track resolution z (μm)	850	600	2400
Total number of readout channels (k)	9 835	133	2608
Total number of cells (M)	9.84	23	2.6
Average occupancy (inner layer) (%)	2.1	2.5	4
Average occupancy (outer layer) (%)	0.6	1.0	3.3

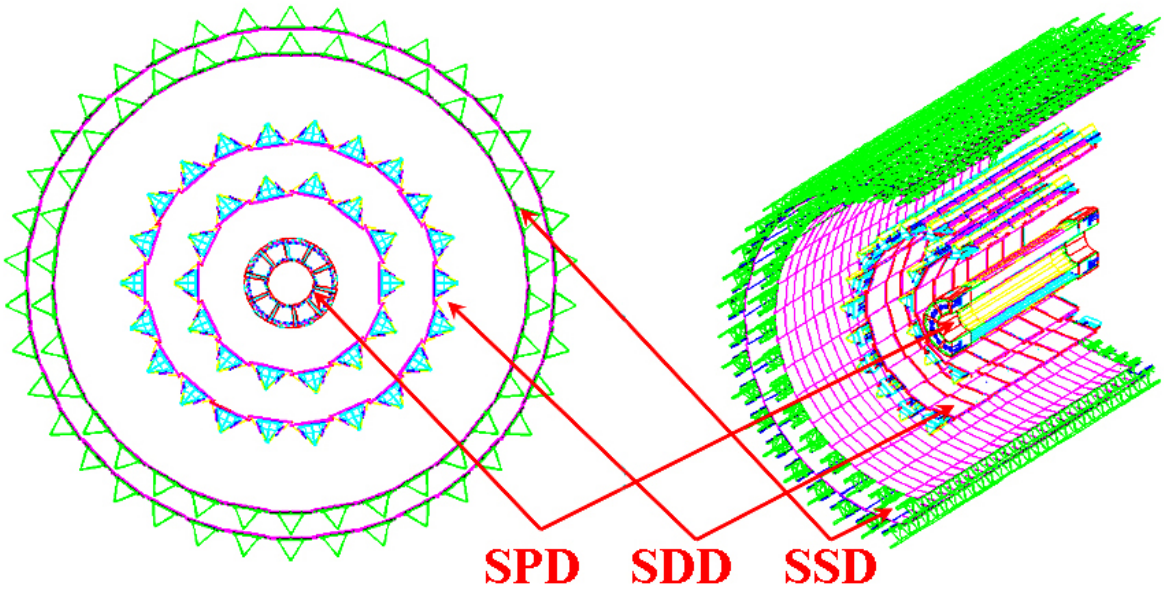

Figure 2.3: Layout of the Inner Tracking System (ITS).

2.2.2 Time Projection Chamber (TPC)

The Time Projection Chamber (TPC) of ALICE is the central tracking device for the charged particles. It is a hollow cylinder [Fig. 2.4] placed surrounding the ITS with an inner radius of 85 cm and outer radius of about 250 cm and has a span of 500 cm along the beam direction. The cylindrical axis of TPC is parallel to magnetic field of L3 solenoid. A conducting electrode at the middle of the cylinder is charged to 100 kV. This electrode along with the two outer surfaces of the cylinder generates the axial electric field of 400 V/cm. The hollow cylinder is filled with the gas mixture of $Ne+CO_2+N_2$ at a ratio of 85:10:5 at atmospheric pressure. When a charged particle passes through the detector, it ionizes the gas. The ionization electrons move towards the end plates of the detector due to electric field. Their arrival times in the end plates are measured precisely with respect to an external reference clock, which helps to find out the charged particle trajectory inside the detector at different instances. The main features of the TPC are listed in table 2.2.

Table 2.2: General parameters of the ALICE TPC.

Pseudo-rapidity coverage	$-0.9 < \eta < 0.9$ for full radial track length $-1.5 < \eta < 1.5$ for 1/3 radial track length
Azimuthal coverage	360°
Radial position (active volume)	$848 < r < 2466$ mm
Radial size of vessel (outer dimensions)	$610 < r < 2780$ mm
Radial size of vessel (gas volume)	$788 < r < 2580$ mm
Length (active volume)	2×2497 mm
Front-End Cards (FECs)	121 per sector $\times$ 36 = 4356
Readout partitions	6 per sector, 18 to 25 FECs each
Total readout control units	216
Total pads — readout channels	557 568
Pad occupancy (for $\mathrm{d}N/\mathrm{d}y = 8\,000$)	40 to 15% inner / outer radius
Pad occupancy (for pp)	5 to 2×10^{-4} inner / outer radius

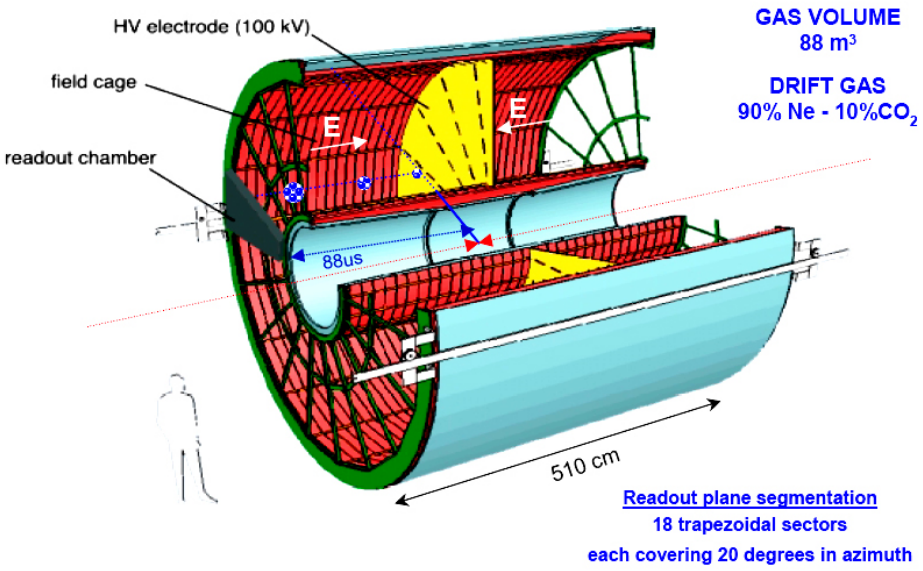

Figure 2.4: A schematic of the Time Projection Chamber (TPC), of ALICE.

2.2.3 Transition-Radiation Detector (TRD)

The schematic design layout and operational principle of Transition Radiation Detector (TRD) is shown in Fig. 2.5. The main motivation of TRD is to separate the electron and pion tracks found by TPC. It is composed of 18 supermodules and each of the supermodules has 5 stacks with 6 layers each. These are placed around TPC

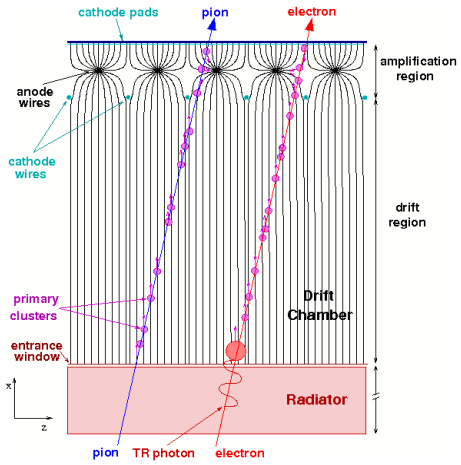

(a) Working principle of Transition Radiation Detectors

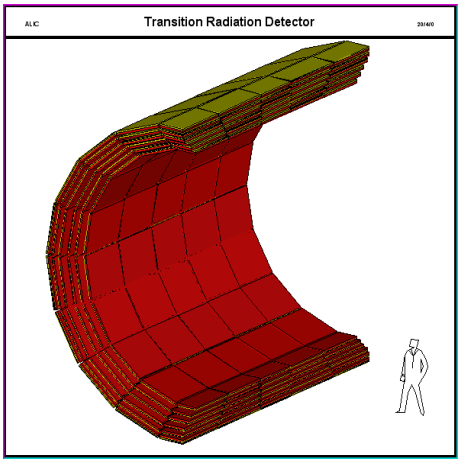

(b) Showing half of the TRD of ALICE

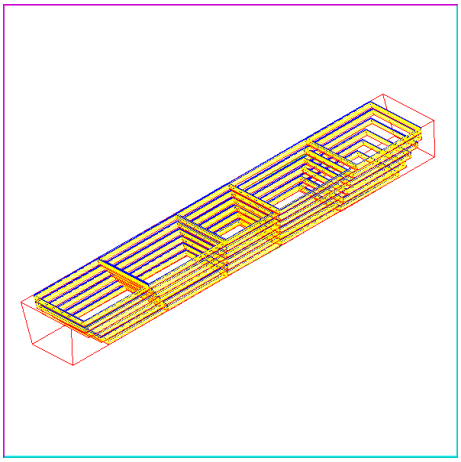

(c) A supermodule of TRD

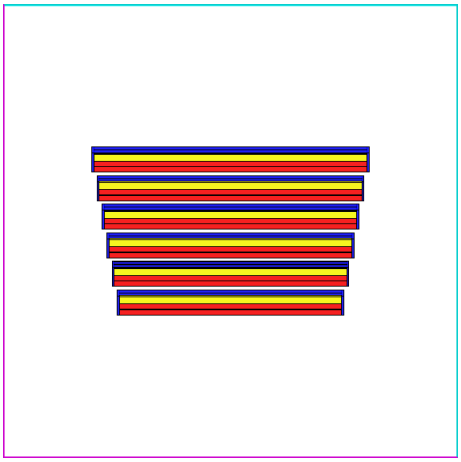

(d) A stack of TRD with six layers, radiator is displayed in red. The yellow coloured layer represents the amplification and drift volume, and the region in blue color contains the readout cards.

Figure 2.5: Transition Radiation Detector (TRD) working principle and module arrangement

over the full azimuthal angle starting at a distance of 260 cm, upto 370 cm. Some important design aspects of TRD are listed in table 2.3. The principle of TRD detector is based on the phenomena of emission of transition radiation (TR) for the passage of a relativistic charged particle through the boundary of two media with different

dielectric constants. The radiator of the TRD serves as inhomogeneous material. The total energy loss by TR depends on the Lorentz factor γ of a charged particle. Since the TR photons are in keV range they are detected by gaseous detector. Since the TR is emitted at a very small angle with respect to charged particles, TRD detects the sum of ionisation loss of charged particle and TR X-rays. To optimise the absorption of X-rays, xenon rich gas mixture ($Xe/CO_2 = 85\%/15\%$) is used. Since the pion is heavier, their ionisation loss is smaller than electron. The pions does not emit TR below ∼100 GeV/c. This is the key principle of TRD to identify pions and electrons, separately.

Table 2.3: Synopsis of TRD parameters.

Pseudo-rapidity coverage	$-0.9 < \eta < 0.9$
Azimuthal coverage	2π
Radial position	$2.9 < r < 3.7$ m
Length	up to 7.0 m
Azimuthal segmentation	18-fold
Radial segmentation	6 layers
Longitudinal segmentation	5-fold
Typical pad size	$0.7 \times 8.8 = 6.2$ cm^2
Number of pads	1.16×10^6
Detector gas	Xe/CO_2 (85%/15%)
Pad occupancy for $dN_{ch}/d\eta = 8000$	34%
Pad occupancy in pp	2×10^{-4}

2.2.4 Time Of Flight (TOF) detector

The Time Of Flight (TOF) detector of ALICE is cylindrical in shape [Fig. 2.6]. It is placed around the TRD starting from radius 370 cm upto 400 cm covering polar angles between 45 degrees and 135 degrees over the full azimuth. It has a modular structure with 18 sectors in φ and each of these sectors is divided into 5 modules along the beam direction. The modules contain a total of 1638 detector elements (MRPC strips), covering an area of 160 m^2 with 157248 readout channels (pads).

It's main task is to identify the charged particles in the intermediate momentum range (from 0.2 to 2.5 GeV/c). The time measurement with the TOF, along with the momentum and track length measured by the tracking detectors, is used to calculate the particle mass. A time resolution of 100 ps provides 3σ π/K separation up to 2.2 GeV/c and K/p separation up to 4 GeV/c. This is performed using the Multi-gap Resistive Plate Chamber (MRPC), which is a stack of resistive glass plates placed inside the cathode plates with an anode plate in between. A high voltage is applied to the external surfaces of the stack. The charged particles ionize the gas and the high electric field amplifies this ionization by an electron avalanche, which are stopped due to the resistive plates in each gap. Therefore, the total signal is the sum of the signals from all gaps, whereas the time jitter of the signal depends on the individual gap width. It is to be noted that the reason for many gaps is to achieve high efficiency and the reason for narrow gaps is to achieve good time resolution. A summary of the main features of the detector is listed in table 2.4.

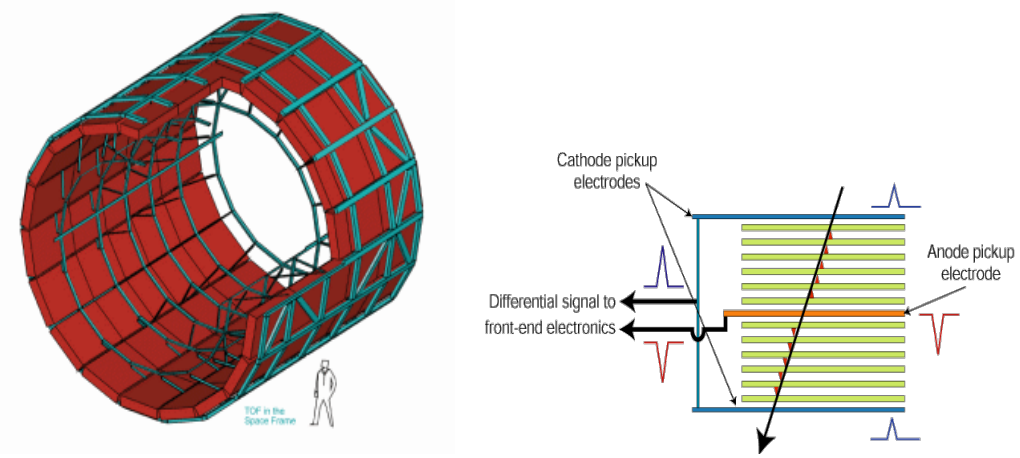

(a) The TOF of ALICE (b) Working principle of MRPC

Figure 2.6: Time Of Flight (TOF) detector arrangement and working principle of MRPC

Table 2.4: Overview of TOF parameters.

Pseudo-rapidity coverage	$-0.9 < \eta < 0.9$
Azimuthal coverage	2π
Radial position	$3.70 < r < 3.99$ m
Length	7.45 m
Segmentation in φ	18-fold
Segmentation in z	5-fold
Total number of modules	90
Detector active area	141 m^2
Detector gas	$C_2H_2F_4$(90%), i-C_4F_{10}(5%),SF_6(5%)
Number of readout channels	157 248
Occupancy for $dN_{ch}/d\eta = 8000$	13% ($B = 0.4$ T)
Occupancy for pp	6×10^{-4}

2.2.5 Electromagnetic Calorimeter (EMCal)

The main physics motivation of Electromagnetic Calorimeter (EMCal) of ALICE is to measure the jet quenching. It also provides fast unbias (L0/L1) trigger for high energy jets and neutral part of jet energy. This unbias trigger has advantage of better selection of high energy jets since jet measurements are solely based on charged particle reconstruction, suffers from measurement bias. The EMCAL increases the jet energy resolution and offers enhanced capability to measure high p_t photons, neutral hadrons and electrons. It is placed inside the L3 magnet and the outer side of the TOF about ≈450 cm from interaction point and covers the pseudorapidity $-0.7 \leq \eta \leq 0.7$. The main physical characteristics are summarised in table 2.5. The EMCAL detector is a layered Pb-scintillator sampling calorimeter [Fig. 2.7] with a longitudinal pitch of 1.44 mm Pb and 1.76 mm scintillator with longitudinal wavelength shifting fiber. A module is a single self contained detector unit. Each module comprises of four independent detector channels/towers giving a total of 1152 per full sized super module. The schematic diagram for detector segmentation of EMCAL modules and

the super modules are shown in Fig. 2.7.

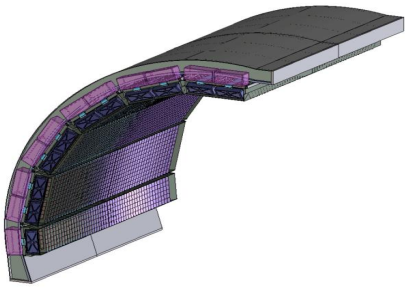

(a) The full EMCAL

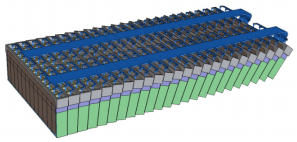

(b) An EMCAL supermodule of 24 taper strips

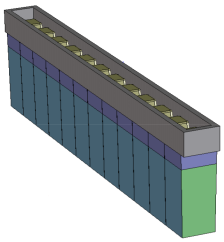

(c) An EMCAL taper strip

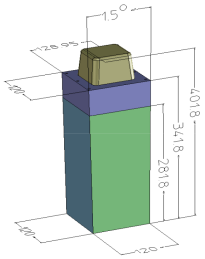

(d) An EMCAL module is a collection of four towers (channels)

Figure 2.7: Electromagnetic Calorimeter (EMCAL) module and detector arrangement.

Table 2.5: Synopsis of EMCAL parameters.

Coverage in pseudo-rapidity	$-0.7 \leq \eta \leq 0.7$
Coverage in azimuthal angle	$\Delta\varphi = 107°$
Distance to interaction point	450 cm
Number of super modules	10 full modules and 2 one third module
Number of modules	3072
Number of towers	12 288
Sampling ratio	1.44 mm Pb / 1.76 mm scintillator
Number of layers	77
Effective radiation length	12.3 mm
Effective density	5.68 gm/cm^2
Tower Size	6.0×6.0×24.6 cm
Weight of super module	≈7.7 metric tons

2.2.6 Photon Spectrometer (PHOS) Detector

The Photon Spectrometer (PHOS) of ALICE is a single-arm electromagnetic spectrometer including a highly segmented ElectroMagnetic CAlorimeter (EMCA) and a Charged-particle Veto (CPV) detector. The design parameters of PHOS are given in Tab. 2.6. PHOS is subdivided into five independent EMCA+CPV units, named PHOS modules [Fig. 2.8(b)], positioned on the bottom of the ALICE setup at a distance of 460 cm from the interaction point. It covers approximately a quarter of a unit in pseudo-rapidity, $-0.12 \leq \eta \leq 0.12$, and 100° in azimuthal angle. It has total area of $\sim$8 m^2.

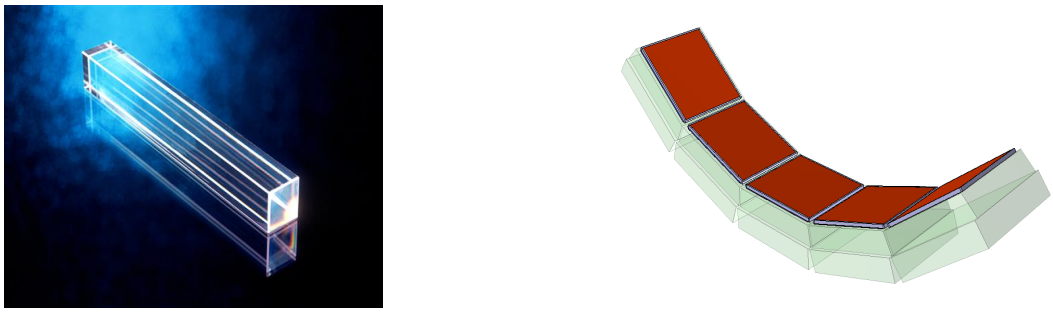

(a) PHOS Crystal

(b) PHOS modules

Figure 2.8: Photon Spectrometer (PHOS) crystal and assembly of modules.

It detects electromagnetic particles in a limited acceptance domain at central rapidity and provide photon identification as well as neutral mesons identification through the 2-photon decay channel.

The principal requirements on PHOS include the ability to identify photons, discriminate direct photons from decay photons and perform momentum measurements over a wide dynamic range with high energy and spatial resolutions.

ElectroMagnetic CAlorimeter (EMCA)

Each EMCA module is segmented into 3584 detection channels arranged in 56 rows of 64 channels. A detection channel consists of a $22\times22\times180$ mm^3 lead-tungstate crystal, $PbWO_4$ (PWO) [see Fig. 2.8(a)], coupled to a 5×5 mm^2 Avalanche Photo-Diode (APD) whose signal is processed by a low-noise preamplifier. The total number of crystals in PHOS is 17 920 representing a total volume of $\sim$1.5 m^3. The main mechanical assembly units in a module is the crystal strip unit consisting of eight crystal detector units forming 1/8 of a row. The APD and the preamplifier are integrated in a common body glued onto the end face of the crystal with optically transparent glue of a high refractive index. The EMCA modules are operated at a temperature of -25 °C to significantly (by about a factor of 3) increase the light yield of the PWO crystals (temperature coefficient $\sim -2\%$ per °C).

Charged-particle Veto (CPV) detector

The CPV detector equipping each PHOS module is a Multi-Wire Proportional Chamber (MWPC) with cathode-pad readout. Its charged-particle detection efficiency is better than 99%. The spatial precision of the reconstructed impact point is about 1.6 mm in both directions.

The CPV consists of five separate modules placed on top of the EMCA modules at a distance of about 5 mm. The material budget is less than 5% of the radiation length. The active area of 14 mm separating the anode from the cathode is filled with a gas mixture is 80%Ar + 20%CO_2 at a pressure slightly (1 mbar) above atmospheric pressure. A total of 256 anode wires, 30 μm in diameter, are stretched 7 mm above the cathode with a pitch of 5.65 mm. They are oriented along the direction of the L3 magnetic field. The cathode plane is segmented into 7168 of 22×10.5 mm^2 pads with

an inter-pad distance of 0.6 mm. The larger dimension is aligned along the wires. The total sensitive area of the CPV module is equal to about 1.8 m^2.

Table 2.6: Synopsis of PHOS parameters.

Coverage in pseudo-rapidity	$-0.12 \leq \eta \leq 0.12$
Coverage in azimuthal angle	$\Delta\varphi = 100^\circ$
Distance to interaction point	4600 mm
Modularity:	5 modules of 3584 crystals
EMCA	
Material	Lead tungstate crystals (PWO)
Crystal dimensions	$22\times22\times180\times$ mm^3
Depth in radiation length:	20
Number of crystals	17 920
Segmentation	3584 crystals/module
Operating temperature	-25 °C
CPV	
Gas	80%Ar/20%CO_2
Thickness	$0.5X_0$
Active area	1.8 $m^2\times14$ mm/module
Wire diameter:	30 μm
Number of wires/module	256
Wire pitch	5.65 mm
Pad size	22x10.5 mm^2
Pad inter-distance	0.6 mm
Number of pads/module	7168

2.2.7 High-Momentum Particle Identification Detector (HMPID)

The High-Momentum Particle Identification Detector (HMPID) has been designed to extend the range for the identification of proton and kaon up to 3 GeV/c and of proton up to 5 GeV/c, on a track-by-track basis. It measures inclusive particle ratios and transverse-momentum spectra in the region relevant for the study of phenomena connected with the pre-equilibrium stage of the nucleus-nucleus collisions. The low rate of high momentum particles in Pb-Pb collisions at the LHC energy

regime justifies the single-arm geometry of the HMPID covering about 5% of the central barrel phase space.

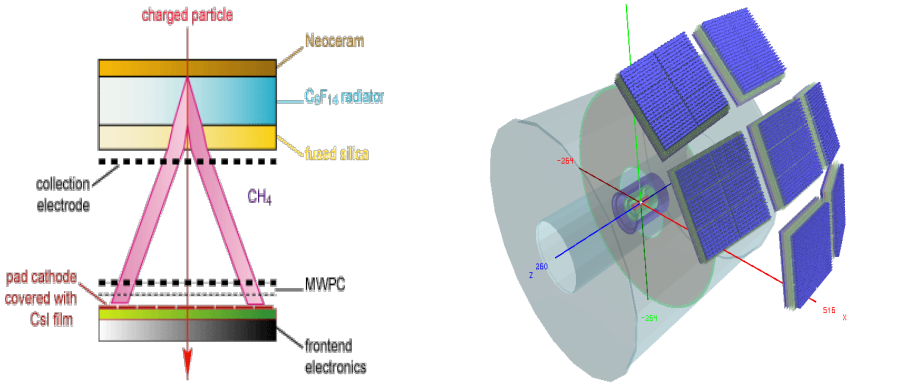

(a) HMPID working principle (b) HMPID position in ALICE

Figure 2.9: Schematic of the working principles of HMPID and detector setup

The ALICE HMPID is based on proximity focusing Ring Imaging Cherenkov (RICH) counters and consists of seven modules mounted in an independent support cradle, which has been be fixed to the space frame, at two o'clock position [Fig. 2.9(b)]. Cherenkov photons, emitted when a fast charged particle traverses the 15 mm thick layer of liquid C_6F_{14} (perfluorohexane), are detected by a photon counter, which uses the technology of a thin layer of CsI deposited onto the pad cathode of a multiwire proportional chamber (MWPC). The HMPID, with its surface of about 12 m^2, represents the largest scale application of such a technique. The Cherenkov photons refract out of the liquid radiator and reach the CsI-coated pad cathode, located at a suitable distance (the proximity gap) that reduces the geometrical aberration to the Cherenkov angle. The electrons released by ionizing particles in the proximity gap, filled with CH_4, are prevented from entering the MWPC sensitive volume by a positive voltage of the collection electrode close to the radiator. The important features of HMPID are listed in table 2.7.

Table 2.7: Synopsis of HMPID parameters.

Pseudo-rapidity coverage	$-0.6 < \eta < 0.6$
Azimuthal coverage (rad)	57.61 deg
Radial position	5 m
Segmentation in φ	3-fold
Segmentation in z	3-fold
Total number of modules	7
Occupancy ($dN_{ch}/d\eta = 8000$)	12%

2.3 Forward and other Detectors

2.3.1 Multiplicity Detectors

The forward detectors of ALICE primarily measures the multiplicity of the particles in order to judge the global characteristics of events.

Forward Multiplicity Detectors (FMD)

The silicon strip Forward Multiplicity Detector (FMD) of ALICE is designed to measure the charged particles that are produced in the collisions and which are emitted at small angles relative to the beam line direction [Fig. 2.10]. The FMD is the primary detector to measure the multiplicity distribution of charged particles over a wide kinematical range (rapidity coverage in the interval $1.7 \leq |\eta| \leq 5.1$) corresponding to an angular interval of about 0.75 degrees to 21 degrees with respect to the beam direction.

In addition, the FMD determines the total particle production in p+p and Pb+Pb collisions at the LHC, to study elliptic flow and multiplicity fluctuations. These quantities are essential for understanding the properties of the Quark Gluon Plasma, and the phase transition from normal matter to quark matter. Furthermore,

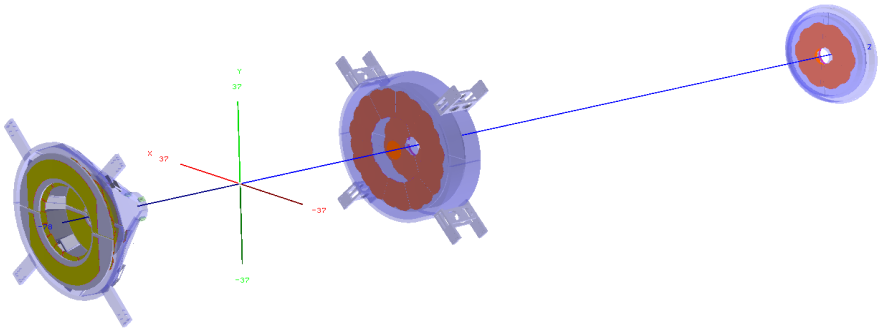

Figure 2.10: The left most FMD module is placed towards the C-side and the module at the right end towards the A-side.

the properties of particle emission at forward angles are sensitive to the properties of the Color Glass Condensate. The pseudo-rapidity coverage of different parts of FMD are listed in table 2.8.

Table 2.8: The distance z, from the detector to the interaction point, the inner and outer radii, and the resulting pseudo-rapidity coverage of each ring.

Ring	z (cm)	R_{in} (cm)	R_{out} (cm)	η coverage
Si1 outer	-75.2	15.4	28.4	$-2.29 < \eta < -1.70$
Si1 inner	-62.8	4.2	17.2	$-3.40 < \eta < -2.01$
Si2 outer	75.2	15.4	28.4	$1.70 < \eta < 2.29$
Si2 inner	83.4	4.2	17.2	$2.28 < \eta < 3.68$
Si3	340.0	4.2	17.2	$3.68 < \eta < 5.09$

V0 Detector

The V0 detector is made of two arrays (V0A and V0C) located asymmetrically on each side of the interaction point. It provides the L0 (zeroth level) trigger for ALICE. The V0A is located 340 cm from the vertex, on the side opposite to the muon spectrometer. The V0C is fixed at the front face of the front absorber, 90 cm from the vertex.

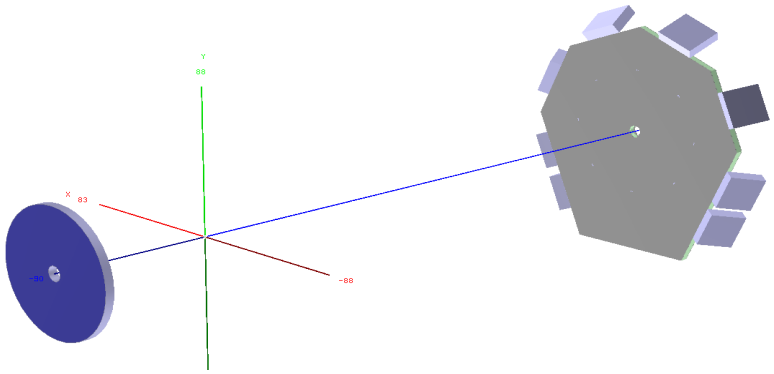

Figure 2.11: V0 detector setup. The detector in the left side and the right side of the figure are, V0C and V0A, respectively.

The V0A/V0C are segmented (Table 2.9, Fig. 2.11) into 32 elementary counters distributed in 4 rings. Each ring covers 0.4–0.6 unit of pseudo-rapidity. The rings are divided into 8 sectors of 45°. The elementary counter consists of scintillator material with embedded Wave-Length Shifting (WLS) fibres. The light from the WLS is collected by clear fibre and transported to PhotoMultiplier (PM) installed at 3–5 m from the detectors, inside the L3 magnet. The time resolution of each individual counter is better than 1 ns.

Table 2.9: V0A and V0C arrays. Pseudo-rapidity coverage and angular acceptance (in degrees) of the rings.

Ring	V0A		V0C	
	η_{max}/η_{min}	$\theta_{min}/\theta_{max}$	η_{max}/η_{min}	$(\pi-\theta)_{min}/(\pi-\theta)_{max}$
1	5.1/4.5	0.7/1.3	$-3.7/-3.2$	2.8/4.7
2	4.5/3.9	1.3/2.3	$-3.2/-2.7$	4.7/7.7
3	3.9/3.4	2.3/3.8	$-2.7/-2.2$	7.7/12.5
4	3.4/2.8	3.8/6.9	$-2.2/-1.7$	12.5/20.1

The V0 detector has multiple roles. It provides:

- a minimum bias trigger for the central barrel detectors
- two centrality triggers in Pb-Pb collisions

- a centrality indicator
- a control of the luminosity
- a validation signal for the muon trigger to filter background in pp mode

T0 Detector

The T0 detector also provides the L0 trigger for ALICE. It consists of two arrays of Cherenkov counters, 12 counters per array. Each Cherenkov counter is based on a fine-mesh photomultiplier tube, 30 mm in diameter, 45 mm long optically coupled to a quartz radiator 30 mm in diameter and 30 mm thick. One of the arrays $T0_R$ is placed 70 cm from the nominal vertex. Such a small distance has been chosen because of the space constraints imposed by the front cone of the muon absorber and other forward detectors. The pseudo-rapidity range of $T0_R$ is $2.9 \leq \eta \leq 3.3$. On the opposite side the distance of the left array $T0_L$ is about 350 cm from the congested central region. $T0_L$ is grouped together with the other forward detectors (FMD, V0, and PMD) and covers the pseudo-rapidity range of $-5 \leq \eta \leq -4.5$. In the radial (transverse) direction both T0 arrays are placed as close to the beam pipe as possible to maximize triggering efficiency.

The triggering efficiency of the detector for minimum bias pp collisions, estimated by Monte Carlo simulations, is about 48% for all inelastic processes. The efficiencies of $T0_R$ and $T0_L$ for pp inelastic processes are 60% and 67%, respectively. The triggering efficiency in heavy ion collisions is, due to the high multiplicities, practically 100%. The basic parameters of the T0 detector are summarized in Tab. 2.10.

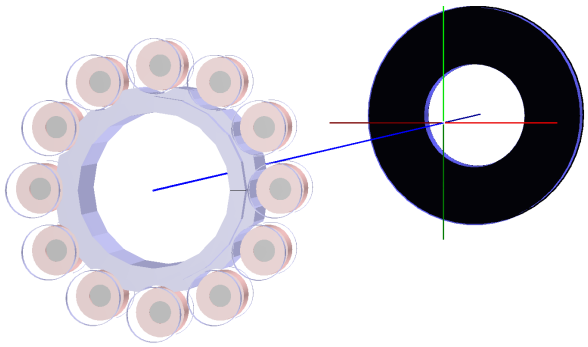

Figure 2.12: The layout for T0 detector. The left half of T0, i.e. $T0_L$ detector (left side module of this figure) is placed towards the A-side and $T0_R$ towards the C-side.

Table 2.10: Overview of the T0 detector parameters.

Parameters	Left array	Right array
z-position (cm)	-350	$+70$
Number of Cherenkov counters	12	12
Pseudorapidity coverage	$-5 \leq \eta \leq -4.5$	$2.9 \leq \eta \leq 3.3$
Detector active area (cm^2)	84.78	84.78
Efficiency with beam pipe (%)	67	60

Photon Multiplicity Detector (PMD)

The objective of ALICE Photon Multiplicity Detector (PMD) is to measure the multiplicity and spacial distribution of photons in the forward direction on an event-by-event basis. The PMD is installed at 360 cm from the interaction point, on the opposite side of the forward muon spectrometer, covering the region $2.3 \leq \eta \leq 3.5$. A lead converter is placed between the veto detector and the preshower plane. The working principle of PMD [Fig. 2.13(a)] relies on the fact that a charged particle produce hits of same dimension on both of the detector. But a photon track does not produce hits on veto detector, whereas a large number of hits are observed in preshower plane. This is due to the conversion of the photon to the pion in the Pb-converter. The important parameters of the PMD are listed in table 2.11.

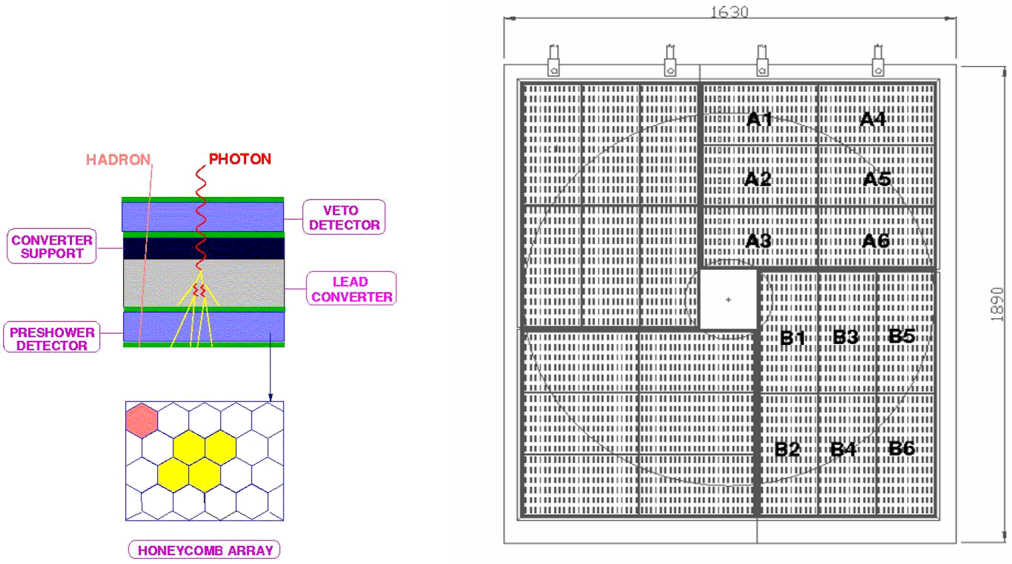

(a) PMD working principle

(b) PMD Super module

Figure 2.13: The working principle and a supermodule layout for the Photon Multiplicity Detector (PMD)

The PMD consists of four supermodules, two of each kind A and B, as shown in Fig. 2.13(b). Two A type supermodules are placed diagonally as shown in this figure, and the B type supermodules are placed in the remaining two diagonally opposite zones. A supermodule is a gas-tight enclosure. There are six identical unit modules in each supermodule. The unit modules are separated among themselves by a thin 100 μm kapton strip supported on a 0.3 mm thick FR4 sheet for rigidity. This provides high voltage isolation among the unit modules.

Each unit module contains a collection of detection elements in the form of honeycomb array [Fig. 2.13(a)]. A honeycomb cell is an proportional counter with an anode wire at the middle. The honeycomb, made of copper sheet, has 48×96 cells covered on both sides by printed circuit boards (PCBs). The inner parts of the PCB provide extensions to the honeycomb cathode. The upper part of the top PCB has tracks that are connected to the cell centres (connecting anode wires).

Table 2.11: Summary of design and operating parameters of the PMD.

Pseudorapidity coverage	$2.3< \eta <3.5$
Azimuthal coverage	2π
Distance from vertex	361.5 cm
Detector active area	2m^2
Detector weight	1200 kg
Number of planes	two (Veto and Preshower)
Converter	$3X_0$ lead
Hexagonal cell cross section	0.22 cm^2
Hexagonal cell depth (gas thickness)	0.5 cm
Detector gas	Ar/CO_2 (70% / 30%)
Cell occupancy for $\text{d}N_{\text{ch}}/\text{d}\eta = 8000$ for veto plane	13%
Cell occupancy for $\text{d}N_{\text{ch}}/\text{d}\eta = 8000$ for preshower plane	28%

2.3.2 Zero-Degree Calorimeters (ZDC)

In the ALICE experiment, the ZDCs are placed at 116 m from the Interaction Point (IP), where the distance between beam pipes (∼8 cm) allows insertion of a detector.

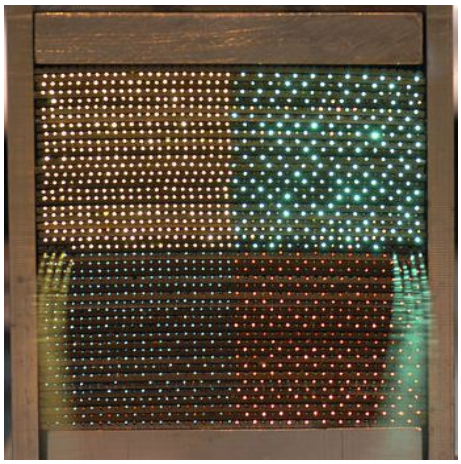

(a) The ZDC front-view shows the lights through the quartz fibres

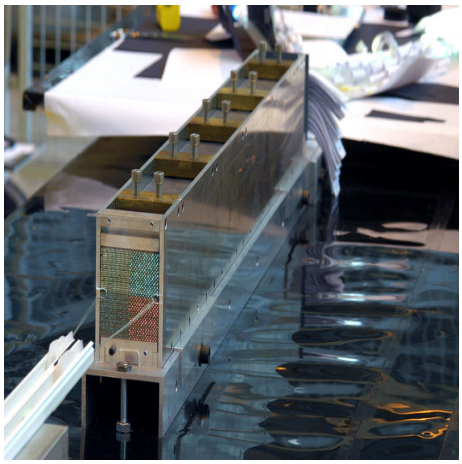

(b) A ZDC module in the laboratory

Figure 2.14: The figure shows the front view(left) and side view(right) of a Zero-Degree Calorimeters(ZDC) module

At this distance, spectator protons are spatially separated from neutrons by the magnetic elements of the LHC beam line. Therefore, two distinct detectors have been

used: one for spectator neutrons, placed at zero degrees relative to the LHC axis, and one for spectator protons, placed externally to the outgoing beam pipe on the side where positive particles are deflected, see Fig. 2.14.

The quartz fibres calorimetry technique has been adopted for the ALICE ZDC. The shower generated by incident particles in a dense absorber (the so-called 'passive' material) produces Cherenkov radiation in quartz fibres ('active' material) interspersed in the absorber. This technique fulfills two fundamental requirements. Firstly, due to the small amount of space available (particularly for the neutron calorimeter), the detectors need to be compact and therefore a very dense passive material must be used for the absorber to contain the shower. Secondly, the ZDC operates in a very high radiation environment (about 10^4 Gy/day is the estimated dose for the neutron calorimeter at a luminosity of 10^{27} cm^{-2} s^{-1} for Pb-Pb collision, where one Gy [gray] unit represents the absorption of one joule of energy, in the form of ionizing radiation, by one kilogram of matter). Radiation hardness is guaranteed by radiation resistance of quartz fibres. Furthermore, Cherenkov effect has two more advantages: it provides a very fast signal due to the intrinsic speed of the emission process and a very low sensitivity to induced radioactivation due to its threshold behaviour. The main design features of ZDC are listed in table 2.12 .

Table 2.12: Dimensions and main characteristics of absorber and quartz fibres for neutron and proton calorimeters.

	ZN	ZP
Dimensions (cm^3)	$7.04 \times 7.04 \times 100$	$12 \times 22.4 \times 150$
Absorber	tungsten alloy	brass
ρ_{absorber} (g cm^{-3})	17.61	8.48
Fibre core diameter (μm)	365	550
Fibre spacing (mm)	1.6	4
Filling ratio	1/22	1/65

2.3.3 ALICE Cosmic Ray Detector (ACORDE)

The ALICE Cosmic Ray Detector (ACORDE) is array of plastic scintillator detectors to provide the cosmic ray trigger for ALICE. At present there are 60 plastic scintillator modules placed on the top of the L3 magnet [Fig. 2.15]. A module consists of two plastic scintillator paddles with 188×20 cm^2 effective area. Each doublet consists of two superimposed scintillator counters. A coincidence signal, in a time window of 40 ns, from the two scintillator paddles generate the cosmic trigger. A PCI BUS electronics card has been developed in order to measure plateau and efficiency of the module counters. The cosmic ray trigger system (CRT) provides a fast level-zero trigger (L0) signal to the central trigger processor, when atmospheric particles impinge upon the ACORDE.

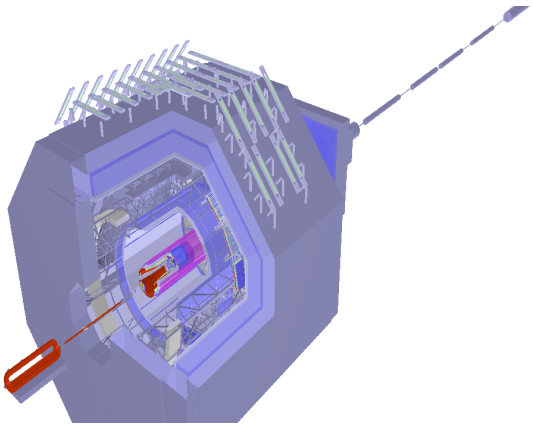

Figure 2.15: The arrangement of ALICE Cosmic Ray Detector (ACORDE) on the L3 magnet.

2.4 Muon Spectrometer

The central interest of Muon Spectrometer of ALICE is to study the properties of heavy quarkonia states ($J/\Psi, \Psi'$ and $\Upsilon, \Upsilon', \Upsilon''$) through their dimuon decay channel in the beam direction [see sec. §1.2.8]. In order to separately identify the resonance

states, the spectrometer needs a mass resolution of 70 MeV/c^2 in the J/Ψ mass region and 100 MeV/c^2 in the Υ mass region. It consists of an arrangement of ten tracking chambers and four trigger chambers, covering an pseudo-rapidity region from -2.5 to -4.0. The important features of the spectrometer can be found at table 2.13

2.4.1 Detector Layout

The Muon Spectrometer is a unique apparatus at the LHC to measure charmonia production down to $p_{\rm t}\sim$ 0. The low $p_{\rm t}$ quarkonia is expected to be sensitive to medium effects like heavy-quark potential screening. The spectrometer is situated from ∼90 cm to ∼1720 cm along the negative z-direction, according to the ALICE co-ordinate system [see Fig. 2.1] and it has polar and azimuthal coverage of $171^\circ \leq \theta \leq 178^\circ$ and 2π, respectively.

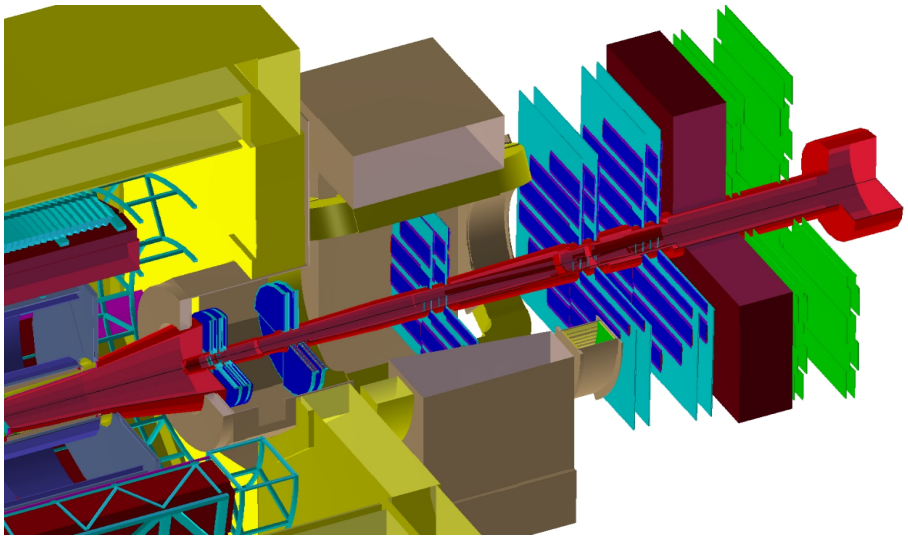

Figure 2.16: The Layout of Muon Spectrometer.

The layout of the muon spectrometer is presented in Fig. 2.16. The spectrometer is composed of the following components:

- **Front absorber**
- **Small Angle Absorber**
- **Dipole Magnet**
- **Tracking Stations**
- **Muon Absorber**
- **Trigger Stations**

Front Absorber

Since the spectrometer is placed along the beam direction, it suffers heavily from high particles flux of low mass hadrons (e.g. proton, π, K). Therefore, the front absorber [Fig. 2.17] has the double task of reducing the forward flux of primary hadrons from nucleus-nucleus collisions by a factor 100 and of decreasing the decay muon background by limiting the free path for primary $\pi, K \rightarrow \mu$ decay. It is comprised with a 4.13 m long central cone located inside the L3 magnet at 90 cm away from IP. The main ingredients of the absorber are graphite, concrete, Lead, polyCH_2, tungsten and steel of radiation lengths (in cm) 13.87, 11.27, 0.05, 46.47, 0.37 and 1.76, respectively.

Small Angle Absorber

The small angle absorber shields the beam pipe along the spectrometer extension. It protects the tracking detectors from particles produced at very small angles and secondaries generated in the beam pipe. It has an open geometry with a 4 cm thick stainless steel outer shield. The section nearest to the IP is made of

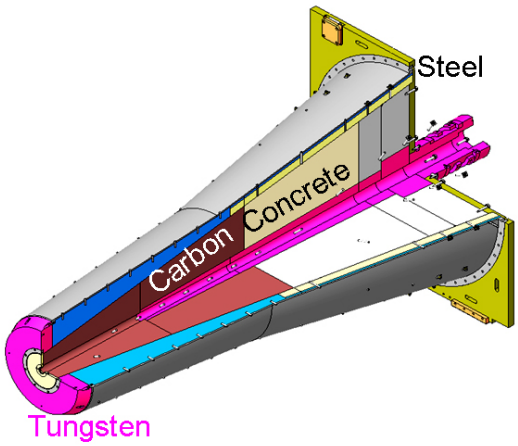

Figure 2.17: The Front Absorber of Muon Spectrometer.

tungsten, while the far end is made of lead. The structure of the small angle absorber end with an iron plug of 1.1 m in diameter and 1 m thick, which protect the trigger detectors against the background particles coming from the LHC Ring.

Dipole Magnet

Figure 2.18: The Dipole Magnet after the first assembly.

The Dipole magnet [Fig. 2.18] placed about 7 m away from the IP, provides the bending power to measure the muon momenta by muon tracking detectors. It is a warm dipole of 850 tons (5 m long,6.6 m wide and 8.6 m high) and is the largest warm dipole in the world with a nominal field of 0.7 T and a field integral of 3 Tm along beam axis. The magnetic field is directed in the horizontal plane perpendicular to the beam direction (x axis) defining a bending plane (zy plane) and a non bending plane (xz plane).

Tracking System

The tracking detector system of Muon Spectrometer is ∼1000 cm long starting from ∼500 cm of the interaction point (IP). It is composed of ten tracking chambers, and each pair of detection chamber is considered as one station. The layout is shown in Fig. 2.16. On each side of the dipole magnet there are two stations with one remaining station situated at the middle of the magnet. In central Pb-Pb collisions, a few hundred particles are expected to hit the muon chambers, with a maximum hit density of about 5×10^{-2} cm^{-2}. Moreover, the tracking system has to cover a total area of about 100 m^2. The basic design criteria of dimuon tracking chamber is to cope with such high particle flux in the forward direction and to achieve a spatial resolution of about 100 μm to distinguish the members of the resonance family. Both of the conditions are found to be satisfied by Cathode Pad Chambers (CPC). Therefore, the tracking detectors are comprised of segmented Cathode with anode wires in between and are operated following the principle of Multiwire Proportional Counters (MWPC) with gas mixture of Ar/CO_2 (80 %/20 %).

The basic geometry of CPC is shown Fig. 2.19 , in which both the cathode planes are divided into sensitive pads, which are used to determined the position of particle traversing the detector. When a charged particle passes through the active gas volume

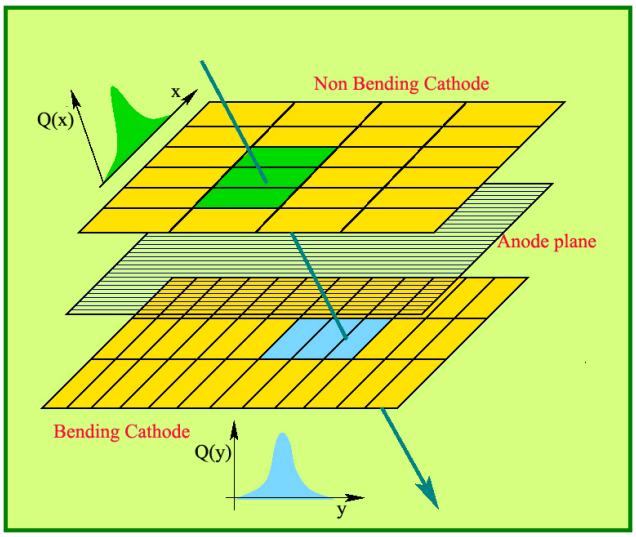

Figure 2.19: Working principle of cathode pad chamber.

of the detector, it produces ionization (electron ion pair) along its trajectories. These primary electrons drift towards the nearest anode wire, where avalanche take place. The pads of specific geometric shape are used to sample the charge induced on the cathode planes. The relative values of the induced charges and the absolute positions of the pads in a charge cluster are used to determine the position of the charged particle passing through the detector.

In order to keep the number of overlapping clusters to be less than 1%, the pad occupancy should be kept below 5%. Thus a large segmentation of the readout pads is needed. For instance, pads as small as 4.2×6 mm^2 are needed for the region of the first station close to the beam pipe, where the highest charged particle multiplicity is expected. Since the hit density decreases with the distance from the beam, larger pads are used at larger radii. This enables keeping the total number of channels to about 1 million.

Multiple scattering of the muons in the chambers is minimised by keeping the material budget less than 3% of the radiation length. Because of the different size

of the stations, (ranging from few square metres for station 1 to more than 30 m^2 for station 5) two different designs have been adopted. The first two stations have a quadrant structure, with the readout electronics distributed on their surface. For the other stations, a slat architecture has been chosen. The maximum size of a slat is 40×280 cm^2 and the electronics is implemented on the top and bottom sides of the slats. Thus, the slats have been overlapped to avoid dead zones on the detector.

The position of the tracking chambers is continuously monitored by a sophisticated system of optical lines inspired to the RASNIK concept. The main components of each optical line are a IR LED, a lens and a CCD or CMOS camera. The relative positions of the different chambers are monitored with an accuracy better than 20 μm by means of about 100 optical lines, while 160 lines are used to monitor the planarity of the chambers.

Muon Filter

The muon filter [Fig 2.20] is a $5.6 \times 5.6 \times 1.2$ m^3 iron wall placed at 15 m from the interaction point, between the last tracking station and the first trigger station. It reduces the back ground on the trigger stations by absorbing the punch-through pions and low momentum muons. The combined effect of the front absorber and muon filter prevents muons with momentum less than 4 GeV/c from reaching the trigger station and enhance the trigger chamber performance.

Trigger system

The motivation of the muon trigger system is to select unlike sign muon pairs from the decay of quarkonia resonances, single muons from heavy flavors and like sign muon pairs for combinatorial background studies. It is found from the simulation

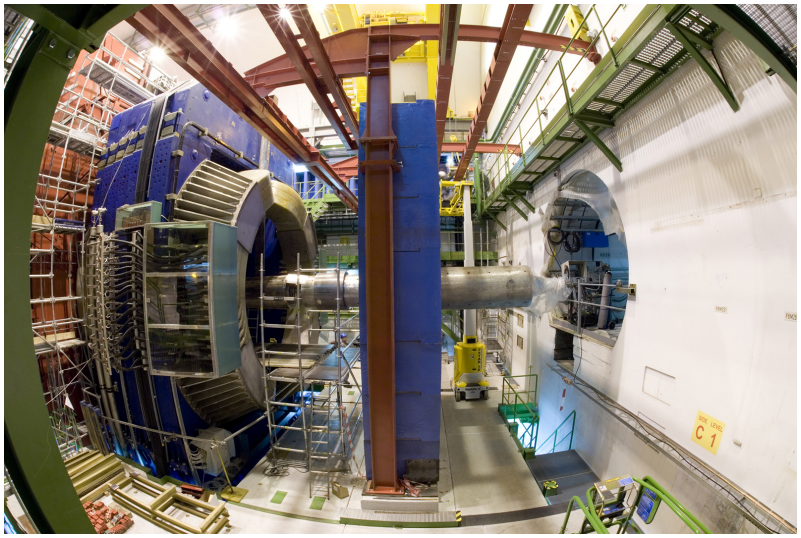

Figure 2.20: A photograph of the Dipole Magnet and Muon Filter.

of central Pb-Pb events that about eight low-p_{t} muons from π and K decays are expected to be detected per event in the spectrometer. To reduce the probability of triggering on events where these low-p_{t} muons are not accompanied by the high-p_{t} ones (emitted in the decay of heavy quarkonia or in the semi-leptonic decay of open charm end beauty), a p_{t} cut has been applied at the trigger level on each individual muon. A dimuon trigger signal is issued when at least two tracks above a predefined p_{t} threshold are detected in an event. According to simulation results, a low-p_{t} cut (1 GeV/c) is used for J/Ψ and a 'high' one (2 GeV/c) for Υ selection. To perform the p_{t} selection, a position-sensitive trigger detector with space resolution better than 1 cm has been designed which can issue trigger within a very short time interval ($\sim$600 ns). This is achieved by Resistive Plate Chambers (RPCs) operated in streamer mode. The trigger system consists of four RPC planes arranged in two stations (MT1 and MT2), one metre apart from each other, placed behind the muon filter about 1600 cm and 1700 cm, respectively, from the IP. Each trigger station is made of two parallel detection planes of 18 single-gap RPCs separated by 15 cm, so that the total number of RPCs is 72. The active area covered by the first station and

the second are $6.12 \times 5.44\ m^2$ and $6.50 \times 5.78\ m^2$, respectively.

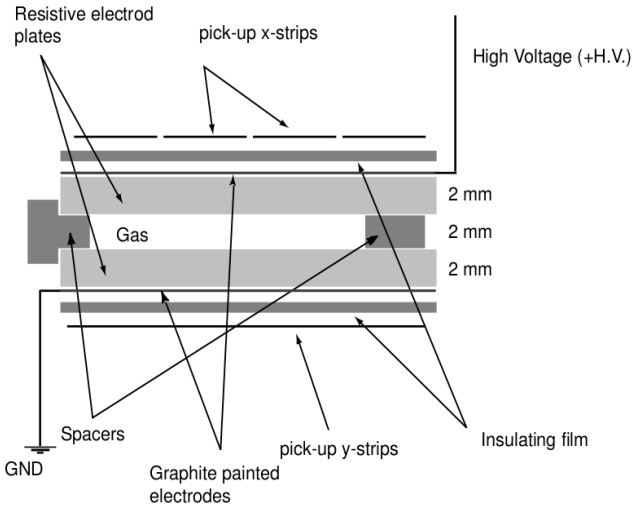

Figure 2.21: A schematic view of a Resistive Plate Chamber.

A RPC is a planner geometry gaseous detector [Fig. 2.21], where the active gas material is flushed through the resistive electrode plates. A High voltage is applied to the plate by means of a conducted layer coated on their outer surfaces. It is kept at a constant distance by plastic spacers placed inside the gas gap. The detector is filled with gas at atmospheric pressure, and kept in flow mode. The voltage required for operation is 4-5 kV/mm. When an ionising particle crosses the gas gap, the liberated electrons gives rise to a discharge on the anode, which are absorbed by organic gas and electronegative gases ($Ar+C_2H_2F_4$+isobuthane+SF_6 at a ratio 49:40:7:1). Since duration of discharge ($\sim$10 ns) is much shorter than the relaxation time of the electrodes, they behave as an insulator through out the whole discharge. The signal can be picked up by induction method using insulated conductive strips placed on the electrodes.

The readout of these detectors is discussed in the following subsection.

2.4.2 Detector Readout

The front-end electronics of the tracking stations are based on a 16-channel chip (MANAS), which includes the following functionalities: charge amplifier, filter, shaper and track & hold. It also includes a 16 to 1 analog multiplexer. The channels of four such chips are fed into a 12-bit ADCs, read out by the MARC chip which includes zero suppression. This chain is mounted on front-end boards (MANUs). A total of 16,816 MANU cards are necessary to read the 1,076,224 channels of the tracking system. Up to 26 MANUs are connected (via PATCH bus) to the translator board which allows the data transfer to the Concentrator ReadOut Cluster Unit System (CROCUS). Each chamber is read out by two CROCUS, leading to a total number of 20 CROCUS. The main tasks of the CROCUS are to concentrate data from the chambers, to transport them to the DAQ and to perform control of the front-end electronics, including calibration and dispatching of the trigger signals. The data link that connects the top most readout element of the detector (i.e. CROCUS for dimuon tracking chambers) to the DAQ is called Detector Data Link (DDL). This scheme is shown in Fig. 2.22.

The RPCs are equipped with dual-threshold front-end discriminators (ADULT), adapted to the timing properties of the detector and reach the time resolution (1–2 ns) necessary for the identification of the bunch crossing. From the discriminators, the signals are sent to the trigger electronics (local trigger cards, based on programmable circuits working in pipeline mode) where the coordinates measured in the first and second stations are compared to determine the muon p_{t}. Due to the short decision time (600–700 ns) of the electronics, the dimuon trigger participates in the ALICE L0 trigger.

Finally, it is to be noted that, according to simulations, the total dimuon trigger

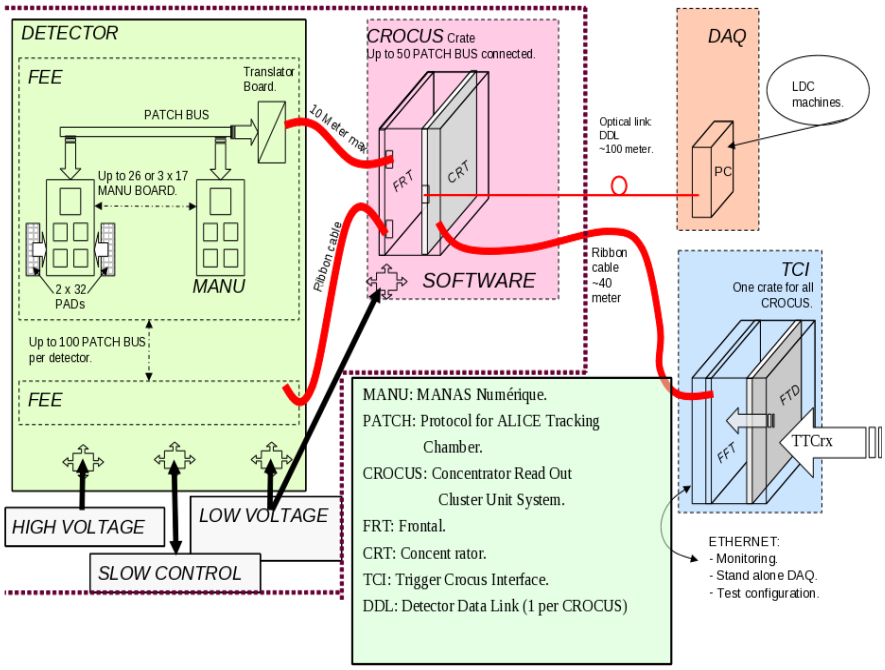

Figure 2.22: A schematic diagram for the Tracking chamber readout.

rate (with low and high-p_t cut) is not expected to exceed 1 kHz, for Pb-Pb collisions. This rate is compatible with the ALICE DAQ bandwidth.

2.4.3 RawData Format

Tracking chamber DDL event

A DDL event has a tree like structure (looped like a Russian doll). It contains, the standard ALICE header of 17 words (32 bits), followed by two data blocks (A and B for two DSPs labeled odd and even, respectively). A block contains the data from five (at most) FRT CROCUS. Each FRT structure consists of ten (at most) bus patches data. Some redundant information exits in the structures for debugging purposes. The 20 DDLs for the tracking chambers ranges from 0xA00 to 0xA13 .

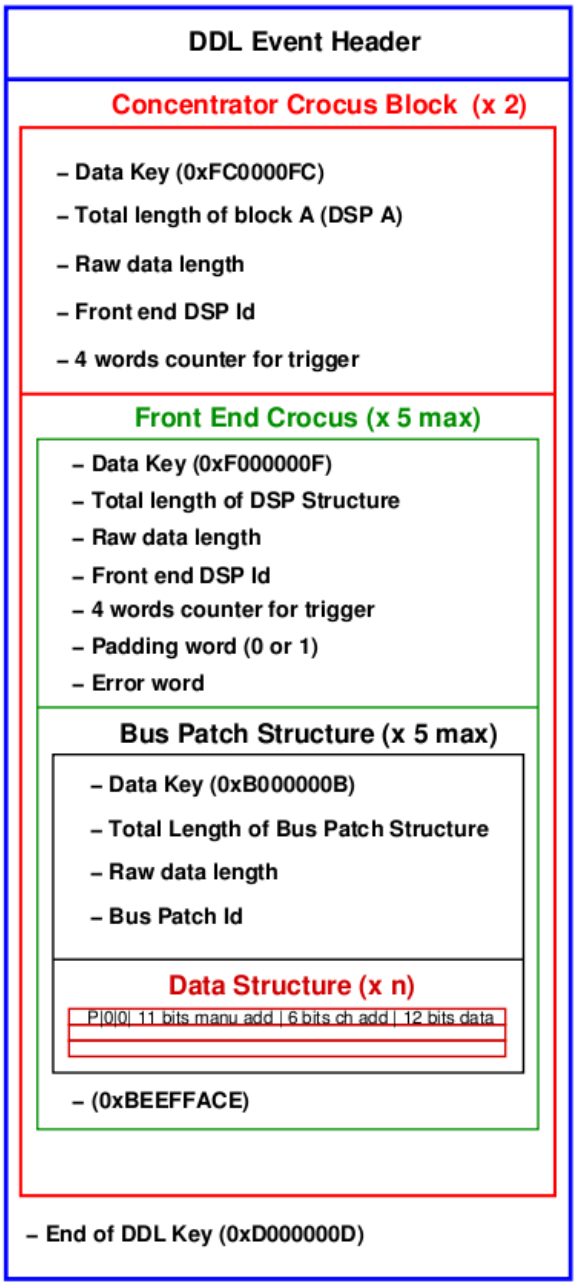

Figure 2.23: Schematic of the DDL raw event for Tracking chambers

Schematic overview of the DDL raw event were shown in Fig. 2.23.

The structure of the different data blocks have been discussed below.

Concentrator CROCUS Block Structure

The block header contains 8 words followed by the Front End CROCUS Structure:

- Data key (0xFC0000FC).
- Total length of block.
- Raw data length : length of the block minus the header (8 words).
- DSP identification.
- L1 trigger word.
- Bunch Crossing Id (for mini-event Id).
- Event Id in bunch crossing.
- Event Id in orbit number Id.

Front End CROCUS Structure

The Front End CROCUS header contains 8 words followed by the bus patch Structure:

- Data key (0xF000000F).
- Total length of DSP structure.
- Raw data length : length of the DSP structure minus the header (i.e. 10 words).
- Front end DSP identification.
- L1 accept in Block Structure (CRT).
- Mini Event Id in bunch crossing.

- Number of L1 accept in DSP Structure (FRT).
- Number of L1 reject in DSP Structure (FRT).
- Padding flag: this number is set to one if the number of rawdata word is odd and set to zero otherwise.
- Error word.

If the padding flag is set to one, an additional word (0xBEEFFACE) is put at the end of the structure to keep the number of words even.

Buspatch Structure

The buspatch header contains 4 words followed by the data:

- Data key (0xB000000B).
- Total length of buspatch structure.
- Raw data length: length of the buspatch structure minus the header (4 words).
- Buspatch identification: this allows to identify the buspatch as well as the corresponding detection element.

Data Structure

The data are packed in 32 bit words; the structure of each word is the following:

- [31]: parity bit : The ADC (MARC) chip set to one the most significant bit (bit 31) of each 32 bit data word if the number of bit equal to 1 in the 31 least significant bits is odd.
- $[29-30]$: must be zero (MBZ).

- [18 − 28]: MANU identification number (11 bits). This number is unique for each detection element.
- [12 − 17]: channel identification number in the MANU card (6 bits).
- [0 − 11]: pad charge digitalized with the ADC (12 bits).

The DDL payload ends with two 32 bit words (0xD000000D) to separate each Concentrator CROCUS structure.

Trigger chamber DDL event

The data flow of the about 21,000 strips has been concentrated in two DARC readout cards. The structure of a trigger DDL event is depicted in Fig. 2.24. The DDL event header contains 8 additional words, followed by 8 regional controller structures, including the 16 local controller structures. There are two types of data structure depending on the type of trigger. For a physics trigger, only data from the detectors are read out, while for software triggers additional information (from scalers) are read out as well.

Header

- Header word:
  - trigger occurrence (2 bits) : 01 = trigger physics 10 = trigger software Start Of Run 11 = trigger software End Of Run 00 = other trigger software
  - application type: dimuon, ZDC,... (3 bits),
  - DARC type: Vadorh, Def,... (3 bits),
  - serial number (4 bits),

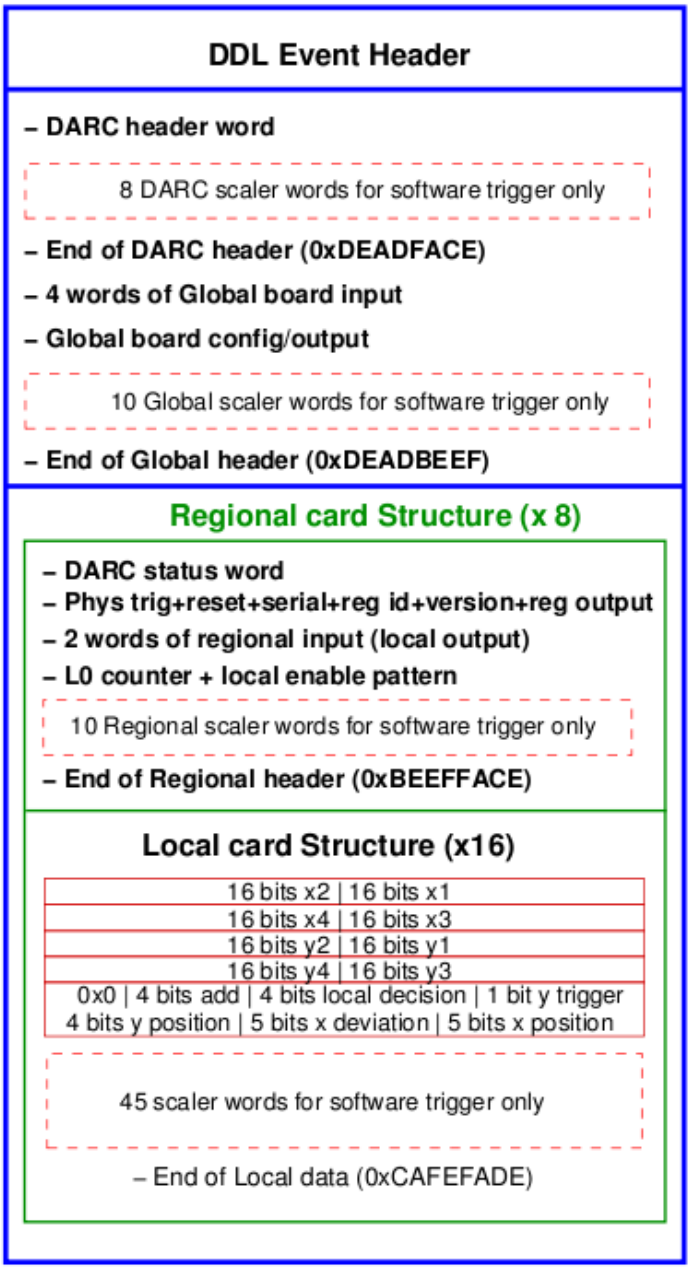

Figure 2.24: Schematic of the DDL raw event of Trigger Chambers.

– version (8 bits),

– VME trigger used (internal) (1 bit),

– global card data occurrence (1 bit),

– central trigger (or LTU) interfaced (1 bit),

  - DAQ interfaced (1 bit),
  - regional cards occurrence (8 bits).

- 8 scaler words (if soft event type)
- separator 0xDEADFACE
- 4 words of global input : 8-bit words coming from each of the 16 regional controllers.
- global card information:
  - configuration (16 bits),
  - output (6 bits) : unlike sign pair (high and low p_{t}), like sign pair (high and low p_{t}) and single muon (high and low p_{t}).
- 10 scaler words (if soft event type).
- separator 0xDEADBEEF. The global card information are only present in one DDL (global card data occurrence bit set to one), in the other the words are set to zero. If there is a software trigger, scaler information from DARC and Global cards are added (see section Scalers events for details).

Regional card structure

The header of this structure consists of four words:

- DARC status word:
  - MBZ (2 bits)
  - error status (8 bits),
    - 1 = physic, 0 = software error

    - regional occurrence
    - full error
    - empty error
    - Darc L2 reject error
    - Darc L2 error
    - Darc L1 error
    - Darc L0 error
  - FPGA number in card (3 bits),
  - MBZ (3 bits),
  - physics trigger occurrence (1 bit),
  - regional card occurrence (1 bit),
  - flag for not fully filled RAM (1 bit),
  - flag for not empty RAM (1 bit),
  - flag for L2 rejected (1 bit),
  - flag for L2 accepted (1 bit),
  - flag for L1 (1 bit),
  - flag for L0 (1 bit),
  - number of events in RAM (4 bits),
  - busy word (4 bits).

  Whenever the regional board is masked or could not be readout the value of the DARC status word is set to 0xCAFEDEAD.

- Regional word:
  - physics trigger occurrence (1 bit),

  - number of reset (6 bits),
  - regional controller serial number (5 bits),
  - regional crate identification (4 bits),
  - FPGA software version (8 bits),
  - regional output (8 bits) :
    * two bits for single high p_t muon (00: none, 01: at least one with positive charge, 10: at least one with negative charge, 11 at least one positive and one negative charge) ;
    * one bit for unlike sign pair of high p_t muon (bit on if + or 0+ or 0 or 00) ;
    * one bit for like sign pair of high p_t muon (bit on if ++ or or 0+ or 0 or 00) ;
    * two bits for single low p_t muon (00: none, 01: at least one with positive charge, 10: at least one with negative charge, 11 at least one positive and one negative charge) ;
    * one bit for unlike sign pair of low p_t muon (bit on if + or 0+ or 0 or 00) ;
    * one bit for like sign pair of low p_t muon (bit on if ++ or or 0+ or 0 or 00).

- 2 words of regional input corresponding to the 16 local controllers data:
  - low p_t word (00: none, 01: at least one with positive charge, 10: at least one negative charge, 11 at least one positive and one negative charge), 2 bits for each local board.
  - high p_t word (00: none, 01: at least one with positive charge, 10: at least one negative charge, 11 at least one positive and one negative charge), 2

bits for each local board.

- L0 counter (16 bits) and enable pattern for local board (16 bits).
- 10 scaler words (if soft event type).
- separator 0xBEEFFACE Followed by the local card structure. If there is a software trigger, scaler information from regional cards are added (see section Scaler events for details).

Local card structure

The local structure format contains 5 words defined as follows:

- 16 bits corresponding to position along X axis in plane 2, first station (x2) and 16 bits corresponding to X in the first plane (x1).
- 16 bits corresponding to position along X axis in plane 4, second station (x4) and 16 bits corresponding to X in the third plane (x3).
- 16 bits corresponding to y2 and 16 bits to y1.
- 16 bits corresponding to y4 and 16 bits to y3.
- 32 bits word (more details can be found in chapter 3.3 in ref. [4]) :
  - 9 bits are set to zero.
  - 4 bits are used to encode the local card identification number in the crate (0-15).
  - 4 bits are used to encode the trigger information from the local card decision: 2 bits for high p_{t} and 2 bits for low p_{t} trigger (least bits). No trigger: 00, trigger for negative particles: 01, trigger for positive particles: 10, trigger with no deviation: 11.

- 1 bit is used for y trigger: trigger occurrence of the local card along the X strips.
- 4 bits are used for y position (if there is a trigger, the parameter y trigger is set to 0, if not, the parameter is set to 1 and the y position is equal to 15).
- 5 bits are used to encode the x trigger and x deviation information 1 bit is used for the sign of the deviation and 4 bits are used for the deviation: (negative particle: sign = 0 and xdev = 1-15; positive particle: sign = 1 and xdev = 1-15; undefined deviation: sign = 0 and xdev = 0; no x trigger: sign = 1 and xdev = 0)
- 5 bits are used for x position.
- 45 scaler words (if soft event type).
- separator 0xCAFEFADE.

For empty or non-notified local card slots, the 5 words are set to the value: 0x10CDEAD. If there is a software trigger, the data structure is replaced by 45 words of scaler information (see next section for details).

Scalers events

Whenever a software trigger (also called checking trigger) occurs a set of additional or replacing data is sent to the DAQ system. There are extra words for the DARC card scalers, global card scalers, regional card scalers and local card scalers. The latter are replacing the physics trigger words.

1. *DARC scaler words*

The 8 scaler words are the following:

- number of L0 triggers received (16 bits), number of trigger L0 used (16 bits),
- number of L1 physics triggers, received (16 bits) and used (16 bits),
- number of L1 software triggers received (16 bits) and used (16 bits),
- number of L2 accept triggers, received (16 bits) and used (16 bits),
- number of L2 reject triggers, received (16 bits) and used (16 bits),
- number of clock cycles,
- number of clock cycles during Hold (dead time),
- spare (16 bits), number of prepulses, received (16 bits).

2. *Global card scaler words*

   The 10 scaler words are the following:

   - number of L0 triggers,
   - number of clock cycles,
   - 6 words for global card output scalers (low and high transverse momentum for unlike, like sign muon pairs and single muons),
   - number of Hold (dead time),
   - spare word.

3. *Regional card scaler words*

   The 10 scaler words are the following:

   - number of clock cycles,
   - 8 words for regional card scalers output,
   - number of clock cycles during Hold (dead time).

4. *Local card scaler words* The 45 scaler words are the following:

   - number of trigger L0,
   - number of Hold (dead time),
   - number of clock cycles,
   - 8 words for local trigger card scalers (low and high transverse momentum for no trigger, positive charge, negative charge and undefined charge scalers),
   - 4 16 words of single counting strips X1 to X4 (or Y1 to Y4) coded on 16 bits each stored two by two in a 32 bits word,
   - switches configuration (10 bits) and the ComptXY (1 bit) (set to 0 for X strip configuration and to 1 for Y strip configuration).
   - spare.

   For empty or non-notified local card slots, the 45 words are set to the value: 0x10CDEAD.

When the data is read from the detectors, it is the responsibility of ALICE Data Acquisition System (DAQ) to process and store them to the data storage. Therefore, the ALICE online systems are discussed in the following chapter.

Table 2.13: Summary of main characteristics of the Muon Spectrometer

Muon detection		
Polar, azimuthal angle coverage	$171^\circ \leq \theta \leq 178^\circ$, 2π	
Minimum muon momentum	$4\,\mathrm{GeV}/c$	
Resonance detection	J/Ψ	Υ
Pseudo-rapidity coverage	$-2.5 \leq \eta \leq -4.0$	$-2.5 \leq \eta \leq -4.0$
Transverse momentum range	$0 \leq p_\mathrm{t}$	$0 \leq p_\mathrm{t}$
Mass resolution	70 MeV	100 MeV
Front absorber		
Longitudinal position (from IP)	$-5030\,\mathrm{mm} \leq z \leq -900\,\mathrm{mm}$	
Total thickness (materials)	$\sim 10\lambda$ (carbon–concrete–steel)	
Dipole magnet		
Nominal magnetic field, field integral	0.7 T, 3 T m	
Free gap between poles	2.972–3.956 m	
Overall magnet length	4.97 m	
Longitudinal position (from IP)	$-z = 9.87\,\mathrm{m}$ (centre of the dipole yoke)	
Tracking chambers		
No. of stations, no. of planes per station	5, 2	
Longitudinal position of stations	$-z = 5\,357, 6\,860, 9\,830, 12\,920, 14\,221\,\mathrm{mm}$	
Anode–cathode gap (equal to wire pitch)	2.1 mm for st. 1; 2.5 mm for st. 2–5	
Gas mixture	80 %Ar/20 %CO_2	
Pad size st. 1 (bending plane)	$4 \times 6,\ 4 \times 12,\ 4 \times 24\,\mathrm{mm}^2$	
Pad size st. 2 (bending plane)	$5 \times 7.5,\ 5 \times 15,\ 5 \times 30\,\mathrm{mm}^2$	
Pad size st. 3, 4 and 5 (bending plane)	$5 \times 25,\ 5 \times 50,\ 5 \times 100\,\mathrm{mm}^2$	
Max. hit dens. st. 1–5 (central Pb–Pb $\times$ 2)	5.0, 2.1, 0.7, 0.5, $0.6 \cdot 10^{-2}$ hits/cm^2	
Spatial resolution (bending plane)	$\simeq 70\,\mu\mathrm{m}$	
Tracking electronics		
Total no. of FEE channels	1.09×10^6	
Shaping amplifier peaking time	$1.2\,\mu\mathrm{s}$	
Trigger chambers		
No. of stations, no. of planes per station	2, 2	
Longitudinal position of stations	$-z = 16\,120, 17\,120\,\mathrm{mm}$	
Total no. of RPCs, total active surface	72, $\sim 150\,\mathrm{m}^2$	
Gas gap	single, 2 mm	
Electrode material and resistivity	Bakelite$^{\mathrm{TM}}$, $\rho = 2 - 4 \times 10^9\,\Omega$ cm	
Gas mixture	Ar/$C_2H_2F_4$/i-buthane/SF_6 ratio 49/40/7/1	
Pitch of readout strips (bending plane)	10.6, 21.2, 42.5 mm (for trigger st. 1)	
Max. strip occupancy of bending (non-bending) plane	3 %(10 %) in central Pb–Pb	
Maximum hit rate on RPCs	3 (40) Hz/cm^2 in Pb–Pb (Ar–Ar)	
Trigger electronics		
Total no. of FEE channels	2.1×10^4	
No. of local trigger cards	$234 + 2$	

Bibliography

[1] ALICE Collaboration. J. Phys. G: Nucl. Part. Phys. **30** (2004) 1517-1763.

[2] ALICE Collaboration. J. Phys. G: Nucl. Part. Phys. **32** (2006) 1295-2040.

[3] ALICE Collaboration. JINST **5** P03003 (2010)

Chapter 3

High Level Trigger

The High Level Trigger (HLT) is one of the four major online data processing system of ALICE. It is motivated by the goal of delivering the best possible trigger cut based on event selection by online reconstruction. Since a typical data rate of 25 GBytes/s is expected for the central Pb-Pb collisions, it becomes inevitable to reduce the background events before it is written to disk. A short description of the main online systems are summarised at the beginning, in order to explain the general data flow scheme of the experiment. This is followed by the detail description of the online and analysis scheme. The last part of this chapter contains the overview of the present HLT functionalities of the MUON detector.

3.1 Overview of ALICE Online Systems

The four main online systems of ALICE are Detector Control System (DCS), Central Trigger Processor (CTP), Data Acquisition System (DAQ) and HLT. These systems are steered by another system known as Experimental Control System (ECS).

The functionality and inter-communication of the five system are explained below.

3.1.1 Detector Control System (DCS)

The primary task of the DCS is to ensure safe and correct operation of the ALICE experiment. It provides the detector configuration, remote control, and monitoring of all experimental equipments.

A tree like software architecture has been used to connect the detector modules to their sub-detectors and devices. The basic building blocks for implementation of the controls hierarchy are Control Units (that model the behaviour and communication between components) and Device Units (that drive the equipment to which they correspond). The DCS uses an implementation based on Finite-State Machines (FSMs), which provides an intuitive and convenient mechanism to model the functionality and behaviour of components.

In addition, to the controlling of all sub-detector equipments, the DCS also interfaces to the various external services needed for the operation of the experiment such as gas, cooling, electricity, safety. Another important task of DCS is to perform the handshaking with LHC control during the beam injection and beam dumping to insure the safety of the subdetectors.

3.1.2 Experiment Control System (ECS)

The architecture of Experiment Control System (ECS) can be realised in terms of a intercommunication of several lower level components.

It has been described in the final section of the last chapter that the data of

detectors are collected by the DDLs. The DDLs are read by the Run Control (RC) manager of DAQ. This has also been used to validate the detector performance using the pedestal, calibration and standalone runs during the detector integration stage at ALICE pit. In the next level the Run Control is integrated with the Detector Control Agent (DCA) and the setup gets connected with the DCS, CTP and HLT. This forms a complete standalone detector configuration connected with all necessary online systems. In the final stage of detector integration, several different types of detectors (or individual DCAs) are connected via a framework called Partition Control Agent (PCA). Thus, the ECS is the central control point of the experiment and provides a overall view of the experiment using the PCAs.

The available resources (DCS, CTP, HLT, DAQ) are described at the central database of ECS. The Experiment Control Agent (ECA) is a utility that manages the database on the basis of the resources that are allocated by the PCA. The commands from PCA flows to the detectors following the simple schematic path of

$$\text{ECS} \Longrightarrow \text{PCA} \Longrightarrow \text{DCA} \Longrightarrow \text{RC},$$

in the hierarchical manner as it has been described above.

The communication technology and the priority logic between the control agents is implemented via Finite-State Machines (FSMs). This provides a natural way of communication, based on the control of objects located in a remote Activity Domain. For instance, a sub-detector can be controlled either by the DCA or from PCA depending on the owner of the control of the detector.

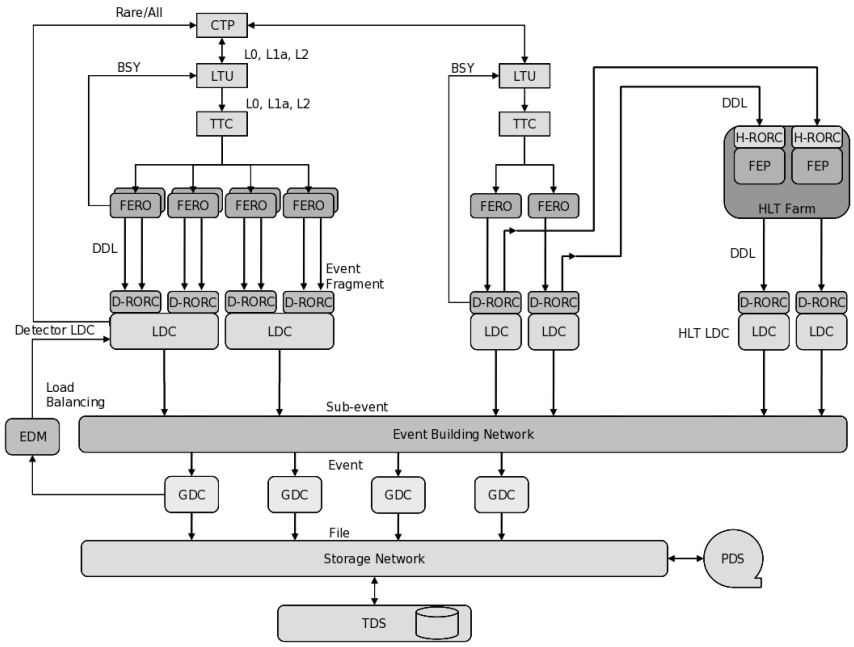

Figure 3.1: A schematic for TRIGGER–DAQ–HLT overall architecture.

3.1.3 Central Trigger Processor (CTP)

The first trigger levels in ALICE (L0, L1, L2) are provided by the following detector systems, V0, T0, PHOS, TRD, Muon Trigger detectors and ACORDE. Each of them generate a number of logic trigger signals which characterize a specific measurement in a particular detector (e.g. multiplicity, high-p_{t}, muon pair). These logical signals (up to a total of 49 inputs) are sent to the Central Trigger Processor (CTP), which is located in the experimental hall. These signals are combined by logical operations inside a FPGA to form the different physics triggers (e.g. minimum-bias or central collisions, high-p_{t} jets etc.). The output trigger signal is sent to a number of Local Trigger Units (LTUs), typically one for each sub-detector, where they are further processed according to the different detector requirements and finally sent back to the detector Front-End Electronics (FEE). In addition, the CTP takes care of downscaling, pile-up protection, check on the ready status of different detectors and read-out memories, trigger priority, and finally synchronization with the machine

clock.

Another feature of the ALICE trigger is the possibility to dynamically configure groups of detectors that participate in the readout of any given event. The TPC is constrained to low trigger rates, both because of drift time and data volume, compared to the other detectors (e.g. the muon arm), which can record events at a much higher rate. Therefore, in order to improve statistics for specific physics channels, groups of detectors, called *trigger clusters*, are read out separately.

As pointed before, the ALICE trigger is organized into three different levels, L0, L1, and L2, which have different latencies. In some detectors the front-end electronics requires a strobe very early, and so a first trigger decision must be delivered within 1.2 μs after the collision takes place. As some trigger detectors are not able to send their input in time, the 'fast' logic is divided into two stages: everything which can be achieved in 1.2 μs is used to make the L0 decision. The detectors which require more time contribute to the L1 decision, which arrives at the detectors after 6.5 μs. The third step, the L2 decision, comes after the end of the drift time in the TPC, i.e. at about 88 μs. The main purpose of this third step is to wait for the end of the past–future pile-up protection. The read-out of the TPC electronics is initiated only upon the receipt of a positive L2 decision.

3.1.4 Data Acquisition's (DAQ)

The function of the DAQ system is to control the dataflow from the detector up to the data storage, to and fro dataflow with High-Level Trigger (HLT) farm, sub-event and complete event building. The DAQ system also includes software packages for raw data integrity and system performance monitoring.

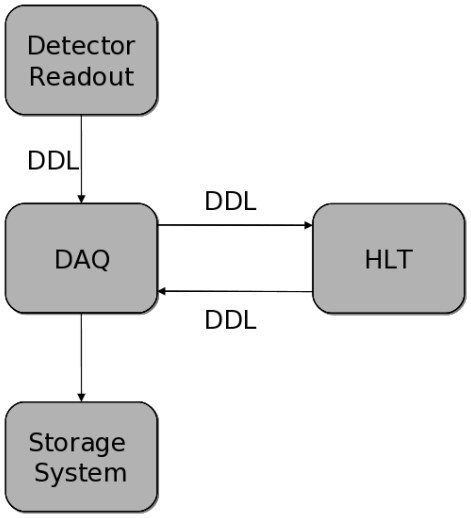

Figure 3.2: A schematic view of DAQ–HLT interface.

The DAQ dataflow starts at the detector FEE, where a logical interface has been defined between the electronics and the DAQ system. This interface is a collection of the hardwares and softwares used for the readout of the different detectors. The hardware consists of a bi-directional optical cable, known as Detector Data Link (DDL) [see sec. §2.4.2]. This is used both for the transfer of physics data from the detector to the DAQ and for the transfer of control commands and configuration parameters in the opposite direction.

Once the data are collected from detector, they are transferred directly to the memory of standard Personal Computers (PCs) via a DDL adapter connected to D-RORC mounted on the PCI bus. Those computers which collect the data from the detectors are called Local Data Concentrators (LDCs). The D-RORC can have a bandwidth of 250 MBytes/s. In addition, it sends a second copy of the raw data via a DDL link to the HLT system.

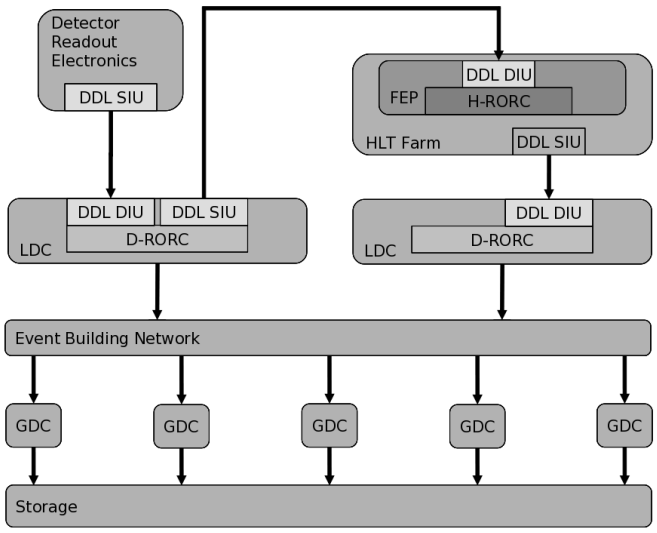

Figure 3.3: A schematic for DAQ–HLT Data Flow overview.

The event building is performed by a switching network with a total internal bandwidth of 2.5 GBytes/s. The data are archived in two steps, Transient Data Storage (TDS) based on disks close to the experiment and Permanent Data Storage (PDS) based on magnetic tapes in the CERN computing centre [Fig. 3.1].

3.1.5 High-Level Trigger (HLT)

The High Level Trigger combines and processes the full information from all major detectors of ALICE. It selects the most relevant data from the large input stream. This includes the reduction of the data volume by an order of magnitude to fit the available storage bandwidth and is achieved by a combination of techniques:

- reducing the event rate by selecting interesting events (software trigger);
- reducing the event size by selecting sub-events (Region of Interest, RoI);
- reducing the event size by advanced data compression.

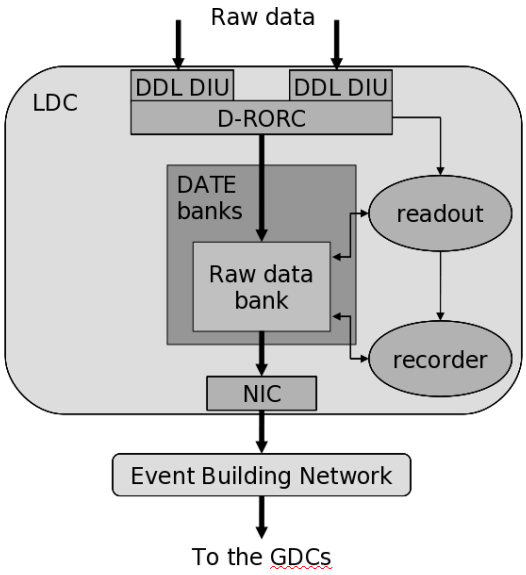

Figure 3.4: A schematic representation of data flow in the LDC of DAQ without the HLT components.

All three tasks require online event reconstruction, which involves clustering and track finding. These items are discussed in detail in the later sections.

The HLT farm is designed to be completely fault-tolerant, avoiding all single points of failures, except for the unique DDL links. A generic data transport framework has been developed based on the Publisher Subscriber (Pub-Sub) principle, which allows the construction of any hierarchy of communication processing elements.

The HLT output [trigger decisions, Event Summary Data (ESD), and modified raw data as appropriate] is forwarded to the DAQ again via DDL connections.

The ECS running modes of HLT during global data taking of ALICE is described in table 3.1. It is to be pointed out that, in modes B and C, HLT is treated like any other detector and generated data are stored as part of the event building.

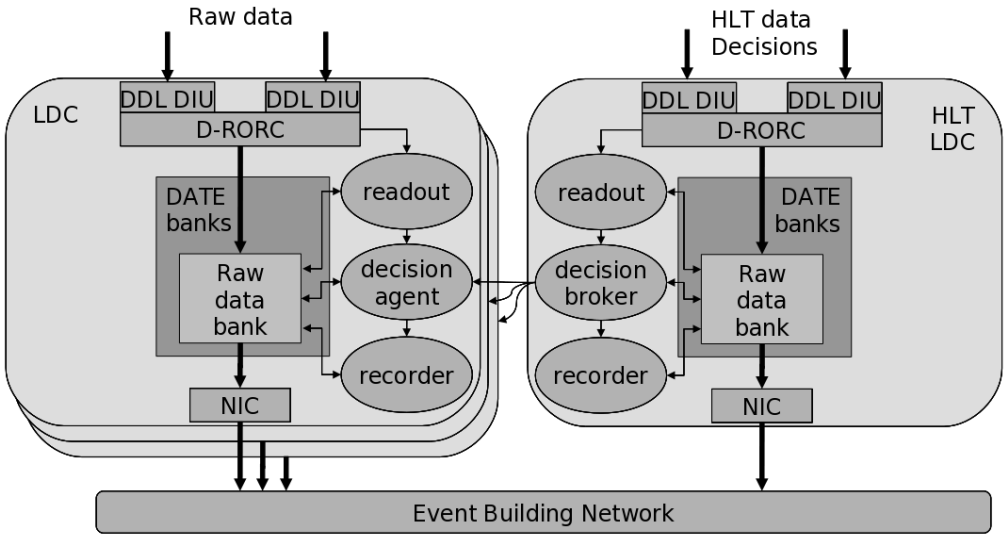

Figure 3.5: A schematic representation of data flow mechanism in the LDC of DAQ when the HLT has been turned on.

Table 3.1: The different HLT modes in ALICE data-taking

(A)	**:**	DAQ is running without HLT.
(B/Test1)	**:**	HLT is included with no HLT output to DAQ and HLT-busy is not respected.
(B/Test2)	**:**	HLT is included with no HLT output to DAQ and HLT-busy is respected.
(B)	**:**	HLT is fully included into the system, which means HLT output is sent to DAQ and HLT-busy is respected. But the HLT trigger decision is not considered.
(C)	**:**	DAQ performs event and sub-event selection based on the trigger information from HLT.

3.2 Dataflow Scheme

The full description of the ALICE data flow scheme can be found at Ref.[1]. A short description is presented here which is related with the data processing in HLT.

The architecture and interlinks of the Trigger, DAQ and HLT systems are illustrated in Fig. 3.1.

The detectors start to record the data as soon it receives the CTP trigger. The data is then collected from the detectors by the DAQ. A copy of the data is sent to HLT, which are processed and the HLT output and/or decision is sent back to DAQ. As soon as the analysed data are received from HLT output DDLs, the data stream moves to the event building process and are stored first into the TDS. The data are finally migrated from TDS to PDS. A schematic view of the DAQ–HLT interface is illustrated in Fig. 3.2. The interface is based on the DDL and the associated Destination Interface unit (DIU) and Source Interface Unit (SIU) cards. The same components are also used to transfer data from the detector FEE electronics to the DAQ system.

Every D-RORC can host two DIUs, which can be used in two ways:

- both can be connected to the front-end electronics and serve as two readout links,
- one DIU can be connected to the front-end electronics while the other is able to transfer a copy of all the raw data to the HLT RORC (H-RORC) mounted on the HLT computers, through the standard DDL [Fig. 3.3].

The H-RORC receives all the raw data as they have been received by the front-end electronics. All the LDCs dedicated to the detectors which make use of the HLT system are equipped with D-RORCs working in the second mode.

The processed data from HLT are received back by the DAQ via the HLT LDCs. These LDCs also receive messages specifying whether to discard or accept a given event. Furthermore, for accepted events, the HLT decision can specify a

pattern of sources for a given event, resulting in a partial readout of the raw data. A decision broker process, running in the HLT LDCs, transfers the HLT information and decision to a decision agent process, running in the detector LDCs, as shown in Fig. 3.5. The figure 3.4 shows the data flow in DAQ in the absence of HLT (i.e. HLT mode "A" as explained in Tab. 3.1).

3.3 HLT Online Framework

It is important to present a basic view of data flow scheme of HLT before the explanation of HLT processing mechanism. Inside the HLT PC farm, the Front End Processors (FEPs) are responsible for zeroth level of data processing, as these are connected to the FEE by the H-RORC. When the H-RORC receives rawdata it is transferred to the memory using DMA (Direct Memory Access) method. In the next step the processing components of the FEPs analyse the data and the output are passed to the next level of computing nodes for subsequent analysis. In this way the rawdata blocks are parallely and independently analysed for every DDLs. The merged data blocks from all or part of FEPs for a given detector are collected and analysed for track formation. Once the tracks and ESDs for every detectors participating in HLT analysis are produced, they are merged and sent to DAQ for event building. On the basis of the event analysis, HLT can issue a trigger about the goodness/badness of the current event depending on the pre-defined trigger criteria. The online analysis scheme of HLT is explained in three subsections :

i) Data Processing and Transport

ii) HLT Output to DAQ

iii) Online Configuration

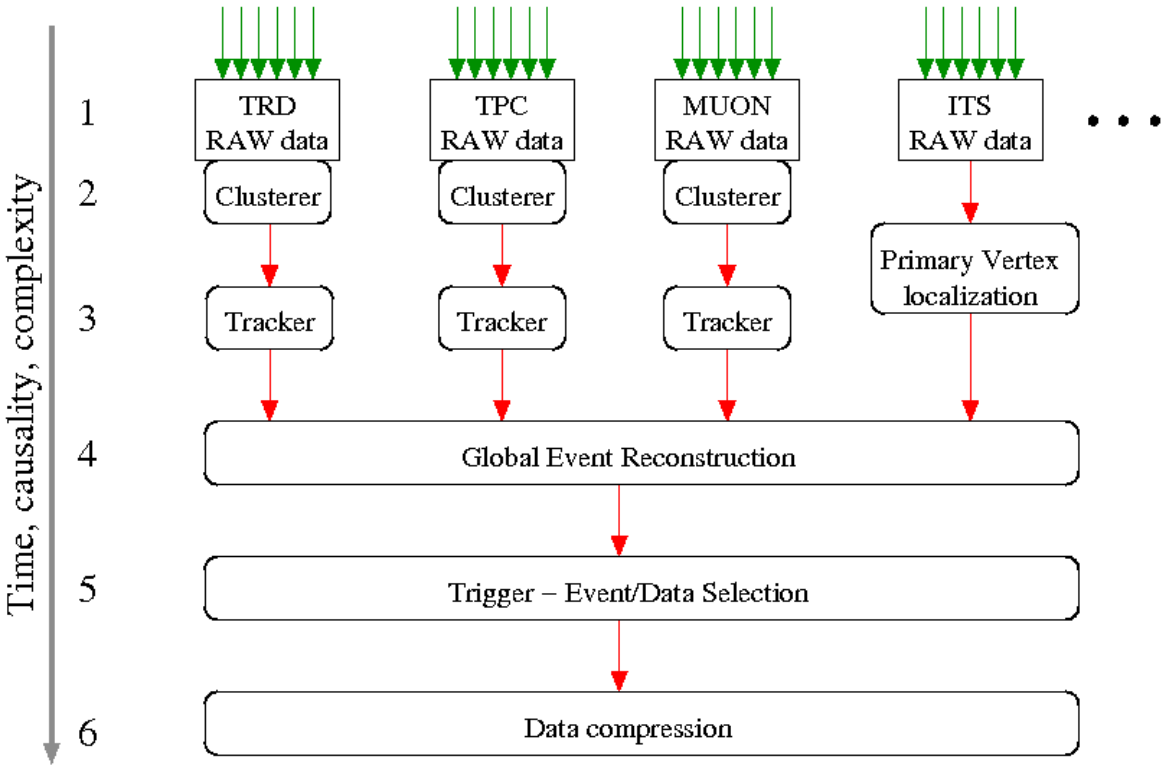

Figure 3.6: The general HLT multi-stage processing scheme.

3.3.1 HLT Data Processing and Transport

Components for Data Processing

The data processing within the HLT hierarchy is carried out by individual processes. These applications are derived from the same base class of the data transport framework which provides the interface. The processes are known as HLT components, following identical working principles. This term is also motivated by the modular concept. The components carry out different tasks in the HLT processing hierarchy, treating input data and producing new data for subsequent components. Each component is an individual process which is initiated at start-up of the processing chain. The state of a component can be changed by commands via network ports. In general, the components of data transport framework can be arranged in three categories :

- *Data Source :* The components that load data from the input device or file into shared memory and create the corresponding data descriptors.

- *Data Processing (Processors) :* The components which subscribe to data of its parents, process the data and publish the result to the next level.

- *Data Sink :* The components that implement the last stage in the chain, doing the appropriate action on the output of the chain [Fig. 3.7].

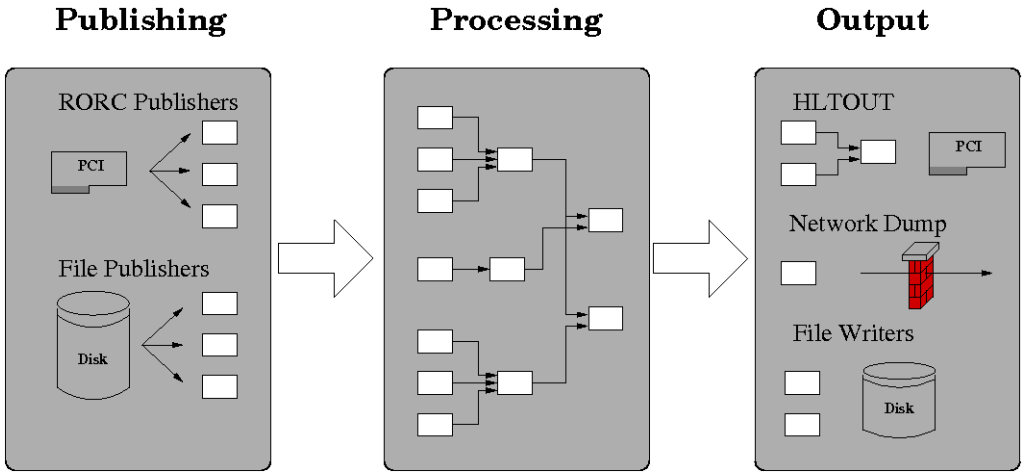

Figure 3.7: The HLT Components schematic

.

Although the HLT is an online framework, the analysis algorithms running on it has to be tested and validated in offline mode well before their proper online implementation. Thus, a special group of processing components has been created by HLT analysis components. They allow the analysis processes to run in either the offline environment or in the online HLT environment without any change in the code or the need of recompilation. A special component of the HLT data transport framework, the *AliRootWrapperSubscriber* is the link between offline analysis components and the online environment.

Publisher-Subscriber Transport Framework

The high overall processing rate demands an efficient framework for fast data transport. A dedicated data transport framework has been developed for this purpose which is known as Publisher-Subscriber framework. It carries out all data transport and communication in HLT [2]. In addition to parallel processing of events, the ALICE HLT's data transport framework allows to split and distribute single events over a set of cluster nodes. The splitting of an event reduces the amount of data to be copied. For instance, in the first step of the analysis, clusters and/or space points are reconstructed from the raw data. Thus, the resulting data volume has already been significantly reduced compared to the raw data.

The entire communication mechanism is designed for a low processing overhead. The figure 3.8 shows the working principle of the online framework. On one node, the data are exchanged via shared memory, a publisher can write the data directly to memory and makes it available for subscribers without any intermediate copying. All processes communicate via *named pipes* (Named pipes implement a method of inter-process communication on Unix/Unix-like systems) and exchange small data description information. The data transport framework takes care of data transport among the nodes transparently. More details about the online framework can be found in [3] and [4].

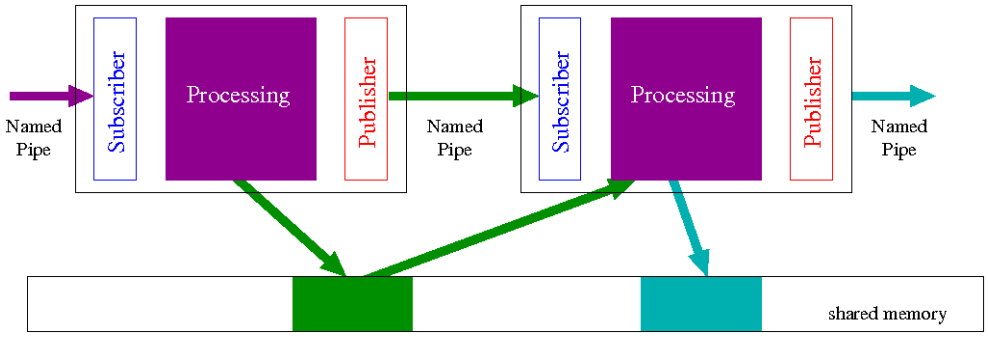

Figure 3.8: The working principle of the HLT data transport framework.

For load balancing, the data stream can be split into several data streams each carrying a smaller data volume,

Furthermore, the distribution of the analysis leads to a short processing time per event and node. This has additional advantage that if one node fails, the data loss is much smaller than in a conventional event building and filtering approach where a complete event or at least the processing time is lost. An intelligent scheduler can restart processes on another node and resume event processing in case of a severe failure of a computing nodes.

It is to be noted that in parallel computing, process synchronization plays an important role, for example a subscriber must not access data until the publisher has announced readiness. The data transport framework carries out all process synchronization.

3.3.2 HLT Output

The primary goal of HLT is to produce separate trigger information of various types. This implies the identification of the events triggered by particle multiplicities, particle energies or transverse momenta, certain decay processes, or distinct particle densities in limited regions of the detector setup.

The event triggering is mostly a yes/no decision, the event is either considered valuable or not. But the result of the online reconstruction needs to be stored together with the trigger information in order to determine the efficiency and selectivity of the trigger in later offline stages of the analysis. In addition, data volume is reduced by selective readout and storing only the relevant part of data. This technique is called **R**egion **O**f **I**nterest readout. The ROI criteria can be applied in the first place on the

level of DDL inputs and HLT simply provides a list of DDLs to be included into final event building. The format is defined in Ref. [5].

All readout lists from the running trigger components are treated by the processes on the HLTOUT nodes and formatted together with the HLTOUT payload into a defined DDL format ([5], [6]).

HLT Output Payload

Beside trigger information, HLTOUT format includes also payload data which DAQ just forwards to storage. As a matter of fact, any output of HLT components can be directed to the HLTOUT and is included in the payload.

Since HLT is an online system, the payload contains information about fully reconstructed events as part of the normal raw data stream. Beside this information which is essential for the evaluation of the trigger, data blocks of varying nature are stored depending on the configuration of the analysis chain.

Compressed Raw Data

A special feature of HLT is the reduction of the data volume by applying appropriate compression techniques. The original data are encoded according to a compression algorithm and stored as a part of the HLTOUT payload. Data compression has been extensively studied for the Time Projection Chamber which is the biggest contributor to the data volume in ALICE [7]

In general there are two data compression paradigms. A Loss-less compression techniques allow to restore the original data from the compressed data set. Higher compression ratios can be achieved by applying specific models suited for the nature

of data and omitting irrelevant information. However, the original data cannot be restored from the compressed data.

In both cases the offline reconstruction will treat the compressed instead of the original data and data flow schemes need to be designed. Thus, it is important to completely separate the reconstruction algorithm and the data input in order to handle different types of compressed data.

3.3.3 HLT Online Configuration

The mode of online HLT analysis is defined by the HLT configuration. For instance, in case of online testing of the analysis components, a online configuration is composed of file publishing, clustering, tracking and display components. Whereas, in experiment the configuration can be imagined as, DDL publishing, clustering, tracking and ESD building. Thus, in the two cases two different component sets are used in the form of two different configurations. Therefore, a configuration selects the components to be used and the rules of communication between them. A configuration describes basic properties of the HLT processing layers,

- Type of the component

  The configuration specifies the application to run.

- Command line arguments of the component

  In order to adapt to different needs, components understand certain command line parameters. The exact format of parameters depends on the implementation of the specific component.

- Interconnections of components

  The configuration specifies all parent processes the component needs to

subscribe to in order to receive data.

- Reserved output buffer size and number of available buffers

  Output data buffers have to be allocated before the processing loop of the component is invoked. The component has a fixed size of memory available in order to write its output. The number of available buffers has an important impact to pipelined processing.

- Process multiplicity

  For load distribution, multiple instances of the same component can run in parallel. The process multiplicity is part of the configuration.

- Fan-in/Fan-out

  The configuration defines the topology of the chain which includes merging of multiple publishers to one consumer (Fan-in) and distribution of one publisher to multiple consumers (Fan-out)

In HLT, a configuration is described in XML notation, which stands for Extensible Markup Language. In general, a Markup Language is an artificial language adding information on how to deal with a certain type of text and content. Markup languages are suited to categorize properties in an hierarchical way and are easy to parse in order to build the structure defined in this markup language.

The HLT configuration defines the execution sequence of the *TaskManager* applications, which run on each node of the computing cluster and supervise all processes on a given node [8]. Since the HLT chain can easily describe several hundreds of components on hundreds of nodes, abstractions of configurations have been introduced with an automated generation of the final configuration [9].

Integration into the ALICE experiment

It is to be noted that, the HLT is integrated into the ALICE experiment by a couple of interfaces. For normal operation, HLT requires not only data exchange with the DAQ but also the availability of calibration data and permanently monitored values from the detector survey. Thus it has to communicate with all other ALICE systems, such as the ECS, DCS, and the offline system. All interfaces are described in detail at [10]. HLT implements a finite state machine as outlined in [11] and Fig. 3.9.

Each state and transition correspond to certain actions and run conditions of the different parts of HLT.

(i) The transition from state **INITIALIZED** to **CONFIGURED** entails the PubSub framework compiling all configuration files. At this stage, no components are yet running, only *TaskManagers* are loaded on the different nodes.

(ii) The transition from state **CONFIGURED** to **READY** by the *ENGAGE* command implies start and setup of all components. After going to state **READY**, HLT can be started by a *START* command and processes events when in state **RUNNING**.

The next section describes the HLT online and offline analysis framework. This will help to understand the implementation of data analysis algorithms in HLT framework.

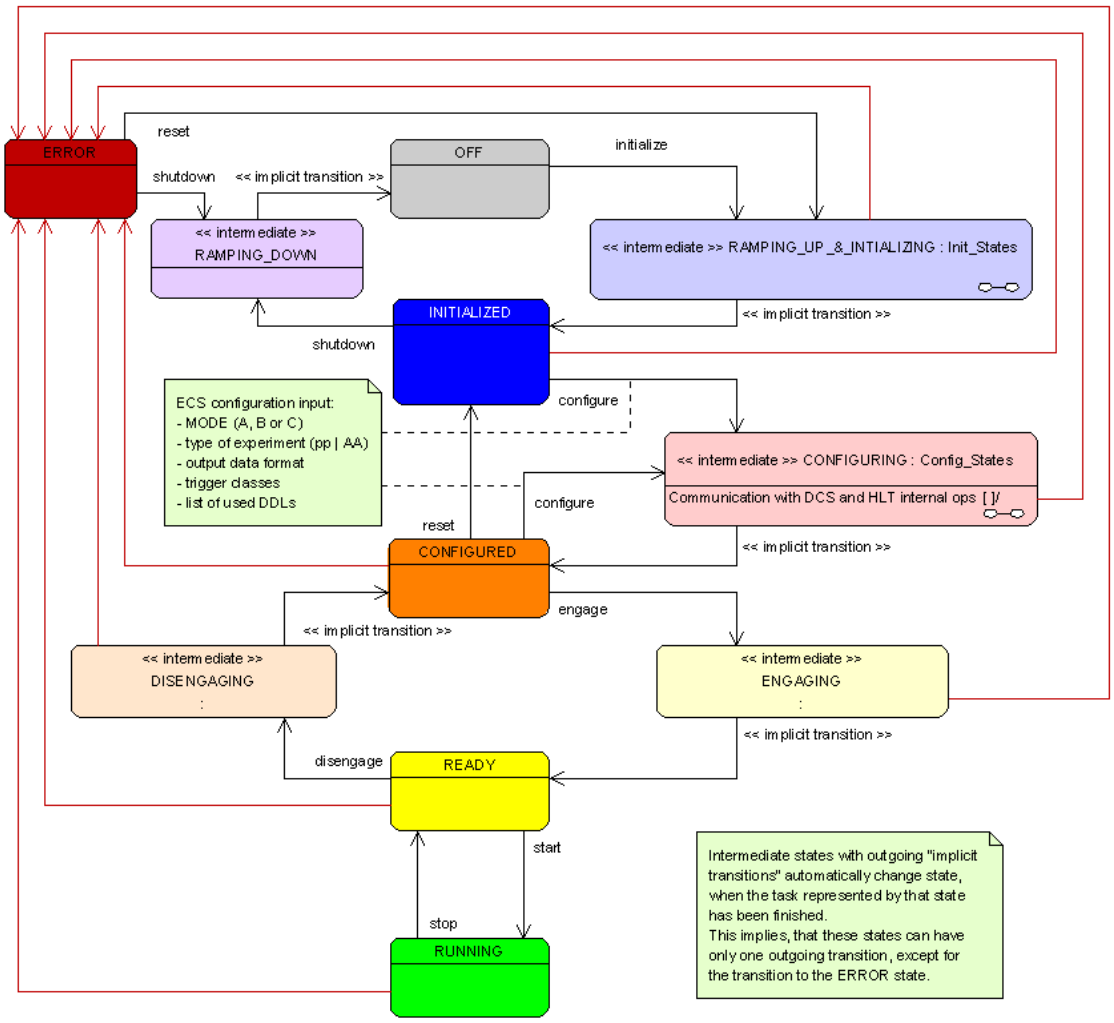

Figure 3.9: The state diagram of the HLT system shows the different states HLT. When the HLT receives command from ECS, the HLT moves between these states depending on the success or the failure of the command. [11].

3.4 HLT Analysis

The validation of HLT trigger selectivity and performance study of the algorithms requires comparison of its components to the offline reconstruction and analysis. Thus, it is important to run online analysis components without any change in the source code. To achieve this the HLT analysis chains have to be present in AliRoot as in the online framework.

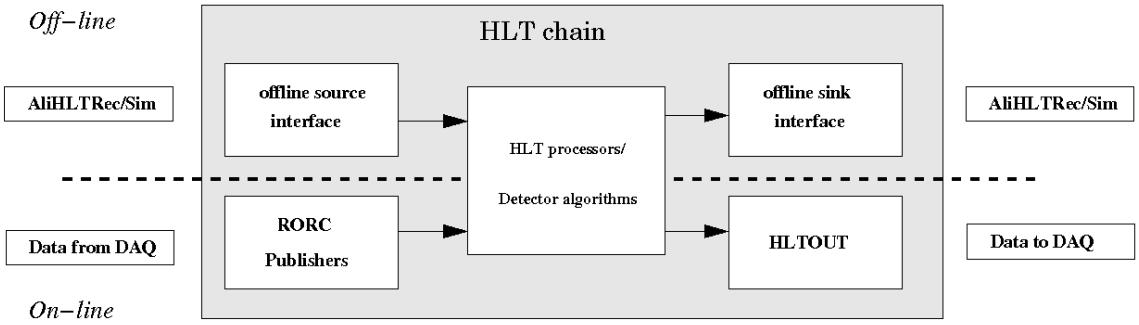

Figure 3.10: The HLT analysis chains in the online and offline modes.

A schematic view of of the online and offline analysis procedures have been shown in Fig. 3.10.

3.4.1 Base Classes and functionalities

Modularization

In the large scale software project, sometimes it is found that a compiled library A depends on a program declared in B, whereas B depends on a program specified in A. This dependency problem is known as *circular library dependency problem*. The HLT analysis framework follows a clear dependency tree in order to avoid the circular library dependency problems. The organization is outlined in Fig. 3.11. The libraries fall in 3 categories, (i) Framework Layer, (ii) Service Layer, and (iii) Module Layer.

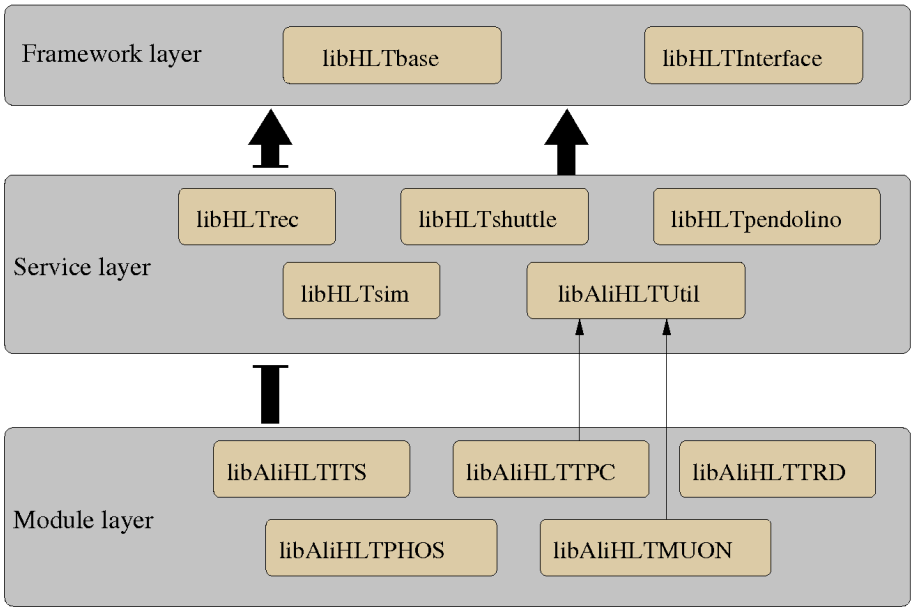

Figure 3.11: The Modular organization of the HLT analysis framework.

- **Framework Layer :** In the Framework Layer, a base library, libHLTbase, provides all functionality needed for HLT analysis. It only depends on ROOT libraries, apart from system libraries. The second library of the Framework Layer, libHLTinterface, implements an abstract interface intended to allow utilization of HLT components in external applications (i.e. the online Pub-Sub).

- **Service Layer :** The Service Layer contains libraries with AliRoot binding functionality, libHLTsim and libHLTrec for the offline simulation and reconstruction, respectively. A utility toolbox, libAliHLTUtil, implements both supporting classes and utility components.

- **Module Layer :** The HLT analysis components of individual detectors are accessed via their corresponding libraries. All these libraries of this category fall under Module Layer. These libraries of this layer depend on the Framework Layers and offline analysis libraries of the given detector. As the libraries of the module layer implement HLT analysis components, they are also referred

as component libraries.

HLT Analysis Component Interface

The main objective of the interface is a unified utilization from the online and offline systems.

The component interface makes use of function overloading supported by C++ classes. A couple of member functions of the base class are defined virtual, indicating the compiler that those functions can be overloaded by child classes. The analysis framework always uses references to objects of type AliHLTComponent for each instantiated object of component implementations. If an overloaded function is present in the child class, it is invoked instead of the base class method. The ability to treat derived class members just like their parent class members is referred in software engineering to be Polymorphism.

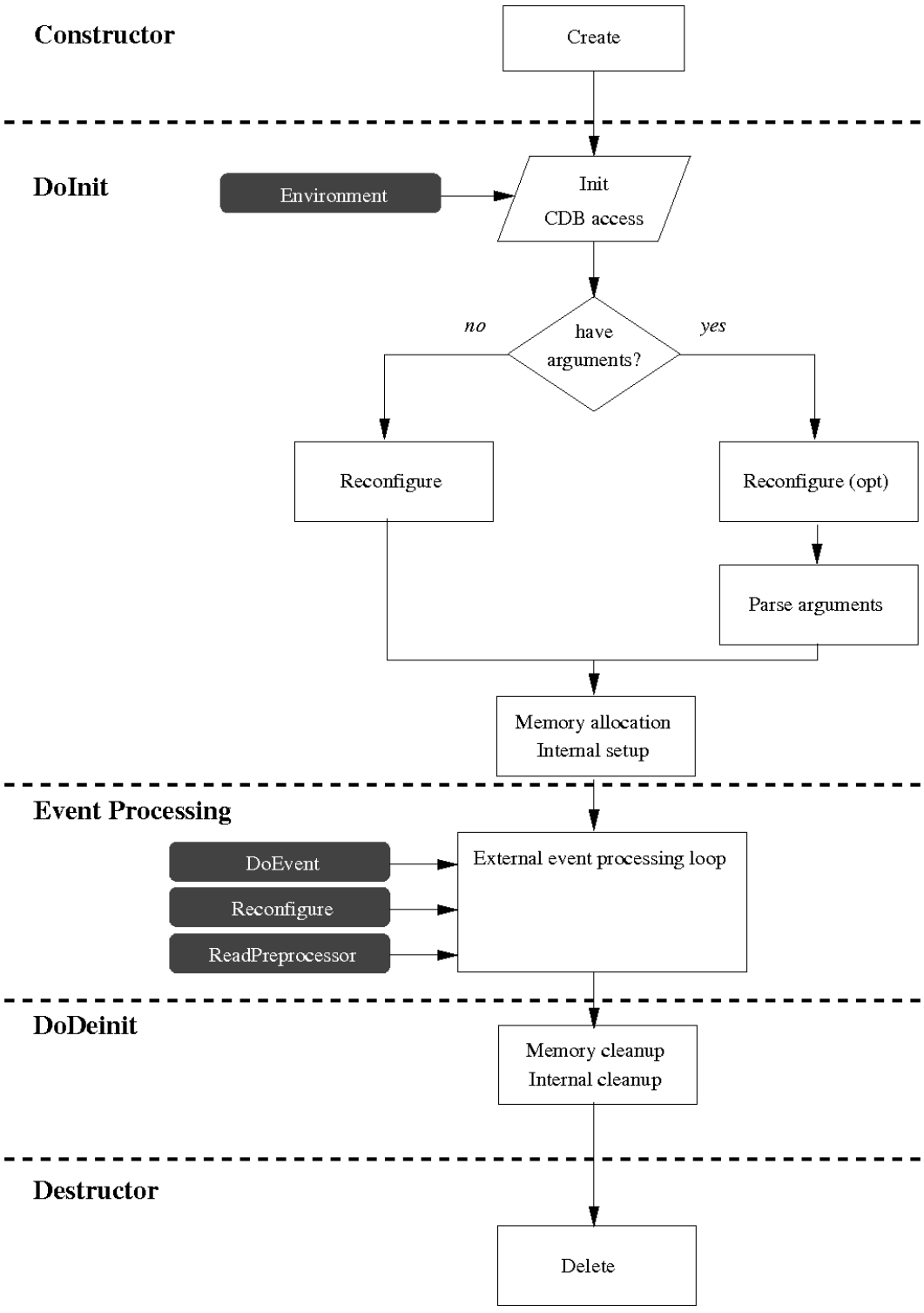

Figure 3.12: The HLT component with overloaded methods.

The HLT work-flow with these overloaded methods are shown in Fig. 3.12. The child classes of the analysis component of an individual detector implement these

methods, namely, *Constructor, DoInit, DoEvent, Reconfigure, ReadPreprocessor, DoDeinit* and *Destructor*. In the online analysis environment these functions are called during the different states of HLT as shown in Fig. 3.9. In the offline analysis, these same methods are called but from the AliSimulation class instead of ECS command. In this way, HLT executes the same analysis components for a given detector, irrespective of the origin of the data - online or offline. Each of these overloaded components is uniquely identified by the *ComponentId*, a character string of arbitrary length and content. It is used by the *ComponentHandler* to register the component and to create instances on demand. For practical reasons, a descriptive name is used, like e.g. *MUONHitReconstructor*. The data processing carried out by the component is characterized by component data types and the amount of data going to be produced with respect to the input data size. A component is furthermore classified by the amount of memory it uses for data processing and the overall processing time.

Module Agents

When a new functionality needs to be announced to the system, it is declared using the Module Agent. The agent defines the properties of the library, in such way that when the offline simulation or reconstruction queries for the HLT analysis, the module agents instantiates the corresponding HLT analysis chain for each of the individual detector. Therefore it is the responsibility of analysis developer to define the functionalities of components via the module agents.

Component Registration

The components are the worker plug-ins for HLT analysis and are created dynamically according to the configuration. As a prerequisite, components must be known to the system. The analysis framework implements a registration scheme which is the backbone for the realization of modularity. The agent needs to implement the function, which is invoked by the system after the library has been loaded.

HLT Offline Configurations

In the online system, configurations are fully separated from the actual implementation of both data transport and analysis.

The offline environment also requires mechanisms to describe an HLT chain and run components in an analysis hierarchy, both in simulation and reconstruction. The AliRoot binding functionality of the HLT analysis framework provides simple notations to specify hierarchies of component for processing. The module agent specifies HLT configurations which are supposed to run as default configurations in the different steps of AliRoot by means of the functions.

3.4.2 Online Interface

The interface between the online data transport framework and the HLT analysis components is provided by a C-interface.

In dynamic libraries, functions in the source code correspond to entry pointers in a compiled library. During program execution, all parameters are stored on the *stack* (in computing architectures, a stack is a special kind of data storage based

on the Last-In-First-Out paradigm) and the program jumps to the address in the library. A C-interface uses this execution sequence by providing the entry pointers to the external application. The figure 3.13 sketches the entry points of the interface used by the online HLT system.

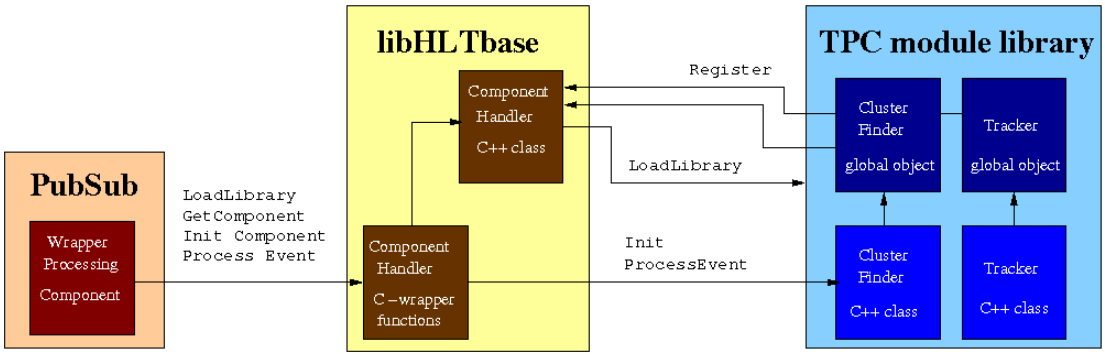

Figure 3.13: The figure shows the utilization of the C wrapper interface by the online HLT.

During initialization of the interface, the internal ComponentHandler and the execution environment is set up. Subsequently, component libraries can be loaded, components be created and events processed.

A special care has to be taken with all memory allocations and data processing as the two (online and offline) frameworks run in different domains. So a memory buffer allocated inside the HLT analysis cannot be freed in the PubSub system without introducing a potential source for memory corruption. Depending on the compilation and running environment, memory management might be different in the two domains.

The interface consists of a set of functions and data structure definitions provided by the HLT analysis framework and is known to the external application. The definitions have three parts,

- Common data structures for data exchange

- Definition of interface functions to be called by external application
- Definition of call-back functions implemented by the external application and called by the interface

The HLT analysis framework implements the corresponding functions in the libHLTinterface library. The defined entries correspond to addresses in the compiled library. Common functionality of the operating system can be used to retrieve the address for a function entry.

3.4.3 Offline Interface

Data processing in AliRoot is mainly divided into three major parts: simulation, reconstruction and analysis ([12]). There is also satellite functionalities like e.g., event visualization. The overall data flow is sketched in figure 3.14. Within this scheme, the reconstruction step takes its input either from simulation of the detector response or real data. Event reconstruction is a centrally managed layer which utilizes all detector raw data, calibration and alignment processes and produces a detailed summary of the event, the *Event Summary Data (ESD)*. This contains all information on particles found in a event. The last step, the actual physics analysis, is naturally distributed and diversified as it depends different physics interests. Thus, based on the ESD, any physics analysis can be run independently of both simulation and reconstruction.

In a complex data analysis system, it is important to study the behavior of the different modules and the system responses with respect to known inputs in order to assure the result of the entire analysis chain. This is, in particular, important in an experiment like ALICE where the experimental observables are inferred based on the reconstructed tracks. Thus, the impact of the detectors and the data processing

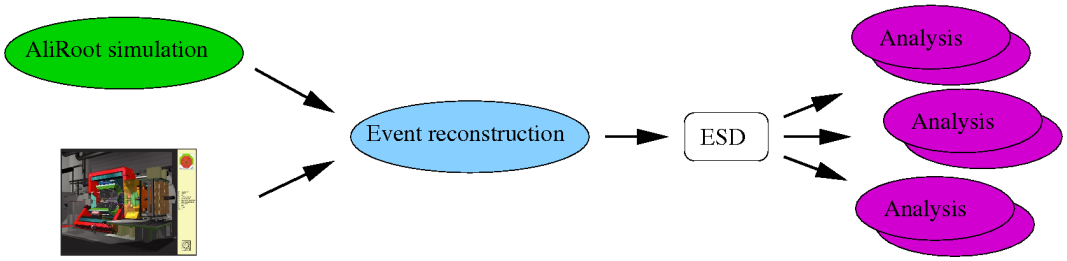

Figure 3.14: The overall AliRoot processing sequence. The event reconstruction is performed on either real raw data or simulated data which produces *Event Summary Data (ESD)* as final output for subsequent physics analysis.

needs to be studied carefully. This simulation study helps to determine,

1. the desired detector performance required for a given physics interest,
2. the data analysis algorithms required to extract the experimental observables for that particular physics interest.

The optimization is done by comparing the values of the reconstructed observables with the input values used for simulation. This approach is similar to signal response studies used in electronics engineering.

HLT has a special position within the described AliRoot processing chain. As a matter of fact, HLT executes *event reconstruction* independently by utilizing the simulated data from sub-detectors. Thus, it is often referred to be as *HLT simulation*. Figure 3.15 sketches the data flow for HLT simulation.

The lower block denoted by HLT system in Fig. 3.15 implements an encapsulated HLT analysis with well defined input and output. It is important to notice that the placement of HLT analysis is flexible and depends only on the availability of customized *input data sources* and *output data sinks*.

Since HLT reconstruction is executed either as part of simulation or online data processing, the result only needs to be extracted during AliRoot reconstruction and

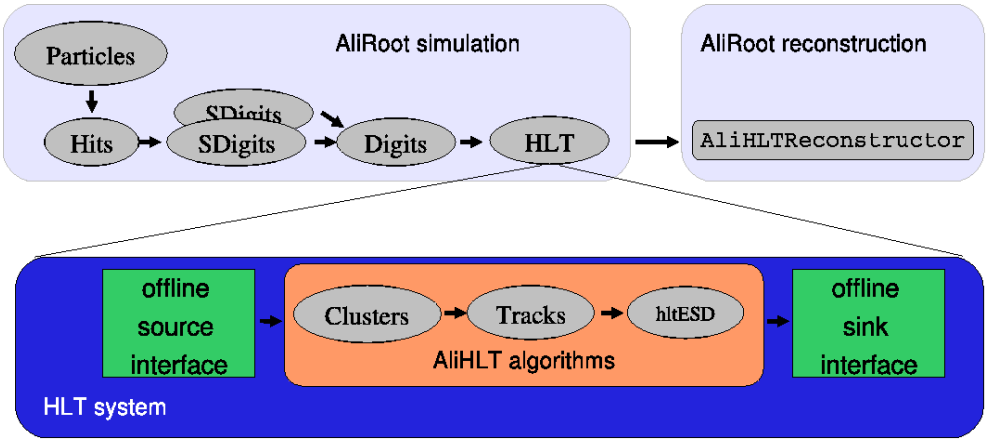

Figure 3.15: The HLT reconstruction in the simulation chain of AliRoot.

stored appropriately.

In order to run the HLT analysis components in a chain-like fashion, the behavior of the online data transport framework has been modeled by the HLT AliRoot integration. The AliHLTSystem class together with a few satellite classes steers HLT analysis chains in AliRoot.

The processing is determined by a configuration describing different components connected to each other. Even though AliHLTSystem uses the same process as the aliroot executable, accessibility to data is strictly limited. As outlined in Fig. 3.10, apart from data input and output, the data processing is exactly identical in both online and offline environment.

AliHLTSystem is able to parse a configuration, build a task list from the entries in the configuration and connect them forming an HLT analysis chain. It also carries out memory allocation and organizes data transport between the components of the chain. The entity of AliHLTSystem can be plugged into the AliRoot processing stream at different places like AliSimulation or AliReconstruction.

3.5 HLT of Muon Spectrometer

3.5.1 Motivation

The main goal of High Level Trigger of Muon Spectrometer is to provide a better transverse momentum (i.e. p_T) cut over that provided by the Muon Trigger stations. In case of central Pb-Pb collision a typical data rate of 500 MB/s is expected for Muon Spectrometer at 1 kHz L0 trigger rate. Therefore, a better estimation of track momentum will help to reject the background events before the data is written to disk. The main challenge of the ALICE HLT project for dimuon spectrometer is to perform a fast analysis at highest possible rate (1 kHz trigger rate) with large particle multiplicity (∼300 particles hits in a given chamber for Pb-Pb collision at $\sqrt{s}$ = 5.5 TeV), with best possible results in terms of resolution and efficiency. As discussed in the last chapter that Muon Spectrometer measures the production cross-section of heavy-quark resonances, such as the J/Ψ, the ϒ and their families, via their decay to muon pairs. The task of identifying muon candidates coming from these resonances becomes complicated because of the presence of muons from pion/kaon decay. However, these muons can be rejected by an appropriate $p_{\rm t}$-cut since their $p_{\rm t}$'s are predominantly low. These $p_{\rm t}$-cuts has been found to be 1 (low $p_{\rm t}$-cut) and 2 GeV/c (high $p_{\rm t}$-cut) for J/Ψ and ϒ , respectively, through simulation studies. The L0 trigger provides an crude estimate of this $p_{\rm t}$-cut due to the poor $p_{\rm t}$ resolution of the trigger chambers. Thus, HLT does a fast online data processing of the tracking chambers, in order to improve the transverse momentum estimate of the tracks.

3.5.2 MUON HLT Module Architecture

The MUON module for HLT analysis has been well integrated inside the AliRoot software package. All of the analysis codes are written in C++ language following the scheme accepted by AliRoot and HLT project. The MUON HLT module is designed to analyse the online experimental data with proper muon L0 trigger. But before applying the analysis methods in the real time complex experiment, it is mandatory to validate analysis algorithms on simulated data, which demands offline execution of the online codes. Therefore analysis programs are arranged accordingly in the OnlineAnalysis and OfflineAnalysis directories inside the path AliRoot/HLT/MUON of offline software. However, the base classes which are important for both ways of analysis execution (i.e. offline/online) reside in AliRoot/HLT/MUON. The utility packages that are useful for dHLT processing, i.e. histogramming, rootification of the MUON HLT data blocks and dumping the MUON HLT data blocks from binary file, are situated inside utils directory of AliRoot/HLT/MUON. Some useful macros and FSM (Finite State Machine) schematic diagrams can be found in macros and docs, respectively, under the same base directory. A major part of this package has been developed as a part of this thesis work.

3.5.3 Dimuon Components

The dimuon HLT (dHLT) analysis methods can be realised in terms of the processing components that have been explained before [sec.§ 3.4.1]. At the input, the dimuon component of the class receives data stream from 20 tracking DDLs and 2 triggers DDLs which are then analysed and final output is merged into global HLT trigger component and global HLT ESD component. A part of analysed data is sent to the TCP port, which are used for the event visualization of Muon Spectrometer in

a machine at the user-end.

The main dimuon HLT analysis components are,

- Hit Reconstruction
- Trigger Reconstruction
- Tracking
- Decision
- ESDMaker
- HLTMuonTrigger

The first and the third items are discussed in short since those are subject to detail explanation in the next chapter.

Hit Reconstruction

The "Hit-Reconstructor" component is steered by AliHLTMUONHitReconstructorComponent class of HLT analysis framework implemented in AliRoot. It receives the raw data streams as inputs, either from DDL links or from simulated files. The outputs of this component are the data blocks of reconstructed particle hits (in short *rechits*) of type AliHLTMUONRecHitStruct as specified in the listing 3.1.

Listing 3.1: AliHLTMUONRecHitStruct, the output block structure of class AliHLTMUONHitReconstructorComponent.

```
1 struct AliHLTMUONRecHitStruct
2 {
```

```
3         // The flags word contains the following bit fields (bit 31 is
4         // most significant):
5         //
6         // bits:  [ 31 -- 16 ][ 15 -- 12 ][ 11 --- 0 ]
7         // field:   reserved    chamber    detElemId
8         //
9         // Where we have,
10        // reserved bits must be set to zero.
11        // chamber - specifies the chamber number in the range
12        // [0..13], 0xF for invalid.
13        // detElemId - specifies the detector element ID number.
14        AliHLTUInt32_t fFlags;
15
16        AliHLTFloat32_t fX; // X coordinate.
17        AliHLTFloat32_t fY; // Y coordinate.
18        AliHLTFloat32_t fZ; // Z coordinate.
19 };
```

Where the AliHLTUInt32_t and AliHLTFloat32_t are unsigned 32-bit integer and 32-bit floating point data types, respectively. The steering class uses the core class AliHLTMUONHitReconstructor, which finds out the reconstructed space points of the muon tracking stations. The output of the Hit-Reconstructor component is sent as the input of the tracker. The machinery of the core class AliHLTMUONHitReconstructor will be discussed in detail in the following chapter.

Trigger Reconstruction

A similar task for muon trigger chamber hit finding is performed by "Trigger-Reconstructor" component AliHLTMUONTriggerReconstructorComponent. Since the areas of strips of Muon Trigger chambers are larger compared to Muon Tracking

chambers, there is no need for clusterization. Therefore, Trigger Reconstruction perform faster operation than the Hit Reconstruction. The Trigger-Reconstructor also receives raw data stream as input and the output (see listing 3.2) is directly fed as input to the tracking component. In addition to the trigger chamber hit points, the data block also contains the momentum vectors. which point towards the origin. It helps to select the search region for track extrapolation through the tracking chambers.

Listing 3.2: AliHLTMUONTriggerRecordStruct, the output block structure of class AliHLTMUONTriggerReconstructorComponent.

```
1  struct AliHLTMUONTriggerRecordStruct
2  {
3          AliHLTInt32_t fId; // Each trigger record should have an ID
4                             // number unique for a given event.
5                             // -1 == invalid.
6
7          // The flags word contains the following bit fields
8          // (bit 31 is most significant):
9          // bits:  [31][30][29 --- 4][ 3 ][ 2 ][ 1 ][ 0 ]
10         // field:  -   +   reserved  hst[3]  hst[2]  hst[1]  hst[0]
11         // Where fields hst[i] indicates if fHit[i] has been filled/set.
12         // Reserved bits should be set to zero.
13         // Particle sign: if '-' is set then particle has minus sign.
14         //                if '+' is set then particle has negative sign.
15         // Either '+' or '-' should be set and if neither then the
16         // particle sign is unknown.
17
18         AliHLTUInt32_t fFlags;
19
20         AliHLTFloat32_t fPx; // Particle momentum X component in GeV/c.
21         AliHLTFloat32_t fPy; // Particle momentum Y component in GeV/c.
22         AliHLTFloat32_t fPz; // Particle momentum Z component in GeV/c.
```

```
23
24          // Particle hit coordinates on trigger chambers 11 to 14.
25          AliHLTMUONRecHitStruct fHit[4];
26 };
```

In case of trigger reconstruction, the core class AliHLTMUONTriggerReconstructor is called by Trigger-Reconstructor component. The core functionality executes the actual finding of trigger chamber hit points.

Tracking

In dHLT, there exists two types of tracking algorithms for Muon Spectrometer HLT analysis. A partial straight line tracking method proposed by F. Manso [see Ref. [13]] and recently introduced full tracker using Kalman Filtering and Cellular Automata approach, which is the part of present thesis work. In case of Manso tracker the inputs are Trigger-Reconstructor and rechits from chamber 7 to 10. Whereas for the Full-Tracker the Hit-Reconstructor inputs and Trigger-Reconstructor inputs from all chambers (except chamber 5 and 6) are utilised.

Manso Tracker : In case of tracking using Manso's algorithm the component AliHLTMUONMansoTrackerFSMComponent controls the main processing, using AliHLTMUONMansoTrackerFSM core analysis class. The output of the Manso tracker is of type AliHLTMUONMansoTrackStruct as shown in the list 3.3.

Listing 3.3: AliHLTMUONMansoTrackStruct, the output block structure of class AliHLTMUONMansoTrackerFSMComponent.

```
1 struct AliHLTMUONMansoTrackStruct
2 {
3          AliHLTInt32_t fId; // Each Manso track should have an ID number
```

```
4                                   //unique for a given event. -1 == invalid.
5
6           AliHLTInt32_t fTrigRec; // The associated trigger record ID used
7                                   // as the seed for the Manso algorithm.
8
9           // The flags word contains the following bit fields
10          // (bit 31 is most significant):
11          // bits:  [31][30][29 --- 4][ 3 ][ 2 ][ 1 ][ 0 ]
12          // field:  -   +   reserved  hst[3]  hst[2]  hst[1]  hst[0]
13          // Where fields hst[i] indicates if fHit[i] has been filled/set.
14          // Reserved bits should be set to zero.
15          // Particle sign: if '-' is set then particle has minus sign.
16          //                if '+' is set then particle has negative sign.
17          // Either '+' or '-' should be set and if neither then the
18          // particle sign is unknown.
19          AliHLTUInt32_t fFlags;
20
21          AliHLTFloat32_t fPx; // Particle's momentum X component in GeV/c.
22          AliHLTFloat32_t fPy; // Particle's momentum Y component in GeV/c.
23          AliHLTFloat32_t fPz; // Particle's momentum Z component in GeV/c.
24          AliHLTFloat32_t fChi2; // The chi squared of the fit of fHit
25                                 // points to the track model. If -1 then
26                                 // no fit done and momentum vector is
27                                 // invalid.
28
29          // Particle hit coordinates on tracking chambers 7 to 10.
30          // fHit[0] is for chamber 7 fHit[1] for chamber 8 etc...
31          AliHLTMUONRecHitStruct fHit[4];
32  };
```

Full Tracker : The online tracking with inputs from all the chambers is performed by the interface class AliHLTMUONFullTrackerComponent, whereas the

AliHLTMUONFullTracker class implements the tracking algorithms and carries out the calculation of track parameter. It produces the output block arrays of AliHLTMUONTrackStruct (see list 3.4).

Listing 3.4: AliHLTMUONTrackStruct, the output block structure of class AliHLTMUONFullTrackerComponent.

```
1  struct AliHLTMUONTrackStruct
2  {
3          AliHLTInt32_t fId; /// Each track should have an ID number
4                             ///unique for a given event. -1 == invalid.
5
6          AliHLTInt32_t fTrigRec; /// The associated trigger record ID
7                                  ///that was matched to the track.
8
9          // The flags word contains the following bit fields
10         // (bit 31 is most significant):
11         // bits:  [31][30][29 - 16][ 15 ][ 14 ]...[ 1 ][ 0 ]
12         // field:  -   +   reserved  hst[15]  hst[14]     hst[1]  hst[0]
13         // Where fields hst[i] indicates if fHit[i] has been filled/set.
14         // Reserved bits should be set to zero.
15         // Particle sign: if '-' is set then particle has minus sign.
16         //                if '+' is set then particle has negative sign.
17         // Either '+' or '-' should be set and if neither then
18         // the particle sign is unknown.
19         AliHLTUInt32_t fFlags;  // Bit fields for the track structure.
20
21         AliHLTFloat32_t fPx; // Particle's momentum X component in GeV/c.
22         AliHLTFloat32_t fPy; // Particle's momentum Y component in GeV/c.
23         AliHLTFloat32_t fPz; // Particle's momentum Z component in GeV/c.
24
25         AliHLTFloat32_t fInverseBendingMomentum; // One over the
26                                                  // momentum of the
```

```
27                                                  // fitted track [GeV/c].
28
29          AliHLTFloat32_t fThetaX; /// The slope of the fitted track in
30                                   ///the non-bending plane.
31
32          AliHLTFloat32_t fThetaY; /// The slope of the fitted track in
33                                   ///the bending plane.
34
35          AliHLTFloat32_t fX; /// Non-bending plane coordinate for the
36                              ///distance of closest approach (DCA) [cm].
37
38          AliHLTFloat32_t fY; // Bending plane coordinate for the DCA [cm].
39          AliHLTFloat32_t fZ; // Z coordinate for the DCA [cm].
40
41          // Chi squared of the track fit.
42          // If set to -1 then no fit was done and the momentum vector
43          ///and DCA coordinate is invalid.
44          AliHLTFloat32_t fChi2; /// The chi squared of the fit of fHit
45                                 ///points to the track model.
46
47          AliHLTMUONRecHitStruct fHit[16];  /// Particle hit coordinates
48                                            ///found by the hit
49                                            ///reconstruction stage.
50 };
```

The following chapter includes a detail description of the tracking algorithms.

Decision

The "Decision" component filters the track results according to the predefined dHLT trigger condition. It is implemented by the AliHLTMUONDecisionComponent

class on the input blocks of AliHLTMUONMansoTrackStruct or AliHLTMUONTrackStruct. It has already been pointed out that the muons from π and K decays can be efficiently suppressed by applying a cut on the p_{t} of these muons. This idea has been adopted in the component to generate the dimuon trigger decision by first applying two p_T cuts to the single tracks: a low cut for the J/Ψ family and a high cut for the Υ family. Finally, the tracks that pass the cuts are counted and a statistics is build up for the tracks that passes the low or high p_T cut. For instance, the decision component looks at pairs of tracks and counts the number of like-sign or unlike-sign pairs where both tracks passed the low or high p_T cut or pairs that did not pass any cuts. There is a provision to calculate the invariant mass of the oppositely charged track pairs that passes the mass cut. The results are encoded into two data blocks, one for trigger decisions for single tracks of type AliHLTMUONTrackDecisionStruct (listing 3.5) and another for the track pairs of type AliHLTMUONPairDecisionStruct (see listing 3.6).

Listing 3.5: AliHLTMUONTrackDecisionStruct, the output block structure of class AliHLTMUONDecisionComponent.

```
1  struct AliHLTMUONTrackDecisionStruct
2  {
3          AliHLTInt32_t fTrackId; // The ID number of the track we are
4                                  // referring to. This could also be
5                                  // a trigger record ID.
6
7          // The trigger bits have the following meaning:
8          // bit:  [31 --- 2][  1 ][  0 ]
9          // field: reserved  hipt  lopt
10         // Reserved bits should be set to zero.
11         // hipt == passed high pt cut. lopt == passed low pt cut.
12         AliHLTUInt32_t fTriggerBits;
13
```

```
14          AliHLTFloat32_t fPt; // The calculated transverse momentum of
15                               //the track in (GeV/c).
16 };
```

Listing 3.6: AliHLTMUONPairDecisionStruct, the output block structure of class AliHLTMUONDecisionComponent.

```
1 struct AliHLTMUONPairDecisionStruct
2 {
3          // The ID numbers of the tracks we are referring to.
4          // These could also be trigger record ID numbers.
5          AliHLTInt32_t fTrackAId;
6          AliHLTInt32_t fTrackBId;
7
8          // The trigger bits have the following meaning:
9          // bit:  [31 --- 7][ 6 ][ 5 ][   4   ][3--2][1--0]
10         // field: reserved  hiM  loM  unlike  hipt  lopt
11         // Reserved bits should be set to zero.
12         // hiM == Pair passed the high invariant mass cut.
13         // loM == Pair passed the low invariant mass cut.
14         // unlike == is the pair an unlike sign pair.
15         // hipt: 0 if neither track has pt > high pt cut, 1 if either has
16         // and 2 if both have. A value of 3 is invalid.
17         // lopt: 0 if neither track has pt > lo pt cut, 1 if either has
18         // and 2 if both have. A value of 3 is invalid.
19         AliHLTUInt32_t fTriggerBits;
20
21         AliHLTFloat32_t fInvMass; // Invariant mass of the track pair
22                                   // assuming they are both muons
23                                   // in (GeV/c^2)
24 };
```

The input arguments of the Decision component are listed below,

- **-lowptcut** *value*

  It sets the low p_t-cut value. The *value* should be a floating point number and has units GeV/c. If this parameter is specified then it will not be loaded from CDB.

- **-highptcut** *value*

  It sets the high p_t-cut value and has the same properties as **-lowptcut**.

- **-lowmasscut** *value*

  It sets the low invariant mass cut value to use when applying the decision. The *value* should be a floating point number and has units GeV/c^2. If this parameter is specified then it will not be loaded from CDB.

- **-highmasscut** *value*

  It sets the high invariant mass cut value to use when applying the decision and has the same properties as **-lowmasscut**.

- **-no_singles_detail**

  If specified the detailed decision information for tracks is not added to the output. Only the scalar values are then stored in the output data block for decisions on single tracks.

- **-no_pairs_detail**

  If specified the detailed decision information for track pairs is not added to the output. Only the scalar values are then stored in the output data block for decisions for track pairs.

- **-warn_on_unexpected_block**

  This will cause the component to generate warnings when it receives non-standard data block types. This option increases the robustness of the component.

- **-cdbpath** *path*

  This allows one to override the path to use for the CDB location. The *path* must be a valid CDB URI. By default the HLT system framework sets the CDB path.

- **-run** *number*

  This resets the run number for CDB objects.

- **-delaysetup**

  If indicated then part of the initialisation of the component is forcefully delayed to the first event received, i.e. the Start-of-Run event.

- **-dumponerror**

  This flag allows to dump the data blocks if an error occurs during the processing of the event.

- **-dumppath** *path*

  Allows one to specify the path in which to dump the received data blocks if an error occurs.

The output of decision component is useful to build the online statistics of the dHLT tracking components and therefore can be sent to the TCP port for display or can be sent to the HLTMuonTrigger component to issue the suitable trigger.

ESDMaker

The "ESDMaker" component (AliHLTMUONESDMaker class) is used to convert the dHLT reconstructed data (AliHLTMUONMansoTrackStruct or AliHLTMUONTrackStruct and AliHLTMUONTriggerRecordStruct as inputs) to AliESDEvent objects. This is stored in ROOT files during offline reconstruction. The

dHLT chain produces TClonesArray of AliESDMuonTrack objects. These are then merged together with ESD tracks from all the other parts of HLT (eg. TPC, TRD ,ITS, PHOS, EMCAL) using global ESD converter to build AliESDEvent. Finally, it is pushed into the HLTOUT DDL to DAQ for event building. The following list contains the optional arguments of ESDMaker component.

- **-make_minimal_esd**

  It indicates that AliESDEvent objects should be created with only the TClonesArray for the muon tracks created. (default is to generate all standard ESD objects)

- **-add_rootified_objects**

  If specified then the any rootified dHLT event data that is found is added to the ESD list of objects as a custom data object.

- **-makeclonesarray**

  This option will cause the component to generate a TClonesArray of MUON ESD tracks and send it as a kAliHLTDataTypeTObject data block type.

- **-makeonlyclonesarray**

  Same as the -makeclonesarray option, however the data blocks with the AliESDEvent object are not generated.

- **-warn_on_unexpected_block**

  If set, then warning messages are generated for any data block types that were not expected. (default is to generate only debug messages)

- **-dumponerror**

  This flag will cause the component to dump the data blocks it received if an error occurs during the processing of an event.

- **-dumppath** *path*

  Allows one to specify the *path* in which to dump the received data blocks if an error occurs.

HLTMuonTrigger

The "HLTMuonTrigger" component uses the decision generated by the AliHLTMUONDecisionComponent as input and creates HLT trigger data blocks suitable for the HLT global trigger framework. In addition, several other data blocks (e.g tracks, rechits, trighits) can also be provided as input to generate the muon trigger. It is important to note that in case of DDL stream as inputs with proper argument "-triggerddls", the component will trigger every single event trigger by Muon Trigger cluster of CTP. The possible list of arguments of this components are,

- **-makestats**

  If specified, the summary statistics scalars object is generated as output. The default is not to generate the statistics object.

- **-triggerddls**

  Indicates that the component should trigger if any DDLs are found in the muon spectrometer.

- **-triggerhits**

  Indicates that the component should trigger if any hits are found in the muon spectrometer tracking chambers. This option requires that this trigger component receives the reconstructed hits data blocks.

- **-triggertrigrecs**

  Indicates that the component should trigger if any muon trigger records are

found. This option requires that this trigger component receives the trigger record data blocks.

- **-triggertracks**

  Indicates that the component should trigger if any track is found.

- **-triggerdimuons**

  Indicates that the component should trigger if any dimuon pair is found.

- **-triggerany**

  This option indicates that it should trigger, if any of the above mentioned trigger condition is satisfied.

It is to be noted that if none of the "triggerddls" ,"triggerhits", "-triggertrigrecs", "-triggertracks" or "-triggerdimuons" options are specified then the default triggering mode is to trigger on tracks and dimuon pairs.

Apart from the above mentioned components there are few less frequently used components, which are explained in brief,

ClusterFinderComponent This cluster finder component (AliHLTMUONClusterFinderComponent class) executes offline algorithms, in the online HLT. It processes the raw data of tracking stations and returns the cluster information in the form of offline cluster (i.e. array of AliMUONVCluster objects). It can also produce dHLT internal hit coordinates (i.e AliHLTMUONRecHitStruct), if "-makehits" option is explicitly specified in component argument.

DigitPublisherComponent The component (class AliHLTMUONDigitPublisherComponent) is used to convert simulated or reconstructed

digits into DDL raw data streams on the fly and publish them. It is useful for running dHLT simulations on digit data where the raw data files are not available. The component is also used for the dHLT simulation under AliSimulation when there is no direct access to a raw data reader.

ClusterHistoComponent This AliHLTMUONClusterHistoComponent class gets the cluster data blocks from Hit-Reconstructor component and produces histograms in the form of ROOT object TH1. These are then transported to the network port for online display.

RawDataHistoComponent This component (class AliHLTMUONRawDataHistoComponent) is useful for performing basic monitoring tasks on the raw data from the muon spectrometer. It will try and decode the data and histogram the following information:

- The distribution of signals per DDL.
- The number of ADC values found per MANU for each DDL.
- The error codes found by the decoders while trying to decode the data for each DDL.

EmptyEventFilterComponent This component class AliHLTMUONEmptyEventFilterComponent is a utility component for debugging. It is used to filter empty dHLT events. (In particular, it was built for the Dec 2007 Cosmic tests, where the muon spectrometer was not expecting hits for most of the events triggered by ACORDE.)

DataCheckerComponent This class AliHLTMUONDataCheckerComponent is used to check and validate the integrity of dHLT internal raw data blocks. If there is any problem then an appropriate error message is logged. This component should be used for debugging and testing only, since the validation procedure can be slow.

RootifierComponent This component class AliHLTMUONRootifierComponent is used to convert all internal raw dHLT data blocks into ROOT object that can be stored in '.root' files in a platform independent manner. This also makes some of the analysis easier because the dHLT internal data are available in the form of TObjects.

The main features of dimuon HLT components are discussed in this section to illustrate the dHLT scheme for fast Hit-Reconstruction and track finding algorithms, which are discussed in the next chapter.

Bibliography

[1] ALICE Collaboration, Technical Design Report: Trigger, DAQ, HLT, DCS, CERN-LHCC-2003-062, 2004.

[2] T. M. Steinbeck, "A modular and fault-tolerant data transport framework", *Ruprecht-Karls-University Heidelberg, Germany*, 2004, [http://arxiv.org/abs/cs/0404014].

[3] T. M. Steinbeck et al., IEEE Trans. Nucl. Sci., vol. **49**, pp. 455-459, 2002

[4] T. M. Steinbeck et al., "New experiences with the ALICE High Level Trigger Data Transport Framework", in *Proc. Computing in High Energy Physics Conf. 2004 (CHEP04)*, 2004 [http://chep2004.web.cern.ch/chep2004/]

[5] R. Divià and T.M. Steinbeck., *Data format and specifications for the HLT-to-DAQ interface*, ALICE-INT-2007-015, ver. 3 2008, [https://edms.cern.ch/document/871995].

[6] R. Divià, P. Jovanovic, P. Vande Vyvre, *Data Format over the ALICE DDL*, ALICE-INT-2002-010, ver. 11 2007, [https://edms.cern.ch/document/340186].

[7] J. Wagner, V. Lindenstruth, M. Richter, T.M. Steinbeck, J. Thäder., *Lossless*

Data Compression for ALICE HLT, ALICE-INT-2008-020, ver. 1 2008, [https://edms.cern.ch/document/948159].

[8] T. M. Steinbeck et al., "A Control Software for the ALICE High Level Trigger", in *Proc. Computing in High Energy Physics Conf. 2004 (CHEP04)*, 2004 [http://chep2004.web.cern.ch/chep2004/]

[9] T. M. Steinbeck, "SimpleChainConfig", *HLT project internal information, University of Heidelberg, Germany*, 2007.

[10] S. Bablok et al., *High level trigger online calibration framework in ALICE*, J. Phys.: Conf. Ser. **119** 022007 (2008)

[11] S.R. Bablok et al., *ALICE HLT interfaces and data organisation* , in *Proc. Computing in High Energy Physics Conf. 2006 (CHEP06)*, Mumbai, India (2006)

[12] The ALICE Collaboration, JINST **3** S08002 (2008) 175.

[13] F. Manso and the Clermont-Fd ALICE group. A first algorithm for a dimuon high level trigger. *ALICE Internal Note*, 2002. ALICE-INT-2002-004.

Chapter 4

Algorithms

This chapter discusses the key ideas of the main dHLT analysis components. It has been explained before (see last chapter) that the motivation of the dHLT is to improve the p_{t}-cut for muons by online reconstruction. This is achieved in two steps.

- **Hit Reconstruction :** Reconstruction of the pad clusters on each individual chamber leading to reconstructed hit points.
- **Track Formation :** Reconstruction of the trajectory of the charged particles using the reconstructed hit points.

The official analysis software, MUON Offline of AliRoot [discussed later in sec. §5.1], solves this problem mainly by Mathieson fitting for cluster reconstruction and Kalman filtering for track formation. It is to be noted that there are alternate clustering and tracking methods for offline analysis. But none of these methods can be applied for online reconstruction. This is due to the fact of time constrain. For instance, the time to reconstruct a simulated central Pb-Pb event using offline analysis takes $\sim$1 second on standard computer of 2.93 GHz clock speed. However in online

analysis this has to be achieved within 1 ms, as the estimated L0 trigger rate for central Pb-Pb collision is 1 kHz. Thus, two separate algorithms for hit reconstruction and track formation have been proposed for online analysis in the present thesis work. In addition, to the problem of full reconstruction, there are challenges of the *online* analysis. These are,

- An online processing has to be robust, so that it can run 24x7 without any system crash. The presence of any small memory leak, or bug in any part of the code will lead to immediate instability.

- The online components should not crash due to any data corruption in the input buffer.

- The event processing has to be done upto a rate of 1 kHz even for the highest multiplicity Pb-Pb collision. This will ensure that the dHLT component will not generate a back pressure to the whole experimental system.

The online algorithm not only has to satisfy these online analysis criteria but also produce results of appreciable quality. In order to check the quality of online reconstruction a detail study on the comparison of online and offline algorithms have been presented in the following chapter. The discussion of a new tracking algorithm is never complete unless it is compared with the existing algorithm. Therefore, a short overview of the Manso's algorithm is included.

The core ideas of online Hit-Reconstruction has been discussed in the following section.

4.1 Hit Reconstruction

4.1.1 Algorithm

It is clear from the above discussion that the motivation of the dHLT Hit Reconstruction analysis is to perform fast identification of a charged particle's trajectory in the spectrometer. Since the algorithm aims to reconstruct the high multiplicity central Pb-Pb events, a study has been performed to estimate the average number of charged particle hits for a given detection plane using HIJING event generator. The result of this simulation study is shown in Fig. 4.1. Each entry of the histogram corresponds a single central Pb-Pb event and the number of hits for that event for a given plane is filled as the value of that entry. Therefore, the mean values of the histogram shows the average number of hit multiplicity for a given detection plane in case of central Pb-Pb collision. It is evident from this study that on average 300 particle hits have to be reconstructed in case of highest multiplicity events.

The first step of cluster reconstruction is the identification of the pad cluster. In offline analysis a cluster is found by a detail scan on the pads with a common boundary following the concept of nearest neighbour. This method of clustering is accurate but slow and thus is not suitable for online analysis. Therefore, the first challenge was to search for an alternate method for fast identification of the charge clusters. This is solved applying the concept of *central pad*. The central pad of a given cluster is the pad with the maximum charge. At the start of the rawdata processing the data array is split into two sets of arrays for pads of bending and non-bending planes. These arrays are called as total hit registers, where the pads are identified by a unique combination of buspatch number with MANU card number and channel number [ref. Chapter 2]. The hit register for bending (non-bending) plane is then scanned along the y-direction (x-direction) to collect the central pads, which

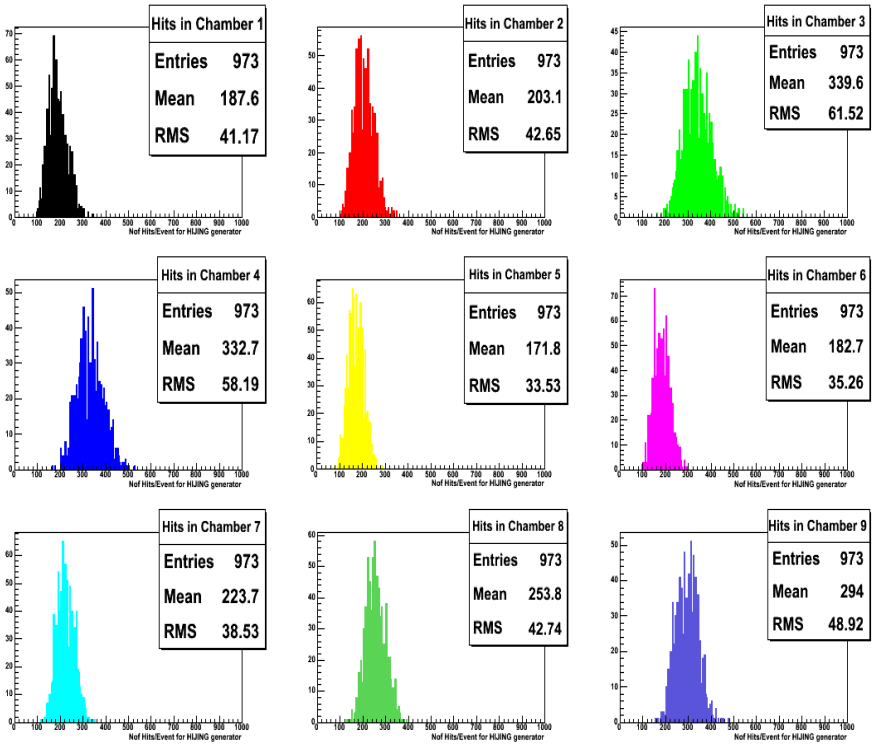

Figure 4.1: A simulation study of hit multiplicity for central Pb-Pb collision in Muon Spectrometer Tracking Chambers. The mean position of the histograms signifies average number of particle trajectories in for a given chamber.

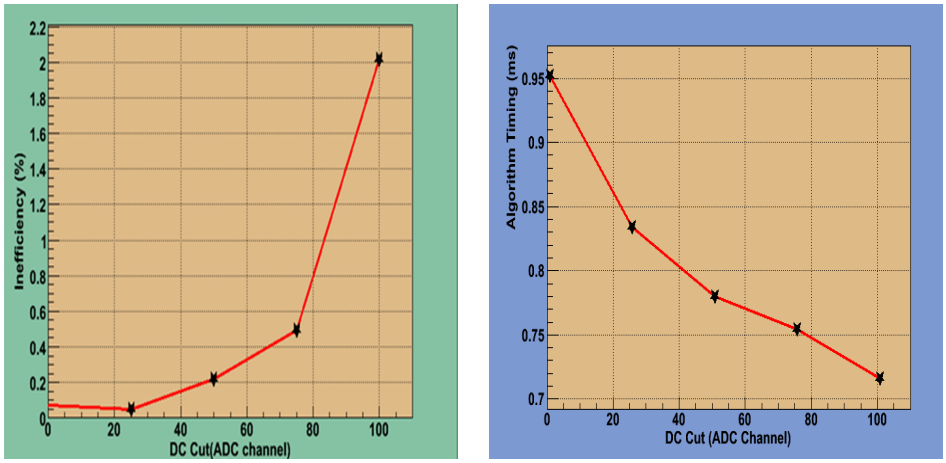

Figure 4.2: The inefficiency of central hit reconstruction (left) and the timing performance on a 2.93 GHz Nihalam processor (right) of the Hit Reconstruction algorithm as a function of the DC cut.

are stored in a different array. In addition to ∼300 hits for Pb-Pb collision there may be pad clusters arising due to noisy electronics. Thus, an intelligent selection of

the central hit is required to avoid these noise clusters. It has been found from the simulation study that a threshold cut on ADC value, while scanning for central pads, helps to remove these noises. This ADC threshold is henceforth referred as DC-cut. It is apparent that if the DC-cut is set to higher value there is a chance to loose clusters originating from charged particle tracks. The effect of DC-cut on efficiency and timing performance of the analysis algorithm are shown in Fig. 4.2. It is realised that a DC-cut of 50 ADC channel is acceptable, which provides the best compromise between the central pad finding efficiency and timing performance of the online code.

Once the central hit for a given cluster is identified, the centre of gravity (COG) of the pad charges of the central pad and its two immediate neighbours are calculated. This gives the reconstructed hit position along the bending (non-bending) direction, when COG method is applied along the y-direction (x-direction) of central pad, respectively.

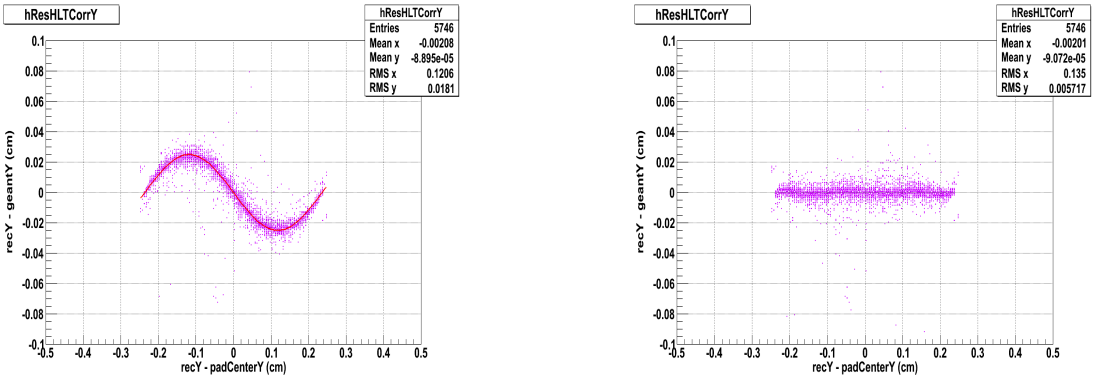

(a) Residual oscillation in reconstructed hit position

(b) Correction of residual oscillation of reconstructed hits by sine curve with negative amplitude

Figure 4.3: A sinusoidal curve of tailing effect. It is observed from the y-axis of the subfigures that, in case of the uncorrected reconstructed hit position (left figure) the Gaussian distribution of (recY-geantY) will have a large *tail* than the corrected subfigure (right). Therefore, this curve signifies the "tailing effect".

The position resolution calculated with COG method suffers due to to finite pad size (5mm in y-direction and 7.5 mm in the x direction). This effect in the bending

direction can be seen in Fig. 4.3(a), where the residue (reconstructed position - true hit position as obtained from GEANT3 [v1-11]) is plotted as a function of (reconstructed position - pad center). It is interesting to note that the wavelength of the oscillation is exactly equal to the pad size. Thus, a correction term for the reconstructed hit can be found as a function of the hit position with respect to the pad center. The Fig. 4.3(b) shows the residue plot after this correction. Finally, the reconstructed hits from the bending and non-bending planes are merged to form the reconstructed (x,y) position of the cluster. A flow chart of the algorithm is given in Fig. 4.4.

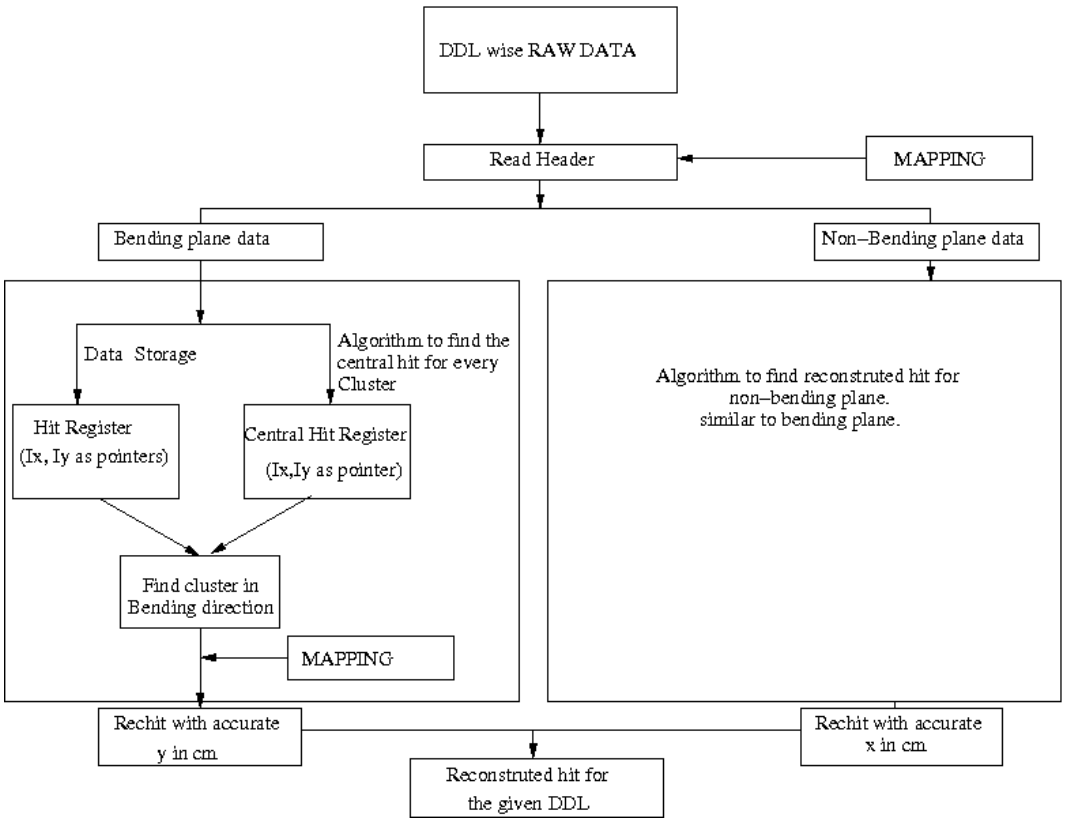

Figure 4.4: The flow chart of hit reconstruction algorithm.

In the next subsection the implementation scheme of Hit Reconstruction algorithm to the HLT framework is discussed.

4.1.2 HLT Interface

It has already been described in brief in the previous chapter that the main classes AliHLTMUONHitReconstructor and AliHLTMUONHitReconstructorComponent are responsible for hit reconstruction in dHLT. The core processing is carried out by AliHLTMUONHitReconstructor, which represents the hit reconstruction algorithm in the form of a C++ code. Each of the method of this class is explained in detail below and the overall processing scheme is shown in Fig. 4.5.

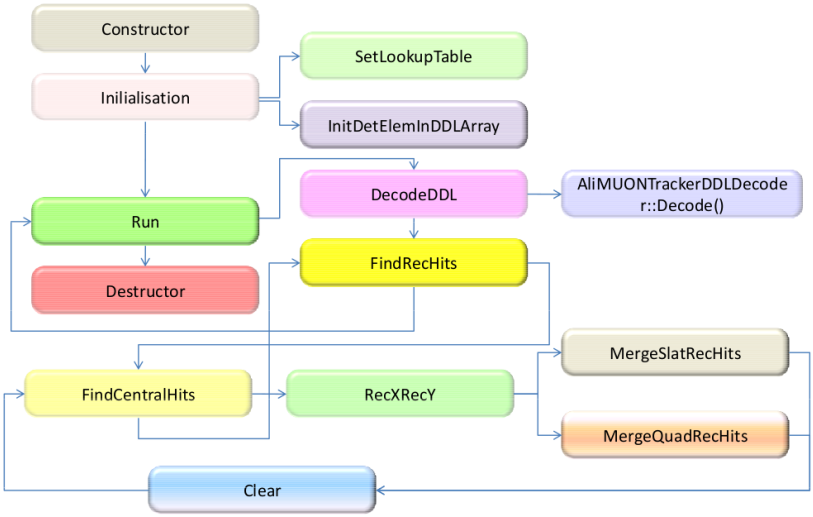

Figure 4.5: A schematic for processing steps of AliHLTMUONHitReconstructor class.

The class AliHLTMUONHitReconstructor mainly consists of a initialisation part (SetLookUpTable and InitDetElemInDDLArray methods) and an execution part which is controlled by the Run function.

SetLookUpTable :

Three pointers are set in the arguments of this method, which are essential during the following analysis. The purpose of these pointers are explained below.

1. The memory location of the geometrical mapping, pedestal and gain for the cathode pads. It has the following data type.

   Listing 4.1: Data Type containing the mapping and calibration values

```
1    struct AliHLTMUONHitRecoLutRow
2    {
3      AliHLTInt32_t fDetElemId;  // The detector element ID of the pad.
4      AliHLTInt32_t fIX, fIY;    // The X,Y number of the pad.
5      AliHLTFloat32_t fRealX, fRealY, fRealZ;
   // The real coordinate
6      //of the pad.
7      AliHLTFloat32_t fHalfPadSize; // half padsize in X for bending
8      //and Y for nonbending
9      AliHLTFloat32_t fPadSizeXY; // padsize in Y for bending plane
10     //and X for nonbending
11     AliHLTInt32_t fPlane;  // The plane and PCB zone ID numbers.
12     AliHLTFloat32_t fPed, fSigma, fA0, fA1; // Calibration values
13     AliHLTInt32_t fThres, fSat; //Calibration values
14   };
```

   This pointer address carries the most important reference data set for hit reconstruction algorithm.

2. The one to one mapping of the unique identity of a pad (combining buspatch number, MANU number, channel number) to the array position of AliHLTMUONHitRecoLutRow is defined as data type IdManuChannelToEntry

Listing 4.2: Data Type specifing the mapping of unique pad identity

```
1  typedef std::map<AliHLTInt32_t, AliHLTInt32_t>
2  IdManuChannelToEntry;
```

It helps in fast identification of a pad instead of searching over the entire hierarchical loop of buspatch, MANU and channel.

3. The last pointer address points towards a list, which contains the maximum number of allowed rawdata for a given buspatch. This is implemented to protect the analysis code from slowing down due to the presence of noisy buspatches. As it is presently set, if the occupancy of a buspatch is found to be higher that 5%, then it is skipped from analysis. This pointer is of same type as of the previous item.

Listing 4.3: Data Type specifing the buspatch occupancy list

```
1  typedef IdManuChannelToEntry MaxEntryPerBusPatch;
```

It is to be noted that the initialization of the mapping and calibration and other entries into the memory is performed by AliHLTMUONHitReconstructorComponent class.

InitDetElemInDDLArray :

It may be recapitulated from the detector description that for a given DDL there are several detection elements. In this method new memory location is allocated to maintain a structured list of number of pads fired per detection element and its summary over the DDL. These memory locations are then filled and utilized in the AliMUONTrackerDDLDecoder::OnData() method during rawdata decoding.

Run :

As it has been shown in the schematic diagram 4.5, the central Run method is executed for every event of Muon Spectrometer. In the input argument, it receives the address of the rawdata stream, the size of the rawdata block, the pointer for the output blocks and size of it. The analysis is done in two steps, in the first stage the rawdata address and it size is handled by DecodeDDL method, which in turn uses AliMUONTrackerDDLDecoder::Decode to decode the rawdata DDL stream. Once it is decoded the data stream is then arranged in proper form, for next stage of hit reconstruction. The central control of analysis is carried out by FindRecHits method, where the decoded rawdata is separately analysed for each detection element. Inside the loop of detection elements, five functions are called to find out hit points as shown schematically in Fig. 4.5.

FindCentralHits :

In this method the central pads are identified separately for each bending or non-bending plane. Since the bending (non-bending) plane gives better resolution in the y-direction (x-direction), the pads are scanned along y-axis (x-axis). If the central pad is found to satisfy the DC cut, the cluster is forwarded to the next processing step, otherwise rejected as noise cluster.

RecXRecY :

This function calculates the reconstructed hit position by the Centre of Gravity (COG) method separately for bending and non-bending planes. For instance, if three consecutive pads with ADC values C_1, C_2, and C_3 are found at y-positions, y_1, y_2,

and y_3, respectively, then the hit centre is calculated as,

$$y_{\rm rec} = \frac{y_1 C_1 + y_2 C_2 + y_3 C_3}{C_1 + C_2 + C_3}$$

This calculation is carried out for each central pad. But the accuracy of the reconstructed position suffers from the oscillation as indicated in Fig. 4.3(a). Thus, a correction of the form

$$Asin(\frac{2\pi}{d}x)$$

is applied, where x = (reconstructed position - pad center), A = normalization constant and d = pad dimension along the high resolution direction. The effect of this correction for residual oscillation is shown in Fig. 4.3(b).

MergeSlatRecHits :

The final merging of bending and non-bending hits is done by two methods. As the name suggests this function merges the reconstructed hits for the slat chambers. In case of merging of slat chamber hits, first the adjacent reconstructed hits $y_{\rm rec}$ ($x_{\rm rec}$) of bending (non-bending) plane are merged which are with same x (y) co-ordinate. In the final step the bending and non-bending hits are merged which are within half-pad size as explained in the algorithm part. Finally, the output data block of type AliHLTMUONRecHitStruct (see list 3.1) is filled to the output buffer. It is to be noted that for online detector diagnostics two additional types of data blocks can also be prepared AliHLTMUONClusterStruct and AliHLTMUONChannelStruct (see list 4.4 and 4.5), which are used for real time histograms.

Listing 4.4: The AliHLTMUONClusterStruct data type

```
1 struct AliHLTMUONClusterStruct
2 {
```

```
3         AliHLTInt32_t fId; // Unique ID for the cluster. It must be at
4                            // least unique for any given event.
5                            //  -1 == invalid.
6
7         AliHLTMUONRecHitStruct fHit; // Corresponding reconstructed hit.
8
9         AliHLTInt32_t fDetElemId;  // Detector ID number from AliRoot
10                                   // geometry on which the cluster
11                                   // was found.
12
13        AliHLTUInt16_t fNchannelsB; // Number of channels/pads in the
14                                    // cluster in bending plane.
15
16        AliHLTUInt16_t fNchannelsNB; // Number of channels/pads in the
17                                     // cluster in non-bending plane.
18
19        AliHLTFloat32_t fChargeB;    //Cluster charge in bending
20                                     // plane. Can be -1 if invalid
21                                     // or uncomputed.
22
23        AliHLTFloat32_t fChargeNB; // Cluster charge in non-bending
24                                   // plane. Can be -1 if invalid
25                                   // or uncomputed.
26 };
```

Listing 4.5: The AliHLTMUONChannelStruct data type

```
1 struct AliHLTMUONChannelStruct
2 {
3         AliHLTInt32_t fClusterId;   // ID corresponding to the
4                                     // cluster this channel is
5                                     // part of. -1 == invalid.
6
7         AliHLTUInt16_t fBusPatch;    // Bus patch to which this
```

```
8                                       // is connected.
9
10          AliHLTUInt16_t fManu;       // The MANU address on
11                                      // electronics.
12
13          AliHLTUInt16_t fChannelAddress; // The channel address
14                                          // on electronics.
15
16          AliHLTUInt16_t fSignal;     // ADC value of signal.
17
18          AliHLTUInt32_t fRawDataWord; // The raw data word as
19                                      // found inthe DDL stream.
20 };
```

MergeQuadRecHits :

It almost does the same merging steps as that of MergeSlatRecHits. But it uses the advantage of finer pad segmentation in the inner region. A pad cluster (3×3) in the inner most zone, is capable to provide adequate resolution in both bending and non-bending directions. Therefore, during the final merging step and if no hits are found on the other plane still that hit on the single plane is considered as a valid reconstructed hit.

Clear :

As it appears from the name, it clears all the pointers and arrays that are used for a given detection element.

The next part explains the methods of the class AliHLTMUONHitReconstructorComponent, which controls the class

AliHLTMUONHitReconstructor to analyse the events. But before that it is important to highlight the following three features of dHLT analysis scheme.

DoInit :

During the initialization process, the DoInit method reads the geometrical mapping of the spectrometer from the Conditional Data Base (CDB) ReadLutFromCDB, or from the text file ReadLookUpTable of predefined format. In either case it loads data format of type AliHLTMUONHitRecoLutRow into the memory. Along with mapping, the retrieval of the last pedestal and calibration run parameters that are stored in the same CDB is also performed inside this method. The calculation of the maximum allowable buspatch occupancy level for each buspatch is also carried out and filled into memory array. The memory addresses are then passed to the initialisation function of AliHLTMUONHitReconstructor.

DoEvent :

This function receives rawdata block addresses from the rawdata publisher component *RORCPublishers* using common HLT data abstraction method. Since HLT is an online system, it is important to pickup the correct data block for a given detector analysis, where the data block identification plays an important role. Once the proper rawdata blocks are found, it calls the AliHLTMUONHitReconstructor::Run() method for hit-reconstruction analysis. The final result is packed into the output blocks using the template class AliHLTMUONDataBlockWriter. It is important to note that during the preparation of the output data stream, it again has to apply the data abstraction, data identification and data specification schemes to publish it to the next processing component.

DoDeInit :

This method clears the memory allocation done by the core analysis component and also calls the destructor of that class. If needed some cleaning of the memory blocks owned by the component class itself can also be performed.

At the end of the hit reconstruction, the tracks are formed using the reconstructed hits. Thus, the following sections discuss the various tracking schemes of Muon Spectrometer, with an emphasis on online FullTracker.

4.2 Track Formation

Once the hit points of the tracking chambers are found, these are connected to form the tracks of the particles through the Spectrometer. As it has been pointed out before, there exits two online tracking methods in dHLT analysis Manso Tracker and Full Tracker. The concepts of online algorithms of tracking has been discussed in the following subsections. Since the quality of the online tracking will be compared with offline analysis, a short description of the offline tracker has been given.

4.2.1 Offline Tracker

The offline tracker uses either the fit of the track parameters (x, y, α, β, q/p) [where $x(y)$ and $\alpha(\beta)$ are the bending (non-bending) co-ordinates, and the corresponding angles, respectively, and q/p represents the charge over momentum] using the MINUIT package of Root or the reconstruction using the Kalman Filter. In the first step the primary track candidates are build using the clusters of station 4 and 5 using all combinations of clusters between the two chambers of station 5

(4). Then the pairs are selected for which the estimated bending momentum and the non-bending impact parameter at vertex are within given error limits. In the next step, the primary tracks are formed with station 4 and 5 and the identical tracks are eliminated. It is then propagated to stations 3, 2 and 1; in each step the track parameters are updated. In the last part, the tracks are extrapolated to the collision vertex which is measured by SPD of Inner Tracking System. The final results of the reconstruction are stored in objects of the class AliESDMuonTrack and saved in AliESD.root file. Three kinds of tracks are saved, tracker tracks matched with trigger tracks, only tracker tracks and only trigger tracks.

4.2.2 Manso Tracker

The primary motivation of dHLT is to reduce the background events by improving the p_{t}-cut resolution provided by the L0 trigger, which depends on the position resolution of the trigger chambers. Manso proposed that since the position resolution of the tracking chambers are better than that of trigger chambers, the extrapolation of the tracks to the fifth and fourth tracking stations will improve p_{t} estimation of the tracks [Ref. [1]]. Therefore, a parametrized Region of Interest (RoI) is defined for the fast track extrapolation,

$$R_s = a.R_p + b$$

where R_s is radius of the RoI and R_p is the position of the RoI with respect to the centre of the detector as shown in Fig. 4.6. The parameters a and b are found as,

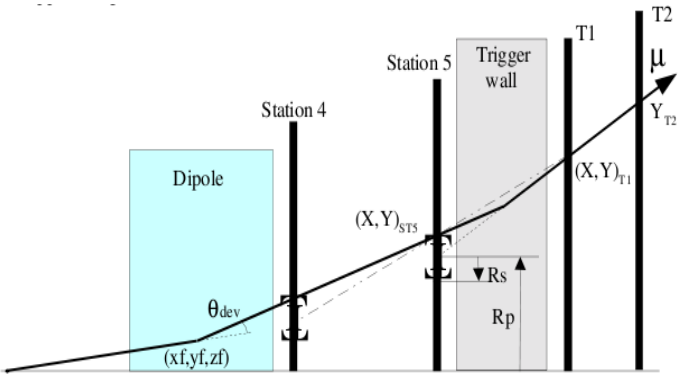

Figure 4.6: The concept of Manso Tracker shows that the tracking upto fourth tracking station improves momentum estimation. This is mainly due to the fact that the tracking chambers have better position resolution than trigger chamber and the track is not deflected by the Muon Filter.

$$\text{Station5} \quad : a = 0.020; \quad b = 3.0$$

$$\text{Station4} \quad : a = 0.016; \quad b = 2.0$$

When the hit points in the fourth and fifth station is found, the track momentum can be calculated using the following formula [2],

$$p = 0.3\frac{qBL}{\theta_d} \tag{4.1}$$

where q is the charge of the particle, B is the magnetic field, L is the length of the dipole. If the hit positions of stations 4 and 5 are at (x_1, y_1, z_1) and (x_2, y_2, z_2) respectively, the deviation of the track due to the magnetic field (θ_d) can be calculated as,

$$\theta_d = \frac{1}{z_f}\left(\frac{y_1 z_2 - y_2 z_1}{z_1 z_2}\right)$$

where z_f represents the z-position at the middle of the dipole. The momentum components are calculated as,

$$p_x = p\frac{x_f}{z_f}, p_y = p\frac{y_f}{z_f}, p_z = \sqrt{p^2 - \left(p_x^2 + p_y^2\right)}$$

where (x_f,y_f) represents the extrapolated track position in the middle of the third station. Thus, the Manso algorithm uses the property of better position resolution of the fourth and fifth tracking station for better estimation of momentum.

4.2.3 Full Tracker algorithm

Basic Concepts

The Manso tracker provides a partial improvement in p_{t} estimation but it is not adequate (discussed in sec. §5.3.2). Therefore, a Full Tracker was proposed [3] which allows track reconstruction upto the front absorber of the Muon Spectrometer.

The Full Tracking formalism can be viewed as a composition of four stages of track reconstruction. The full tracking also starts from trigger chambers and a straight line track is drawn upto the seventh chamber, since it is the first chamber after the dipole magnet. In the second step of tracking, the tracklets are calculated in station 1 and 2 using Cellular Automata method since this method does not need any a priori knowledge of the seed of the tracking. When the tracklets are found in the front and rear side of the spectrometer, they are matched using χ^2 test of Kalman filtering. If a track passes the Kalman testing, the track parameters are improved by the track extrapolation through parametrised front absorber.

The various stages of the Full Tracker are described below.

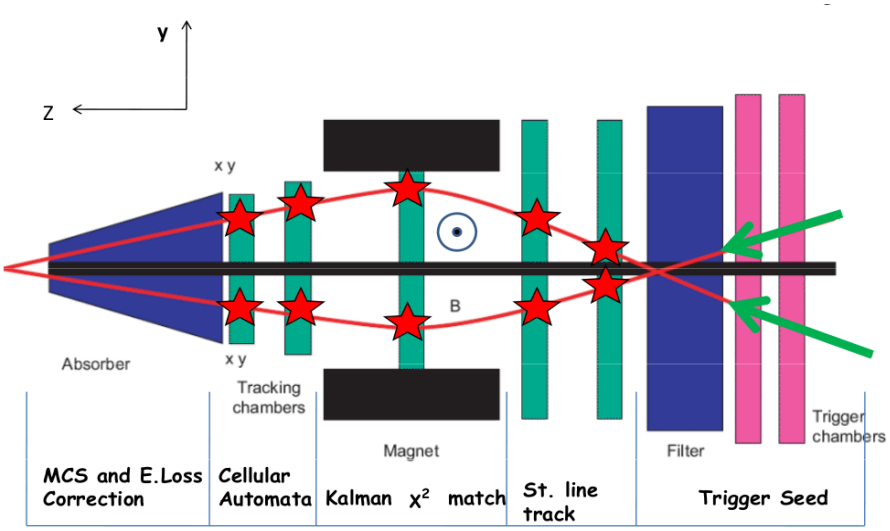

Figure 4.7: The concept of Full Tracker shows various methods of tracking for different segments of Muon Spectrometer. A track following method is used for the fourth and fifth station, whereas for the first and second station the Cellular Automaton is used. The segmented tracks from the rear and the front side of the Spectrometer are matched using Kalman χ^2 technique. Finally, the tracks are extrapolated to the origin through the front absorber, using parametrised corrections originating from the multiple Coulomb scattering and energy loss of the track in the absorber.

Trigger Chamber Tracking

The Muon Trigger stations are operated in streamer mode and provides the level zero (L0) trigger for the Muon Spectrometer. The global trigger processors provides the track parameters (p_x, p_y, p_z) for the tracks formed in the Trigger stations.

Tracking in Station 4,5

The tracking of the Full Tracker starts from this step, as the trigger track is already calculated during the issuance of the hardware trigger. The track segment of the trigger station is then extrapolated to the fifth tracking station using straight line extrapolation. Since the Muon Filter is situated in between the trigger and tracking chambers of Muon Spectrometer, care has been taken during this extrapolation for

deflection of the track in this iron wall. Since the effect of magnetic field is almost zero on fourth and fifth station, the track is extended further through straight line extrapolation. It is to be noted, in the real experimental condition, all the detectors may not function properly. Thus, a track is validated, if three out of four tracking chambers have hits associated with that track.

Tracking in Station 1,2

Since the extrapolation of the track to the third station involves the added complexity of the magnetic field, it has been skipped. This also saves vital time. As an alternative scheme, tracking in Station 1 and 2 has been proposed by forming tracklets in these stations. So the important criterion is that, one has to do the tracking without any seed or any priori information of the track direction. Therefore, the method of Cellular Automation [4, 5] is used for track finding which is a fast method and needs no a priori information of the direction of the tracks. The main features of the Cellular Automation are :

- The cell state is discrete [either living (1) or dead (0)]
- The number of neighboring cells is fixed, in most of the cases they are the nearest cells.
- The rules describing the dynamics of the evolution of the cellular automaton depend on the type problem.
- The cell states change simultaneously i.e. they are clocked.

A detail description of the Cellular Automata can be found in the Appendix A.

In present case, we have virtually segmented the detector in cells and any cell containing a hit point is living, otherwise is dead. In the next step the living cells of the consecutive chambers are connected for a given station, with the condition that the living cells from other chambers have to be its closest neighbour. The rule of evolution or the rule of survival is based on the selection that there has to be a neighbour in the adjacent station and if extrapolated to third station should match the track extrapolated in the backward direction from fourth and fifth station. The tracklets found in this method are validated using the same criteria as applied in case of tracking in stations 4 and 5, i.e. the tracklet is valid if there are three hit points out of the four detector planes. If needed, this condition can also be loosen to one hit per station.

Connect and Validate Track in Station 3

It has been discussed above that, a tracklet in the front section of the spectrometer may get connected to more than one tracklets in rear section or a tracklet of the rear chambers can get connected with more than one tracklets of the front chambers. These are ghost tracks and can be removed by two different techniques, namely,

- Chi-square text of Kalman filtering method [6, 7, 8].
- The extrapolation of tracklets through magnetic field, using track propagation method. (e.g. G3HELIX or G3HELX3 of Geant3)

In case of p-p events χ^2-test of Kalman Filtering is applied to evaluate the χ^2 of the tracks and removal of ghost tracks based on best chi-square selection. However, in case of Pb-Pb events the ghost tracks are removed through the track extrapolation in

magnetic field by Geant methods. But in this case also the χ^2 of the set of tracks after ghost removal is calculated by Kalman Filter. The χ^2-test of Kalman Filter which has been used in connecting and validating tracks through station 3 is described in brief below.

The Kalman Filter is a recursive tool for the prediction of the state of the system at a future point, and constantly updating the quality of prediction of the next future point by incorporating the immediate future point into the parameter for future prediction. This is done in three steps,

- Prediction is the estimation of the state vector at a future time.

- Filtering is the process to update the predicted state vector at point (k) based on the observations at points up to $(k-1)$ by adding the observation at point (k).

- In smoothing step the filtered state at site $(k' < k)$ is updated by using all the observations made at points upto (k).

In the present algorithm, the first two steps have been applied and the χ^2 is defines as (see Appendix on Kalman Filter and [8]),

$$\chi_k^2 = \chi_{k-1}^2 + \left(\boldsymbol{m}_k - \mathcal{H}_k \boldsymbol{a}_k\right)_k^T \mathcal{G}_k \left(\boldsymbol{m}_k - \mathcal{H}_k \boldsymbol{a}_k\right) + \left(\boldsymbol{a}_k - \boldsymbol{a}_k^{k-1}\right)^T \left(\mathcal{C}_k^{k-1}\right)^{-1} \left(\boldsymbol{a}_k - \boldsymbol{a}_k^{k-1}\right)$$

where,

χ^2_{k-1}	=	chi-square upto point $k-1$
$\boldsymbol{a}_k$	=	new estimate of state vector at point k
$\boldsymbol{a}_k^{k-1}$	=	prediction of state vector at k with the information unto $k-1$
$\mathcal{C}_k^{k-1}$	=	covariance matrix for the state vector
$\boldsymbol{m}_k$	=	measurement vector at point k
$\mathcal{H}_k\boldsymbol{a}_k$	=	measurement vector at point k if measurement noise is zero
$\mathcal{G}$	=	inverse of the covariance matrix for measurement noise.

The second term of the above expression represents the error matrix associated with the process noise at site k, and the third term represents the measurement noise for the same site. A summary of the Kalman filtering formulas are found at Appendix B.

Track Extrapolation through Muon Absorber

Since the track suffers substantial energy loss and scattering during its passage through the Front Absorber, it is very important to include these effects in estimating the momentum of the tracks. The energy loss is calculated using the Bethe-Bloch formula for ionisation energy loss. In case of multiple Coulomb scattering the composite effect of the different absorber materials is estimated using the Branson correction. If θ is the polar angle of a track at vertex with respect to the z-axis which passes through the front absorber. The Branson method gives the convenient way of the estimation of θ using the particle direction at the rear end of the front absorber [9].

A detail study of these effect can be found in the Appendix C.

4.2.4 Implementation in HLT

The Full Tracker analysis is carried out by two main classes. AliHLTMUONFullTracker is the core analysis class which performs all the track property calculations while AliHLTMUONFullTrackerComponent is the component class which controls the core class to execute the tracking analysis on behalf of HLT chain. The schematic diagram of the Fig. 4.8 explains the track parameters calculation methods of AliHLTMUONFullTracker class.

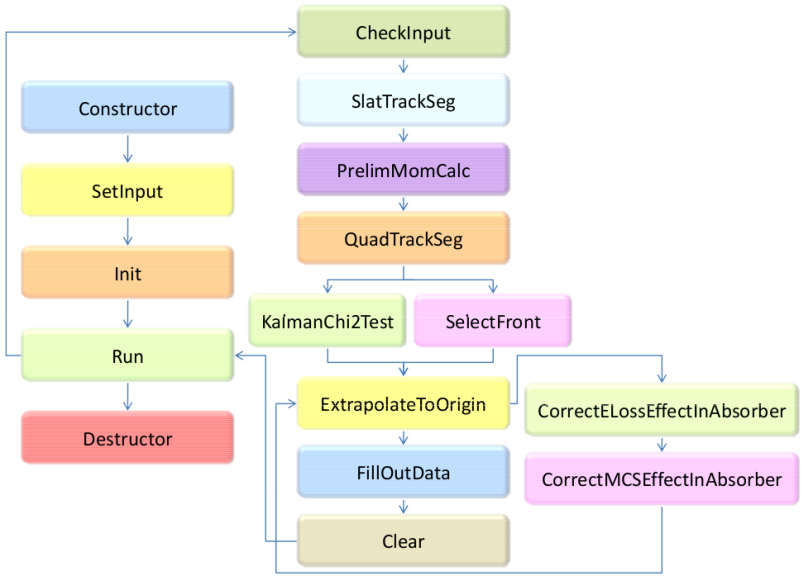

Figure 4.8: The schematic diagram of the functions of Full Tracker AliHLTMUONFullTracker class.

Init :

During initialisation of the Full Tracker class, the geometrical segmentations of the Muon Spectrometer is loaded from CDB. The other important parameter loaded from CDB is the value of the L3 and dipole magnetic fields. If the magnetic field

values are set by other components, that values are used instead. Otherwise the default instance is created with (+/+) magnetic field direction. The other important task of Init method is to book a memory map for detection elements.

SetInput :

This method copies the pointer address of the input data sets into an array of pointers and a counter keeps the record of number of triggers and hit reconstruction blocks. A test is performed in this method to assure that the number of data points do not overflow the size specified for the array of pointers. In addition, the detection element list is used to identify the proper data blocks which have valid detection element number. The SetInput function and the Run methods are called for each Muon trigger event.

Run :

The central control of the analysis is carried out by the Run method. It uses the method CheckInput to start the processing and stops at the Clear function as shown in Fig. 4.8. As the argument it receives the event number and the pointer to the output data block (of type AliHLTMUONTrackStruct) and the size of the output data.

CheckInput :

This method serves the most vital part of the analysis, protecting the code from incomplete data blocks. During the data taking, there are "soft" triggers from Muon Trigger, for the calibration purpose. Thus, these events has no tracking data. This type of events are skipped from this method. Furthermore, in case of detector

problem is it possible that some of the DDLs are switched off, which are also properly accounted in this method.

SlatTrackSeg :

The tracking process starts only when there is one reconstructed hit in each of the last two tracking stations. In the next step for each trigger record the associated tracks is searched within a predefined window. At present, the search windows are wide open (twice the simulated results), tuned to the cosmics result analysis. This will be optimised later, after the analysis of experimental data of sufficient statistics. If a track segment is found in station four and five, it is extrapolated to the third station to create a virtual hit point on that chamber. This hit point is utilised in the QuadTrackSeg method.

PrelimMomCalc :

It is possible that there are no track segments found in the first two stations either due to detector or tracking inefficiency. In both cases the full tracking is not possible for these tracks. But the track momentum is calculated using the same formula that has been used for the Manso Tracker in Eqn. 4.1.

It is obvious that the momentum calculated from the half tracks suffers from bad reconstruction resolution compared to the full tracks, since the half track calculation depends on approximate evaluation of θ_d. But this partial tracking method helps to improve the efficiency of online dHLT tracking performance.

QuadTrackSeg :

The QuadTrackSeg starts with checking for single hits in first and second stations. If there is no track in the rear end, the tracking in the first and second stations are skipped. In the first step, a set of tracklets are formed among the chambers of a given station. Then these tracklets are joined within certain boundary cuts on mutual angle and orientation to form a track segment. Finally the track segments are extrapolated to the middle of the third station and its position is compared with one obtained from SlatTrackSeg. If matching is found within a suitable limit then the next step of track matching is performed for those track segments.

KalmanChi2Test :

In the Kalman χ^2 test method, all the tracks, that are found by the SlatTrackSeg method are checked with the track segments found in QuadTrackSeg. If the track segments from the rear and front end of the spectrometer are matched using the χ^2 minimization test, they are saved into the array for full tracks. The track parameters are recomputed for the tracks in the arrays of full tracks.

SelectFront :

The SelectFront uses a simpler test to match the tracks from SlatTrackSeg with the tracks from QuadTrackSeg. A rough estimate of the track momentum is calculated for the track in the last two tracking stations. This is used to predict the hit position in the third and subsequently second tracking station. The track segment on the first two tracking stations if found to be closer to that extrapolated line from rear end are declared as matched track segment pair.

ExtrapolateToOrigin :

In the ExtrapolateToOrigin method, the correction for Multiple Coulomb scattering (MCS) and energy loss are applied to correct the track momentum.

Clear :

As the name suggests this method cleans any dynamic memory allocation and reset the counters for next event.

This chapter has illuminated the key ideas of tracking and clustering in the Muon Spectrometer, which are compared and validated with detail simulation results in the following chapter.

Bibliography

[1] F. Manso and the Clermont-Fd ALICE group. A first algorithm for a dimuon high level trigger. *ALICE Internal Note*, 2002. ALICE-INT-2002-004.

[2] ALICE Collaboration, Technical Design Report of the Dimuon Forward Spectrometer, CERN/LHCC 9922, 13 August 1999.

[3] Indranil Das, Sukalyan Chattopadhyay A new formalism of full tracking in dimuon high level trigger. *DAE-BRNS Symposium on Nuclear Physics*, 2009.

[4] A. Glazov, I. Kisel, E. Konotopskaya and G. Ososkov. Nucl. Instr. and Meth. A **329** (1993) 262-268.

[5] I. Kisel. Nucl. Instr. and Meth. A **566** (2006) 85-88.

[6] R.E. Kalman. Trans. ASME-Journal of Basic Engineering **82** (Series D) (1960) 35-45.

[7] P. Billoir, R. Fruehwirth and M. Regler. Nucl. Instr. and Meth. A **241** (1985) 116-131.

[8] R. Fruehwirth. Nucl. Instr. and Meth. A **262** (1987) 444-450.

[9] J.P.Cussonneau, P.Lautridou, L.Luquin, V.Metivier, A.Rahmani, V.Ramillien, T.Reposeur and A.Morsch. Tracking Peformances of Several Front-Absorber Designs. Report. *ALICE Internal Note*, 1998, INT-98-27

Chapter 5

Simulation Studies and Validation of Algorithms

This chapter describes the performance of Full Tracker in a simulated environment which closely matches the experimental condition. The tracking and clustering codes depend on different selection windows, either due to detector boundary conditions (i.e maximum angle of the tracks or tracks pointing towards the origin) or the region of physics interest (p_{t}-cut of 1 GeV/c and 2 GeV/c). The ranges of these selection windows are obtained from simulation studies. This offline analysis environment is described in the first section, which is followed by the results of simulation studies of Hit Reconstruction and Full Tracker algorithms, respectively. In the last section, the commissioning of the Full Tracker in the online environment of HLT computing cluster is discussed.

5.1 AliRoot Simulation Scheme for Muon Spectrometer

The AliRoot simulation framework provides and maintains the exact detector simulation, reconstruction and analysis for ALICE detector. In the first step of particles generation, all primary and daughter particles are produced using the Monte Carlo generators (e.g. HIJING, PYTHIA, DPMJET, HERWIG). In addition, it is also possible to create particles of fixed and predefined spectrum from parametrized (i.e. where p_{t}, rapidity, azimuthal and polar angles are input parameter) generators. Once the particles are produced they are transported through the detectors and the detector responses are simulated via GEANT3 or GEANT4 or FLUKA. In the next stage of digitization, the analog detector signal is converted to ADC output to produce digits, which mimics the actual detector behaviour during the electronic readout. The digits are then converted into the structured raw data format, which is identical to that collected in real experimental environment. The offline analysis of HLT uses these as input and the results are saved in the ESD format (HLTESD), which are simultaneously stored along with the simulated rawdata data set. This analysis part in AliRoot has already been discussed before in sec. §3.4.3. At the end of the HLT analysis process a Quality Assurance (QA) analysis of the data is carried out, which marks the end of offline simulation by AliRoot.

The reconstruction of rawdata is performed in three basic steps. In the first step, the rawdata is decoded and the corresponding calibration is applied to recreate the digits. In case of Muon Trackers the set of digits which form a charge cluster is found out by scanning the neighbouring digits. The charge distribution of the cluster is then reconstructed using Mathieson function. Once the reconstructed hit positions are obtained, the tracking using Kalman filter starts from the rear end of the

spectrometer. It goes on attaching clusters with minimum χ^2 of track parameters, till it reaches to the first Muon chamber. In the final step of the offline reconstruction the tracks are filled into the ESD tree and the offline ESD tree is stored into a rootified file along with the tree that contains ESD objects of HLT.

5.2 Results of Hit Reconstruction

5.2.1 Reference Data Sets for Hit Reconstruction

The quality of the track parameters like momentum and rapidity, relies mostly on position resolution of the space points that forms the tracks. Thus, it is very important to study the position resolution and the efficiency of the hit reconstruction algorithm in order to test the quality of the fast algorithm. Therefore, the AliGenBox generator of AliRoot has been used to simulate the tracks within given a momentum range. The setup of the generator is listed in 5.1.

Listing 5.1: Particle generator for a given p_{t}window

```
96      if (!strcmp(option,"box")) {
97        AliGenBox *gener = new AliGenBox(1);
98        gener->SetPtRange(0.5,20.0001);
99        gener->SetPhiRange(0., 360.);
100       gener->SetThetaRange(171.000,178.001);
101       gener->SetPart(kMuonMinus);              // Muons
102       gener->SetOrigin(0.,0., 0.);  //vertex position
103       //Sigma in (X,Y,Z) (cm) on IP position
104       gener->SetSigma(0.0, 0.0, 0.0);
105     }
```

The complete configuration file can be found in the AliRoot at $ALICE_ROOT/MUON/Config.C. A set of 10000 events have been generated and reconstructed. The list 5.2 and 5.3 presents the muon offline simulation and reconstruction macros, respectively. The generated p_{t} distribution is shown in figure 5.1. It is to be noted that, the analysis of present chapter has been carried out with AliRoot version v4-18-Release, unless otherwise stated.

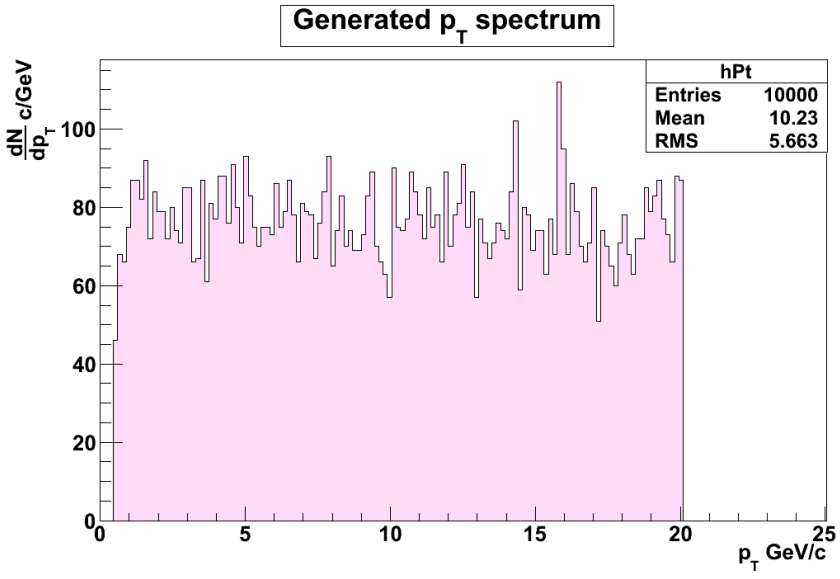

Figure 5.1: The p_{t} spectrum of the generated particles of the reference data set shows the inclusive p_{t} measurement.

Listing 5.2: Simulation macro for muon offline analysis.

```
1  void runSimulation(int seed, int nevents, const char* config)
2  {
3    // Uncomment following lines to run simulation with
4    // local residual mis-alignment
5    // (generated via MUONGenerateGeometryData.C macro)
6    // AliCDBManager* man = AliCDBManager::Instance();
7    // man->SetDefaultStorage("local://\$ALICE_ROOT/OCDB");
8    // man->SetSpecificStorage("MUON/Align/Data",
9    // "local://\$ALICE_ROOT/OCDB/MUON/ResMisAlignCDB");
10
11   AliSimulation MuonSim(config);
```

```
12      MuonSim.SetSeed(seed);
13      MuonSim.SetTriggerConfig("MUON");
14      MuonSim.SetWriteRawData("MUON HLT","raw.root",kTRUE);
15
16      MuonSim.SetMakeDigits("MUON");
17      MuonSim.SetMakeSDigits("MUON");
18      MuonSim.SetMakeDigitsFromHits("");
19
20      MuonSim.SetRunHLT("libAliHLTMUON.so
21      chains=dHLT-sim-fromRaw-fullTracker");
22
23      MuonSim.SetRunQA("MUON:ALL");
24
25      MuonSim.Run(nevents);
26      //gObjectTable->Print();
27
28  }
```

Listing 5.3: Reconstruction macro for muon offline analysis

```
1   void runReconstruction(int seed,const char* input,const char* recoptions)
2   {
3     AliCDBManager* man = AliCDBManager::Instance();
4     man->SetDefaultStorage("local://\$ALICE_ROOT/OCDB");
5
6     gRandom->SetSeed(seed);
7
8     AliReconstruction* MuonRec = new AliReconstruction("galice.root");
9     MuonRec->SetInput(input);
10    MuonRec->SetRunVertexFinder(kFALSE);
11    MuonRec->SetRunLocalReconstruction("MUON");
12    MuonRec->SetRunTracking("MUON");
13    MuonRec->SetFillESD("HLT");
14    MuonRec->SetOption("HLT", "libAliHLTMUON.so");
```

```
15      MuonRec->SetLoadAlignData("MUON");
16      MuonRec->SetNumberOfEventsPerFile(1000);
17      MuonRec->SetOption("MUON",recoptions);
18      MuonRec->SetRunQA("MUON:ALL");
19      MuonRec->SetQAWriteExpert(AliQAv1::kMUON);
20
21      // uncomment the following lines
22      // if you want to set custom RecoParam
23      //
24      // instead of getting them from the OCDB
25      //  AliMUONRecoParam *muonRecoParam
26      //                          = AliMUONRecoParam::GetLowFluxParam();
27      //  muonRecoParam->SaveFullClusterInESD(kTRUE,100.);
28      //  MuonRec->SetRecoParam("MUON",muonRecoParam);
29
30      MuonRec->Run();
31
32      delete MuonRec;
33
34      //gObjectTable->Print();
35  }
```

5.2.2 Resolution and Efficiency

The residuals between the reconstructed hits and the original Geant hits for the Hit Reconstruction algorithm and Offline Clusterfinder method are compared in Fig. 5.2 and Tab. 5.1. It is evident from the figure and the table that the hit reconstruction of the bending plane is more accurate than the non bending plane. This is due to the fact that the resolution in the bending direction is determined along the anode wires and the pad dimension is 5 mm, while the non-bending resolution

is determined perpendicular to the anode wires. Thus, this resolution is purely determined by anode wire spacing (2.5 mm) and expected to be $2.5/\sqrt{12}$ mm. It is also found from the figures that for bending plane the Hit Reconstruction has an average resolution of 33 ± 9 μm, which is close to the offline resolution of 21 ± 5 μm. However, for non-bending plane the offline (876 ± 55 μm) and HLT (896 ± 31 μm) shows almost same resolution, which is close to the expected value. The overall efficiency is almost the same between online and offline Hit Reconstruction algorithms and is 98%.

A comparison of the figures clearly shows that the online resolution is worse by a factor of 1.5 compared to the offline resolution. However, it is to be noted that the online algorithm does not perform clustering and reconstructs the hit position by centre of gravity method (as described in the last chapter) instead of detailed Mathieson fit. Thus, the fast online algorithm makes a small compromise on the resolution but ensures a large gain in timing without loosing efficiency which is the essential criterion.

5.2.3 Other important histograms from Hit Reconstruction

Since HLT algorithm provides real-time reconstruction of the charge clusters, it can be used as a tool for online investigation of the working conditions of the detectors. This online evaluation of the quality of the experimental run can save a lot of analysis time. Three QA histograms have been described below.

- Charge per cluster : This histogram represents the MIP signal for the Muon Chambers [see Fig. 5.3(a)]. The mean of this histogram is directly proportional to the gain of the chamber. Thus, monitoring this mean as a functions of different DDLs, ensures an uniformity of overall gain of Muon Tracking system.

Table 5.1: A comparison of resolution and efficiency of Hit Reconstruction algorithm with Offline clustering method, based on the simulation results

		Offline Clustering		dHLT Hit Reconstruction	
Chamber	Plane	Resolution(μm)	Efficiency	Resolution(μm)	Efficiency
Chamber 1	bending	12.0±0.0	99.67%	14.6±0.0	98.65%
	non-bending	760.5±0.5	99.67%	838.8±0.6	98.65%
Chamber 2	bending	11.9±0.0	99.82%	16.0±0.0	99.8%
	non-bending	771.5±0.5	99.82%	836.0±1.0	99.8%
Chamber 3	bending	21.7±0.0	99.91%	43.3±0.0	99.91%
	non-bending	913±1.0	99.91%	938.4±0.7	99.91%
Chamber 4	bending	22.1±0.0	99.81%	43.3±0.0	99.76%
	non-bending	897.2±0.6	99.81%	913.1±0.7	99.76%
Chamber 5	bending	24.3±0.0	98.64%	34.9±0.0	98.6%
	non-bending	898.5±0.6	98.64%	903.9±0.6	98.6%
Chamber 6	bending	24.6±0.0	98.57%	36.0±0.0	98.55%
	non-bending	910.6±0.6	98.57%	908.5±0.6	98.55%
Chamber 7	bending	25.5±0.0	98.47%	35.2±0.0	98.44%
	non-bending	898.0±1.0	98.47%	906.5±0.6	98.44%
Chamber 8	bending	25.4±0.0	98.38%	34.7±0.0	98.38%
	non-bending	900.1±0.6	98.38%	904.2±0.6	98.38%
Chamber 9	bending	25.6±0.0	98.53%	35.2±0.0	98.51%
	non-bending	906.1±0.6	98.53%	910.0±0.6	98.51%
Chamber 10	bending	24.9±0.0	98.37%	34.7±0.0	98.35%
	non-bending	901±1.0	98.37%	902.6±0.6	98.35%

In case of inadequate high voltage, the MIP signal will be incomplete.

- Number of pads per cluster : As the name suggests it presents the size of the clusters. Any abrupt change in this size also represent an abnormal behaviour of the detector. A typical distribution is shown in figure 5.3(a).

- Ratio of bending to non-bending charge : Since the two cathode planes are placed symmetrically about the anode wire plane, the ratio of the bending to the non-bending charges should be the close to 1 (one) in ideal scenario. Thus, a significant deviation will indicate a problem in the readout of either the bending or non-bending plane. The Fig. 5.3(b) shows the distribution for the first chamber.

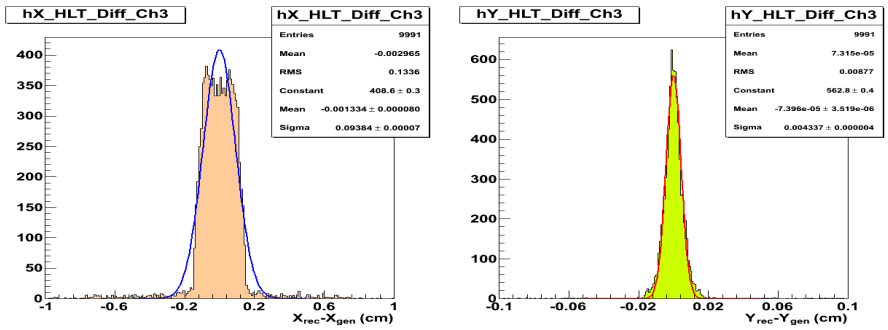

(a) HLT Hit Reconstruction resolution for chamber 3

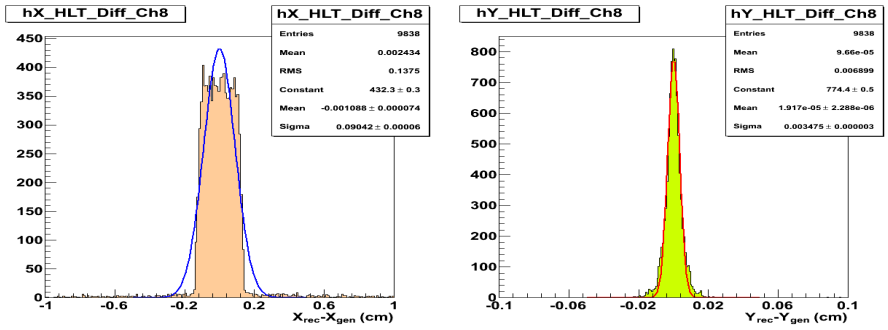

(b) HLT Hit Reconstruction resolution for chamber 8

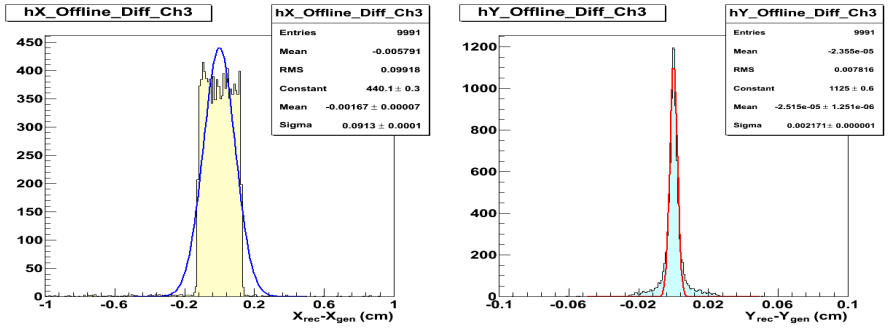

(c) Offline Clusterfinder resolution for chamber 3

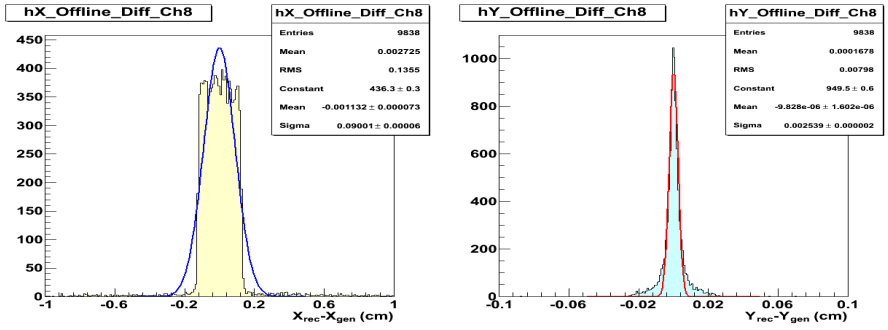

(d) Offline Clusterfinder resolution for chamber 8

Figure 5.2: The subfigures 5.2(a) and 5.2(b) show the resolution of Hit Reconstruction algorithm for chamber 3 and 8, respectively. The same for Offline Clusterfinder are shown in subfigures 5.2(c) and 5.2(d), respectively.

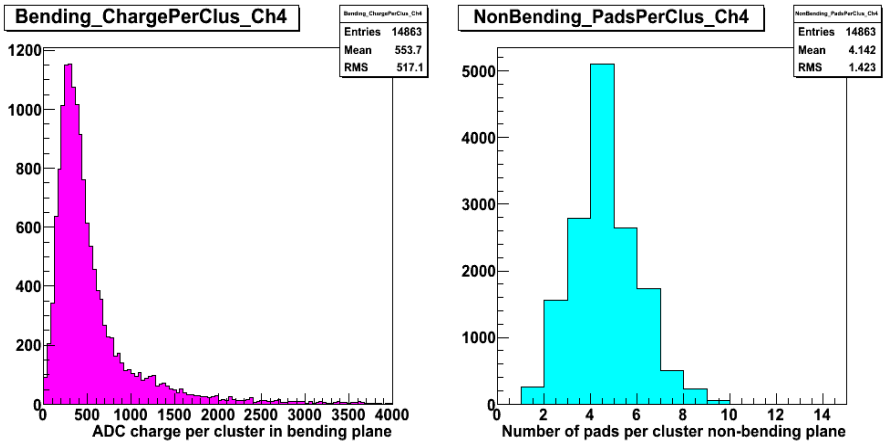

(a) The charge per cluster(left) and Number of pads per cluster (right) plotted from the reference data set

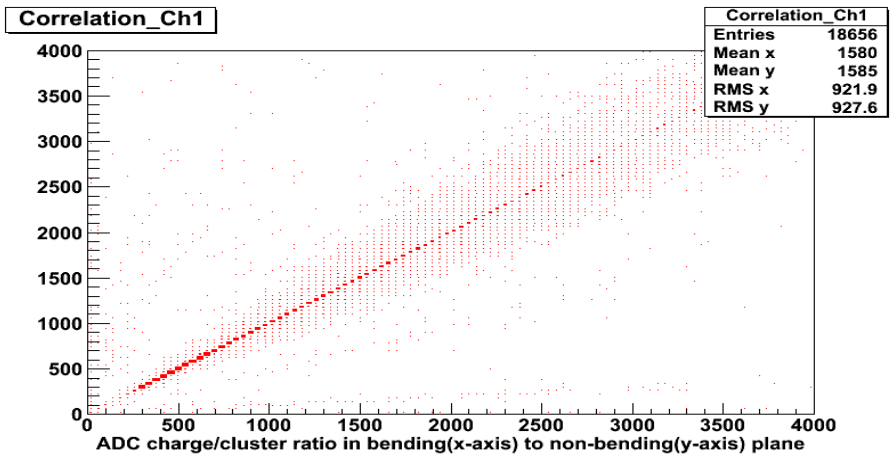

(b) The ratio of Bending to non-bending ADC charges

Figure 5.3: The subfigures show different Quality Assurance (QA) histograms.the distribution of the charged particle hits.

5.3 dHLT Full Tracking Offline Validation

5.3.1 Reference Data Sets for Tracker comparison

The p_t resolution of the Full Tracker has been tested with four sets of rawdata which are simulated at fixed (or delta) p_t values. This data set is then used to test the quality of p_t reconstruction by the Full Tracker and it's comparison with the Offline Tracker and Manso Tracker.

The first set of data of muon tracks are generated for 1000 events. Various sets are generated for p_t = 0.5 GeV/c, 1.0 GeV/c, 1.5 GeV/c, 2.0 GeV/c and 2.5 GeV/c. The window of p_t from 0.5 GeV/c to 2.5 GeV/c is explicitly selected as 1 GeV/c and 2 GeV/c are the planned to be the low and high p_t-cuts to clean the J/Ψ and Υ spectrum. In order to generate data set for p_t = 0.5 GeV/c the event generator of list 5.1 has been used, with a change of

```
98      gener->SetPtRange(0.5,20.0001);
```

to

```
98      gener->SetPtRange(0.5,0.5001);
```

Similar changes are applied for the generation of other delta p_t spectra.

In the next set of data, 10000 single muon events are generated in the p_t-range of 0.5 to 5.0 GeV/c to compare the p_t-cut efficiencies of the three trackers.

The third set of data consists of 1000 events each for J/Ψ and Υ without any background. The following configuration parameters for J/Ψ generation is shown in 5.4.

Listing 5.4: Parametrised particle generator for J/Ψ

```
136   if (!strcmp(option,"paramJpsi")) {
137     AliGenParam *gener = new AliGenParam(1, AliGenMUONlib::kJpsi);
138     gener->SetMomentumRange(0,999);
139     gener->SetPtRange(0,100.);
140     gener->SetPhiRange(0., 360.);
141     gener->SetCutOnChild(1);
142     gener->SetChildPhiRange(0.,360.);
143     gener->SetChildThetaRange(171.0,178.0);
144     gener->SetOrigin(0,0,0);
145     gener->SetForceDecay(kDiMuon);
146     gener->SetTrackingFlag(1);
147     gener->Init();
148   }
```

In case of parametrised ϒ generation only the option AliGenMUONlib::kJpsi is changed into AliGenMUONlib::kUpsilon.

In the fourth set of data the J/Ψ and ϒ signals are merged with the hadronic backgrounds generated from HIJING generator using,

Listing 5.5: Parametrised HIJING generator for $\frac{dN_{ch}}{d\eta} = 8000$ in $|\eta| \leq 1$

```
484     case kParam_8000:
485       {
486         comment = comment.Append(":HIJINGparam N=8000");
487         AliGenHIJINGpara *gener = new AliGenHIJINGpara(86030);
488         gener->SetMomentumRange(0, 999999.);
489         gener->SetPhiRange(0., 360.);
490         // Set pseudorapidity range from -8 to 8.
491         Float_t thmin = EtaToTheta(8);    // theta min. <----> eta max
492         Float_t thmax = EtaToTheta(-8);   // theta max. <----> eta min
493         gener->SetThetaRange(thmin,thmax);
494         gGener=gener;
```

```
495         }
496         break;
```

The full configuration for HIJING generation can be found at $ALICE_ROOT/macros/ConfigPPR.C A study of the signal events with and without the presence of the background helps to estimate the convoluted efficiency and resolution of the three trackers.

5.3.2 Resolution and Convoluted Efficiency

The test has been carried for the first data set, with a given p_t at 2.0 GeV/c [Fig. 5.4(a)]. This p_t has been reconstructed using the Offline Tracker (Fig. 5.4(b)), Manso Tracker (Fig. 5.4(c)) and Full Tracker (Fig. 5.4(d)). It is evident from the figures 5.4(c) and 5.4(d) that the resolution of the Full Tracker ($\sim$ 74 MeV/c) is much better than the Manso's Tracker ($\sim$ 180 MeV/c). In addition, the peak position (2.0 GeV/c) is improved in case of Full Tracker. A detail analysis of track matching of the generated particles to the reconstructed one, shows that Manso Tracker and the Full Tracker are affected by the problem of ghost tracks. But the incorporation of the ghost tracks does not affect the efficiency of the online Full Tracker, which can be found in Table 5.2. The efficiency of the different tracking approaches are compared for different p_t values. For a given tracking algorithm, the efficiency has been determined by comparing the space points of the reconstructed tracks with the space points of the generated tracks. If 70% of the reconstructed track points are found to match with the simulated track points, it is considered as a valid reconstructed track. It is clear from the table that Offline Tracker is the most efficient tracker, where as the Full Tracker shows the close agreement with the Offline Tracker. Although the efficiency of the Manso Tracker increases for higher p_t, the efficiency is far worse than the other

two trackers in case of low momentum particles.

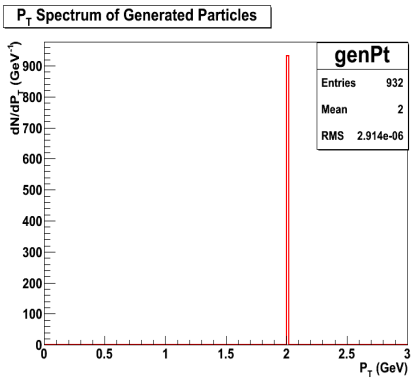

(a) The p_t spectrum plotted from Monte Carlo generation

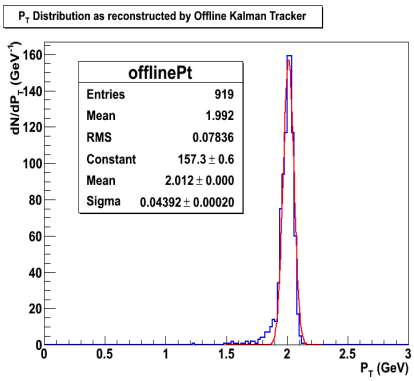

(b) The reconstructed p_t spectrum using ALICE Offline reconstruction

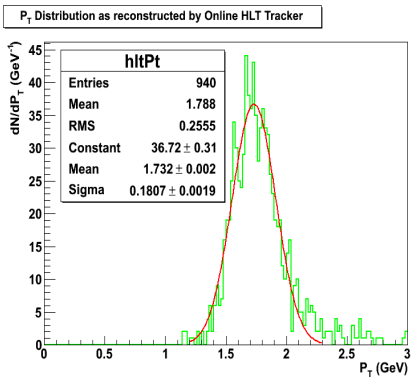

(c) The reconstructed p_t spectrum using Manso's approach

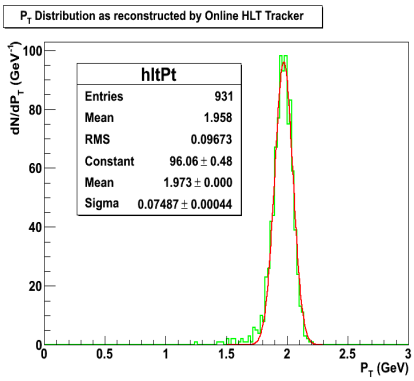

(d) The reconstructed p_t spectrum using the Full Tracker method.

Figure 5.4: The comparison of different tracking approaches for the generated spectrum at (a). The (b), (c) and (d) shows the reconstructed p_t spectrum for Offline, Manso and Full Tracker methods, respectively.

In the table 5.3, the resolution of the different trackers are compared. The resolution represents the standard deviation (σ) value for the given p_t. It can be inferred from this the table that the resolution for Offline Tracker is nearly constant over the p_T range but for Manso and Full Tracker the resolution deteriorates for higher p_T. However, the Full Tracker resolution is found to be much better than the Manso Tracker.

Table 5.2: p_t Efficiency of different tracking approach

	Offline (%)	Full Tracker (%)	Manso Tracker (%)
0.5 GeV/c	96.49 ± 0.91	95.61 ± 0.91	71.56 ± 0.74
1.0 GeV/c	99.57 ± 0.53	97.57 ± 0.52	86.86 ± 0.48
1.5 GeV/c	98.86 ± 0.47	97.95 ± 0.47	88.84 ± 0.44
2.0 GeV/c	98.61 ± 0.46	98.50 ± 0.46	88.72 ± 0.42
2.5 GeV/c	98.83 ± 0.46	97.98 ± 0.45	88.92 ± 0.42

Table 5.3: p_t Resolution of different tracking approach

	Offline (MeV/c)	Full Tracker (MeV/c)	Manso Tracker (MeV/c)
0.5 GeV/c	33.8 ± 0.7	44.7 ± 1.0	84.5 ± 3.7
1.0 GeV/c	34.9 ± 0.2	47.0 ± 0.3	127.0 ± 1.3
1.5 GeV/c	39.8 ± 0.2	61.6 ± 0.4	146.9 ± 1.7
2.0 GeV/c	43.9 ± 0.2	74.9 ± 0.4	180.7 ± 1.9
2.5 GeV/c	40.5 ± 0.1	78.8 ± 0.5	175.3 ± 2.7

In figure 5.5, the efficiencies of the p_t-cut for the three cases have been investigated. The second data set have been used for this evaluation. It is evident that the p_t-cut efficiency of Manso Tracker is very low. The desired efficiency is reached only 0.5 GeV/c above the p_t-cut. However, it is capable of improving the p_t-cut from L0. The Full Tracker on the other hand provides a sharp p_t-cut which is comparable to that from offline analysis. Thus, this figure clearly summarizes the improvement achieved by the Full Tracker over the Manso Tracker and is expected to ensure the same efficiency as the offline reconstruction.

5.3.3 Dimuon mass distribution

The third set of simulated data is used to study the resonance spectrum in the absence of background. In the figure 5.6, the J/Ψ resonance has been reconstructed using Offline Tracker, Manso Tracker and Full Tracker from the decay muons. It is seen from the figure that in terms of resolution the Full Tracker is much better

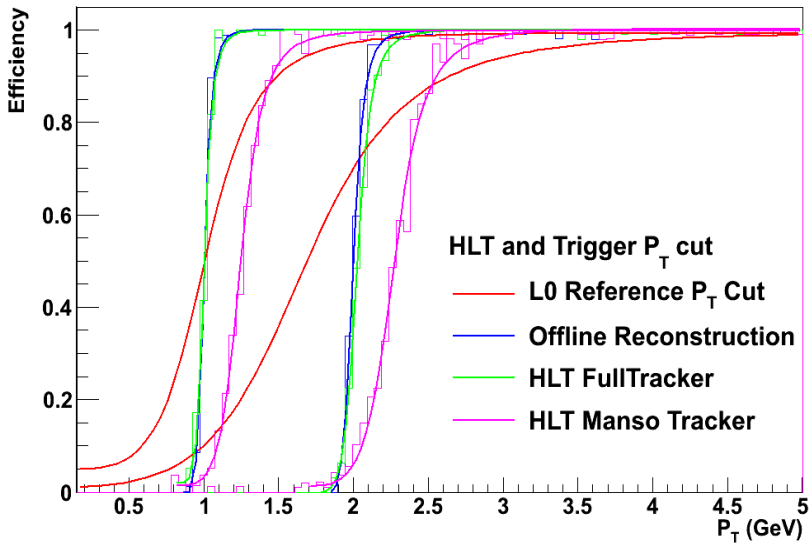

Figure 5.5: The plot shows the p_t-cut efficiency as found for L0 trigger, Manso Tracker, Offline Tracker and Full Tracker.

compare to the Manso Tracker and reconstructs more tracks as found by the Offline Tracker, which confirms the reasonable efficiency of the Full Tracker.

Finally, the effects of transverse momentum cuts on the dimuon invariant mass spectrum have been demonstrated in Fig. 5.7 using the fourth data set. In the first three histograms Fig. 5.7(a), Fig. 5.7(b) and Fig. 5.7(c) the inclusive invariant mass spectrums of two oppositely charged muons in presence of HIJING background has been shown for Offline, Manso and Full Tracker, respectively. The combinatorial background in the low mass region is due to the muons coming from the decay of pions and kaons. The next set of figures Fig. 5.7(d), Fig. 5.7(e) and Fig. 5.7(f) show the effect of 1 GeV/c p_t-cut on the invariant mass spectrum the for Offline, Manso and Full Tracker, respectively. This exercise has been repeated for Υ with and without p_t-cut at 2.0 GeV/c. The mass resolution of the three tracking methods for the two types of resonances are summarised in table 5.4. It is again established from these comparisons that the Full Tracker produces better results than the Manso Tracker. In fact the quality of reconstruction by Full Tracking method is in close agreement

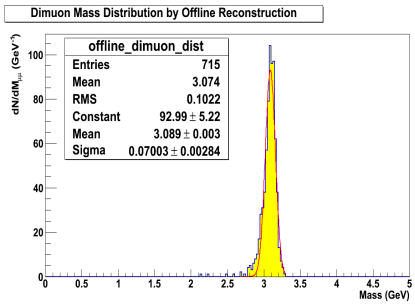

(a) Invariant dimuon mass distribution without any without any background by Offline

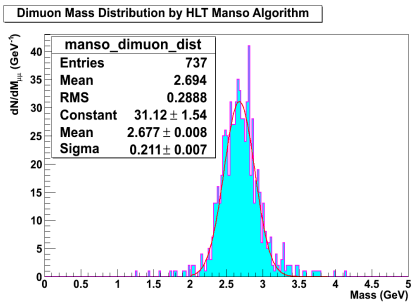

(b) Invariant dimuon mass distribution by Manso Tracker

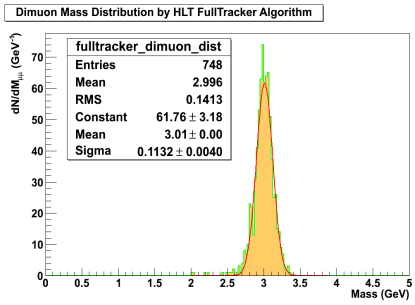

(c) The Full Tracker result of invariant dimuon mass distribution

Figure 5.6: The invariant mass of J/Ψ in case of no hadronic background by different tracking approaches.

with the Offline results. Thus, the comparison tests show that the Full Tracker has reasonable p_T efficiency and resolution when compared with Offline Tracker but most importantly, it is three orders of magnitude faster than Offline Tracker. This is the essential requirement of a real time analysis tool.

Table 5.4: Resolution of Invariant Mass distribution with and without p_t-cut

	J/Ψ (MeV/c)		Υ (MeV/c)	
	no p_t-cut	at p_t =1.0 GeV/c	no p_t-cut	at p_t =2.0 GeV/c
Offline	66.4±4.2	58.1±3.4	106.6±5.9	106.4±5.9
Full Tracker	104.1±9.8	106.0±11.7	237.1±17.8	236.6±17.7
Manso Tracker	318.6±12.4	255.7±11.8	482.5±27.5	472.1±27.1

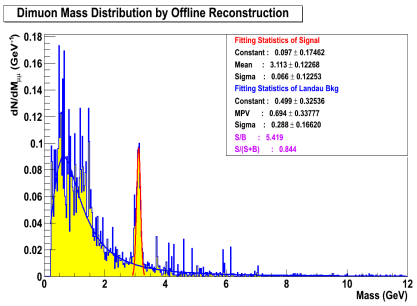

(a) Invariant dimuon mass distribution without any p_t-cut as reconstructed by Offline algorithm

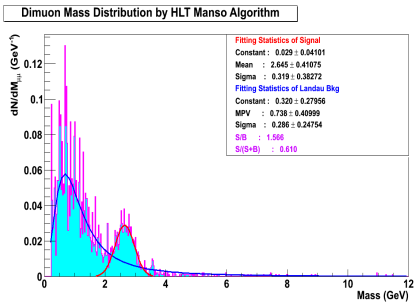

(b) Invariant dimuon mass distribution by Manso Tracker without any p_t-cut

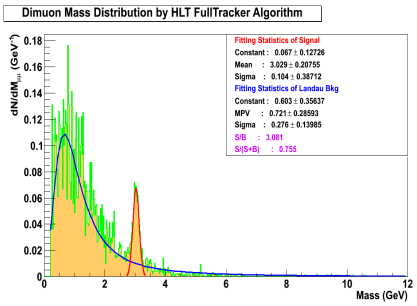

(c) The Full Tracker result of invariant dimuon mass distribution without any p_t-cut

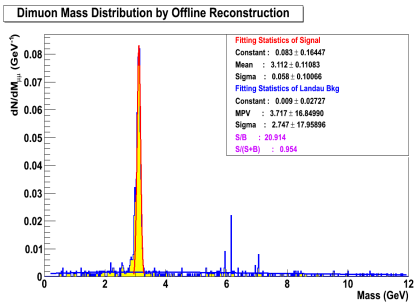

(d) Invariant dimuon mass distribution with p_t-cut at 1.0 GeV/c as reconstructed by Offline algorithm

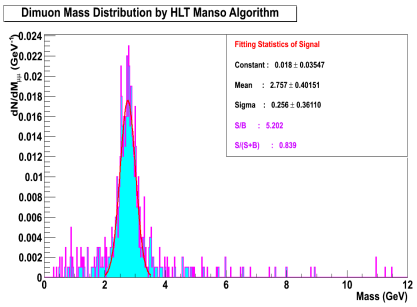

(e) Invariant dimuon mass distribution by Manso Tracker with a p_t-cut at 1.0 GeV/c

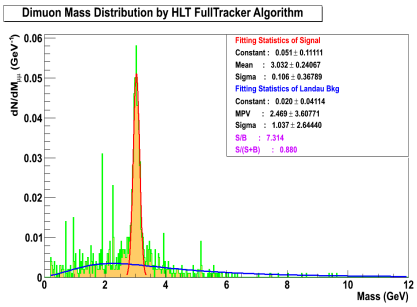

(f) The Full Tracker result of invariant dimuon mass distribution with a p_t-cut at 1.0 GeV/c

Figure 5.7: The dimuon invariant mass spectrum shows J/Ψ signal merged with HIJING background for various tracking algorithms. In subfigures (a), (b) and (c) the mass spectrum has been plotted without any p_t-cut. Whereas the effect of p_t-cuts on the invariant dimuon mass spectrum by different trackers are shown in subfigures (d), (e) and (f).

5.4 Online Commissioning of Full Tracker

The online performance of the full tracker has been tested in ALICE HLT computer farm, with the simulated Pb-Pb data generated by HIJING Monte Carlo codes. The main motivation of this test are explained below,

- Timing Estimation : The first important test for the online tracking is the rate of data processing. It has to satisfy the timing constrain of 1 kHz processing rate as expected in case of central Pb-Pb collision.

- Long Time Stability : The online Full Tracker has to be absolute free from any memory leak, fault tolerant against any corrupted data blocks and several other real time computation challenges. Thus, rigorous tests with simulated Pb-Pb events have been checked for the stability of the chain over long time.

- Requirement for Extra Resource : A series of tests have been carried out with different particle multiplicities. This is important to scale the requirements of resources during the optimised beam condition of Pb-Pb collision. Therefore, the benchmark results of this test provide the scalability factors for the future heavy ion runs.

5.4.1 Configuration

In order to carry out the above tests, different sets of HIJING Monte Carlo data have been simulated for $\left(\frac{dN}{d\eta}\right)_{|\eta|\leq 1}$ = 1000, 2000, 4000, 6000 and 8000 with the similar configuration as described in list 5.5. It is equally important to explain the HLT cluster specification in order to understand the test bench of performance study of the FullTracker. The HLT consists of several computer nodes dedicated for

each detector group of ALICE. The Dimuon part of the HLT consists of five nodes (FEPs) with direct connection to DDLs. There are two other computing nodes (CN) dedicated for dHLT online data processing. The specifications of the nodes are given in table 5.5-5.6,

Table 5.5: Processor and memory configuration of front-end-processing nodes

processor :	0
vendor_id :	AuthenticAMD
cpu family :	16
model :	4
model name :	Quad-Core AMD Opteron(tm) Processor 2378
stepping :	2
cpu MHz :	2400.000
cache size :	512 KB
physical id :	0
siblings :	4
core id :	0
cpu cores :	4
apicid :	0
initial apicid :	0
fpu :	yes
fpu_exception :	yes
cpuid level :	5
wp :	yes
flags :	fpu vme de pse tsc msr pae mce cx8 apic sep mtrr pge mca cmov pat pse36 clflush mmx fxsr sse sse2 ht syscall nx mmxext fxsr_opt pdpe1gb rdtscp lm 3dnowext 3dnow constant_tsc rep_good nonstop_tsc extd_apicid pni monitor cx16 popcnt lahf_lm cmp_legacy svm extapic cr8_legacy abm sse4a misalignsse 3dnowprefetch osvw ibs skinit wdt
bogomips :	4787.14
TLB size :	1024 4K pages
clflush size :	64
cache_alignment :	64
address sizes :	48 bits physical, 48 bits virtual
power management:	ts ttp tm stc 100mhzsteps hwpstate
MemTotal:	12343632 kB
MemFree:	7891860 kB
Buffers:	271292 kB
Cached:	1537608 kB
SwapCached:	0 kB

Table 5.6: Processor and memory configuration of computing nodes

processor :	7
vendor_id :	GenuineIntel
cpu family :	6
model :	23
model name :	Intel(R) Xeon(R) CPU E5420 @ 2.50GHz
stepping :	6
cpu MHz :	2493.900
cache size :	6144 KB
physical id :	1
siblings :	4
core id :	3
cpu cores :	4
apicid :	7
initial apicid :	7
fpu :	yes
fpu_exception :	yes
cpuid level :	10
wp :	yes
flags :	fpu vme de pse tsc msr pae mce cx8 apic sep mtrr pge mca cmov pat pse36 clflush dts acpi mmx fxsr sse sse2 ss ht tm pbe syscall nx lm constant_tsc arch_perfmon pebs bts rep_good aperfmperf pni dtes64 monitor ds_cpl vmx est tm2 ssse3 cx16 xtpr pdcm dca sse4_1 lahf_lm tpr_shadow vnmi flexpriority
bogomips :	4987.66
clflush size :	64
cache_alignment :	64
address sizes :	38 bits physical, 48 bits virtual
MemTotal:	16469864 kB
MemFree:	9558952 kB
Buffers:	198248 kB
Cached:	3737556 kB
SwapCached:	0 kB

These FEP and CN machines are dedicated to run certain Dimuon HLT components. For instance, the FEP nodes are connected to DDLs of the detectors therefore, the Hit Reconstruction algorithm is executed in these nodes. The reconstructed hits are forwarded to the Full Tracker components which run in the CN-machines. The software versions used during this study are tabulated at 5.7.

Table 5.7: Software version of HLT cluster used for online performance test

1) BASE/base	9) DATATRANSPORT/20091127.074300
2) DEFINITION/base	10) ECSPROXY/v1.5.4-20091127.074300
3) ALIEN/v2-17	11) PENDOLINO/v1.3-v4-18-Rev-05
4) FASTJET/2.4.1	12) HCDBMANAGER/v1.5-v4-18-Rev-05
5) ROOT/v5-26-00b	13) CONTROL/HEAD_2010-03-03
6) GEANT3/v1-11	14) HLT/HEAD_2010-03-03-prod
7) TAXI/v2.2-v4-18-Rev-05	15) HLTdevel/HEAD_2010-03-12-custom-prod
8) ALIROOT/v4-18-Rev-05	

While the BASE, DEFINITION are the basic modules for HLT cluster software operations and the interface between HLT and other online systems are maintained by the TAXI, PENDOLINO, ECSPROXY, HCDBMANAGER. The DATATRANSPORT and CONTROL modules constitute of the online data transport framework. The rest of the modules comprise the HLT analysis part.

In online analysis the data exchange between the different components and different computer nodes are defined in a configuration file of XML file format. A typical data transport configuration used for online testing is listed in 5.6.

Listing 5.6: XML Configuration file for PbPb test

```
<?xml version="1.0" encoding="ISO-8859-1"?>
<SimpleChainConfig2 ID="DIMUON" verbosity="0x30">
  <infoblock>
    <author>indra</author>
    <date>Friday 12 February 2010</date>
    <description>Full Tracker chain for Dimuon</description>
  </infoblock>
  <ALICE>

    <!-- <Sources type="ddl"> -->
    <Sources type="file">

      <!-- TEMPLATE BEGIN -->
      <DDL>DIMU</DDL>
      <Directory>/tmp/HIJING-4000/raw*</Directory>


    </Sources>

    <FilePublisherOptions>-eventtime 333</FilePublisherOptions> <!--
    333 corresponds to  3 kHz-->
    <RORCShm blocksize="50k" blockcount="100"/>

    <DIMU>
      <TRG>
        <Partition>
          <Component ID="TrigRec">
            <ComponentID>MUONTriggerReconstructor</ComponentID>
            <Options>-ddlid \${DDL} -bfieldintegral 3 -cdbpath
            local://\${ALIHLT\_HCDBDIR} -suppress_partial_triggers
            -tryrecover -dontprintwrongeventerror </Options>
            <Parent>DDL</Parent>
```

```
33              <Shm blocksize="2k" blockcount="1000"/>
34              <Multiplicity>2</Multiplicity>
35              <Library>libAliHLTMUON.so</Library>
36            </Component>
37          </Partition>
38        </TRG>
39
40
41        <TRK>
42          <Partition>
43            <Component ID="HitRec">
44              <ComponentID>MUONHitReconstructor</ComponentID>
45              <Options>-ddlid \${DDL} -cdbpath
46              local://\${ALIHLT\_HCDBDIR} -tryrecover
47              -dontprintparityerrors</Options>
48              <Parent>DDL</Parent>
49              <Shm blocksize="5k" blockcount="1000"/>
50              <Multiplicity>2</Multiplicity>
51              <Library>libAliHLTMUON.so</Library>
52              <ForceFEP/>
53            </Component>
54          </Partition>
55        </TRK>
56
57        <Process ID="Merger" type="prc">
58          <Command>Relay</Command>
59          <Parent>TrigRec</Parent>
60          <Parent>HitRec</Parent>
61          <Multiplicity>1</Multiplicity>
62          <Shm blocksize="6k" blockcount="5000"/>
63        </Process>
64
65        <Component ID="Tracker">
```

```
66          <ComponentID>MUONFullTracker</ComponentID>
67          <Options>-cdbpath local://\${ALIHLT\_HCDBDIR}</Options>
68          <Parent>Merger</Parent>
69          <Shm blocksize="2k" blockcount="5000"/>
70          <Multiplicity>27</Multiplicity>
71          <Library>libAliHLTMUON.so</Library>
72        </Component>
73
74        <Component ID="Decision">
75          <ComponentID>MUONDecisionComponent</ComponentID>
76          <Options>-lowptcut 1 -highptcut 2 -lowmasscut 2.5 -highmasscut
77          7 </Options>
78          <Parent>Tracker</Parent>
79          <Shm blocksize="2k" blockcount="5000"/>
80          <Multiplicity>1</Multiplicity>
81          <Library>libAliHLTMUON.so</Library>
82        </Component>
83
84
85        <Component ID="MuonTrig">
86          <ComponentID>MuonSpectroTrigger</ComponentID>
87          <Options>-triggerhits</Options>
88          <Parent>Merger</Parent>
89          <Shm blocksize="2k" blockcount="5000"/>
90          <Multiplicity>1</Multiplicity>
91          <AddLibrary>libAliHLTMUON.so</AddLibrary>
92          <Library>libAliHLTTrigger.so </Library>
93        </Component>
94
95        <Component ID="MuonESD">
96          <ComponentID>MUONESDMaker</ComponentID>
97          <Options>-makeonlyclonesarray</Options>
98          <Parent>Tracker</Parent>
```

```
99          <Parent>Merger</Parent>
100         <Shm blocksize="2k" blockcount="5000"/>
101         <Multiplicity>1</Multiplicity>
102         <Library>libAliHLTMUON.so</Library>
103       </Component>
104
105     </DIMU>
106
107     <Component ID="GlobalTrigger">
108       <ComponentID>HLTGlobalTrigger</ComponentID>
109       <Options></Options>
110       <Parent>DIMU/MuonTrig</Parent>
111       <Shm blocksize="2k" blockcount="5000"/>
112       <Multiplicity>3</Multiplicity>
113       <AddLibrary>libAliHLTMUON.so</AddLibrary>
114       <Library>libAliHLTTrigger.so</Library>
115     </Component>
116
117     <Component ID="GlobalESD">
118       <ComponentID>GlobalEsdConverter</ComponentID>
119       <Options></Options>
120       <Parent>DIMU/MuonESD</Parent>
121       <Shm blocksize="2k" blockcount="5000"/>
122       <Multiplicity>9</Multiplicity>
123       <Library>libAliHLTGlobal.so</Library>
124     </Component>
125
126     <Dump>
127       <Type>tcp</Type>
128       <Parent>GlobalESD</Parent>
129       <Parent>GlobalTrigger</Parent>
130       <Parent>DIMU/Merger</Parent>
131       <Parent>DIMU/Tracker</Parent>
```

```
132         <Parent>DIMU/Decision</Parent>
133         <AllEvents/>
134         <Node>cndimutrg19</Node>
135         <!-- needed to specify the port explicitly for display -->
136         <Port>49152</Port>
137       </Dump>
138
139   </ALICE>
140
141 </SimpleChainConfig2>
```

5.4.2 Benchmark Results of Online Trackers

The main motivation was to test the speed of the Full Tracker and it's comparison with the existing Manso Tracker. For this purpose, the configuration (see list 5.6) has been tested to reach at the speed of ∼1 kHz as this is the design goal of dimuon HLT for Pb-Pb run. It is to be noted that the data processing rate is limited by the slowest component of the chain. Therefore, in case of Full Tracker and Manso Tracker chain the performance was slowed down due to the Full Tracker and MUONHitReconstructor component, respectively. The data processing rate of the trackers are reported in tables 5.8 and 5.9.

The stability of the dHLT chain has been individually checked for both the of trackers with HIJING 4000 and real p-p data set (Run : 104867) for ∼23 hours and no connection error problem or memory leaks has been found.

The monitoring of the processor, memory and network load during the data processing is important to understand the behavior of the components. An interesting phenomena is observed from above results. A falling trend is found for input to output

Table 5.8: The results of online performance test with HIJING 1000,2000,4000 particle generators of ALICE. (Bytes/s)

HIJING-1000

Components	Nof. Proc.	Input	Output	I/O	Speed (Hz)
HitRec	2	2356752	289488	8.14	
TrigRec	2	3920384	29080	134.8	
MansoTracker	1	10770140	68004	158.37	1518.7
FullTracker	3	6053463	202092	29.95	1015.8
FullTracker (-usefast)	1	8482980	235232	36.06	1578.25
Decision	1	197716	75732	2.61	
MuonESD	1	276068	266625	1.04	
MuonTrig	1	6177120	360584	17.13	

HIJING-2000

Components	Nof. Proc.	Input	Output	I/O	Speed (Hz)
HitRec	2	2163968	431504	5.01	
TrigRec	2	4366336	98528	44.32	
MansoTracker	1	20743172	171132	121.21	1537.08
FullTracker	7	13794396	531188	25.82	1072.96
FullTracker (-usefast)	1	17706308	502260	35.25	1528.56
Decision	1	587396	118004	4.98	
MuonESD	1	691684	359597	1.35	
MuonTrig	1	13214472	359597	36.75	

HIJING-4000

Components	Nof. Proc.	Input	Output	I/O	Speed (Hz)
HitRec	2	2808000	900800	3.12	
TrigRec	2	3015168	159792	18.86	
MansoTracker	1	37964572	315784	120.22	1430.26
FullTracker	Processor Multiplicity 27 is required to run at the rate of 1kHz, which not available in dimuon node group. This has been tested with extra support of cnemcal nodes				
FullTracker (-usefast)	3	25222260	729396	34.58	1051.19
Decision	1	775952	131448	5.9	
MuonESD	1	1108532	756535	1.47	
MuonTrig	1	25241508	343147	73.56	

data size (I/O) ratio of the dHLT components from HIJING 1000 to HIJING 8000. This is expected since the number of tracks increases with particle multiplicity. But

Table 5.9: The results of online performance test with HIJING 6000 and 8000 particle generators of ALICE. (Bytes/s)

HIJING-6000

Components	Nof. Proc.	Input	Output	I/O	Speed (Hz)
HitRec	2	4292816	1817472	2.36	
TrigRec	2	3387904	179000	18.92	
MansoTracker	1	53250336	363528	146.48	1287.35
FullTracker	Not possible to test				
FullTracker (-usefast)	6	42754776	794640	53.8	1100.1
Decision	1	855356	154072	5.55	
MuonESD	1	1136676	710296	1.6	
MuonTrig	1	39724188	348411	114.01	

HIJING-8000

Components	Nof. Proc.	Input	Output	I/O	Speed (Hz)
HitRec	2	4408512	2350448	1.88	
TrigRec	2	8659456	851408	10.17	
MansoTracker	1	49116536	500456	98.14	1056.61
FullTracker	Not possible to test				
FullTracker (-usefast)	Processor Multiplicity 15 is required to run at the rate of 1kHz. But in that case none of the following components, (Decision, MuonESD, MuonTrig) can not be included due to present cndimuon nodes limitation to 16 processors.				
Decision	1	490936	350116	1.4	
MuonESD	1	1237992	834009	1.48	
MuonTrig	1	50566808	318472	158.77	

surprisingly, the I/O ratio for "MuonTrig" component, increases with multiplicity instead of falling down. To explain this, it is important to note that according to the configuration in list 5.6, the "MuonTrig" has been running with

option,

```
87 <Options>-triggerhits</Options>
```

It means that MuonTrig component issues a positive flag if any hit or track is found. In case of Pb-Pb collisions, there is large particle multiplicity in the detector,

```
= 2010-03-14 19:08:49+01:00 ============================================================
                          CPU    %user     %nice   %system   %iowait    %steal     %idle
cndimutrg19: 07:08:49 PM    all    17.62      0.00     17.27      0.00      0.00     65.11
cndimutrk19: 07:08:49 PM    all    18.51      0.00     25.49      0.00      0.00     56.00
fepdimutrg: 07:08:48 PM    all     8.46      0.00      9.47      0.00      0.00     82.07
fepdimutrk1: 07:08:49 PM    all    47.26      0.00      6.43      0.00      0.00     46.31
fepdimutrk2: 07:08:49 PM    all    65.68      0.00      8.00      0.00      0.00     26.32
fepdimutrk4: 07:08:47 PM    all    35.24      0.00      7.82      0.00      0.00     56.95
fepdimutrk5: 07:08:49 PM    all    35.64      0.00      5.98      0.00      0.00     58.38
fepspare0: 07:08:49 PM    all    26.00      0.00      5.84      0.00      0.00     68.16

= 2010-03-14 19:08:46+01:00 ============================================================
                       kbmemfree kbmemused  %memused kbbuffers  kbcached kbswpfree kbswpused  %swpused  kbswpcad
cndimutrg19: 07:08:45 PM   3161996  13298808     80.79    303448  11411340   7282680         0      0.00         0
cndimutrk19: 07:08:46 PM   1041008  15419796     93.68    217816  13507416   7282548       132      0.00         0
fepdimutrg: 07:08:46 PM   7597744   4735208     38.39    455968   3100832   4018168         0      0.00         0
fepdimutrk1: 07:08:46 PM    395220  11937732     96.80    512416   8088464   4018048       120      0.00       120
fepdimutrk2: 07:08:45 PM    132628  12200324     98.92    509380   8375292   4018048       120      0.00       120
fepdimutrk4: 07:08:46 PM    129768  12203184     98.95    498124   8176188   4018052       116      0.00       116
fepdimutrk5: 07:08:46 PM    114312  12218640     99.07    525620   8373140   4018168         0      0.00         0
fepspare0: 07:08:46 PM    113720  12219232     99.08    458148   8351108   4018168         0      0.00         0


= 2010-03-14 19:08:37+01:00 ============================================================
                          IFACE   rxpck/s   txpck/s    rxkB/s    txkB/s   rxcmp/s   txcmp/s  rxmcst/s
cndimutrg19: 07:08:36 PM     eth1 100237.25  54809.80 112818.95   4127.36      0.00      0.00      0.00
cndimutrk19: 07:08:37 PM     eth1 116995.05 146426.73  59827.06 117467.50      0.00      0.00      0.00
fepdimutrg: 07:08:37 PM     eth1   4409.45   5265.35    538.79   2359.00      0.00      0.00      0.00
fepdimutrk1: 07:08:37 PM     eth1   6237.84   8584.68    678.54   7328.81      0.00      0.00      0.00
fepdimutrk2: 07:08:37 PM     eth1  10224.00  13432.00   1015.89  12910.69      0.00      0.00      0.00
fepdimutrk4: 07:08:37 PM     eth1   6068.29   8536.59    626.26   7535.57      0.00      0.00      0.00
fepdimutrk5: 07:08:36 PM     eth1   8872.00  12351.00    847.48  11342.11      0.00      0.00      0.00
fepspare0: 07:08:37 PM     eth1   7339.00   9908.00    762.21   8524.34      0.00      0.00      0.00
```

Figure 5.8: The CPU Memory and Network Load has been monitored for HIJING 8000 using dmon (distributed monitoring) commands of HLT cluster. It is to be noted that fepspare0 was connected with the DDL links coming from the third muon tracking station as fepdimutrk3 was under repair during the test.

therefore, the MuonTrig issues positive signal more frequently.

The values of the processing rates of these tables (5.8 and 5.9) have been calculated using the "StatusDump" command of data transport framework. In addition, there are commands to monitor CPU load, memory and network usage of cluster group, which are known as "dmon" (distributed monitoring). The monitoring results [see Fig. 5.8] with dmon commands during the execution of Pb-Pb chain test shows good agreement with the results from "StatusDump" command.

The average transmitted datasize from the five tracking front end processor is, $\frac{7328.81+12910.69+7535.57+11342.11+8524.34}{5} = \frac{47641.52}{5} = 9528.304$ kBytes/s. Whereas the StatusDump results show that, there are about 2350.448 kBytes/sec output from each of the HitRec component. Four such components are running on each dimuon FEP nodes (excluding the hits from third station since it does not contribute to the Trackers), which result to $4 \times 2350.448 = 9401.792$ kBytes/s. For TrigRec components also they are of same order.

To summarize it can be concluded, that,

- The full tracker can run at 1kHz rate and scales with the processor multiplicity.
- The stability of the chain (with both trackers) has been tested for long time with clear startup and clean shutdown.
- If the Full Tracker is planned to reconstruct the high multiplicity Pb-Pb collisions, eight more computing machines (i.e. 32 processors) are required to be added to the present Dimuon node group.

The analysis of the experimental data demonstrates the final validation of the online algorithms, which are presented in the next chapter.

Chapter 6

Experimental Results and Performance Study

This chapter describes the online performance of the dHLT algorithms during the comic runs and proton-proton collisions at 7 TeV energy of LHC. In addition, it contains the analysis techniques of the experimental data with the online algorithms in the offline mode. Since the development of online analysis framework and the integration to ALICE detector have evolved in parallel, each data set was analysed with different versions of dHLT components. For instance, the cosmic runs have been analysed with primary version of the Full Tracker whereas the 7 TeV data have been reconstructed with most updated versions of the Full Tracker.

The real-time performance of dHLT analysis components with the cosmic setup is discussed in the first section, whereas the p-p data analysis is reported in the second half.

6.1 Cosmic Runs of Muon Spectrometer

There were several cosmic data taking periods in ALICE before the first p-p collision, where each cosmic run period continued for about one to three months of data collection. The main goal of these cosmic setup was to test the stability of the detectors and online systems (HLT, DCS, DAQ and CTP) of ALICE. There was no physics proposal of ALICE with the set of cosmic runs, however, a group of central barrel detectors (ITS, TPC etc.) have used these cosmic tracks for the alignment of the detection elements. Thus, the two magnets (L3 and dipole) were off during these run period, except for the last one where dHLT did not join due to technical problem. In present section the Dimuon HLT analysis results are shown for two sets cosmic runs corresponding to partial and complete Spectrometer setup. In both cases, dHLT participated to the global data taking in a mode where HLT busy was respected by DAQ but no HLT output was sent to DAQ (i.e mode B/Test2 in ALICE experimental term [sec. §3.1.5]).

6.1.1 First Cosmic Run

The first online performance of the dHLT analysis chain with experimental data has been successfully tested in the cosmic run period during February-March of 2008. It is to be noted that the Muon Spectrometer was not fully operational in that cosmic run and only the first two Tracking stations were ready along with only the right half of the Trigger stations. Although the trigger was issued by the full trigger station but the hit information from the left side was not available. Since the Full Tracker was not integrated to the framework and the Manso Tracker could not be applied due to the absence of 4^{th} and 5^{th} Tracking station, the dHLT online analysis was configured with,

$$\text{DDLPublisher} \Longrightarrow \text{Hit Reconstruction} \Longrightarrow \text{TCP Dump} \Longrightarrow \text{EventDisplay}.$$

Apart from the first real-time performance of dHLT analysis, the main achievement of first cosmic run was the development of the online event display with AliEve. A snapshot of one typical cosmic event is shown in Fig. 6.1. The cosmic runs were mainly

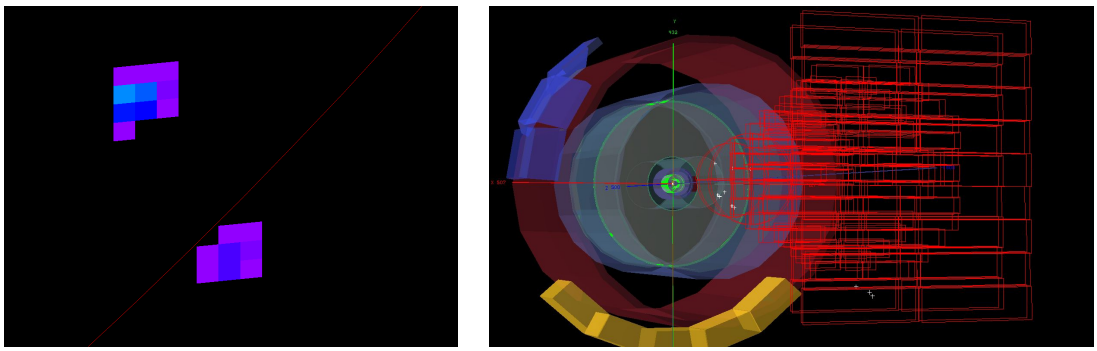

(a) Online display of clusters (b) Online display of track during the first cosmic run

Figure 6.1: An online event display of cosmic run

triggered by the ACORDE (placed on the top of L3) trigger and very few runs have been recorded with the Muon Trigger. As the Muon Spectrometer is placed along the horizontal direction, it receives very few cosmic tracks due to substantial earth payload. In addition, the tracks triggered by ACORDE were mostly limited within the L3 region, very few slant tracks were recorded in the first two tracking stations of Muon Spectrometer. Thus, a typical trigger rate of ∼0.1 Hz was observed with Muon Trigger, whereas for ACORDE it was ∼100 Hz. A total of ∼8800 events passed through the dHLT chain when summed over all runs.

The First Cosmic Track

The first slant muon track with ACORDE trigger was observed in Run 23549 on the first March of 2008 [Fig. 6.2(a) and 6.2(b)]. It was an important achievement of the cosmic run period, since it confirmed that all hardware components and all

online software components of the detectors are functioning as expected.

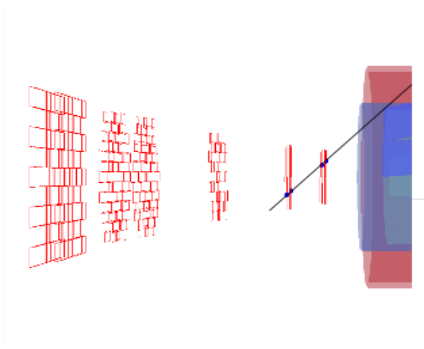

(a) Side View

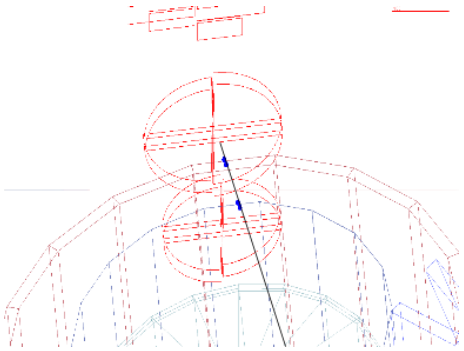

(b) Top View

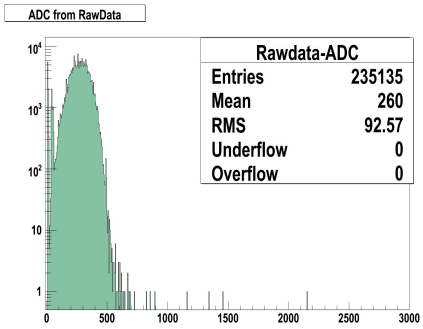

(c) Rawdata distribution in ADC unit (x-axis)

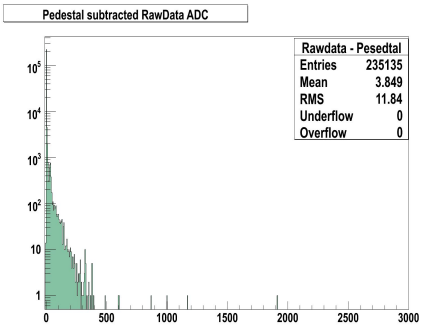

(d) Pedestal subtracted rawdata distribution in ADC (x-axis)

Figure 6.2: The first cosmic track observed in Muon Spectrometer from Run 23549 has been shown in (a) and (b). The following two sub-figure (c) and (d) show the charge distribution and pedestal distribution of the run containing the first track, respectively.

The track has been found by the offline analysis of data with online algorithms. To achieve this, the data of the online dHLT analysis chain has been stored by TCP-Dump component. These were then collected and analysed in offline mode to produce the ADC histogram and pedestal subtracted ADC histogram as shown in Fig. 6.2(c) and 6.2(d), respectively. In the next stage the events were selected based on a threshold cut on charge per cluster basis. The final set of events were sequentially displayed and analysed using AliEve. Thus, the zeroth level of study has been carried out to find the first track in Muon Spectrometer.

The first horizontal track through the Muon Tracking and Trigger station [see Fig. 6.3(a)] was found in run 24841 on third day of March, 2008, two days after the first track.

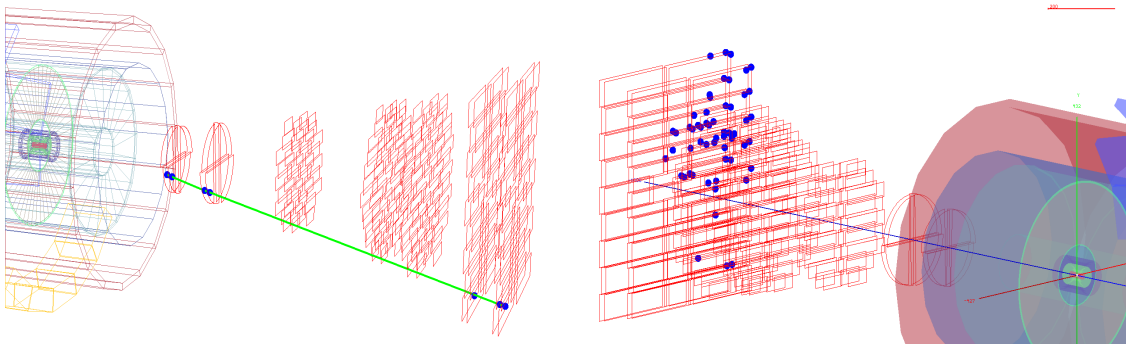

(a) The first track through the Muon Tracking and Trigger detectors

(b) A Cosmic shower event

Figure 6.3: The first cosmic full track together in the Muon Trigger and Tracking stations (Run 28841) and a snapshot of very frequent cosmic shower events.

Online Detector Diagnostics

In the cosmic run the dHLT was running with simplest analysis configuration. But even that short configuration was very helpful for the online diagnostics of detectors. Some of the interesting observations are listed below :

- **Cosmic shower :** It was found (HLT event-display) during the experiment that the upper part of Muon Trigger detector often had large number of hits. These were due to the large cosmic shower events. An online screen-shot of such event is shown in Fig. 6.3(b).

- **Sudden malfunctioning due to pedestal shift :** It was observed few times, that after long period of normal operation, the zero suppression for a certain bus patch would fail leading to large data size. Such a scenario is shown in Fig. 6.4(a) and 6.4(b). However, it went back to normal operation again in the

next run. In the later analysis it was found that, the problem occurred due to pedestal shift.

- **Hot spot :** A hot spot on a detection element are some specific channels which becomes noisy over different runs. It was found that a hot spot did not necessarily stays noisy in every the subsequent runs but reappeared over and over again throughout the entire cosmic data taking period. One such behaviour for MANU 1122 of buspatch 728 is shown for run 25910 and 25915 in Fig. 6.4(c) and 6.4(d), respectively. This was traced to a faulty MANU card in the readout chain.

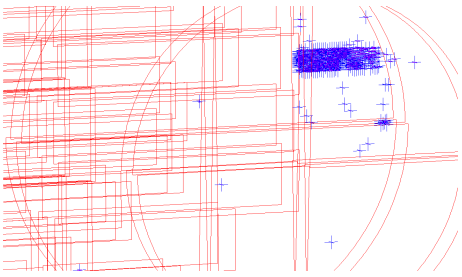

(a) Sudden malfunctioning of part of detector with normal noise cut on data

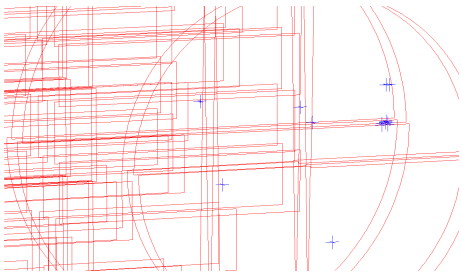

(b) Sudden malfunctioning goes away with extra 10 ADC channel noise cut on top of conventional noise cut

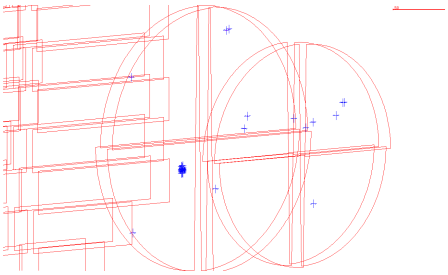

(c) Hot spot on a part of detector (Run 25910)

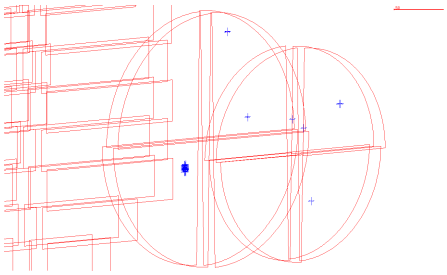

(d) Hot spot on a part of detector (Run 25915)

Figure 6.4: The dHLT serves as an online monitor for detector problems.

In this way, the first online performance of dHLT analysis established itself an excellent detector monitoring tool for quick and fast detector diagnostics.

Data Analysis of Cosmic Runs

At the end of the cosmic run period a selected set of "good runs" (as defined by Muon Run Coordinator) have been analysed with the online algorithms in offline mode. In the first step the raw-data has been decoded and processed to produce the hit points in station 1 and 2 using the dHLT Hit Reconstruction algorithm. The hit points were then joined to form the track using to Cellular Automaton (CA) method. It has been explained in the appendix that the CA first creates the tracklets (connected hit points in consecutive chambers of a station), which are later joined to form a complete track. Thus, the tracks have been grouped in two categories, the tracks with two tracklets out of possible three (trigger tracklet, tracklets in first and second stations) are called general tracks, whereas the tracks with all three tracklets are called golden tracks.

Table 6.1: Run statistics table for cosmic data analysis

Run	Events	Hit Rec. able Events	Shower Events	Tracks	Golden Tracks
26024	508	392	184	24	11
25985	2209	1628	795	72	6
25960	846	661	316	39	17
25954	65	42	15	6	3
25944	129	100	51	5	2
25915	805	591	270	31	10
25911	209	166	83	12	6
25910	15	11	3	1	0
25898	792	584	290	24	4
25862	331	252	123	1	0
25836	1326	1003	471	10	5
25821	1014	733	339	4	2
25793	263	190	104	9	0
24943	72	0	0	0	0
24925	166	120	64	6	2
24841	16	16	0	3	2
total	8766	6489	3108	247	70

The summary of the results are tabulated in 6.1. The third column gives the

number of events for which hit reconstruction could be achieved (i.e. 6489) in station 1 and 2, out of 8766 trigger from the Muon Trigger station. It is also evident from the table that ∼48% of the reconstructable events is contaminated with the cosmics shower, where a cosmic shower event have been defined as the event with more than 8 hits in the Muon Trigger stations. The third and fourth column reveal that for each run the number of shower events are almost half of the number of reconstructable events. This is due to the fact that half of the hit position readout of Trigger stations was not functional. Thus if the Trigger station was fully operational during the cosmic run in terms of hit position and trigger readouts then, the results of third and fourth column would have been the same. The number of horizontal tracks were very rare which is reflected in the fifth column of the table that shows that only 3.8% of the reconstructable events form general tracks. The number of golden tracks are even fewer, about 1% of the reconstructable events are found to contain a golden tracks.

A super imposed picture of all these tracks is shown in Fig. 6.5. It is interesting to note from the figure that the number of tracks in the upper half of the Muon Spectrometer is much less than the lower part. Since the earth payload is much more at the bottom compared to the upper part of ALICE, it is reasonable to assume that all the recorded tracks were originated from top surface of ALICE cavern. For this reason fewer tracks have been observed in the upper half of the spectrometer. Thus, the tracks originating from top-right (Fig. 6.5(b)) entered the spectrometer from the front while these originating from top-left entered from the back side. But there is a predetermined hardware delay between the first and second trigger stations which takes into account the flight time of the muons to traverse the distance of 1 m. Due to this delay, there is a inherent bias of trigger matching for tracks coming from the front side.

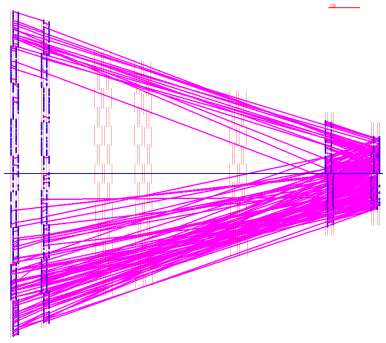

(a) Track superposition side view

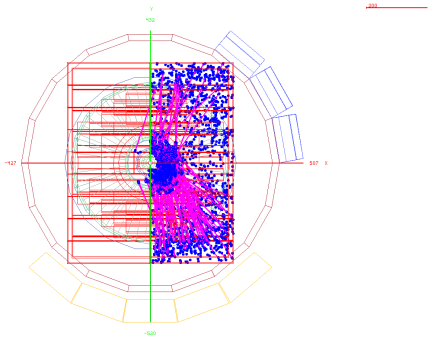

(b) Track superposition front view

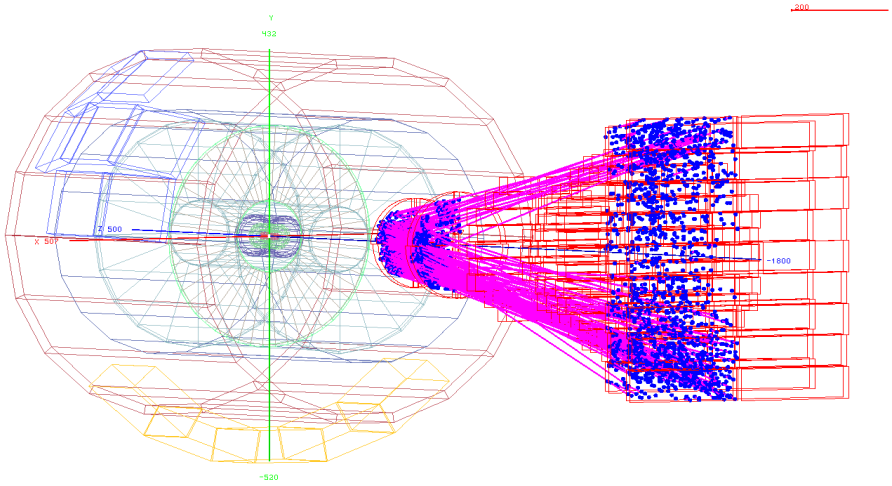

(c) Track superposition angle view

Figure 6.5: The superposition of all available cosmic tracks of the first cosmic run.

6.1.2 Second Cosmic Run

The next cosmic run period took place during the March-April of 2009, when the dHLT components and most of the Muon Spectrometer (except the problems with few buspatches of chamber 9 and 10 of the Tracking stations) was fully operational. The dipole magnet was off during the data taking therefore the physics analysis was not possible. However, on the HLT side, the full analysis chain have been switched on with DDLPublisher $\Longrightarrow$ Hit Reconstruction $\Longrightarrow$ Manso Tracker $\Longrightarrow$ MuonDecision $\Longrightarrow$ TCP Dump $\Longrightarrow$ EventDisplay. This was important to test the online performances

of the code with real data from all the tracking stations and real-time problems.

The dimuon HLT operation was stable during this global data collection. In these runs dHLT included the online histograms of charge per cluster and number of fired pads per cluster to the online display. It has been explained before (sec. §5.2.3) that these plots are important to investigate the cluster size and the cluster charge, which reflects the high voltage characteristics of the detector. Therefore, the plots were helpful for online data quality monitoring of the detector. A sample histogram set for run 67303 is shown in figure 6.6.

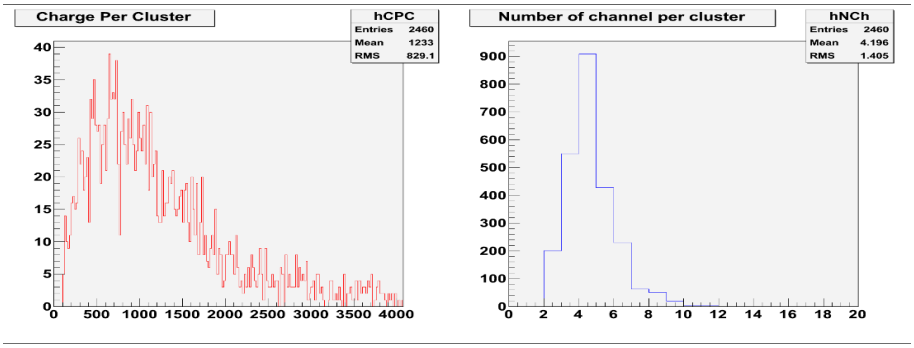

Figure 6.6: The distribution of charge per cluster (left) and number of pads per cluster (right) summed over all chambers displayed at ACR during the cosmic run.

Cosmic Run Analysis

The cosmic data have been replayed again for offline analysis with the online algorithms, which included both approaches of Manso Tracker and straight line tracking with Cellular Automata. A total of 73 selected cosmics runs have been analysed following the same procedure as described in the previous subsection. In order to analyse the data with CA, it was updated to include tracklets in the fourth and fifth station during formation of a track. Therefore, the definition of general and golden track has been modified compared to the first cosmic run period.

General Track : 1 tracklet in station 1 or 2 + 1 tracklet station 4 or 5 + 1 tracklet

in Muon Trigger stations

Golden Tracks : 3 tracklets in Muon Tracking stations + 1 tracklet in Muon Trigger stations

One general and one golden track is shown in Fig. 6.7(a) and 6.7(b), respectively. In total 71557 events have been analysed from 73 runs, which contains 1986 general tracks and 1009 golden tracks. The charge distribution and size of the associated clusters with the general tracks is shown in Fig. 6.7(c). The shape of the charge per cluster histograms closely follow the Landau distribution which is the property of minimum ionising particles. A super position of general tracks from 5 runs are shown in Fig. 6.8.

It is important to note that there were no Cosmic Run analysis results with offline software when the first analysis with dHLT algorithm was reported in the ALICE Offline Week [April, 2008]. However, in the second Cosmics Run both groups (dHLT and Muon Offline) had presented their results separately in Annual Muon Spectrometer Workshop [June, 2009]. But since the two collaborations have followed different approaches for tracking and data analysis techniques, the offline and dHLT results could not be compared. In addition, there were no physics observables due to absence of dipole magnet.

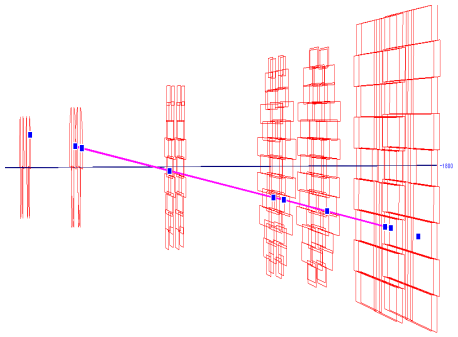

(a) A general track

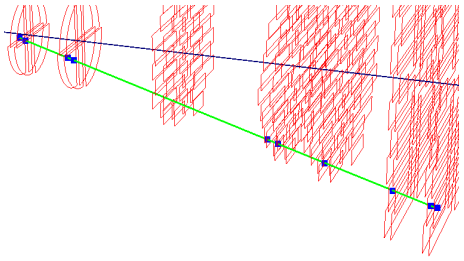

(b) A golden track

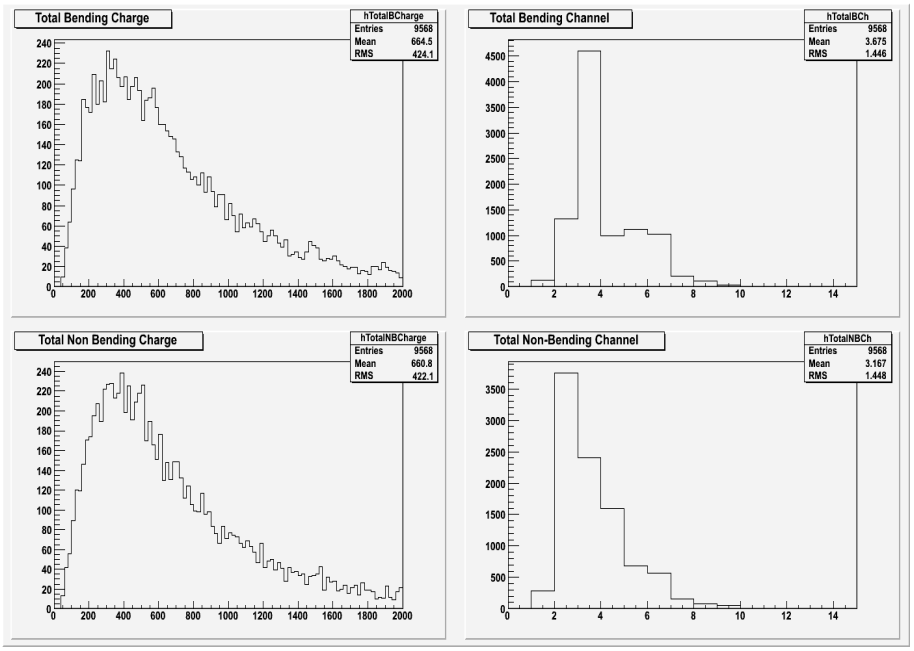

(c) The charge per cluster and pad per cluster distribution associated with general tracks

Figure 6.7: The results of offline analysis using online algorithms.

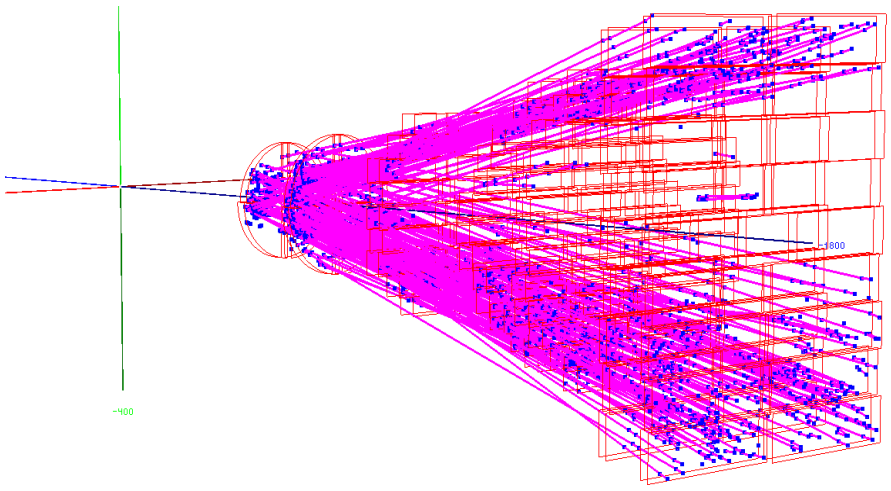

Figure 6.8: The superimposed tracks of the five runs in second cosmic run.

6.2 pp Colliding beam at Center of Mass Energy $\sqrt{s}$=7 TeV

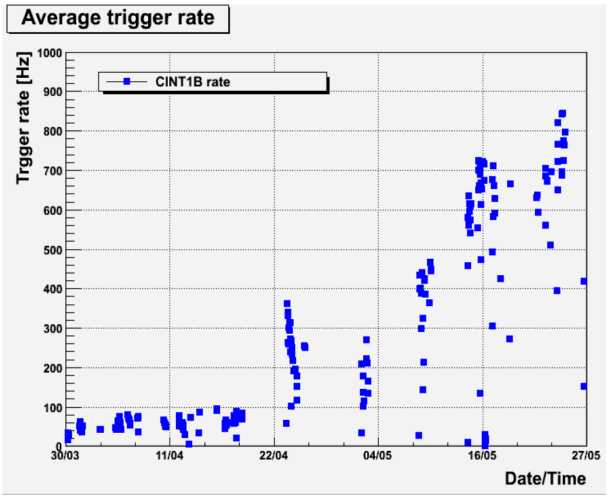

Figure 6.9: The interaction trigger rate as seen by ALICE during April-May,2010.

The most updated version of the Full Tracker analysis code was integrated to the HLT online framework before the proton-proton (p-p) collision at 7 TeV energy. The run period of March-May of 2010 was covered with a dHLT configuration of, DDLPublisher $\Longrightarrow$ Hit Reconstruction $\Longrightarrow$ Full Tracker $\Longrightarrow$ MuonDecision $\Longrightarrow$ MuonESD. A copy of MuonESD was sent to the DDL output, which was connected DAQ, and another copy was sent to TCP-Dump for the event display. In the p-p collisions, the HLT was running in a mode where the ESD output was sent to the DAQ but no HLT triggering decision was provided (in ALICE technical term "HLT mode B"). The ESD output of HLT was finally written to the disk along with the rawdata.

It is to be noted that, the above configuration have been presented in its' simplest form. The real-time HLT configuration was more complicated with interconnections of different detectors (e.g. ITS, TPC, TRD, EMCAL, PHOS etc.).

It was observed, that interaction trigger rate (minimum bias) had gradually increased from 100 Hz to 900 Hz over the month, as shown in Fig. 6.9 and accordingly, the Muon Trigger rate went from 10 Hz to 40 Hz. During the p-p collision, there was one critical problem to be reported. The Muon Trigger station had implemented the calibration events (also known as scaler events [sec. §2.4.3]) related with trigger electronics calibration after every 30 seconds in between the physics run. This feature was not present during the cosmic run, and therefore, it had generated a problem in the data taking with dHLT components. After suitable modification in the online code these events were skipped. An online Full Tracker display during the p-p run at ACR has been shown in Fig. 6.10.

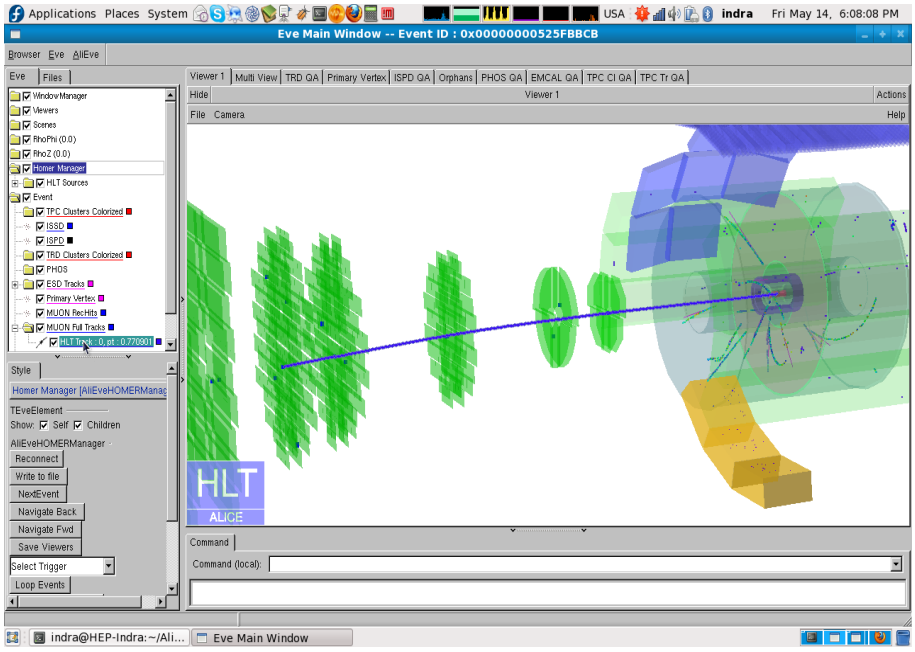

Figure 6.10: First online full track as observed in run 119842.

The other online histograms and the future quality assurance (QA) plots have been discussed in the following section. The final validation based on dHLT and offline analysis using the experimental data stored in GRID, has been described in the subsequent subsection.

6.2.1 Online Event Display

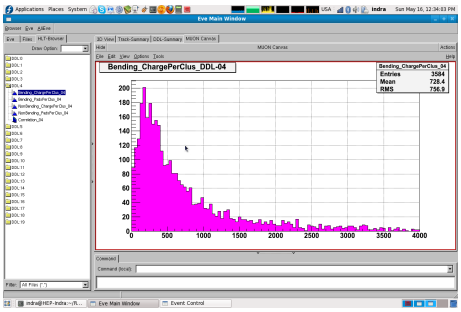

(a) The charge per cluster distribution

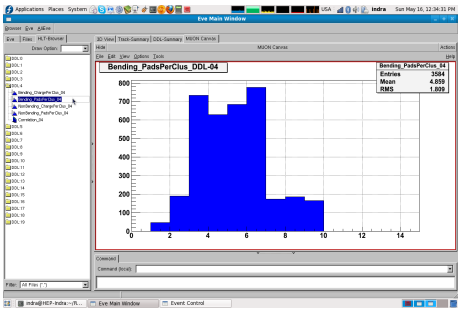

(b) The distribution of number pads per cluster

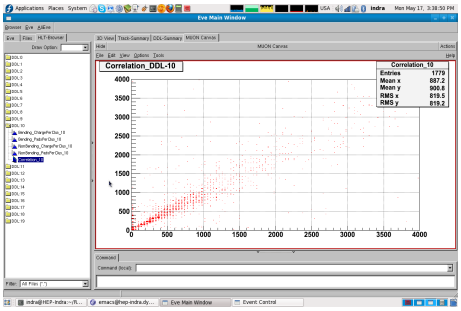

(c) The charge correlation of bending and non-bending plane

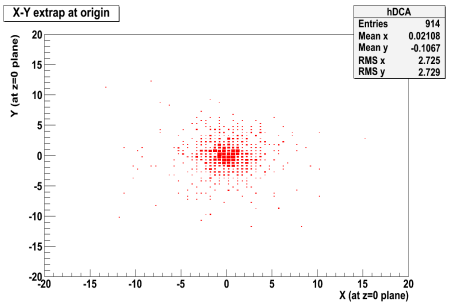

(d) Distance of Closest Approach (DCA)

Figure 6.11: The HLT online Quality Assurance (QA) plots at ACR during the p-p collision at $\sqrt{s}$=7 TeV.

The online event display for p-p run was improved to include the histograms to check the quality of the run and preliminary physics results. A description of the online histograms are summarised in the following items.

- **Charge per cluster :** The charge per cluster distribution has been ported to the display for each plane of a given DDL. It is to be noted that in the last cosmic there was an inclusive spectrum summed over all DDLs. The role of these plots have already been discussed before (sec. §5.2.3). An improper setting of the detector high voltage (possible fault in DCS) or the presence of copious noisy clusters can be identified from these plots [see Fig. 6.11(a)].

- **Pad per cluster :** This plots have also been displayed for every single plane of

a given DDL and the role of these plots has been discussed before (sec. §5.2.3) as well [see Fig. 6.11(b)].

- **Ratio of the bending to non-bending charge :** The ratio of charge per cluster of bending to non-bending plane should be close to unity, since the two cathodes are equidistant from the anode plane. This was found to be true for all detection elements for most of the clusters. But if in a DDL, there is a significant departure, it will indicate a readout error (may be due to trip in low voltage supply) for either bending or non-bending plane. The charge correlation plot have been discussed before and presented with the simulation results (sec. §5.2.3). The experimental correlation plot of individual DDL and summary of all DDLs are shown in Fig. 6.11(c) and bottom-left figure of 6.12, respectively.

- **Total charge per data link :** In experiment it is cumbersome to look into every single DDLs, thus several summary plots have been produced. One such summary plot shows the total charge distribution for all DDL connections in top-left of Fig. 6.12.

- **Trigger type :** This histogram shows the trigger types of the event as selected by the Trigger station. The possible values are, single low $p_{\rm t}$, single high $p_{\rm t}$, unlike sign low $p_{\rm t}$, unlike sign high $p_{\rm t}$, like sign low $p_{\rm t}$, like sign high $p_{\rm t}$ [see bottom-right of Fig. 6.12]. If the a track is identified by trigger chamber the associated trigger type will be displayed in this histogram.

- $p_{\rm t}$ **spectrum :** The inclusive transverse momentum of the tracks detected by dHLT Tracker are shown in this spectrum. The top-left histogram of Fig. 6.13 shows the online $p_{\rm t}$-spectrum as calculated by Full Tracker.

- **Clusters of the track :** The number of clusters associated with the

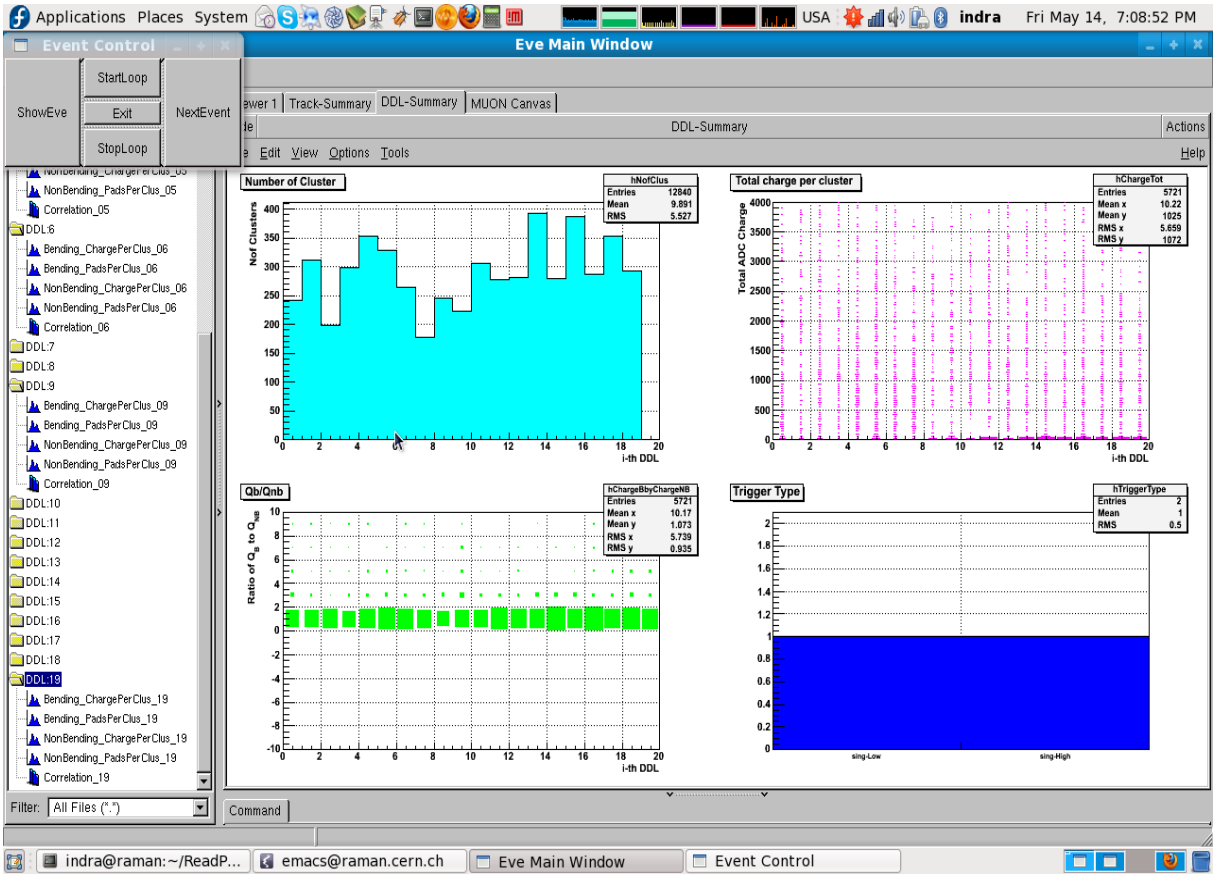

Figure 6.12: Summary of distribution of charge/cluster, pads/cluster and ratio of bending to non-bending charges in twenty individual DDLs. The type of trigger issued by trigger station is shown in the lower right corner. The HLT online plots in the p-p collision at $\sqrt{s}$=7 TeV.

reconstructed tracks are shown in this histogram [see top-right histogram of Fig. 6.13]. In case of Manso Tracker and Full Tracker this is limited to four and eight, respectively.

- **Vertexing :** Since in dimuon HLT a parametrised calculation is performed to include the Muon Absorber effect in case of Full Tracker method, a zeroth level of vertex histograms have been produced. It shows the distance of closest approach of tracks to the vertex at the z=0 plane [see Fig. 6.11(d) and bottom-left figure of snapshot 6.13]. Similar online display of vertex distribution for p-p collision at $\sqrt{s} = 900$ GeV has been reported in Ref. [1].

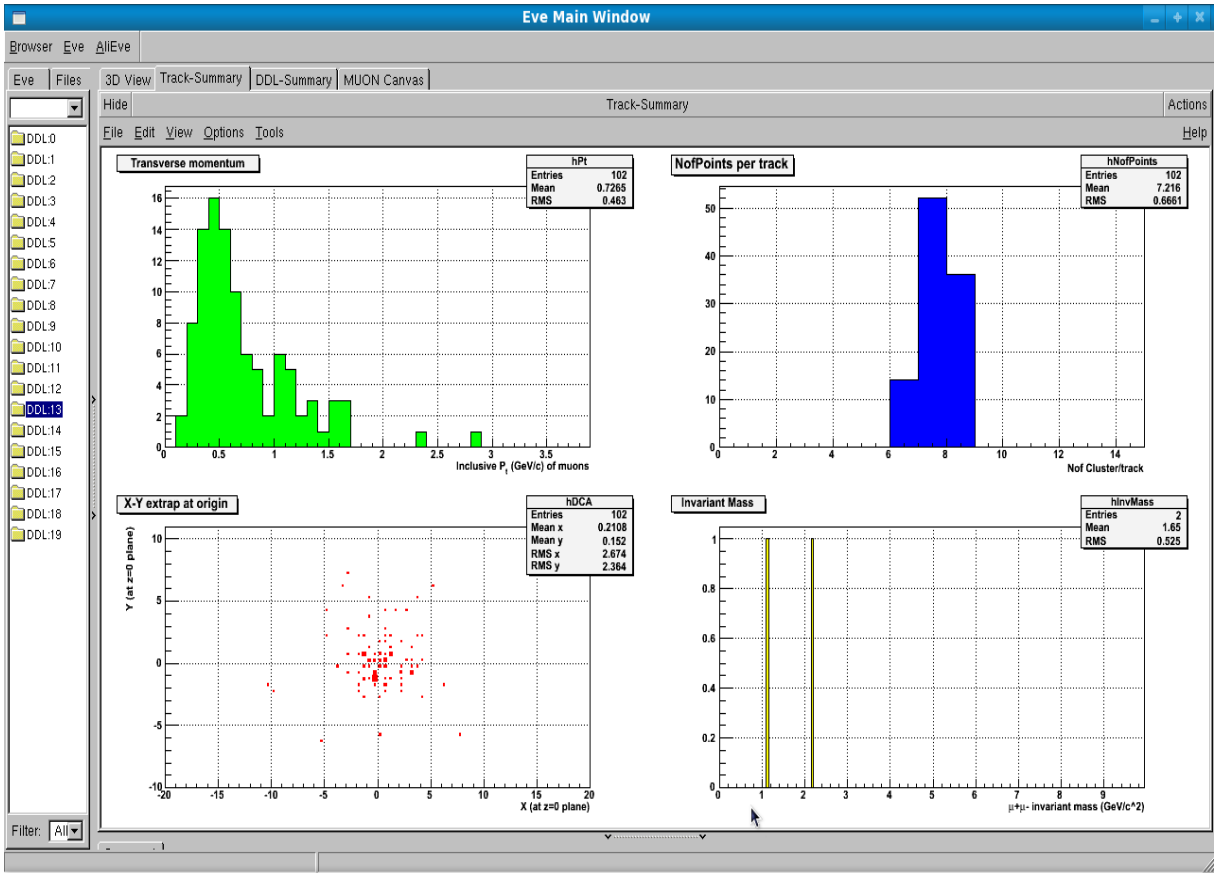

Figure 6.13: The HLT online track summary plots at ACR during the p-p collision at $\sqrt{s}$=7 TeV. The sub-figures, clock-wise from the top left, are inclusive p_{t} spectrum, number of clusters in track, dimuon invariant mass distribution and vertex distribution.

- **Invariant mass plot :** As the final result of the dHLT online analysis the invariant mass plot have been produced. This is again a preliminary plot, which does not include any efficiency or acceptance correction [see bottom-right of Fig. 6.13].

6.2.2 Muon QA plots from HLT

The appreciation of these HLT QA plots in the Muon Spectrometer community has opened a possibility to publish them as Muon QA plot in future data taking. Therefore, a set of histograms for run 120003 at 7 TeV energy, are shown in Fig. 6.14,

which are proposed to validate the quality of the experimental data for Muon Spectrometer using the results of dHLT online analysis. The two figures at the top represents the mean value of charge per cluster histogram for 20 tracking chamber DDLs for bending and non-bending cathodes. These plots reflect the gain of the individual half detector planes of the Spectrometer. It is evident from the figure that the chambers of second station (DDL number 5,6,7,8) had appreciably lower gain during this run. Thus, this QA plots can be used to fine tune the high voltage settings for individual quadrants so that there is a gain uniformity among different tracking planes of the spectrometer. However, since there are number of detection elements per DDL (2 for station 1 and 2 and 13 for station 3,4,5), it is not possible to identify if one of the high voltage setting has tripped or has stayed in BEAM-TUNE setting. This is because this element will not produce any charge cluster and the mean value of the charge cluster histogram will be filled with entries from detection elements which have the proper high voltage setting. Thus, in order to get a better QA, a third histogram has been proposed which shows the number of pad clusters for each DDL. It is interesting to note that although the gain of the chambers of second station was low, the number of identified pad clusters were large. This is possible as the average electronic noise for second station is quite low ($\sim$1.2 ADC channel). On the other hand it is interesting to note that the second DDL has less pad clusters although the gain of the chamber was substantially large. The fourth histogram is the overall QA for the individual tracking planes. It shows the number of pad clusters per DDL which has been associated with reconstructed tracks. This online histogram shows the power of online tracking for the Full Tracker. It is quite obvious from the histogram that all the planes participates uniformly in reconstruction of the tracks. Thus, this run, on the whole, was a physics validated run. It should be noted that in the present scenario, the Full Tracker does not includes the pad clusters of station 3. It is foreseen to include this station in near future, when the upgradation of the

dHLT resources will be completed.

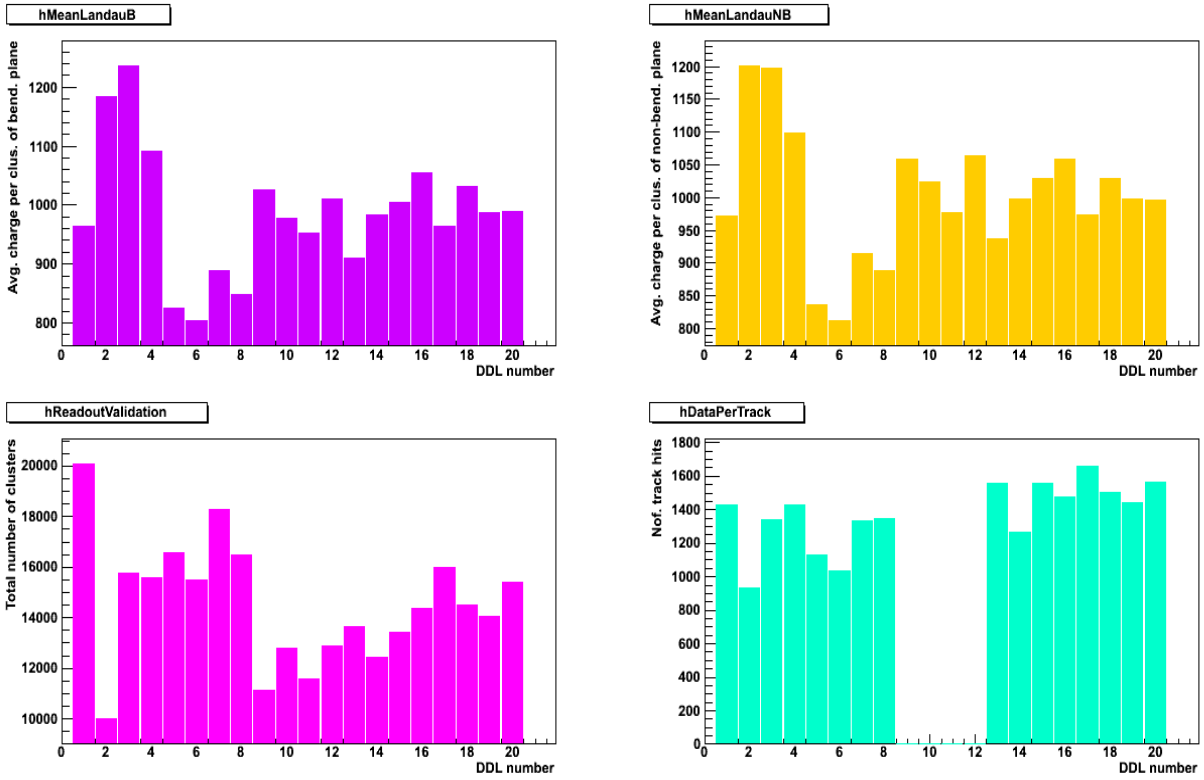

Figure 6.14: An proposed QA for Muon Spectrometer in future ALICE data taking has been prepared from the data of p-p collision of Run 120003 at 7 TeV energies. The plots along the clock-wise direction from top-left are, mean value of the Landau distribution of charge per cluster for bending plane, same for non-bending plane, number of the reconstructed hit points associated with track, the ratio of bending to non-bending per charge DDLs.

6.2.3 GRID Analysis and Comparison of the trackers

The analysis of the p-p data at $\sqrt{s}$= 7 TeV was motivated to test the quality of the dHLT triggering algorithm on experimental data set. Therefore, the analysis have been performed using the AliEn software on the data set stored in GRID. The AliRoot version "VO_ALICE@AliRoot::v4-20-04-AN" has been used for this purpose. In case of the offline results, the plots were produced by the PASS1 (first reconstruction of the real data) reconstruction of the corresponding data set.

This analysis have been carried out in two steps. At the beginning a set of 54 runs have been selected which have been tagged as "good" runs by Run Coordinator [see Tab. 6.2]. These runs were then reconstructed using the dHLT analysis tool, which have produced about 85,000 files corresponding to each rootified rawdata files of 54 runs, which contains the ESD objects of dHLT muon tracks. In the next step the muon tracks from the offline ESD objects and dHLT ESD objects have been

Table 6.2: Table contains the list of runs analysed for pp collision at $\sqrt{s}$= 7 TeV

126097	126088	126087	126081	126078	126073	126008	126007
126004	125855	125848	125847	125844	125843	125842	125632
125630	125628	125296	125292	125186	125156	125139	125134
125131	125101	125100	125097	125085	125083	124608	124607
124606	124605	124604	124603	124600	124388	124380	124378
124374	124371	124367	124364	124362	124360	124359	124358
124355	124187	124186	124183	122375	122374		

compared for every single events. All calculations have been performed over GRID. The tracks statistics have been summarised in the following histograms.

- p_{t} **spectrum :** In the p-p data collection of 7 TeV, there were no hardware L0 trigger, in order to perform inclusive measurements. The event averaged p_{t} spectrum of the tracks that are validated by the Muon Trigger stations is shown in Fig. 6.15. This plot reflects the unique feature of Muon Spectrometer to measure the momentum of the particles upto very low p_{t} value.

- η **spectrum :** The angular distribution of the tracks are best described in terms of the pseudorapidity (η) distribution. Thus the event averaged η spectrum is plotted in Fig. 6.16.

- **Effect of p_{t} cut on Invariant mass plot :** It has been pointed out several times that the motivation of dHLT is to provide a better transverse momentum cut on the muon tracks to clean the backgrounds mainly coming from pions and

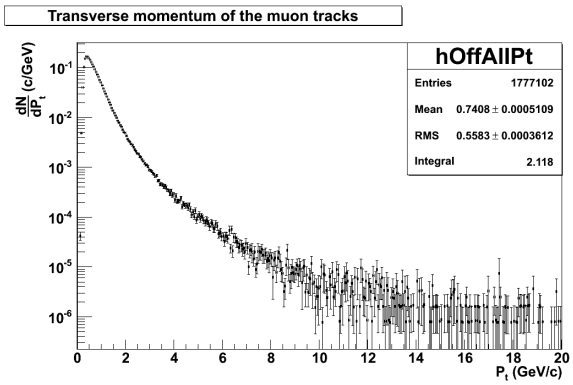

Figure 6.15: The p_{t} spectrum for all tracks validated by the L0 trigger (Event averaged)

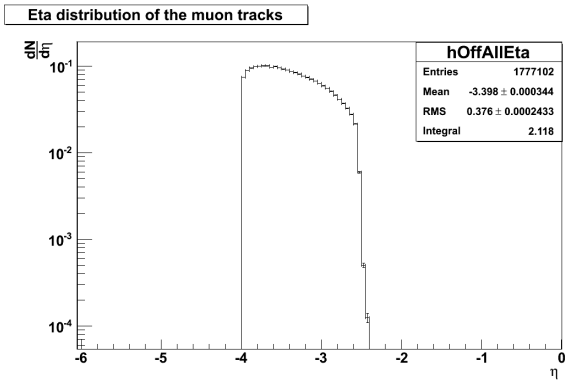

Figure 6.16: The η spectrum for all tracks validated by the L0 trigger (Event averaged)

kaons. Therefore, in the analysis it has been checked that if one or more muon pairs of opposite signs have found for a given event. If the p_{t} of the both of the tracks have been found to be more than certain cuts (0.5 GeV/c and 1.0 GeV/c) as calculated separately by dHLT and Muon Offline logic, the event was said to validated by dHLT and Muon Offline, respectively. The two p_{t}-cuts have been chosen to clean the invariant mass spectrum. It has been shown in the previous chapter that simulation supports a p_{t}-cut of 1 GeV/c to clean the background for central Pb-Pb collisions. But in the p-p collisions one does not know a priori the correct value of p_{t}-cut, thus another lower p_{t}-cut of 0.5 GeV/c

have been chosen. Once the event have been validated, in the next step the invariant mass spectrum was calculated and filled for the oppositely charged tracks to the corresponding histograms of dHLT and muon offline.

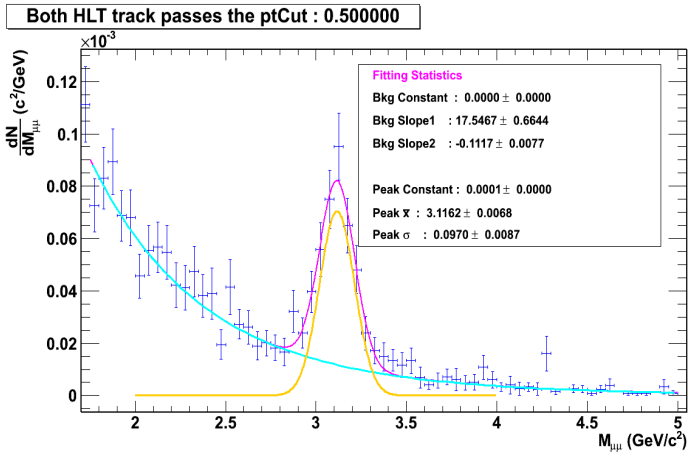

(a) Effect of dHLT trigger decision on mass spectrum for p_t-cut of 0.5 GeV/c

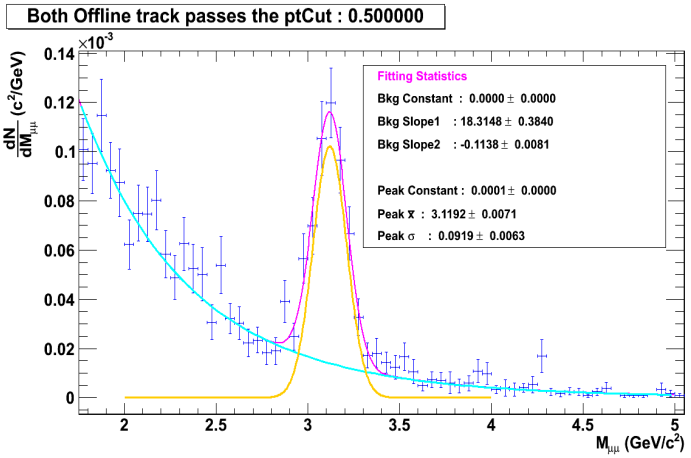

(b) Effect of Offline decision on mass spectrum for p_t-cut of 0.5 GeV/c

Figure 6.17: The effect of 0.5 GeV/c p_t-cut by dHLT and Offline reconstruction algorithms on reference experimental data set.

This can be explained better with an example. Suppose, for a given event, dHLT read the p_t of oppositely charged tracks pair as 0.7 GeV/c and 0.9 GeV/c then the event is said to be validated by the dHLT decision for 0.5 GeV/c p_t-cut but

not validated for the 1.0 GeV/c p_{t}-cut. It may happen that the p_{t} of that same pair of tracks have been found as 0.3 GeV/c and 0.4 GeV/c by offline analysis. In that case the event has not been validated by offline for both p_{t}-cut of 0.5 GeV/c and 1.0 GeV/c. Therefore only the invariant mass histogram of dHLT decision, corresponding to p_{t}-cut 0.5 GeV/c will be filled. Therefore, the trigger efficiency of online tracks can be compared with that obtained from detailed Offline reconstruction. The two invariant mass spectra, obtained from dHLT trigger and Offline reconstruction has been plotted for the p_{t}-cut of 0.5 and 1 GeV in Fig. 6.17(a),6.18(a) and Fig. 6.17(b), 6.18(b), respectively.

The Fig. 6.17(a) and 6.17(b) show clearly the J/Ψ peak but with substantial background from low momentum particles. The spectrums are clean when a 1.0 GeV/c p_{t}-cut is applied. The results of offline triggering and the dHLT trigger shows a reasonable agreement. It is found from Fig. 6.17(a) Fig, 6.17(b), Fig. 6.18(a) and Fig. 6.18(b), that there is a scope to improve the dHLT trigger to reach the J/Ψ resolution of offline.

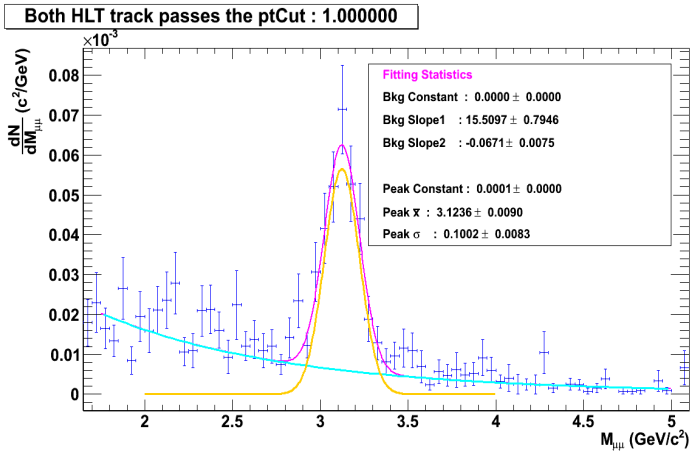

(a) Effect of dHLT trigger decision on mass spectrum for p_t-cut of 1.0 GeV/c

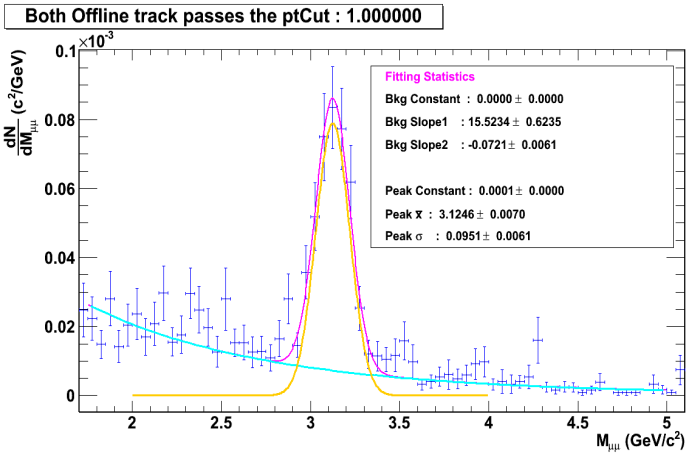

(b) Effect of Offline decision on mass spectrum for p_t-cut of 1.0 GeV/c

Figure 6.18: The ongoing analysis results show effect of 1.0 GeV/c p_t-cut by dHLT and Offline reconstruction algorithms on reference experimental data set.

6.3 Pb-Pb Colliding beam at $\sqrt{s}$=2.76 TeV/nucleon

The first Pb-Pb collision in LHC at $\sqrt{s_{NN}}$=2.76 TeV took place in the beginning of November of 2010. The dHLT chain was found to break when events with very large data blocks were transmitted. These events occured largely due to pedestal shifts in station 4 and 5 and led to the overflow of memory buffer. During 2011

shutdown, effort are being made to correct for this problem at hardware level. On the other hand the dHLT resources are being augmented which will allow more stable operation during the heavy ion run. Thus, the problem is expected to be solved in future runs involving Full Tracker. In the meantime, during the rest of Pb-Pb run of 2010, dHLT was operated with the partial tracker. It is to be noted that the successful execution of online HLT components in the highest possible primary charged particle multiplicity $\left.\frac{dN_{ch}}{d\eta}\right|_{\eta\leq 0.5} = 1584 \pm 4(stat.) \pm 76(sys.)$ [Ref. [2]] within 5% centrality marked new era of online computing. Since the dHLT validation for Pb-Pb collisions is still ongoing, only a snapshot of Pb-Pb collisions has been shown in Fig. 6.19

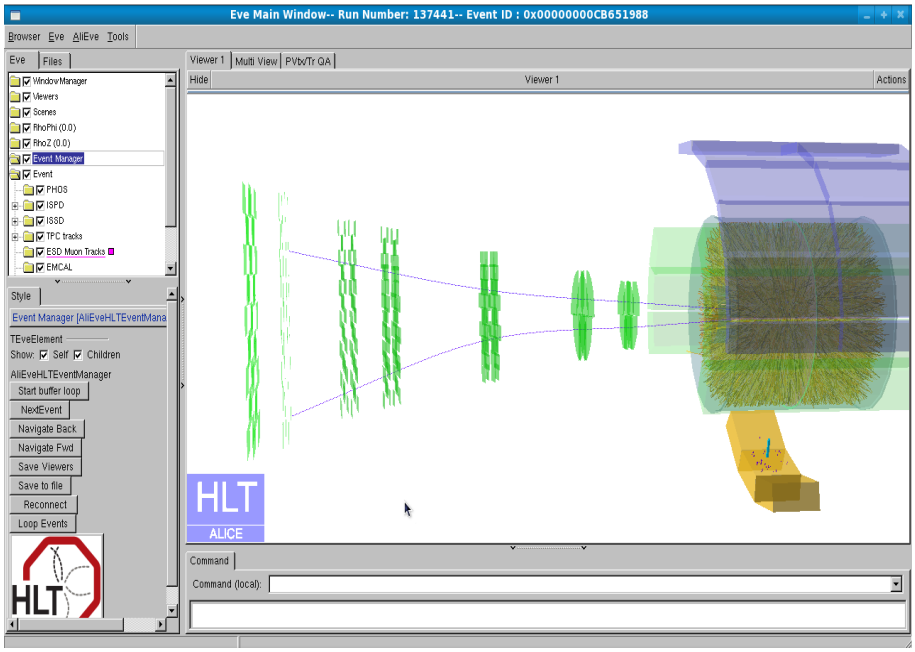

Figure 6.19: Online display of oppositely sign dimuon tracks during the Pb-Pb collisions at $\sqrt{s}$=2.76 TeV/A in Run 137441

Bibliography

[1] ALICE Collaboration, Eur. Phys. J. C (2010)65:111-125.

[2] ALICE Collaboration, arXiv:1011.3916v2 [nucl-ex].

Chapter 7

Summary

This chapter summarizes the motivation, development, implementation and final results of the present thesis work. The first chapter gives a description of the nucleus-nucleus collisions, which mimics early state of the universe few micro seconds after the Big Bang. The most exciting feature of heavy ion collision is to probe the expected formation of quark gluon plasma. The concept of phase transition of nuclear matter to quark matter has been discussed in the framework of standard model. This phase transition will be investigated in ALICE. Thus, the main physics observables of ALICE has been reviewed which includes the possible signals of hot quark matter.

An accurate identification of the QGP signals need detail data analysis and hence require proper understanding of detector components. Therefore, the following chapter focuses on the description of the ALICE detector with a special emphasis on Muon Spectrometer. In particular, the readout electronics and rawdata format have been explained in detail.

The need of online data analysis for ALICE has been highlighted in the third chapter and the High Level Trigger system has been described in detail. It has

been pointed out that the framework provides the possibility for processing the algorithms both in online and offline environments, without any change in the analysis components. Thus, the operational details of HLT in online and offline mode have been described. In the final part of this chapter some of the important Dimuon High Level Trigger processing components have been explained.

The core processing algorithms have been discussed in the fourth chapter, which are Hit Reconstruction and Full Tracking algorithms. The Hit Reconstruction algorithm has been explained in detail with its key features responsible for fast tracking. In case of Full Tracker algorithms, the different parts of the high performance tracking have been separately discussed in detail. The associated tuning parameters of the algorithms, as implemented in HLT framework have been described subsequently.

The testing and validation of the dHLT analysis algorithms with the simulated data set is the subject of the fifth chapter. The performance and quality of the Hit Reconstruction has been illustrated in the first part of this chapter. It shows that the detail offline clustering algorithm has bending resolution of $\sim$20 μm and the dHLT algorithm gives $\sim$33 μm. But most importantly, the Hit Reconstruction is more than 1000 times faster than the offline clustering process, which makes this fast algorithm better suited for online processing. The Full-Tracker also performs $\sim$100 times faster than the detail offline Kalman tracking method. This comes at a cost of 1.3 and 1.7 times worse p_{t} resolution at 1.0 GeV/c and 2.0 GeV/c, respectively. It is to be noted that the Manso Tracker can analyse data at a 10^4 times faster rate than offline, but resolution is worse by a factor of 3.7 and 4.1 at the given p_{t} values of 1.0 GeV/c and 2.0 GeV/c, respectively. The effect of these resolutions has been summarized in p_{t}-cut efficiency plot of Fig. 5.5, which shows that for both the p_{t}-cuts, the results of Offline Tracker and Full Tracker matches closely and provide better p_{t}-cuts compared

to Manso Tracking. The online validation of Full Tracker with the simulated data has been demonstrated in the last section of this chapter. These results are based on the exhaustive performance test of the complete dHLT analysis chain in the HLT cluster framework at CERN. It has been shown that the Hit Reconstruction and Full Tracker satisfies all the necessary conditions for high performance online analysis component.

In the sixth chapter, the online performance of the dHLT analysis chain has been discussed with experimental data. This is divided into two parts. In the first part the online execution of the dHLT components has been explained with the cosmic muon data set. In these cosmics runs dHLT played an important role for the online event display at ALICE control room. For instance, the first identification of the cosmic track in Muon Spectrometer has been announced by dHLT. The discrepancy between the tracks with positive and negative angles has been pointed out from the dHLT analysis, which was later understood as due to the predefined delay setup in the timing logic circuit of Muon Trigger station. In the second part of the chapter the LHC data of proton-proton collisions at 7 TeV energies has been analysed with the dHLT components and Offline method. Only the Full Tracker has been used for the p-p data analysis since the Manso Tracker already fails to achieve the sufficient tracking resolution with the simulated data. The dimuon invariant mass distributions with p_{t}-cut of 1 GeV/c show that the efficiency of offline and dHLT triggering closely matches. However, the dHLT triggering needs to be improved by 2.5% to reach the offline p_{t}-cut efficiency.

The HLT is still in developing stage and detail validation tests for each subdetector is foreseen by comparing the online histograms with the detail Offline reconstruction. Once this is achieved, HLT framework will be ready for the generation of rare physics triggers. It is to be noted that the CTP trigger logic is hard coded for individual trigger detectors of ALICE and is designed to collect as inclusive data

as possible. But since a large fraction of ALICE detectors participates in HLT framework, the various observables obtained from online reconstruction can be used to generate rare physics stamps for particular events.

In this regard, the p_{t} estimation for the muon tracks can be further improved by accessing the vertex information from the HLT-ITS component. The rare J/Ψ or Υ triggers in Muon Spectrometer can be identified in dHLT as two muons both with large p_{t} and these events can be tagged along with other signals from different subdetectors like PHOS (direct photon), FMD (charged particle multiplicity in forward direction), ITS (centrality), TPC (jet trigger) etc.

As a concluding note, this thesis work includes the development, implementation, execution and validation of new formalisms of online data analysis for Muon Spectrometer. The associated algorithms have emerged as an powerful online tool for real time data analysis for LHC collisions. In this way, the work carried out for the degree of "Doctor of Philosophy" becomes a important gear wheel of the gigantic experiment, named ALICE.

Appendix A

Concepts of Cellular Automata

The concepts of cellular automata became popular by Conway's model of *Game of Life*. The exciting part of this model is that it has some feature that closely corresponds to the living cells. The state of cell is governed by some rule imposed by the 'game of life' model,

- The cell state is discrete [either living (1) or dead (0)]
- The number of neighboring cells is fixed, in most of the cases they are the nearest cells.
- The rules describing the evolution of the cells depend on the type problem.
- The cell states change simultaneously i.e. they are clocked.

The model can be explained using the figure of A.1, if the rule of birth, death are presumed as,

- Birth : If a dead cell has three living neighbours, that cell will become alive.

- Death : If a cell has less than two neighbours, it dies of loneliness. If there are more than three neighbours, the area is overpopulated and the cell dies "of" "starvation".

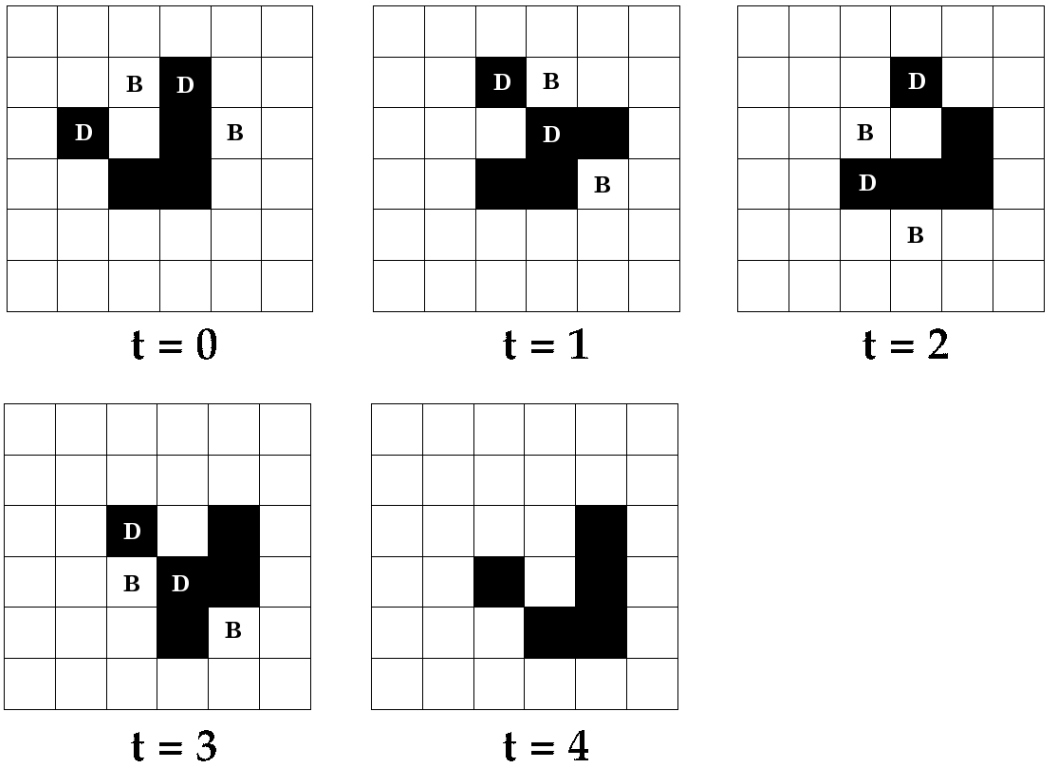

Figure A.1: A glider example for Cellular Automata

The dead cells are shown as colorless boxes in the figure A.1 whereas the dark colored cells represent the living cells. At $t = 0$ of the figure, the colorless cells that are marked as **B** has exactly three neighbours. Therefore in the next time instant at $t = 1$, these give birth of new cells. In addition, the figure at $t = 0$ has some dark cells which are marked as **D**. These boxes represent the cells that dies in the next time instant at $t = 1$ due to loneliness. An example of death of cell due to starvation can be found for the cell in the third row and fourth column of $t = 1$. This cell has four neighbouring cells therefore it dies at $t = 2$. It is interesting to note form the set of figures, that the pattern at $t = 0$ repeats itself at $t = 4$. As if the pattern

moves through the cell grid from top left to the right bottom. This type of cellular automaton is known as glider motion through the grid.

The successful implementation of cellular automata for track formation in high energy physics experiments has been presented by Ivan Kisel [1]-[4]. A two dimensional description of the cellular automata has been discussed in this appendix, which provides the basic understanding of this pattern recognition algorithm. In Fig. A.2 a set of detector layers are shown with the particle hits from charged particle track. The point of collision can be imagined to the left side of Fig. A.2. Thus, the detectors are numbered in increasing order from the left to the right direction.

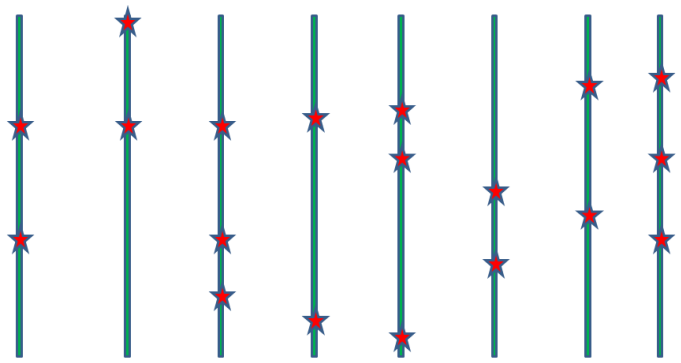

Figure A.2: An array of two dimensional detectors with particles hits.

The track formation for this problem following the cellular automata can be achieved in four steps,

1. Tracklet generation
2. Tracklet connection by neighbour finding
3. Automaton evolution

4. Final selection of track candidates

A.1 Tracklet generation

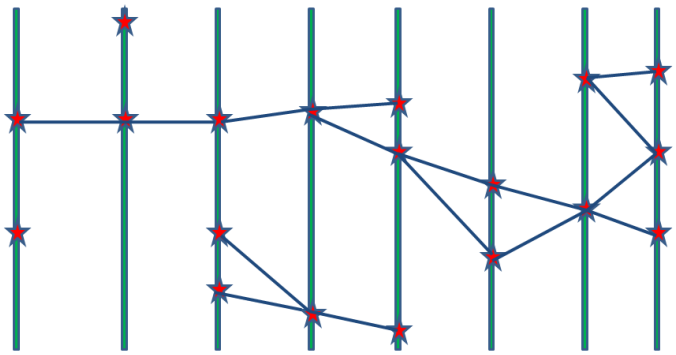

Figure A.3: The tracklet generation by connecting the hits of adjacent chambers.

In the step of tracklet generation, the hits of the adjacent chambers are connected by straight lines as shown in Fig. A.3. This reduces the combinatorics as early as possible in the algorithm. The measurements, which are within the allowed limit of geometrical constraints, are used to form tracklets. For instance, the slope of the line between the two measurements. Another possible cut is the requirement that the tracklets point towards the primary vertex. It helps to skip the noises which are not in the immediate vicinity of the tracks. One such sample noise hit can be found at the top side of the second chamber, which is not connected to any tracklet. This property of the tracker is a key factor for its' fast processing rate even at the presence of considerable noise.

A.2 Tracklet connection

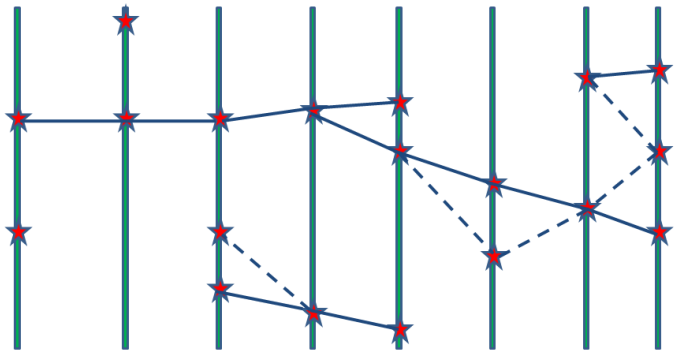

Figure A.4: The tracklet connection

The aim of this stage is to form a relationship between a combination of two tracklets which look like they might have been originated from a particle traveling through the detector. This is performed by implementing another cut on the angle of track. Since in high energy physics experiments, there are large number of tracks, this step allows to filter the candidates of the longest tracks. The rest of the tracks can be identified and recovered after the evolution step of the track formation. The neighbouring tracklets can be selected as,

- A χ^2-test of the local track fit parameters for each of the two tracklets.
- By searching windows around the projected position of the tracklet into the next layer.
- Using an additional cuts on any other parameter (e.g. momentum or angle), but this is only applicable in case of large number noise in the vicinity of the track.

The connected tracks are shown as the continuous lines, whereas the fake clusters are connected by broken lines in Fig. A.4.

A.3 Track evolution

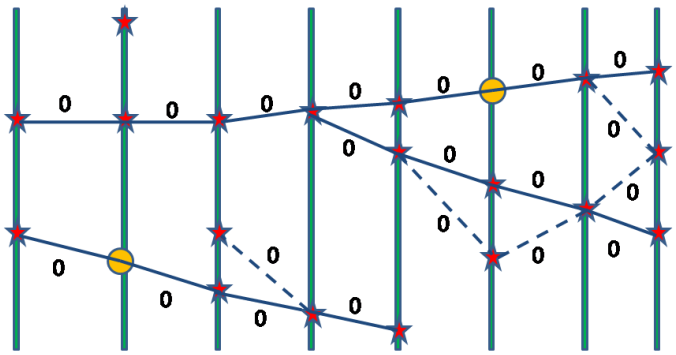

Figure A.5: The creation of virtual hits

When the neighbourhood of a tracklet is defined, the track formation enters into the evolution step of the cellular automaton. The goal is to collect the chains of tracklets, with each tracklet chain being a candidate for a track. The long chains are favoured over short ones because the track parameters or the momentum for track going through the whole detector can be measured more precisely than the incomplete tracks. Therefore, it is the task of the evolution of the cellular automaton to dig out the long chains before the shorter ones.

This task is divided into two segments. In the first step the death and the birth of virtual hits are looped following the basic rule of game of life (as stated above). This continues until a stable configuration is confirmed by cyclic redundancy check

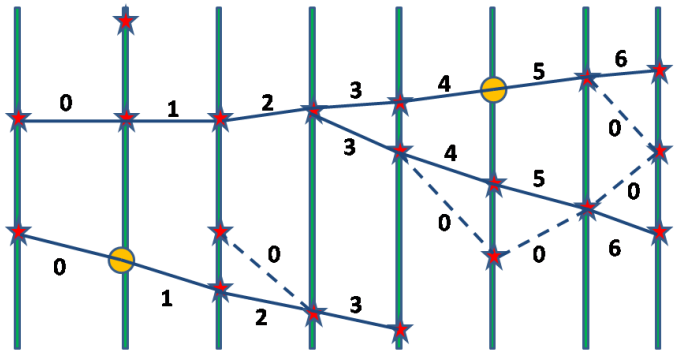

Figure A.6: The ranking of the tracklets.

(CRC). The generated virtual hits are shown in the Fig. A.5 as the circle in the second and sixth detection plane.

In the second step, the tracklets are ranked in such way that a hierarchical connection is established between them. Initially each of tracklet is assigned to rank 0, including those which are discarded in track connection, as shown in Fig. A.5. Then the rank counter of each tracklet is incremented if one of its neighbours has a counter which is at least as high as its own present counter. For example, a tracklet has a counter 3 and neighbours with counters 0, 1, 2 and 3. Then, the new counter of the tracklet will be 4 for the next step. The evolution stops when all counters have stabilised. The final step of evolution is shown in Fig. A.6.

The reason to rank the tracklets which failed in tracklet connection stage is to improve statistics so that no good track candidates are lost. The exact value of χ^2 limit for neighbour selection is either fixed via simulation result or on a set of experimental data. This makes the limit of χ^2 is a soft parameter.

A.4 Track collection

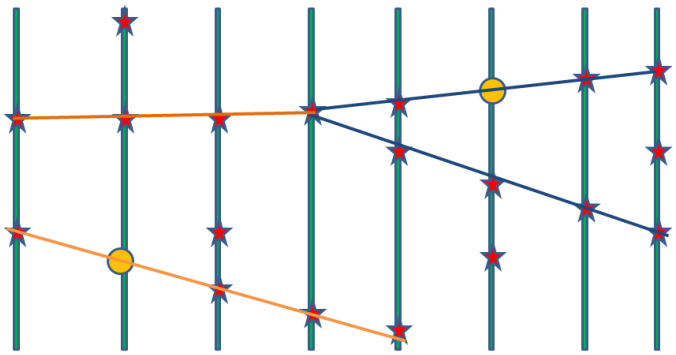

Figure A.7: The collection of tracks shows the final set of tracks.

After the evolution phase, the tracklets with the highest counter are those which form the longest tracklet chains. The tracklet with highest counter in the chain serves as the starting seed, the track is followed by selecting the tracklets for which the rank decreases by -1. It may also happen that there are chains with smaller counter value for initial seeding, for instance the track at the bottom has highest counter 3 [see Fig. A.6], which is much less than the longer chains with highest counter as 6. The collection of those tracks (with highest counter 3) depends on the motivation of the experiment. The general assumption is to collect the track of the longest chains first and then the shorter ones. It continues till all the tracks of minimum predefined length are collected.

At the final state of the track collection a track fitting can be employed to measure the momentum the tracks depending on the intention of the developer.

The final set of the tracks for the given problem are shown in Fig. A.7.

Bibliography

[1] A. Glazov, I. Kisel, E. Konotopskaya and G. Ososkov. Nucl. Instr. and Meth. A **329** (1993) 262-268.

[2] I. Kisel, V. Kovalenko, F. Laplanche, and others (NEMO Collaboration). Cellular automaton and elastic net for event reconstruction in the nemo-2 experiment. . *Technical report* (1997)

[3] I. Abt, D. Emeliyanov, I. Kisel, and S. Masciocchi. Nucl. Instr. and Meth. A **489** (2002) 389-405.

[4] I. Abt, D. Emeliyanov, I. Gorbounov, and I. Kisel. Cellular automa-ton and kalman filter based track search in the hera-b pattern tracker. *Technical report* (2002).

Appendix B

Kalman Filter for Track Fitting

Kalman filter [1] is one of the most promising tool for optimal solution to many tracking and data prediction task. It was originally invented for ballistic missile guidance.

Suppose $\mathbf{a}_{k-1}$ represents the state vector at any site $k-1$,

$$\mathbf{a}_{k-1} = \begin{pmatrix} \boldsymbol{x} \\ \boldsymbol{p} \end{pmatrix}_{k-1}$$

with process noise $\boldsymbol{w}_{k-1}$. Then using the radar detected position and velocity at site $k-1$ and with measurement noise $\boldsymbol{\epsilon}_{k-1}$, the state vector can be predicted for next site k. The estimation of state vector $\mathbf{a}_k$ improves in the next step, when the measurement of the current site k is taken into account. In this way the Kalman filter can be used for better prediction of next site in a recursive manner.

In general a system is subject to random disturbances (process noise) during its evolution following an equation of motion. The goal is to derive the best estimate of

this system's state at a given point from information collected at multiple observation points. In order to achieve this, it is assumed that a system is specified by a p-dimensional column vector $\overline{\boldsymbol{a}}_k$ at site k, where the bar over $\boldsymbol{a}_k$ signifies the true value and without bar it represents an estimated value at site k. The system equation that describes the evolution of the state vector from site $k-1$ to k can be written in the following form,

$$\overline{\boldsymbol{a}}_k = \mathcal{F}_{k-1}\overline{\boldsymbol{a}}_{k-1} + \boldsymbol{w}_{k-1} \tag{B.1}$$

where $\boldsymbol{w}_{k-1}$ represent the process noise as before and $\mathcal{F}_{k-1}$ is a $(p \times p)$-matrix, known as state propagator. It is also assumed that process noise has no bias, i.e, $< \boldsymbol{w}_{k-1} >= 0$ and the covariance is given by,

$$\mathcal{Q}_{k-1} = \left\langle \boldsymbol{w}_{k-1}\boldsymbol{w}_{k-1}^T \right\rangle \tag{B.2}$$

In practice a state vector cannot be directly measured, but the observables of the state vector at the measurement site is calculated. A set of observed values of these observables at site k, forms a n-dimensional column vector called as measurement vector $\boldsymbol{m}_k$. The relation between the measurement vector and state vector forms a measurement equation,

$$\boldsymbol{m}_k = \mathcal{H}_k\overline{\boldsymbol{a}}_k + \boldsymbol{\epsilon}_k \tag{B.3}$$

where $\mathcal{H}_k$ and $\boldsymbol{\epsilon}_k$ represents the $(n \times n)$ dimensional measurement matrix and measurement noise, respectively. The measurement noise is presumably unbiased, i.e.

$< \boldsymbol{\epsilon}_{k-1} >= 0$ and has a covariance given by,

$$\mathcal{V}_k = (\mathcal{G}_k)^{-1} = \left\langle \boldsymbol{\epsilon}_k \boldsymbol{\epsilon}_k^T \right\rangle \tag{B.4}$$

It is further assumed that all $\boldsymbol{\epsilon}_k$ and all $\boldsymbol{w}_k$ are independent and have mean value zero.

The evolution of the state vector is indicated by the index k, where k may be discrete time instant as in case of tracking of space craft or hit points in the detector as in case of high energy experiment. In both type of cases there are three type of operations to be performed to establish the Kalman machinery or the recurrence formulae,

- *Filtering* is the estimation of the state vector at present site, based upon all previous measurements.
- *Prediction* is the estimation of the state vector at next site.
- *Smoothing* is the re-estimation of the state vector at the past site based on all measurement taken upto the present site.

It can be described in terms of schematic figure B.1. After the initialisation step the Kalman gain matrix (see below) is updated in prediction step. The next step is to include the measurement in the account and accordingly the estimation is improved. Then the covariance matrix is updated for the next site and the guess for the next site $k + 1$ is calculated subsequently.

Thus, using the following notations based on Eqn. B.1-B.4, the fomulae for prediction, filtering and smoothing are given below [see Ref. [2]]. It is to be noted that for filtering step two approaches are described. The Kalman gain matrix formulation

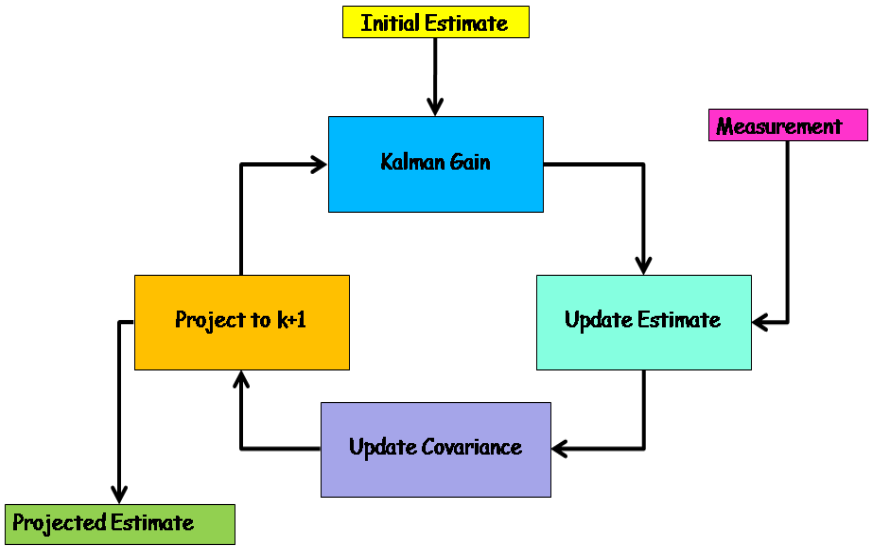

Figure B.1: Kalman recurrence logic for updated evaluation of the state vector

is the most widely used scheme, but there exists also the weighed mean approach which has been followed in this thesis for the particle tracking in Muon Spectrometer.

$\boldsymbol{a}_k^i$: Estimate of $\overline{\boldsymbol{a}}_k$ using measurement upto site i (i.e. $\boldsymbol{a}_k^k = \boldsymbol{a}_k$ for simplicity)

$\mathcal{C}_k^i$: Covariance matrix (or error matrix) for $\boldsymbol{a}_k^i$ (i.e. $\mathcal{C}_k^i = \left\langle \left(\boldsymbol{a}_k^i - \overline{\boldsymbol{a}}_k\right)\left(\boldsymbol{a}_k^i - \overline{\boldsymbol{a}}_k\right)^T \right\rangle$)

$\boldsymbol{r}_k^i$: Residual of measurements as $\boldsymbol{r}_k^i = \boldsymbol{m}_k - \mathcal{H}_k \boldsymbol{a}_k^i$

$\mathcal{R}_k^i$: Covariance matrix for $\boldsymbol{r}_k^i$ (i.e. $\mathcal{R}_k^i = \left\langle \boldsymbol{r}_k^i \boldsymbol{r}_k^{iT} \right\rangle = \left\langle \left(\boldsymbol{m}_k - \mathcal{H}_k \boldsymbol{a}_k^i\right)\left(\boldsymbol{m}_k - \mathcal{H}_k \boldsymbol{a}_k^i\right)^T \right\rangle$)

- *Prediction :*

Extrapolation of the state vector,

$$\boldsymbol{a}_k^{k-1} = \mathcal{F}_{k-1}\boldsymbol{a}_{k-1}$$

Extrapolation of the covariance matrix,

$$\mathcal{C}_k^{k-1} = \mathcal{F}_{k-1}\mathcal{C}_{k-1}\mathcal{F}_{k-1}^T + \mathcal{Q}_{k-1}$$

Residuals of predictions,

$$\boldsymbol{r}_k^{k-1} = \boldsymbol{m}_k - \mathcal{H}_k\boldsymbol{a}_k^{k-1}$$

Covariance matrix of predicted residuals,

$$\mathcal{R}_k^{k-1} = \mathcal{V}_k + \mathcal{H}_k\mathcal{C}_k^{k-1}\mathcal{H}_k^T$$

- *Filtering :* (Using the gain matrix formalism)

Update of the state vector,

$$\boldsymbol{a}_k = \boldsymbol{a}_k^{k-1} + \mathcal{K}_k\left(\boldsymbol{m}_k - \mathcal{H}_k\boldsymbol{a}_k^{k-1}\right)$$

Kalman gain matrix,

$$\mathcal{K}_k = \mathcal{C}_k^{k-1}\mathcal{H}_k^T\left(\mathcal{V}_k + \mathcal{H}_k\mathcal{C}_k^{k-1}\mathcal{H}_k^T\right)^{-1} = \mathcal{C}_k\mathcal{H}_k^T\mathcal{G}_k$$

Update of the covariance matrix,

$$\mathcal{C}_k = (I - \mathcal{K}_k \mathcal{H}_k)\, \mathcal{C}_k^{k-1}$$

Filtered residuals,

$$\boldsymbol{r}_k = \boldsymbol{m}_k - \mathcal{H}_k \boldsymbol{a}_k = (I - \mathcal{H}_k \mathcal{K}_k)\, \boldsymbol{r}_k^{k-1}$$

Covariance matrix of filtered residuals,

$$\mathcal{R}_k = (I - \mathcal{H}_k \mathcal{K}_k)\, \mathcal{V}_k = \mathcal{V}_k - \mathcal{H}_k \mathcal{C}_k \mathcal{H}_k^T$$

χ^2 increment,

$$\chi^2_+ = \boldsymbol{r}_k^T \mathcal{R}_k^{-1} \boldsymbol{r}_k$$

χ^2 update,

$$\chi^2_k = \chi^2_{k-1} + \chi^2_+$$

- *Filtering :* (Using the weighted mean formalism)

Update of the state vector,

$$\boldsymbol{a}_k = \mathcal{C}_k \left[\left(\mathcal{C}_k^{k-1} \right)^{-1} \boldsymbol{a}_k^{k-1} + \mathcal{H}_k^T \mathcal{G}_k \boldsymbol{m}_k \right]$$

Covariance matrix update,

$$\mathcal{C}_k = \left[\left(\mathcal{C}_k^{k-1} \right)^{-1} + \mathcal{H}_k^T \mathcal{G}_k \mathcal{H}_k \right]^{-1}$$

χ^2 increment,

$$\chi^2_+ = \boldsymbol{r}_k^T \mathcal{G}_k \boldsymbol{r}_k + \left(\boldsymbol{a}_k - \boldsymbol{a}_k^{k-1}\right)^T \left(\mathcal{C}_k^{k-1}\right)^{-1} \left(\boldsymbol{a}_k - \boldsymbol{a}_k^{k-1}\right) \tag{B.5}$$

χ^2 update,

$$\chi^2_k = \chi^2_{k-1} + \chi^2_+ \tag{B.6}$$

- *Smoothing :*

Smoothed state vector,

$$\boldsymbol{a}_k^n = \boldsymbol{a}_k + \mathcal{A}_k \left(\boldsymbol{a}_{k+1}^n - \boldsymbol{a}_{k+1}^k\right)$$

Smoother gain matrix,

$$\mathcal{A}_k = \mathcal{C}_k \mathcal{F}_k^T \left(\mathcal{C}_{k+1}^k\right)^{-1}$$

Covariance matrix of the smoothed state vector,

$$\mathcal{C}_k^n = \mathcal{C}_k + \mathcal{A}_k \left(\mathcal{C}_{k+1}^n - \mathcal{C}_{k+1}^k\right) \mathcal{A}_k^T$$

Smoothed residuals,

$$\boldsymbol{r}_k^n = \boldsymbol{r}_k - \mathcal{H}_k \left(\boldsymbol{a}_k^n - \boldsymbol{a}_k\right) = \boldsymbol{m}_k - \mathcal{H}_k \boldsymbol{a}_k^n$$

Covariance matrix of smoothed residuals,

$$\mathcal{R}_k^n = \mathcal{R}_k - \mathcal{H}_k \mathcal{A}_k \left(\mathcal{C}_{k+1}^n - \mathcal{C}_{k+1}^k\right) \mathcal{A}_k^T \mathcal{H}_k^T = \mathcal{V}_k - \mathcal{H}_k \mathcal{C}_k^n \mathcal{H}_k^T$$

It is to be mentioned that Eqn. B.5 together with Eqn. B.6, has been used in

the thesis work to improve the particle track parameters.

Bibliography

[1] R.E. Kalman. Trans. ASME-Journal of Basic Engineering **82** (Series D) (1960) 35-45.

[2] R. Fruehwirth. Nucl. Instr. and Meth. A **262** (1987) 444-450.

Appendix C

Effect of Muon Absorber on Track Parameter

Since the Muon Spectrometer is placed in the forward direction of ALICE, it suffers from high flux of hadrons along the beam direction. Therefore, two absorbers have been used : the beam shielding, which covers the beam pipe and the front absorber that reduces the hadrons by two orders of magnitude within the acceptance region of $2^o < \theta < 9^o$. The front absorber has an additional responsibility to decrease the decay muon background, by limiting the free path of the muonic decay of π's and K's toward the Muon Spectrometer. This is achieved, as the absorber is placed closed to the vertex at 90 cm from the interaction point.

C.1 Geometry of Muon Absorber

ALICE is composed of a large variety of detector systems and so special care has been taken to select the materials for front absorber. Otherwise the back scattering

from the absorber may create undesirable backgrounds to the other detectors inside the L3 magnet. Another impact of this absorber has been observed in the dimuon invariant mass distribution of the Muon Spectrometer. It is important of to find the vertex as accurately as possible in order to measure the momentum of the particles. Therefore low-Z materials are used for the front part and high-Z materials are placed in the rear part of the absorber.

The present geometry of the absorber, shown in Fig. C.1, is investigated using the geometry package of ROOT. A navigation pointer is propagated through the absorber from front part to rear region of the absorber in small steps. It keeps on recording the type of material in two dimensional histograms. Finally the two dimensional histograms are plotted on canvas, which produces the cross-sectional view of the upper half of y-z plane of the absorber presented in Fig. C.1.

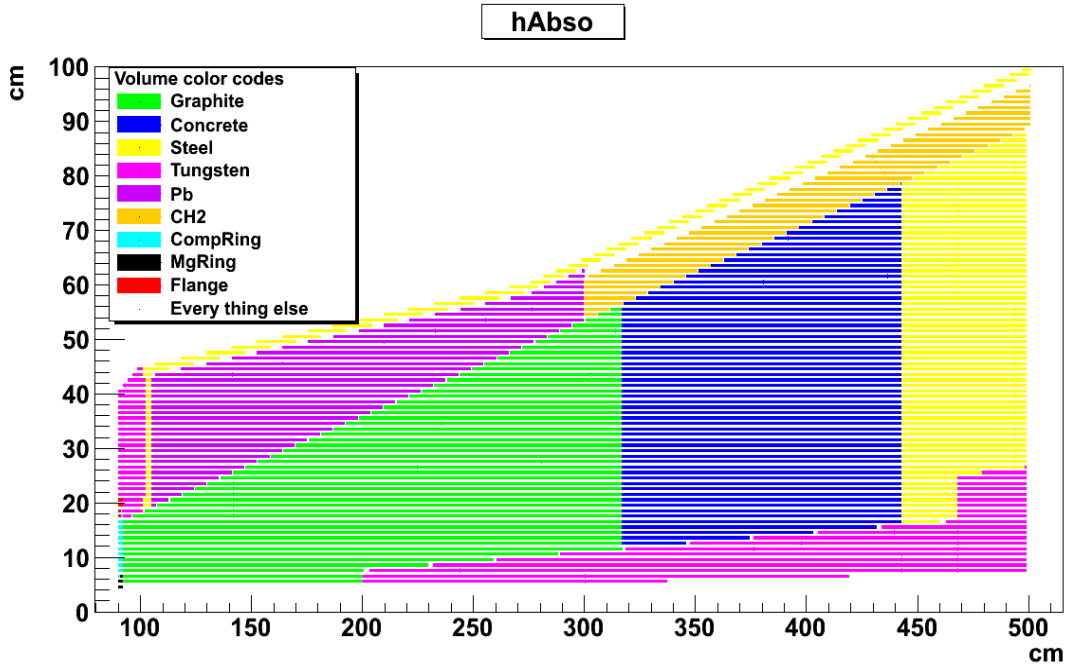

Figure C.1: A cross-sectional view of front absorber in y-z plane.

C.2 Absorber effect on mass spectrum

The effect of absorber on the dimuon invariant mass spectrum has been observed in for multiple Coulomb scattering and energy loss. These effects are demonstrated using the figure C.2 and C.3. Two data-sets of parametrised Υ have been generated with and without the absorber. In Fig. C.2, the invariant mass spectrum of the oppositely charged muon pairs are shown in the case where there is no absorber. Ideally this should be close to the delta function but it has a width (∼60 MeV) limited by the finite detector resolution and performance of the tracker.

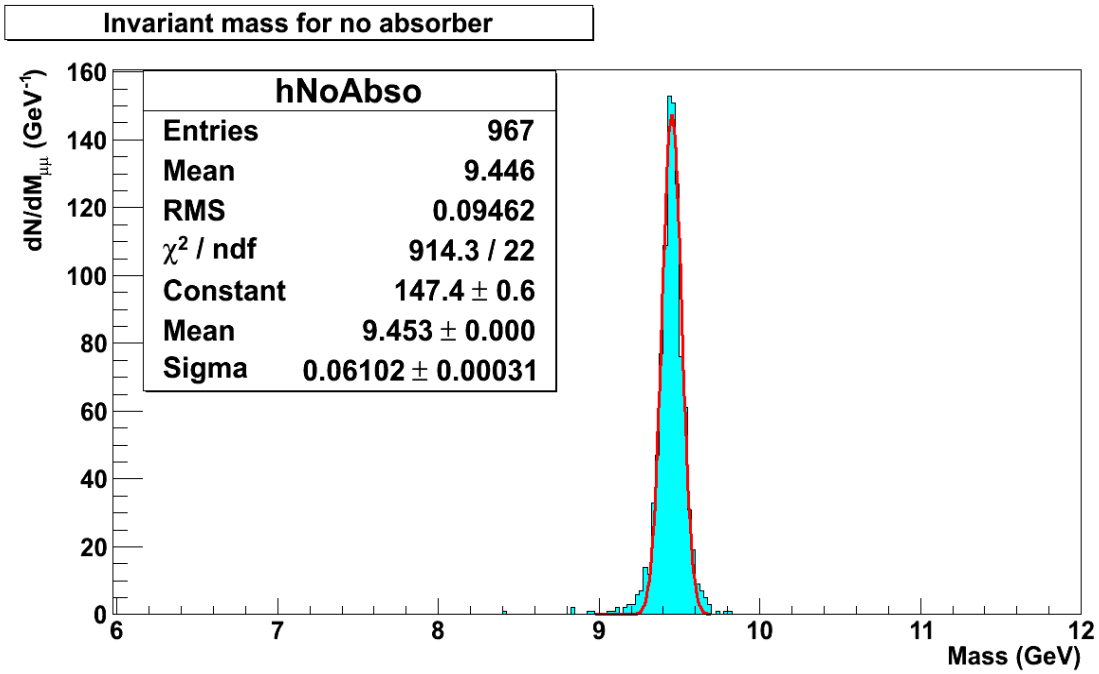

Figure C.2: Invariant mass spectrum of Υ without the absorber and in a ideal situation without any pion or kaon background.

The histograms of Fig. C.3 shows the effect of the absorber on mass spectrum. As it can be observed, the absorber increases the width of the mass spectrum to ∼300 MeV and it is shifted by ∼400 MeV from peak position at 9.4 GeV. If the correction due to multiple Coulomb scattering is considered then this reduces to 166

MeV, but the peak is still shifted to 8.9 GeV instead of 9.4 GeV. The mean position of the spectrum can be corrected if the ionisation energy loss is taken into account. When both of the corrections are applied together, one gets back the Υ spectrum with proper correction for multiple Coulomb scattering and energy loss. The quantitative formulation of these effect are presented below.

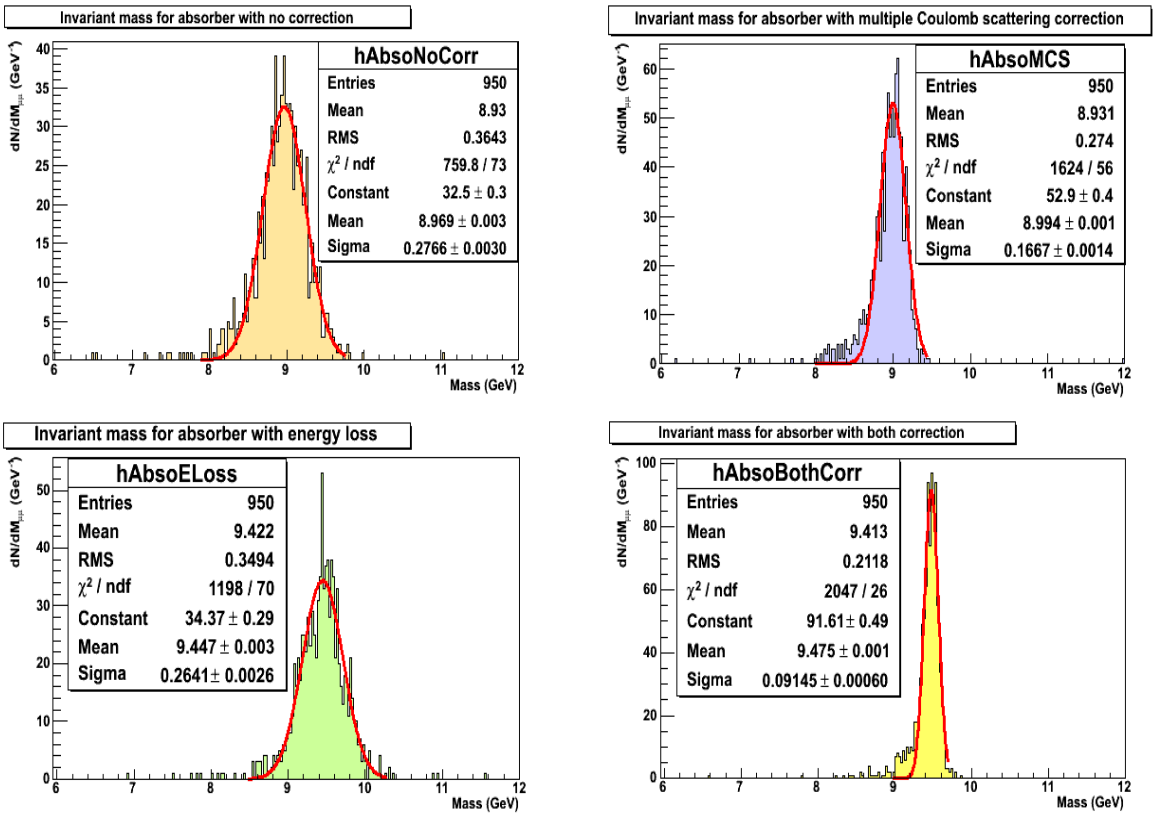

Figure C.3: Effect of absorber on mass spectrum of parametrised Υ : a) Effect of absorber on mass spectrum (top-left), b) Effect of absorber on mass spectrum when only the correction due multiple Coulomb scattering is applied, (top-right) c) Effect of absorber on mass spectrum when only the correction due to energy loss is applied (bottom-left), d) Effect of absorber on mass spectrum when both the corrections are applied (bottom-right).

The energy loss is mainly due to the ionization energy loss process, since the radiative energy loss plays the major role only after few hundred GeV [1]. Thus, the

ionisation energy loss is calculated with the Bethe-Bloch formula [2],

$$-\frac{\mathrm{d}E}{\mathrm{d}x} = \kappa z^2 \cdot \frac{Z}{A}\frac{1}{\beta^2}\left[\ln\frac{2\gamma^2\beta^2 m_e c^2}{I} - \beta^2\right] \quad ,$$

with,

$$\kappa = 4\pi N r_e^2 m_e c^2 \quad .$$

where N is the Avogadro number, z is the charge of the external particle in the absorber, r_e is the classical electron radius, m_e is the electron mass, Z is the atomic number of the absorber material, A is the atomic mass of the absorber material, I is the mean excitation energy of the material, and β and γ are the conventional relativistic parameters.

The other important effect is the scattering of the particles inside the Front Absorber. It is measured in terms of the angle (θ) between the track and the beam axis. However, if the invariant mass is calculated by assuming this scattering angle then the mass resolution gets worse. Therefore, a correction in the angular measurement ($\Delta\theta_B^2$) is performed following the Branson correction [3].

$$\Delta\theta_B^2 = \alpha^2(F_0 - \frac{F_1^2}{F_2})$$

Where the F_0, F_1, and F_2 are, respectively, the 0^{th}, 1^{st} and 2^{nd} moment of (z) calculated with the inverse radiation-length $X_0(z)$ distribution,

$$\begin{aligned} F_0 &= \int_0^L \tfrac{dz}{X_0(z)} \\ F_1 &= \int_0^L z\tfrac{dz}{X_0(z)} \\ F_2 &= \int_0^L z^2\tfrac{dz}{X_0(z)} \end{aligned}$$

and α (=0.0136/p, with p in GeV/c) is inversely proportional to total momentum.

A detailed derivation can be found in the reference [1]. When both these effects are incorporated, the reconstructed transverse momentum matches closely to the Monte Carlo value.

Bibliography

[1] Homepage of Andreas Morsch
[http://morsch.web.cern.ch/morsch/MUONdoc/Contents.html]

[2] H.A. Bethe and J. Ashkin. Passage of radiation through matter, in "Experimental Nuclear Physics" (E. Segre, ed). Report. *vol. 1 Part 2, (John Wiley and Sons, New York)*, 1959, pp. 166-357

[3] J.P.Cussonneau, P.Lautridou, L.Luquin, V.Metivier, A.Rahmani, V.Ramillien, T.Reposeur and A.Morsch. Tracking Peformances of Several Front-Absorber Designs. Report. *ALICE Internal Note*, 1998, INT-98-27

List of Publications

Journal Publications :

1. **"ALICE: Physics performance report, volume II"**,
   The ALICE Collaboration et. al.,
   J. Phys. G **32** (2006) 1295-2040
   [http://iopscience.iop.org/0954-3899/32/10/001/pdf/0954-3899_32_10_001.pdf]

2. **"The ALICE experiment at the CERN LHC"**,
   The ALICE Collaboration et. al.,
   JINST **3:S08002** (2008)
   [http://iopscience.iop.org/1748-0221/3/08/S08002/pdf/1748-0221_3_08_S08002.pdf]

3. **"Heavy flavour physics in ALICE"**,
   The ALICE Collaboration et. al.,
   J. Phys. G **35** (2008) 104144
   [http://iopscience.iop.org/0954-3899/35/10/104144/pdf/0954-3899_35_10_104144.pdf]

4. **"The ALICE muon spectrometer and related physics"**,
   The ALICE Collaboration et. al.,
   J. Phys. G **35** (2008) 104145
   [http://iopscience.iop.org/0954-3899/35/10/104145/pdf/0954-3899_35_10_104145.pdf]

5. **"Alignment of the ALICE Inner Tracking System with cosmic-ray tracks"**,
   The ALICE Collaboration et. al.,
   JINST **5:P03003** (2010)
   [http://iopscience.iop.org/1748-0221/5/03/P03003/pdf/1748-0221_5_03_P03003.pdf]

6. **"First proton-proton collisions at the LHC as observed with the ALICE detector: Measurement of the charged particle pseudorapidity density at $sqrts$ = 900 GeV"**,

The ALICE Collaboration et. al.,
Eur. Phys. J. C **65** 1-2 (2010) 111-125
[http://epjc.edpsciences.org/articles/epjc/pdf/2010/01/10052_2009_Article_1227.pdf]

7. **"Charged-particle multiplicity measurement in proton-proton collisions at $\sqrt{s}$ = 0.9 and 2.36 TeV with ALICE at LHC"**,
The ALICE Collaboration et. al.,
Eur. Phys. J. C **68** (2010) 89-108
[http://epjc.edpsciences.org/articles/epjc/pdf/2010/07/10052_2010_Article_1339.pdf]

8. **"Charged-particle multiplicity measurement in proton-proton collisions at $\sqrt{s} = 7$ TeV with ALICE at LHC"**,
The ALICE Collaboration et. al.,
Eur. Phys. J. C **68** (2010) 345-354
[http://epjc.edpsciences.org/articles/epjc/pdf/2010/08/10052_2010_Article_1350.pdf]

9. **"Midrapidity antiproton-to-proton ratio in pp collisions at $\sqrt{s} = 0.9$ and 7 TeV measured by the ALICE experiment"**,
The ALICE Collaboration et. al.,
Phys. Rev. Lett. **105** (2010) 072002
[http://prl.aps.org/pdf/PRL/v105/i7/e072002]

10. **"Two-pion Bose-Einstein correlations in pp collisions at $\sqrt{s}$ = 900 GeV"**,
The ALICE Collaboration et. al.,
Phys. Rev. D. **82** (2010) 052001
[http://prd.aps.org/pdf/PRD/v82/i5/e052001]

11. **"Transverse momentum spectra of charged particles in protonproton collisions at $\sqrt{s} = 900$ GeV with ALICE at the LHC"**,
The ALICE Collaboration et. al.,
Phys. Lett. B. **693** (2010) 53-68
[http://dx.doi.org/10.1016/j.physletb.2010.08.026]

12. **"Charged-particle multiplicity density at mid-rapidity in central Pb-Pb collisions at $\sqrt{s_{NN}}$ = 2.76 TeV"**,
The ALICE Collaboration et. al.,
[arXiv:1011.3916v2 [nucl-ex]]

13. **"Elliptic flow of charged particles in Pb-Pb collisions at 2.76 TeV"**,
The ALICE Collaboration et. al.,
[arXiv:1011.3914v1 [nucl-ex]]

14. **"Suppression of Charged Particle Production at Large Transverse Momentum in Central Pb-Pb Collisions at $\sqrt{s_{NN}}$ = 2.76 TeV"**,
The ALICE Collaboration et. al.,
[arXiv:1012.1004v1 [nucl-ex]]

Other Refereed Publications :

ALICE Internal Note :

1. **"RawData format for the MUON spectrometer"**,
Ch. Finck, L. Aphecetche, A. Baldisseri, V.Barret-Ramillien, J.-L.Berney, V.Chambert, **I.Das**, I.Hrivnacova, B.Y.Ky, Y.Le Bornec, F. Lefevre, S.Pal, Ch.Renard, S.Rousseau, A.Szostak and N.Willis,
ALICE Internal Note, ALICE-INT-2005-012,
[https://edms.cern.ch/document/591904/3]

2. **"ALICE Dimuon High Level Trigger : Project Review"**,
Bruce Becker, Roger Fearick, Artur Szostak, Gareth de Vaux, Zeblon Vilakazi, Corrado Cicalo, Davide Marras, Gianluca Usai, Sukalyan Chattopadhyay, **Indranil Das**, Sabyasachi Siddhanta, Volker Lindenstruth, Timm Steinbeck and Florent Staley,
ALICE Internal Note, ALICE-INT-2007-022,
[https://edms.cern.ch/document/878756/1]

Publications in Conferences/Symposiums :

1. **"Heavy quark resonance suppression in relativistic heavy ion collision"**,
I.Das, S.Chattopadhyay, A.K.Dutta-Majumdar, P.Roy, P.Bhattacharya, B.Sinha,
XVI DAE-BRNS High Energy Physics Symposium (Nov 29 - Dec 3, 2004).

2. **"J/Ψ Suppression as a signure of QGP"**
I.Das, S.Chattopadhyay, A.K.Dutta-Majumdar, P.Roy, P.Bhattacharya, B.Sinha,
DAE-BRNS Symposium on Nuclear Physics (Dec 6-10, 2004), Vol 45B, p. 484, 2004.

3. **"Hit reconstruction algorithm for high level trigger of dimuon spectrometer of ALICE"**,
S.Chatterjee, **I.Das**, S.Pal, S.Chattopadhyay,
DAE-BRNS Symposium on Nuclear Physics (Dec 12-16, 2005), Vol 50, p. 402.

4. **"Single muon p_t-distribution from open and hidden charm (bottom) at s1/2 = 5.5 ATeV"**,
Indranil Das, Sanjoy Pal,
DAE-BRNS Symposium on Nuclear Physics (Dec 12-16, 2005), Vol 50, p. 403.DAE Sym.

5. **"Production of Cathode Pad Chambers for 2nd Muon Tracking Station of ALICE"**,
M.Danish Azmi, S.Bose, S.Chattopadhyay, D.Das, **I.Das**, P.Datta, A.K.Dutt-Majumdar, M.Irfan, S.Jana, I.A.Khan, S.Pal, L.Paul, P.Roy, T.Sinha, B.C.Sinha,
DAE-BRNS Symposium on Nuclear Physics (Dec 12-16, 2005), Vol 50, DAE Sym.

6. **"Study of Characteristics of Production Batch MANAS chips"**,
M.Danish Azmi, S.Chattopadhyay, **I.Das**, S.Pal, P. Roy, S.Sarkar, S.Sen, T.Sinha. B.C.Sinha,
DAE-BRNS Symposium on Nuclear Physics (Dec 12-16, 2005), Vol 50, p. 449.

7. **"High Voltage characteristic of large area Cathode Pad Chambers for Muon Spectrometer of ALICE"**,
M.Danish Azmi, S.Bose, S.Chattopadhyay, D.Das, **I.Das**, M.Irfans, S.Das, S.Pal, L.Das, T.Sinha and B.C.Sinha,
Quark Matter (2008).

8. **"Commissioning tests of the 2nd Muon Tracking Station of ALICE"**,
M.Danish Azmi, S.Bose, S.Chattopadhyay, D.Das, **I.Das**, L.Das, S.Das, M.Irfans, S.Pal, T.Sinha and B.C.Sinha,
DAE-BRNS Symposium on Nuclear Physics (2008).

9. **"The first Muon Track in ALICE Dimuon Spectrometer"**,
Indranil Das, Sukalyan Chattopadhyay,
DAE-BRNS Symposium on Nuclear Physics (2008).

10. **"A new formalism of full tracking in dimuon high level trigger"**,
Indranil Das, Sukalyan Chattopadhyay,
DAE-BRNS Symposium on Nuclear Physics (2009).

11. **"The ALICE Dimuon Spectrometer High Level Trigger"**,
Bruce Becker, Sukalyan Chattopadhyay, Corrado Cicalo, **Indranil Das**, Gareth de Vaux, Roger Fearick, Volker Lindenstruth, Davide Marras, Abhijit Sanyal, Sabyasachi Siddhanta, Florent Staley, Timm Steinbeck, Artur Szostak, Gianluca Usai, Zeblon Vilakazi,
IEEE NSS conference Oct 2008 Dresden, Germany.